ACOUSTIC VELOCITY AND ATTENUATION OF ROCKS: ISOTROPY, INTRINSIC ANISOTROPY, AND STRESS INDUCED ANISOTROPY

A DISSERTATION

SUBMITTED TO THE DEPARTMENT OF GEOPHYSICS

AND THE COMMITTEE ON GRADUATE STUDIES

OF STANFORD UNIVERSITY

IN PARTIAL FULFILLMENT OF THE REQUIREMENTS

FOR THE DEGREE OF

DOCTOR OF PHILOSOPHY

By

Hezhu Yin

December 1992

I certify that I have read this dissertation and that in my opinion it is fully adequate, in scope and quality, as a dissertation for the degree of Doctor of Philosophy.

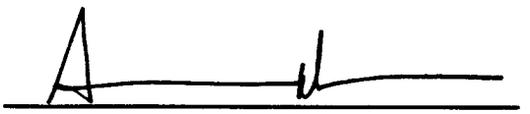

Amos Nur (Principal Advisor)

I certify that I have read this dissertation and that in my opinion it is fully adequate, in scope and quality, as a dissertation for the degree of Doctor of Philosophy.

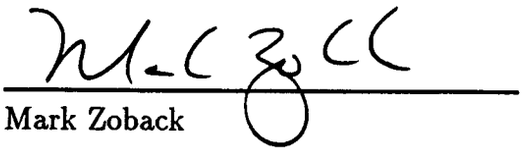

Mark Zoback

I certify that I have read this dissertation and that in my opinion it is fully adequate, in scope and quality, as a dissertation for the degree of Doctor of Philosophy.

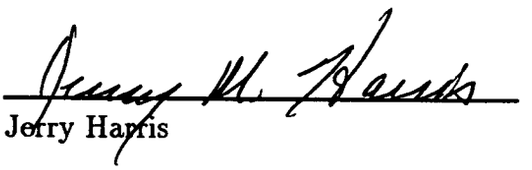

Jerry Harris

I certify that I have read this dissertation and that in my opinion it is fully adequate, in scope and quality, as a dissertation for the degree of Doctor of Philosophy.

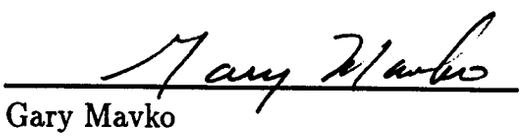

Gary Mavko

Approved for the University Committee on Graduate Studies:

Dean of Graduate Studies

Abstract

Acoustic properties of reservoir rocks depend in complex ways on many physical parameters, only some of which are independent of each other. An improved understanding of the interrelationships among rock acoustic properties and petrophysical parameters has been essential to merge geophysical observations with petrophysical parameters for refined characterization of geological subsurface structures and more successful exploration of petroleum reservoirs. In this dissertation, I present results from new studies of geophysical and petrophysical properties of sedimentary rocks via sophisticated experiments and physical modeling approaches that investigate isotropic, intrinsic anisotropic, and stress-induced anisotropic properties of rocks.

In the interrelationships among seismic properties and petrophysical parameters of the rocks featured in this dissertation, I first address the designated experiments and data, and then treat theoretical analysis and modeling.

In chapter 2, I discussed a series of intensive experiments on unconsolidated sand-clay mixtures and glass-beads. The results clarified the nature of the relationships among porosity and clay-content, permeability and clay-content, cementation and porosity, and their effects on the acoustic properties at various confining pressures under both dry and saturated conditions. More importantly, a qualitative transition of acoustic properties as function of clay-content between shaly-sand and sandy-shale is characterized by a "critical clay-content" in the data.

Consequently, I devised and discussed a new physical concept, namely "critical porosity", in chapter 3 in the context of acoustic velocity as function of porosity, and acoustic velocity as function of clay-content. I have successfully applied the critical porosity concept in modeling clay-effect correction on velocity through an analysis of the past experimental data in Stanford Rockphysics database.

During the data analysis of the critical porosity modeling, I realized that some

scatter around the model might be caused by velocity anisotropy of rocks, such as Berea Sandstone with its 10% intrinsic velocity anisotropy. In chapter 4, I focused on experimental studies of velocity and attenuation anisotropy in shaly rocks. I experimented with shaly rocks not only because many shaly rocks are intrinsically anisotropic, but also because the elastic properties of shaly rocks have been difficult to predict, and have been a challenging subject in rockphysics. In three sets of Freeman Jewett shale samples, I observed intrinsic transverse isotropic pattern under both dry and saturated conditions. More importantly, I observed time-dependent variations of acoustic velocity and attenuation during the pore-pressure equilibrium process, and the results led to a new method to measure the hydraulic permeability of these low permeable rock samples. Under controlled high pore-pressures, I also measured these shale samples' acoustic velocity and attenuation, and the results provide insight to the applicability of effective pressure theory to such low permeable rocks.

Finally, I studied stress-induced acoustic velocity and attenuation anisotropy via a special experimental apparatus that applied true three-dimensional polyaxial loading to eight rock samples examined. The data show that three-dimensional stress may cause orthorhombic acoustic velocity and attenuation anisotropy. The results suggest that stress-induced anisotropy is a function of finite strain, hence, three-dimensional stress patterns are more observable in soft-rocks than in hard-rocks when using dynamic acoustic measurements. To express more clearly the relationship between attenuation anisotropy and the three-dimensional stress pattern, I developed a pseudo-hodogram method to visualize the three-dimensional attenuation anisotropy.

Acknowledgements

I wish to express my sincerest gratitude to Amos Nur. This dissertation profited greatly from his advice, and I am indebted to him for his continuous financial support throughout my stay at Stanford.

I wish to thank all the members of my dissertation committee: Burt Auld, Jerry Harris, Gary Mavko, Norman Sleep, and Mark Zoback for their critical comments and thoughtful discussions.

I wish to thank all the friends, professors, and students who made my studying years at Stanford an experience both unique and enjoyable.

This dissertation has greatly benefited from thoughtful discussions with Richard Nolen-Hoeksema, Jack Dvorkin and Dan Moos.

Over my five years at Stanford, it has been a great experience to be part of the Stanford Rockphysics and Borehole Project (SRB) research group. I wish to thank all former and present students of SRB for their stimulating discussions, creative support, and continuing friendship. I am especially grateful to Margaret Muir for her kindness and resourcefulness ever since my arrival at Stanford.

I wish to thank my mother Shengjin Jin for her motivation and encouragement in my study at Stanford.

Finally, my special thanks go to Jenny Z. Li, my wife, not only for her moral support, but also for her technical assistance. With her talented computer programming skill, she has written or debugged many modeling programs needed in this dissertation. Special thanks also go to Lillian C. Yin, my daughter, because her innocent laugh and lovely face has enriched my daily life, and also because her seemingly childish but genuinely motivated questions have inspired me throughout these Stanford years.

Four years ago, Lillian was 5. During her first visit to the SRB lab, she asked

me "Dad, why doesn't your lab have any window?" I said, "Because it is in the sub-basement, underground." "Oh..." she said, "But if you had a window here, couldn't you see the underground rock better with your eyes than with those waves on your computer screen here?"

Now, had I had a glass window to see underground outside the SRB lab, I wonder how differently I would have viewed the rocks featured in this dissertation. If computer screen is accurate, the underground must be... may be... colorful!?

"A fool may ask more questions in an hour than a wise man can answer in seven years." Well... So long, Stanford.

Contents

List of Figures

List of Tables

Chapter 1

Introduction

Seek truth from facts.

— Chinese proverb

The need to extract more information about petrophysical properties of the subsurface from geophysical measurements has inspired a great deal of research in the field of rockphysics. I view rock's lithology, porosity, permeability, density, pore-geometry, fluid saturation, sorting, grain size, roundness, cement, etc. as its petrophysical properties; and its acoustic velocities, attenuation, impedance, etc. as geophysical properties that can be observed both in laboratory and in-situ through seismic measurements. With the development of more sophisticated in-situ geophysical measurements and with increased use of amplitude variations, such as in full-waveform acoustic logging, amplitude versus offset (AVO) multi-component 3-D seismic surveys, vertical seismic profiling (VSP), and cross-well logging, a better understanding of the relations between geophysical observation and petrophysical parameters has become an ever more urgent need. The present dissertation is one among several efforts to relate petrophysical parameters of rocks, namely porosity, clay-content, and permeability, to observable geophysical measurements, such as P-wave and S-wave velocities, under a simulated in-situ stress environment through extensive laboratory

experiments and physical modeling.

1.1 Facts related to the geophysical properties of rocks

It has been reported that seismic properties of rocks are affected by

1. porosity,
2. fractures and cracks,
3. density,
4. clay-content,
5. lithology,
6. saturation,
7. pore fluids,
8. permeability,
9. diagenetic history,
10. cementation,
11. temperature,
12. pore pressure,
13. lithostatic or tectonic stresses.

These petrophysical and environmental parameters are often not independent. Also, at various scales, the preferential grain-orientation, interbedded shaly formations, and local or tectonic stress fields may cause observable anisotropic phenomena both in-situ and in laboratory.

1.2 Goal of the thesis

Noting the many theoretical or modeling papers published in rockphysics literature, I sought to help balance the field with new experimental research and physical modeling. The present dissertation addresses the interrelationships among geophysical properties and petrophysical parameters of rocks with emphases on *experimental investigation and physical modeling* of isotropy, intrinsic anisotropy, and stress-induced anisotropy in geophysical observations.

Most theories and models used to predict the values of seismic properties—perhaps the most common and useful geophysical property—are phenomenological, but natural rocks are complicated enough that invariably important parameters affecting seismic properties of rocks might be left out if there have been no accompanying

experiments. Whenever possible, I have deliberately designed experiments which rely on state-of-the-art laboratory measurements throughout this dissertation. Mathematical modeling is a powerful tool in dealing with the quantities, magnitudes, their relationships, and quantitative attributes; but a physical modeling approach may reveal the nature, the changes, the interaction, and the qualitative attributes of the matter. I focus on physical modeling approach with appropriate reasoning, rather than just a model originated from data fitting, in this dissertation. Experimental data and physical modeling together should yield a better understanding of rocks characteristics and associated wave phenomena.

1.3 Summary of the thesis

I begin in Chapter 2 by conducting an extensive series of experiments on the effects of compaction and clay-content on porosity, permeability, and their interrelationships with velocities. I measured porosity, permeability, P-wave, and S-wave velocities of unconsolidated dry and brine saturated clean Ottawa sand, pure kaolinite, and ten of their mixtures with different kaolinite weight percent at various confining pressures, up to 50 MPa, and at both dry and brine saturated conditions. With clay-content as a variable, porosity is minimized at 20%—40% clay by weight depending on confining pressure. With classification of pore-filling clay and matrix clay, the porosity minimums of the mixtures were explained by a physical definition of porosity in mixtures of spherical particles. Permeability is a strong function of clay-content when clay-content is less than the above minimums. Permeability is fairly independent of clay-content for clay above that minimums. My analysis suggests that clay affects permeability mostly through pore-size distribution, and less through the bulk porosity of the mixtures. I used a statistical method of calculating the pore-size distribution used in the Kozeny-Carman Equation, which showed good agreement between the measured data and the modeling method. I observed a peak in P-wave velocity

versus clay- content at about 40% clay by weight. I explained the observations by simple physical models, modified "isostrain-average" and "isostress-average", which acceptably represent the data. The key to obtaining these robust physical models is the critical clay-content, below which the sand-matrix is stress-bearing, and above which clay matrix and sand grains are equally stress-bearing. I also investigated a less well-studied effect on rock elastic properties—the cementation effect—by varying amounts of epoxy "cement" in glass beads. I observed P-wave and S-wave velocity at different epoxy "saturation", confining pressure, and different stages of epoxy curing time. The results showed that a few percent of epoxy cementation can yield tremendous velocity changes. These extensive experiments revealed not only the nature of the interrelationships among porosity, clay-content, permeability, cementation, and their effects on acoustic velocities, but they also marked a qualitative leap of elastic properties as a function of porosity in porous media. This insight led to a new physical concept—"Critical Porosity".

In Chapter 3, I present a physical model of a solid-fluid two phase composite, the *Critical Porosity Model.* The model resulted from a further examination of the data in Chapter 2, and the massive SRB rock property database. Critical Porosity is a conceptual boundary between the solid-host and fluid-host porous media, a boundary that marks qualitative phase transition of elastic properties in porous media. I discuss the physical insight of Critical Porosity and its intuitive mathematics with the concepts of "quantitative change" and "qualitative change". I apply the concept of Critical Porosity to clay-effects correction on velocity with isostrain and isostress mechanisms. The results show excellent agreement between our physical models and the measured data.

In Chapter 4, I analyze anisotropy in both the time and frequency domains. I investigate P-wave and S-wave anisotropy of Freeman Jewett Shale under both dry and brine saturated conditions with confining pressure varying from 5 to 50 MPa.

I measure three sets of samples to identify the anisotropic properties of these samples. I observe not only their intrinsic anisotropic properties, but also their time-dependent velocity and attenuation variations. Monitoring of the pore-pressure equilibrium state enhances permeability estimates through the acoustic measurements. The experimental results show that velocity and attenuation anisotropy are indeed intrinsic properties of the poorly consolidated Freeman Jewett Shale, and the anisotropy is due to preferential orientation of its mineral grains and interbedded clay layers. The magnitude of the anisotropy in Freeman Jewett Shale decreases with increasing confining pressure as cracks along the bedding planes are closed.

In Chapter 5, I investigate stress-induced velocity and attenuation anisotropic properties of rocks. With a specially designed set-up, I attached three pairs of multi-component ultrasonic transducers on all six faces of a cubic test sample to measure one compressional wave and two orthogonally polarized shear waves along each of the three principal directions of the cubic rock sample under "true triaxial loading". I test eight rock samples: one granite, one dolomite, two sandstones, one siltstone, two shales, and one loose Ottawa Sand. I have observed strong P-wave velocity anisotropy, striking S-wave splitting, and attenuation anisotropy under the polyaxial loading process. I describe a physical anisotropy model—orthorhombic anisotropy of both velocity and attenuation under the polyaxial loading.

In Appendix A, I fill in some background materials on laboratory ultrasonic measurement. These materials have guided my design of the ultrasonic measurements throughout this dissertation.

In Appendix B, I review the fundamentals of acoustic anisotropy assumed in Chapter 4 and Chapter 5.

Finally, Appendix C is a technology disclosure to review the trends and the developments of contemporary cross-well logging source design, and to reveal the details of the U.S. patent, No. 5,069,308, *Low Impedance Down-Hole Acoustic Source for*

Well Logging—an optimal impedance matching design. This disclosure was a natural result of a field experiment at Palo Alto bay marsh, "the in-situ marine sediment velocity measurement", using my specially designed low-impedance acoustic transducer in 1989.

Chapter 2

Effects of compaction, clay-content and cementation on porosity, permeability and velocities in granular materials

Genuine knowledge comes from practice. How does a pear taste? You must try it out yourself.

— Chinese Proverb

To estimate petrophysical parameters (porosity ϕ and permeability k) through geophysical measurements (P-wave and S-wave velocities), an extensive series of experiments were designed to study the effects of compaction and clay-content on porosity, permeability, and velocities of granular materials in this chapter. Porosity, permeability, and ultrasonic P-wave and S-wave velocities were measured among unconsolidated clean Ottawa sand, pure kaolinite, and ten of mixtures varied by kaolinite weight percent at both dry and brine saturated conditions, and at various confining pressures up to 50 MPa.

With clay-content as a variable, porosity is minimized at 20% - 40% clay by weight depending on confining pressure. Through classification of pore-filling clay and matrix

clay, the porosity minimums of the mixtures at various pressures were explained by a physical definition of porosity in two-size particles mixture. Permeability is most affected when clay-content is less than the above minimums, called here the critical clay-content, and fairly independent of clay when clay-content is greater than the critical clay-content. A peak in P-wave velocity versus clay-content was found at about 40% clay by weight.

The effect of cementation on elastic properties of rock, was studied by compounding glass beads and epoxy as cement to form a quantifiable facsimile of a natural granular medium. P-wave and S-wave velocities were measured at different epoxy saturations, confining pressures, and with different states of epoxy solidification over various epoxy curing times. The results reveal that a few percent of cement yields tremendous velocity changes. The experimental observations were the key to solid agreements between my physical models and the measured data.

2.1 Introduction

How and which physical properties affect seismic properties in unconsolidated or poorly consolidated rock has long been topical among those interested in both reservoir and civil engineering. For decades, researchers have focused on the effect of porosity on velocity and formulated relations between velocity and porosity, such as, Voigt (1928), Reuss (1929), Wood (1941), Wyllie (1956), and Raymer et al. (1980). Despite widespread use, such averaging models have failed to account for scatter in the velocity-porosity data of unconsolidated sediments and can barely be used for predictive purposes (Nobes et al., 1986). For consolidated sediments, work by Tosaya et al. (1982) and Han et al. (1986) have shown that much of the scatter in the velocity–porosity relationship may be attributed to clay content. Similarly, both field and laboratory observations have revealed that clay-content and the location of clay within rock grains and pore-spaces dominates the porosity-permeability relationships

(Nearsham, 1977; and Heron, 1987). Although the effects of compaction on velocity have been studied theoretically and experimentally on sands, glass beads and shale (Domenico, 1977; Digby, 1981; and Johnston, 1987), at the time of my work, I did not find that *experimental* studies had been designed to address the effects of clay content and lithology on velocity in unconsolidated sediments, nor had studies been made to address the effects of cementation on velocity in granular sediments.

This chapter addresses laboratory experiments on acoustic velocities and permeability as a function of clay content at various confining pressures, and over varied mixtures of sand and clay. The chapter also addresses the effects of cementation on acoustic velocities in mixtures of glass beads and epoxy.

2.2 Sand-clay mixture: a synthetic sediment

2.2.1 Sample preparation and experiment

The samples of sand-clay mixture were prepared by mixing various proportions of clean Ottawa sand with pure kaolinite powder at room dry condition. The Ottawa sand was composed of well-rounded and well- sorted quartz grains of 260 ± 60 microns average grain diameter. The clay consisted of kaolinite poweder with particle size from 2 to 10 microns. Each sample weighed 100 gram and its clay weight fraction ranged from 0 to 100%. Weighed samples were placed in sealed plastic bags and shaken in a standard way until sand and clay particles appeared visually homogeneous and well mixed. Four separate sample sets were prepared for measurements of (1) helium porosity; (2) nitrogen gas permeability; (3) ultrasonic velocities under vacuum-dry condition at various confining pressures; and (4) ultrasonic velocities under brine saturated condition at various confining pressures. Each set consists of 12 samples: pure Ottawa sand, 5%, 10%, 15%, 20%, 25%, 30%, 40%, 50%, 65%, 85% by weight of kaolinite mixed with Ottawa sand, and pure kaolinite.

P-wave and S-wave velocity were measured simultaneously at ultrasonic frequency

using the pulse transmission technique The central frequency of the P-wave and S-wave transducers were 1.0 MHz, and 0.6MHz, respectively. The samples were placed in a two-inch diameter cylindrical tygon tube with two piezoelectric transducers attached as end plugs. Samples were then subjected to a vacuum of five microns mercury ($5 \times 10^{-3} torr$) for about ten minutes to one hour before ultrasonic measurements were taken under dry condition. To achieve the most complete possible saturation, pore pressure was first applied from the bottom end of the sample to sweep out remaining air with brine (0.5 molar concentration of sodium chloride). The ultrasonic velocity measurements were carried out as confining pressures were varied from 2.5MPa to 50MPa, with pore pressure kept constant at 1 MPa. Pore pressure was maintained by a hydraulic intensifier, and valves were designed to monitor pore-pressure at both ends of a sample. Assuming that the the grain compressibility is negligible with respect to bulk compressibility, and that pore volume change is thus equal to bulk volume change, porosity variations were measured by calibrating expelled volume of pore fluid while changing the confining pressure. The sample's length change was monitored inside the pressure cell by using a third piezoelectric transducer in order to achieve a correct path length of ultrasonic pulse waves (Figure 2.1).

The initial porosity of the samples in room-dry condition were measured with a helium porosimeter built by *Frank Jones and Associates Inc.,* of Tulsa, Oklahoma at helium pressure equal to 100 psi (0.7MPa). Based on measured porosity, sample dimension and weight, Ottawa sand grain density and kaolinite particle density were estimated, and they equal $2.65 \pm 0.01\ g/cm^3$, and $2.52 \pm 0.01\ g/cm^3$, respectively. The initial porosity, the helium porosity, was estimated within a relative error of $\pm 2\%$, but the porosity values estimated through the calibration of expelled pore fluid while confining pressure increased inside the experimental pressure cell were within an relative accuracy of $\pm 5\%$. This is because low permeability in high clay-content samples increased the time required for pore-pressure equilibration.

Gas permeability of each sample was measured with a nitrogen gas permeameter manufactured by *Ruska Instrument Corporation.* The relative accuracy of the measured permeability is within ±5% for the samples of clay-content less than 20%, and within ±10% for the samples of clay-content more than 20%.

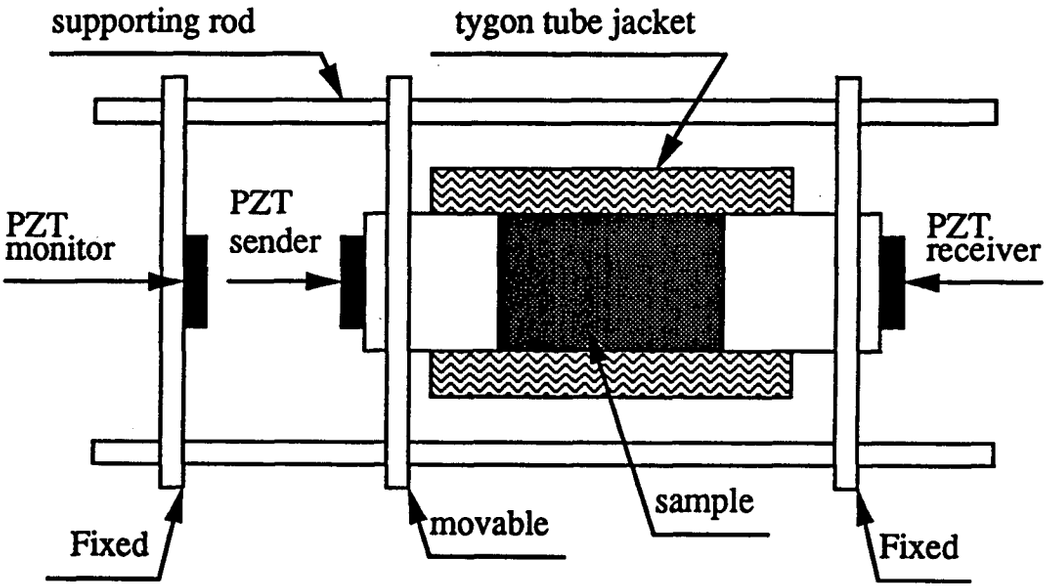

Figure 2.1: Schematic of the experimental set-up. The set-up was placed inside pressure cell for the loaded measurements. Note that a third transducer (monitor) was used to measure sample length changes as confining pressure changed.

2.2.2 Critical clay-content and topology of sand-clay mixture

The haphazard packing of binary sphere mixtures has been well documented in the field of powder technology. It has been well demonstrated that porosity depends not only on grain packing type, but also on grain sorting. The pure Ottawa sand we measured has initial porosity near 39% at room dry condition (close to the ideal "simple hexagonal" packing), while the pure kaolinite has an initial porosity about 62% (even much higher than the "simple cubic packing). The difference in packing between sand and clay is essentially due to the fact that surface forces can be practically disregarded

for the sand with its grain size around 200 microns, whereas surface forces are predominant for kaolinite with its particle size less than 10 microns. The deviation of this clay packing from ideal sphere packing is due largely to the the packing of the clay as particle clusters, rather than in the type of singular clay particles.

The packing of binary mixtures depends primarily on the diameter ratio of its constituent particles. When the diameter ratio is greater than 100, packing of the mixture is close to ideal. That is, the small spheres do not disturb the original packing of the large spheres and vice-versa. Then, there must be a *percolation threshold* to discriminate the characteristic differences between principal sand packing and principal clay packing. I shall call such a percolation threshold the *Critical Clay-content* (Figure 2.2).

Below the Critical Clay-content, sand packing dominates the sample's character, and sand grains bear most confining stress; above the Critical Clay-content, clay packing dominates the sample's character, sand and clay share confining stress equally.

2.2.3 Compaction, clay-content and porosity

In sand-clay mixtures, we may find the value of the Critical Clay-content by looking at the sand porosity. When porosity of the binary packing is expressed in terms of the porosity of its two end members (pure sand and and pure clay), the following relationships, derived from the definition of porosity, describe the dependence of the mixture's porosity on clay-content by weight or by volume.

Case 1. $V_c < \phi_s$**:**

When the clay volume fraction V_c is less than the pure sand porosity ϕ_s, clay particles primarily fill the sand grains' pore space, and porosity of the mixture ϕ_m decreases linearly with increasing clay volume fraction.

$$\phi_m = \phi_s - V_c(1 - \phi_c), \quad if\ V_c < \phi_s, \tag{2.1}$$

where ϕ_c is the porosity of pure clay. Equation 2.1 is valid from zero clay-content to that the clay entirely fills all pore space in the sand matrix.

Case 2. The Critical Clay-content, $V_c = \phi_s$:

When the clay volume fraction equals the sand porosity, the mixture's porosity is

$$\phi_m = \phi_s - V_c(1 - \phi_c) = \phi_s\phi_c, \qquad if\ V_c = \phi_s, \tag{2.2}$$

and this is the value of the *Critical Clay-content.* As we will see later, the value of $\phi_s\phi_c$ varies with confining pressure, because sand porosity decreases more slowly than does clay porosity with increasing confining pressure.

Case 3. $V_c > \phi_s$:

When the clay volume fraction exceeds the sand porosity, the sand lattice will be expanded and become disconnected, and the porosity of mixture will increase linearly with the increasing clay content due to the replacement of voidless sand grain volume by the porous clay clusters.

$$\phi_m = V_c\phi_c, \qquad if\ V_c = \phi_s, \tag{2.3}$$

Figure 2.2 is an illustration on the above three cases of clay-content classification and Critical Clay-content.

Clay weight fraction W_c and clay volume fraction V_c:

To predict porosity of the sand-clay mixtures with the above classifications, substituting pure sand and pure clay (the end members of the mixtures), and comparing results with the measured data, we must first convert clay weight fraction into clay volume fraction.

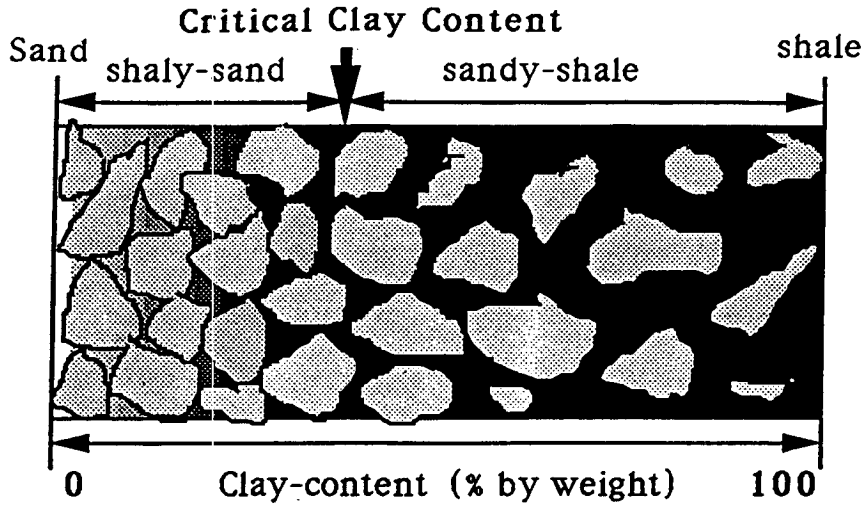

Figure 2.2: An illustration of three cases of clay-content classification and Critical Clay-content.

By physical definition, clay weight fraction W_c may be expressed as the ratio of clay mass to the total mass of the sand-clay mixture:

$$W_c = \frac{V_c(1-\phi_c)\rho_c}{V_c(1-\phi_c)\rho_c + (1-\phi_s)\rho_s}, \quad if \;\; V_c < \phi_s, \tag{2.4}$$

and

$$W_c = \frac{V_c(1-\phi_c)\rho_c}{V_c(1-\phi_c)\rho_c + (1-V_c)\rho_s}, \quad if \;\; V_c \geq \phi_s, \tag{2.5}$$

where ρ_c and ρ_s are the grain density of pure clay and pure sand, respectively.

Critical Clay-content as function of confining pressure:

We are but one step away from plugging our weight fraction and volume fraction relations into porosity and clay-content relations, thus modeling porosities of the mixtures with pure sand and pure clay data.

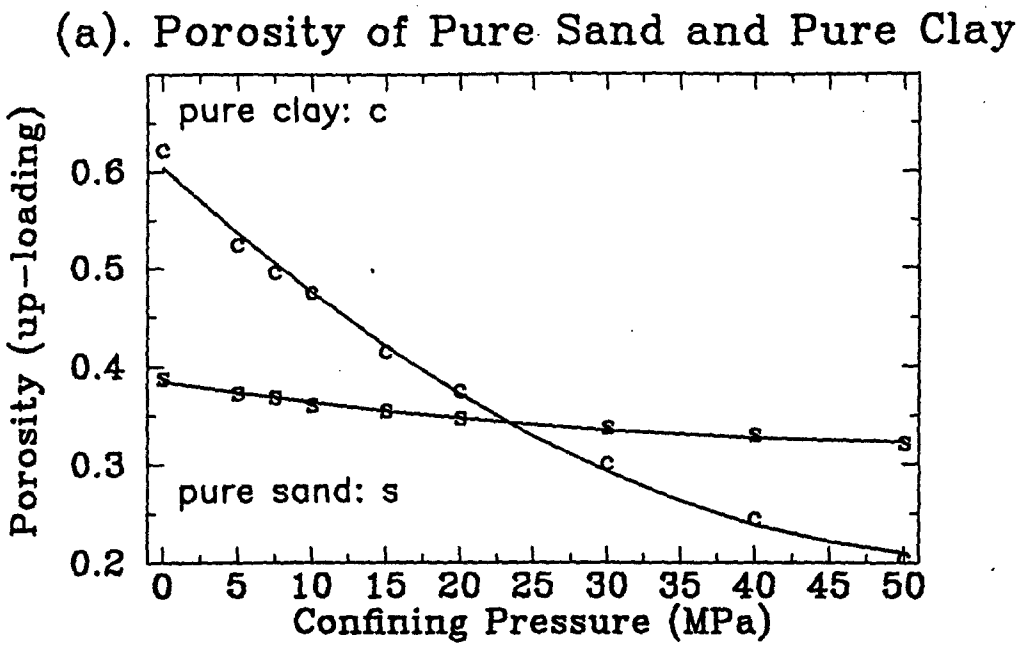

Figure 2.3-a: Measured porosity of pure sand and pure clay as function of confining pressure P_c. Note that porosity of pure clay has higher gradient as function of confining pressure than pure sand.

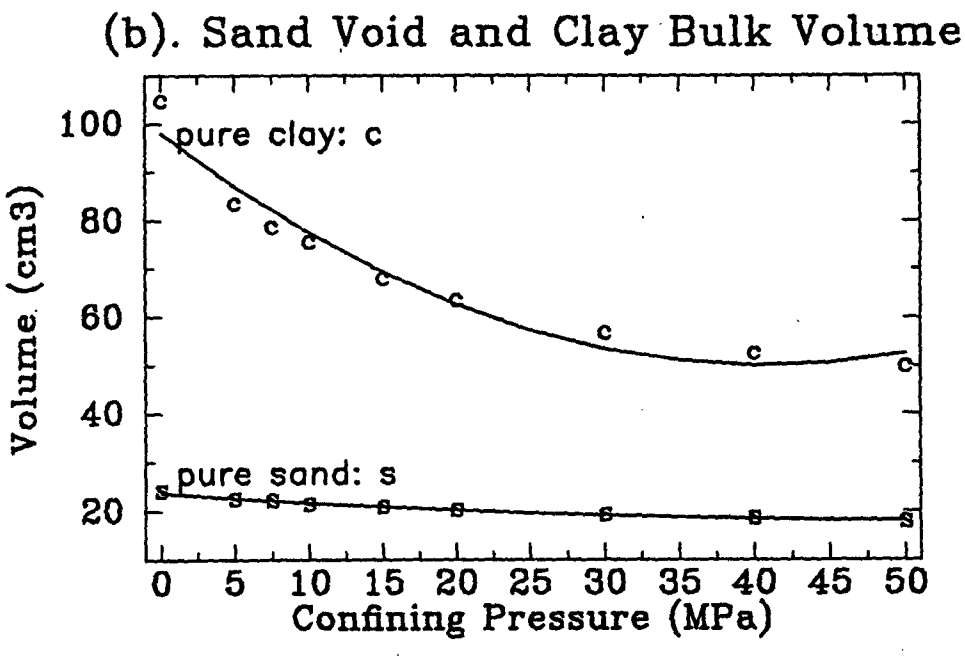

Figure 2.3-b: Void volume of 100 g pure sand (v_s), and bulk volume of 100 g pure clay (v_c) as function of confining pressure.

We have seen that Critical Clay-content acts as a percolation threshold between a sand skeleton-supported mixture and a clay matrix-supported mixture (Figure 2.2). But then, how we can determine the value of the Critical clay-content when $V_c(P_c)$ or $\phi_s(P_c)$ varies with confining pressure differently, e.g., $V_c(P_c) \neq \phi_s(P_c)$ at the same confining pressure P_c? Figure 2.3-a is a plot of the measured porosities of pure sand and pure clay as function of confining pressure.

To model mixture's porosity in the entire range of clay-content, I calculated the void volume of 100 gram pure sand v_s, and the bulk volume of 100 gram pure clay v_c. The results are plotted in Figure 2.3-b.

Regressing these two end members of the mixture as function of pressure through the least-square method, we get

$$\begin{cases} v_s(P_c) = 23.5954 - 0.2177P_c + 0.0021P_c^2, & \text{for pure sand;} \\ v_c(P_c) = 98.0618 - 2.3557P_c + 0.0289P_c^2, & \text{for pure clay;} \end{cases} \tag{2.6}$$

where v_c and v_s are the void volume of the pure sand weighed 100 gram and the bulk volume of the pure clay weighed 100 grams, respectively, and P_c is confining pressure.

With the above regression results, we can calculate the entire range of the sand void volume and the bulk volume of the clay as function of clay-content simply by scaling their weight fractions. I plotted partial results to define the Critical Clay-content as a function of confining pressure in Figure 2.4. The plot allows us not only to see the variation of sand void volume Δv_s and clay bulk volume Δv_c as function of pressure at a constant clay-content, but also to recognize that a given amount of clay ΔW_c by weight can be compacted into sand void space to reconnect its separated sand grain lattice at a given increment of confining pressure. Note that the Critical Clay-content values are the cross points of the sand void volume (solid lines) and clay bulk volume (dashed lines) at a given confining pressure.

With the Critical Clay-content at each given pressure, and the relation between clay volume fraction and clay weight fraction in Equation 2.4 and Equation 2.5,

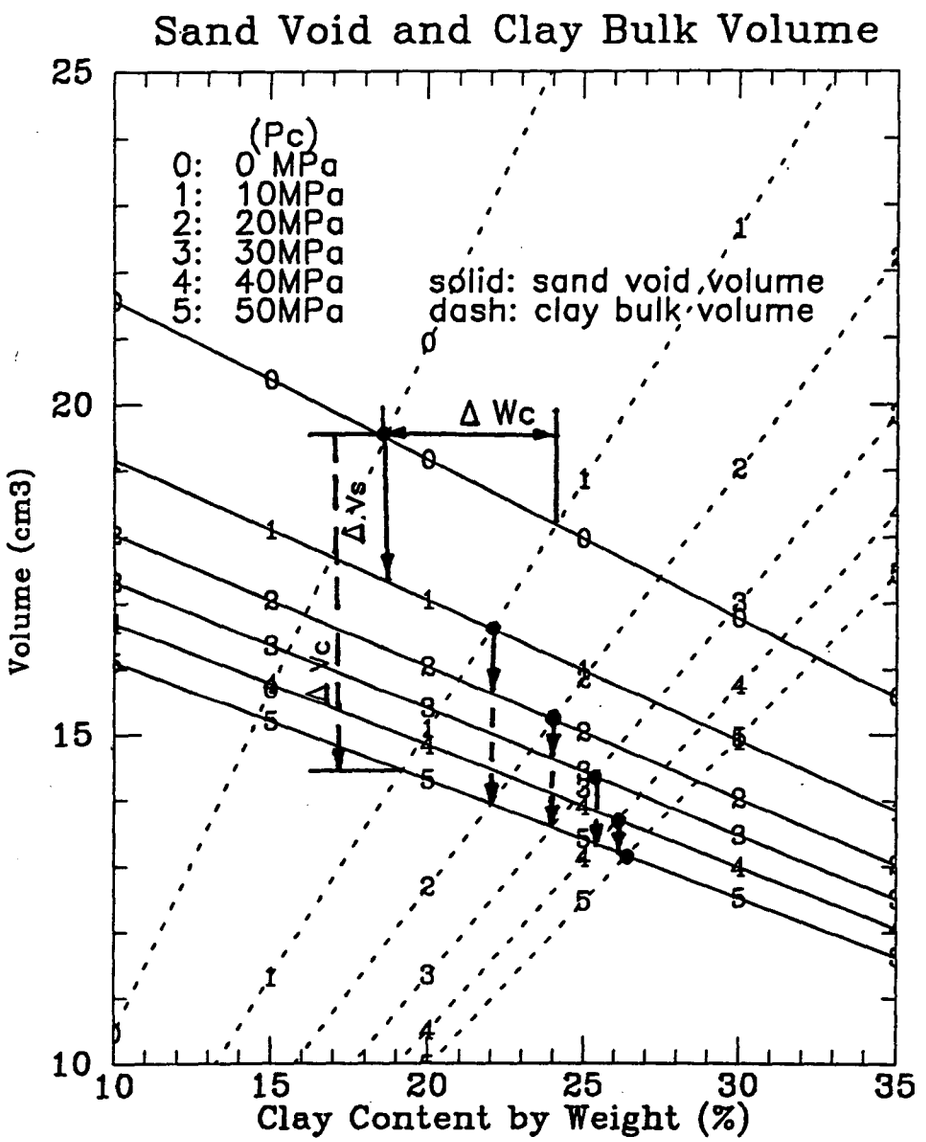

Figure 2.4: Cross plot of sand void volume and clay bulk volume as function of confining pressure. Note that the Critical Clay-content values are the cross points of the sand void volume (solid lines) and clay bulk volume (dashed lines) at a given confining pressure.

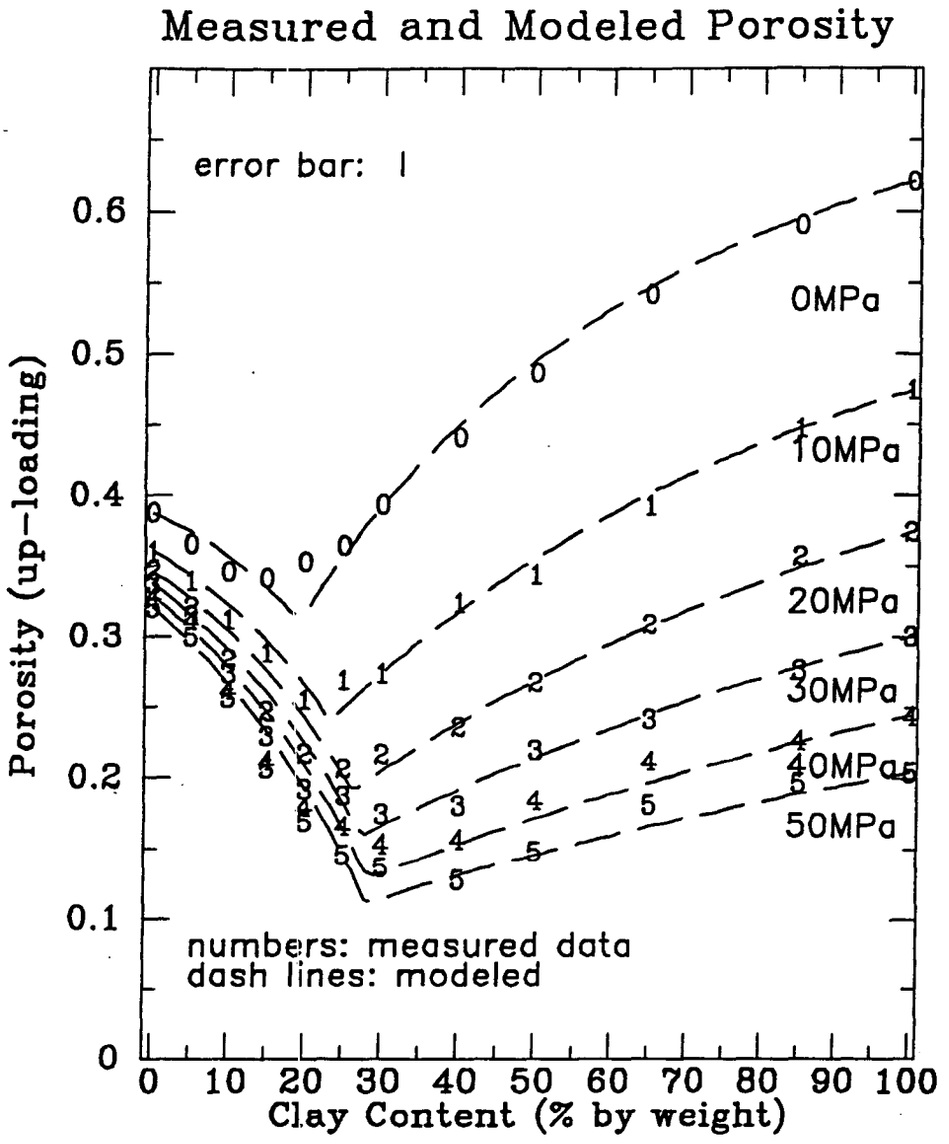

Figure 2.5: Porosity as a function of clay-content at various confining pressures. The modeling results show excellent agreement with measured data.

I modeled the mixtures' porosity as function of clay-content by weight at various confining pressures. The results show excellent agreement between the measured data and the model (Figure 2.5).

2.2.4 Clay-content, pore-size distribution and permeability

For years, much research has been conducted to infer permeability from porosity data. Perhaps the main reasons for this is that porosity can be more easily measured both in-situ and in the laboratory. Among the fruits of those studies, Kozeny-Carman equation is well recognized and widely used.

There are several versions of the Kozeny-Carman equation. I first chose the simplest version, a straight pipe with radius R, to examine whether or not permeability has anything to do with porosity, then, I used a statistical characterization of pore size distribution and modeled permeability of sand-clay mixture with the "*Hydraulic Radius Model*" derived by Carman in 1937.

A new look at Kozeny-Carman Equation:

A combination of Darcy's and Poiseuille's laws yield the permeability of a straight pipe in a unit cube as

$$k = \frac{\phi^3}{2S^2} \tag{2.7}$$

where k is the permeability, ϕ is the porosity, S is the specific surface area. In this equation, porosity ϕ appears cubed, and therefore plays the most important role.

The specific surface area of a single straight pipe in an unit cube equals that the pipe's area ($2\pi R_1 \times 1$) devided by the cube's volume ($1 \times 1 \times 1$), that is $2\pi R_1$. Porosity of the unit cube is $\phi = \pi R_1^2$ (Figure 2.6-a). This leads to

$$k = \phi \frac{R_1^2}{8} = \frac{\pi R_1^4}{8} \tag{2.8}$$

where the radius R_1 appears in the fourth power, looking even more dominant an effect on permeability.[1]

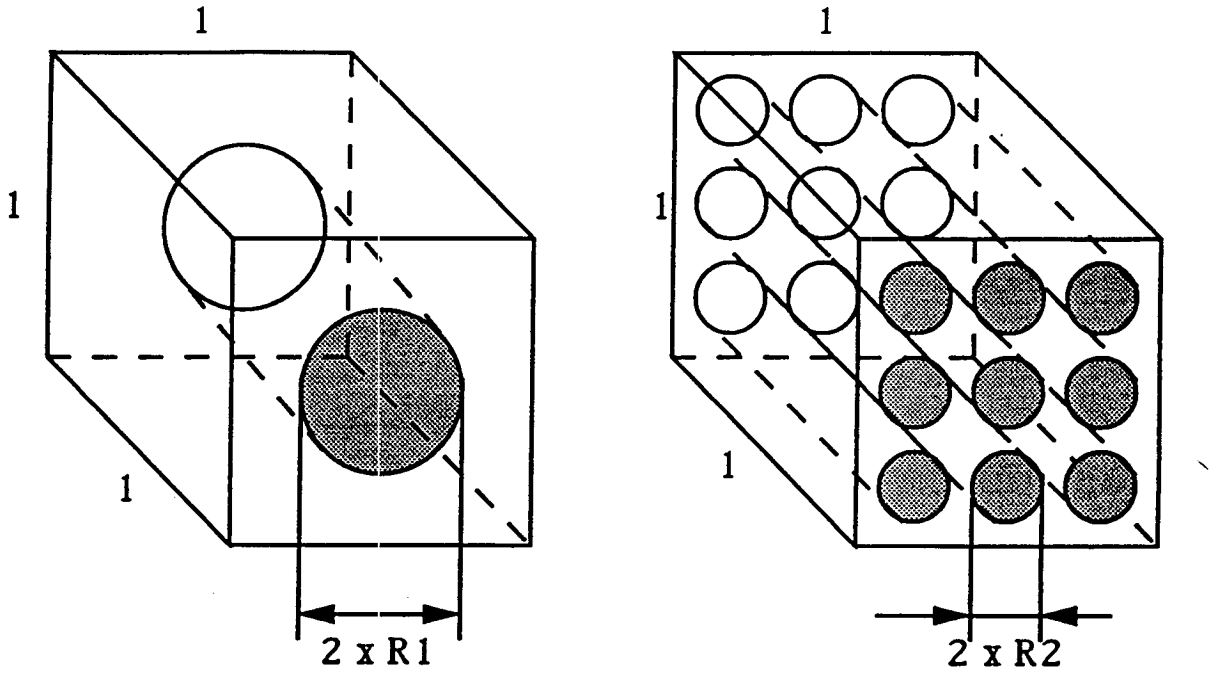

Figure 2.6: A schematic diagram of two media with same porosity, but completely different permeabilities as described by the Kozeny-Carman relation.

In contrast with the single straight pipe, a network of n capillary tubes, each of radius R_2 (Figure 2.6-b), may lead to the same permeability equation (Eq. 2.7) by combining Darcy's law and poiseuille's law as the single straight pipe, yet have a distinct predicted permeability when using the capillary tubes' radius R_2 in Equation 2.8.

Assuming that the single straight pipe and a network of n cylindrical capillary tubes within a unit cube have same porosity, $\phi_1 = \phi_2$, then, $\pi R_1^2 = \pi n R_2^2$, and $R_1/R_2 = \sqrt{n}$. Inserting this into Kozeny-Carman equation, we may conclude that the two media with same porosity value have two different permeabilities, and the ratio of the two permeabilities is

[1] $\phi = \pi R_1^2$ has no dimension. It appears to have dimension of length squared because of the unit length cube assumption, and it leads to a pseudo dimension for permeability in Equation 2.8.

$$\frac{k_1}{k_2} = \frac{1}{n} \tag{2.9}$$

where the k_1 and k_2 are the permeability of the single straight pipe with radius R_1 and the network with number n cylindrical capillaries and radius R_2, respectively.

Obviously, permeability strongly depends on the *pore size* and the *pore geometry*, and permeability does not depend on the porosity alone.

Clay-content and pore-size distribution:

One possible approach to a more detailed description of pore size distribution in a porous medium is to introduce statistical characterization of the porous medium itself.

The specific surface area S of porous medium is defined as the total interstitial surface area of pores A_s found in a unit bulk volume V_b of the porous medium as stated before. For example, the specific surface area of a porous medium composed of identical spheres of radius R in cubical packing is $S = (4\pi R^2 \times n^3)/(2nR)^3 = \phi/(2R)$.

Generally, fine grained material's specific surface area is vastly larger than does coarse material. If a granular mixture with porosity ϕ and bulk volume V_b consists of m fractions, each fraction made up of N_i identical spheres with radius R_i, then, the total interstitial area A_s and the solid sphere volume V_s are

$$\begin{cases} A_s = \sum_{i=1}^{m} 4\pi R_i^2 N_i \\ V_s = \sum_{i=1}^{m} (4/3)\pi R_i^3 N_i = (1-\phi)V_b \end{cases} \tag{2.10}$$

If we regard all contacts among spheres as mathematical points, zero contact area, then the average specific surface area $\bar{S}$ is:

$$\bar{S} = \frac{\sum_{i=1}^{m} 4\pi R_i^2 N_i}{[\sum_{i=1}^{m} (4/3)\pi R_i^3 N_i]/(1-\phi)} = 3(1-\phi)\sum_{i=1}^{m} \frac{f_i}{R_i} = \frac{3(1-\phi)}{\bar{R}} \tag{2.11}$$

where $f_i = 4\pi R_i^3 N_i / 3V_s$ is the volume fraction of the ith sphere fraction, and $\bar{R}$ is the harmonic mean radius. The *pore size distribution parameter* here is equals to $3(1-\phi)\sum_{i=1}^{m} f_i/R_i = 3(1-\phi)/\bar{R}$.

In the case of our sand-clay mixture, we find

$$\bar{S} = 3(1-\phi)\sum_{i=1}^{m}\frac{f_i}{R_i} = 3(1-\phi)\left(\frac{1-\phi_s-V_c}{R_s}+\frac{V_c}{R_c}\right) = 3(1-\phi)\left(\frac{V_s}{R_s}+\frac{V_c}{R_c}\right) \quad (2.12)$$

where ϕ is the mixture's total porosity, V_s and V_c are the volume fractions of sand grains and clay particles, R_s and R_c are radii of the sand grains and clay particles, respectively.

In fluid flowing through open channels, the *hydraulic radius* R is defined as the ratio of fluid-filled conduit volume to conduit wetted surface area. Considering a porous medium as a network of n interconnected channels, one may find the relationship between R and specific surface S as $R = \phi/S$. With the hydraulic radius $R = \phi/S$ concept, Carman (1937) obtained a relation of permeability as function of porosity and specific surface area (Bear 1972, p. 166)

$$k = \frac{\phi^3}{5S^2}. \quad (2.13)$$

This version of Kozeny-Carman equation is also called *Hydraulic Radius Model.*

Replacing S with the pore-size distribution parameter $\bar{S}$ obtained in Equation 2.12, we have

$$k = \frac{\phi^3}{45(1-\phi)^2(V_s/R_s+V_c/R_c)^2} \quad (2.14)$$

Combining the mixtures' total porosity and clay-content relation obtained from Equation 2.1 to Equation 2.5 with this permeability, porosity, pore size distribution relation, I calculated the permeability as function of clay-content by weight, and as function porosity. The results show good agreement between the model and the measured data (Figure 2.7).

Figure 2.7 shows that permeability is strongly dependent on clay content for shaly sands, and a *percolation threshold* may be defined by the value of *Critical Clay-content.*

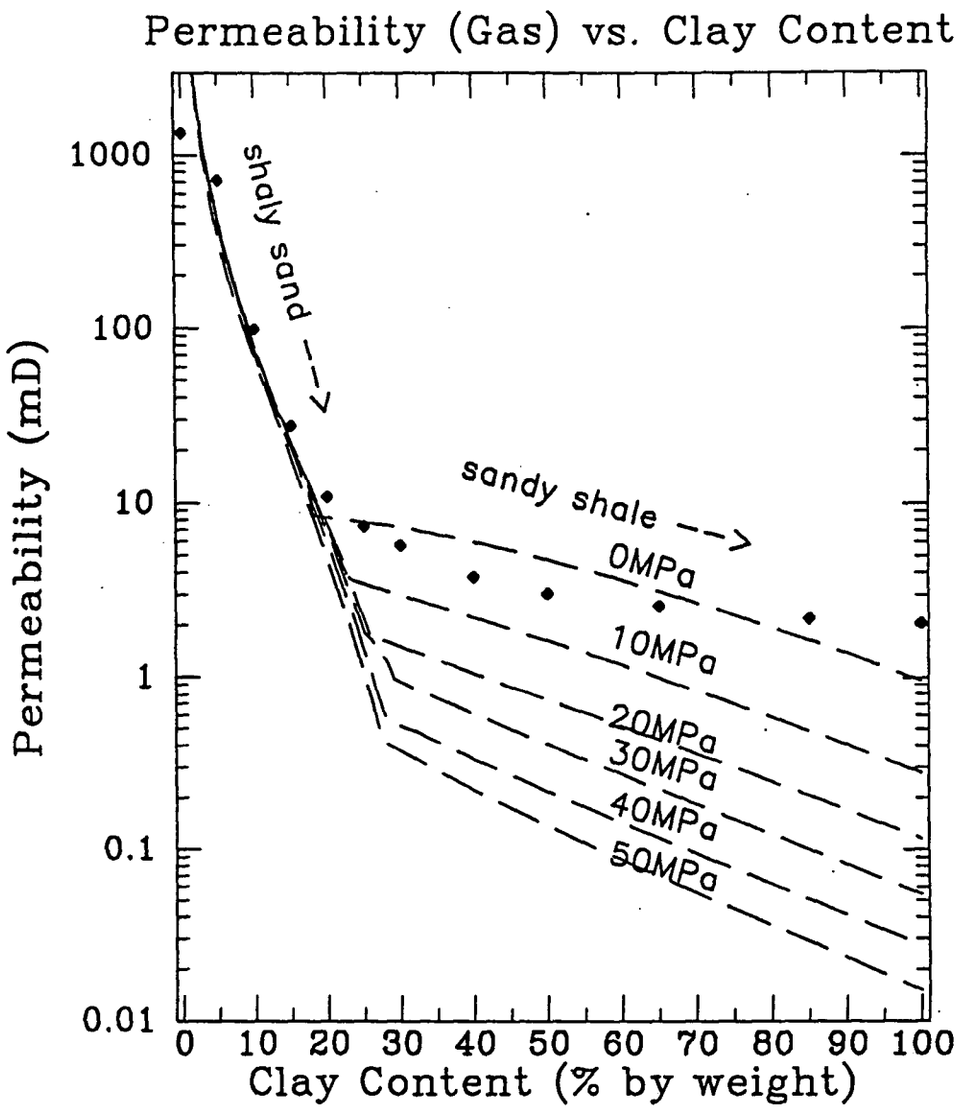

Figure 2.7: Measured and modeled permeability vs. clay content. The measured data are considered to represent zero confining pressure. Note that a percolation threshold may be defined by pressure dependent Critical Clay-contents.

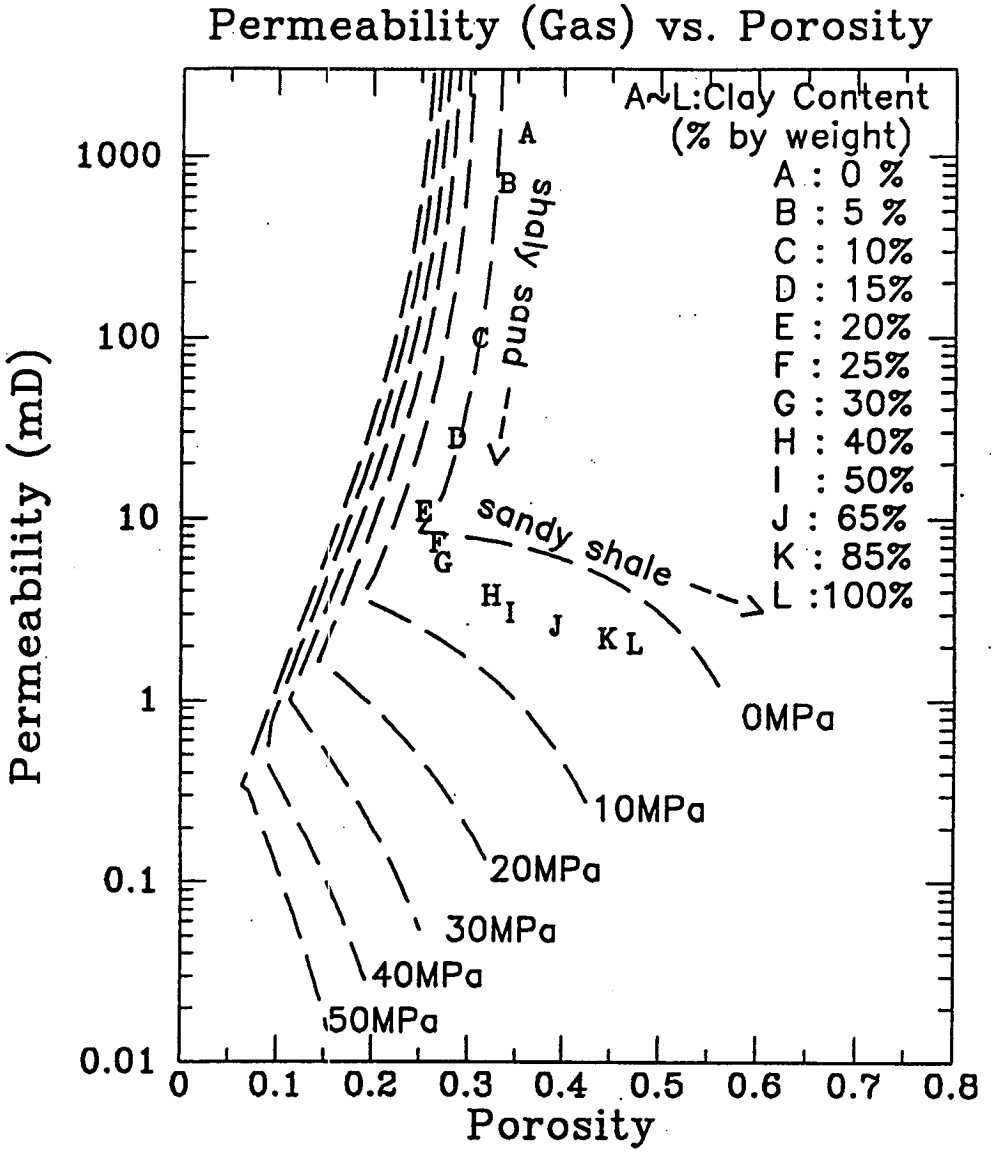

Figure 2.8: Measured and modeled permeability vs. porosity. Apparently, permeability can not be uniquely related to porosity.

Below the Critical Clay-content, permeability logarithmically decreases with increasing clay-content; above the Critical Clay-content, permeability is much less sensitive to clay-content, but remains dependent on confining pressure. This is because clay-content is the major factor affecting the pore-size distribution which in turn exerts a dominant influence on permeability.

Figure 2.8 is the plot of permeability vs. porosity for our sand-clay mixtures, and the modeled values at various confining pressures. It is clear from this plot that permeability is not uniquely related to porosity. Permeability may not be solely expressed as a function of porosity, but other important parameters, such as pore size distribution.

2.2.5 Compaction, clay-content and velocity

I have shown how the porosity and permeability could be successfully modeled in the entire range of sand-clay mixtures using only the end members of the mixtures: pure sand and pure clay. Could we also model acoustic velocities of the whole range of our sand-clay mixtures in the same way?

With the measured velocity, porosity, and density data on hand, I calculated bulk modulus, Young's modulus, and shear modulus as functions of clay content by weight. The results are plotted in Figure 2.9.

Bulk modulus shows strongest dependency on clay-content and confining pressure. Shear modulus shows less dependency on confining pressure, and hardly any dependency on clay-content. The shear modulus is much smaller than the bulk modulus (about 1/10), indicating that the influence of shear modulus of clay-water composite may be neglected in a first-order approximation.

We have seen how Critical Clay-contents characterizing the sand grain supported matrix and clay particle supported matrix. I will still use the Critical Clay-content defined above to describe these two distinct lithologic types: the "shaly-sand" ($V_c < \phi_s$), and the "sandy-shale" ($V_c > \phi_s$).

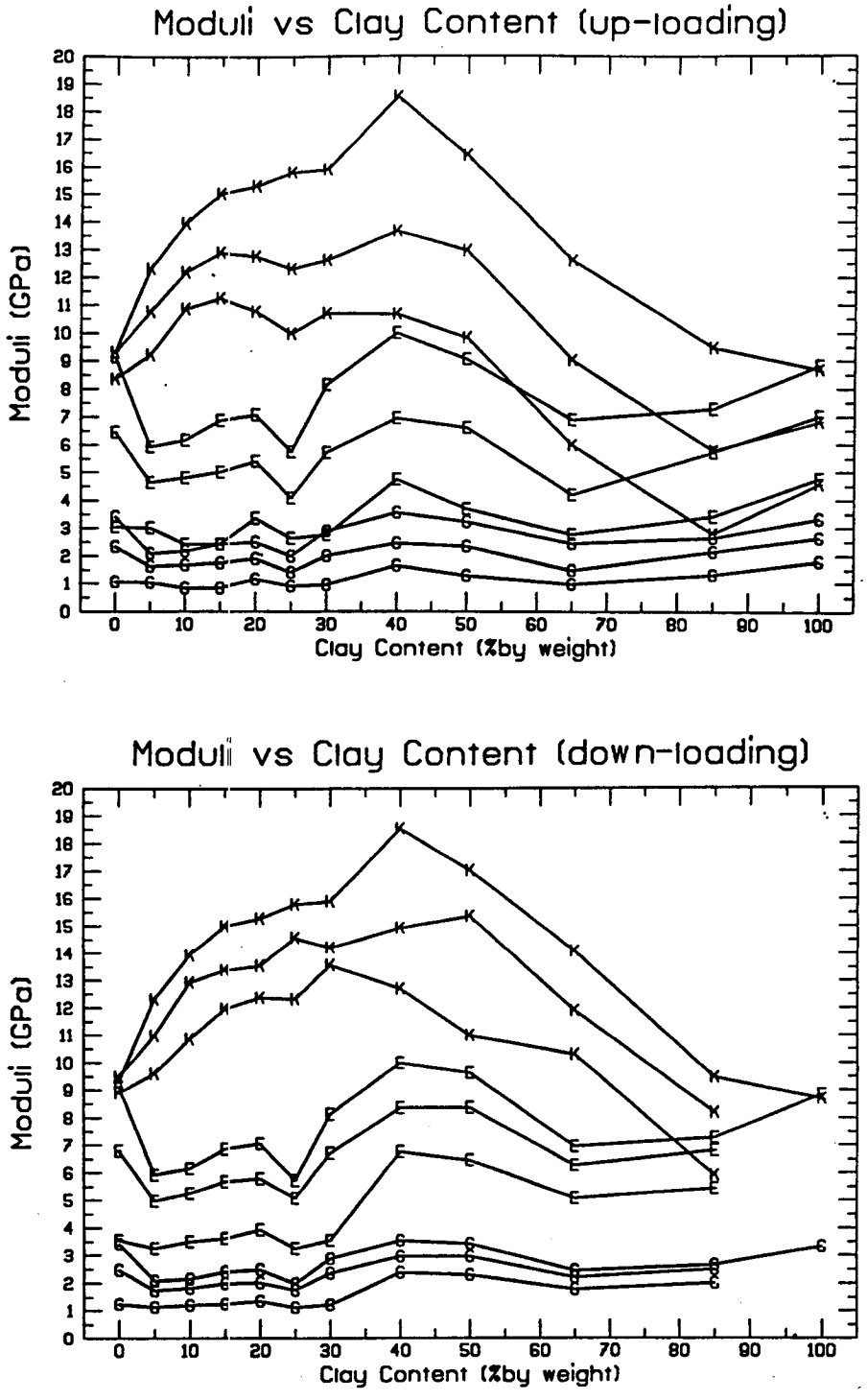

Figure 2.9: Bulk modulus (K), Young's modulus (E), and shear modulus (G) were calculated with the measured data as function of clay content by weight. Each modulus was calculated at three different confining pressures, 50MPa (top), 30MPa (middle), and 10MPa (bottom).

Case 1. $V_c < \phi_s$:

When clay volume fraction V_c is less than the sand frame porosity ϕ_s, one can assume that the clay particles are dispersed within the pore space of the load-bearing sand (pure sand to shaly-sands). Then, clay may be treated as a component of the pore filling materials which stiffen the pore space but not bear the bulk load. In this case, a modified "isostrain" mechanism may be used in modeling the mixtures' bulk modulus, shear modulus, and density as follows:

$$\begin{cases} K = (1 - \frac{V_c}{\phi_s})K_s + \frac{V_c}{\phi_s}K_{cr} \\ G = (1 - \frac{V_c}{\phi_s})G_s + \frac{V_c}{\phi_s}G_{cr} \\ \rho = (1 - \phi_s)\rho_s + V_c(1 - \phi_c)\rho_c + [\phi_s - V_c(1 - \phi_c)]\rho_w, \end{cases} \tag{2.15}$$

where ρ, ρ_s, ρ_c, and ρ_w are the density of mixture, the density of pure sand grains (quartz), the density of clay mineral (including bound water), and the density of saturating fluid (brine) respectively; K, K_s, and K_{cr} are the the bulk modulus of mixture, the bulk modulus of the pure sand, and the bulk modulus of the mixture at critical clay-content ($V_c = \phi_s$); G_s, G, and G_{cr} are the shear modulus of the pure sand, the shear modulus of mixture, and the shear modulus of the mixture at critical clay-content ($V_c = \phi_s$). Note that the averaged clay-content V_c/ϕ_s was used here.

This method assumes that the pore filling materials (clay and pore fluid) have zero shear modulus. We have observed the pore-filling clay-water mixture has a finite shear modulus in Figure 2.9. However, the shear modulus is much smaller than the bulk modulus (about 1/10), indicating that the influence of shear modulus of clay-water composite may be neglected in a first-order approximation and that the isostrain mechanism is applicable to this case. Note that the shear modulus shows only small variations in the entire range of sand-clay mixtures.

Case 2. $V_c \geq \phi_s$:

When clay volume fraction V_c is greater than the sand frame porosity ϕ_s, one can assume that the clay particles may overfill the pores of sand matrix and break apart

the sand lattice (sandy-shale to pure shale). Hence the isostress mechanism may be applied. The bulk modulus and shear modulus may then be expressed as:

$$\begin{cases} \frac{1}{K} = \frac{1-V_c}{1-\phi_s}\frac{1}{K_{cr}} + \frac{V_c-\phi_s}{1-\phi_s}\frac{1}{K_c} \\ \frac{1}{G} = \frac{1-V_c}{1-\phi_s}\frac{1}{G_{cr}} + \frac{V_c-\phi_s}{1-\phi_s}\frac{1}{G_c} \\ \rho = (1-V_c)\rho_s + V_c(1-\phi_c)\rho_c + V_c\phi_c\rho_w \end{cases} \tag{2.16}$$

where ρ, ρ_s, ρ_c, and ρ_w are the density of mixture, the density of pure sand grains (quartz), the density of clay mineral (including bound water), and the density of saturating fluid (brine) respectively; K, K_c, and K_{cr} are the the bulk modulus of mixture, the bulk modulus of the pure clay, and the bulk modulus of the mixture at critical clay-content ($V_c = \phi_s$); G_c, G, and G_{cr} are the shear modulus of the pure clay, the shear modulus of mixture, and the shear modulus of the mixture at critical clay-content ($V_c = \phi_s$). Note that Equation 2.15 and 2.16 are identical when $V_c = \phi_s$, the "Critical Clay-content". Theoretically, the bulk modulus of the mixture at the critical clay-content K_{cr} may be found by equating Equation 2.15 with Equation 2.16.

Clay-content and P-wave velocity:

With the density and bulk modulus defined above, the P-wave and the S-wave velocities may be predicted by

$$V_p = \sqrt{\frac{K + 4G/3}{\rho}} \tag{2.17}$$

and

$$V_s = \sqrt{\frac{G}{\rho}}. \tag{2.18}$$

The modeled P-wave velocity and the measured data show good agreement (Figure 2.10).

The measured porosity versus clay-content at various confining pressures during up-loading and down-loading are listed in Table 2.1. And the measured P-wave and

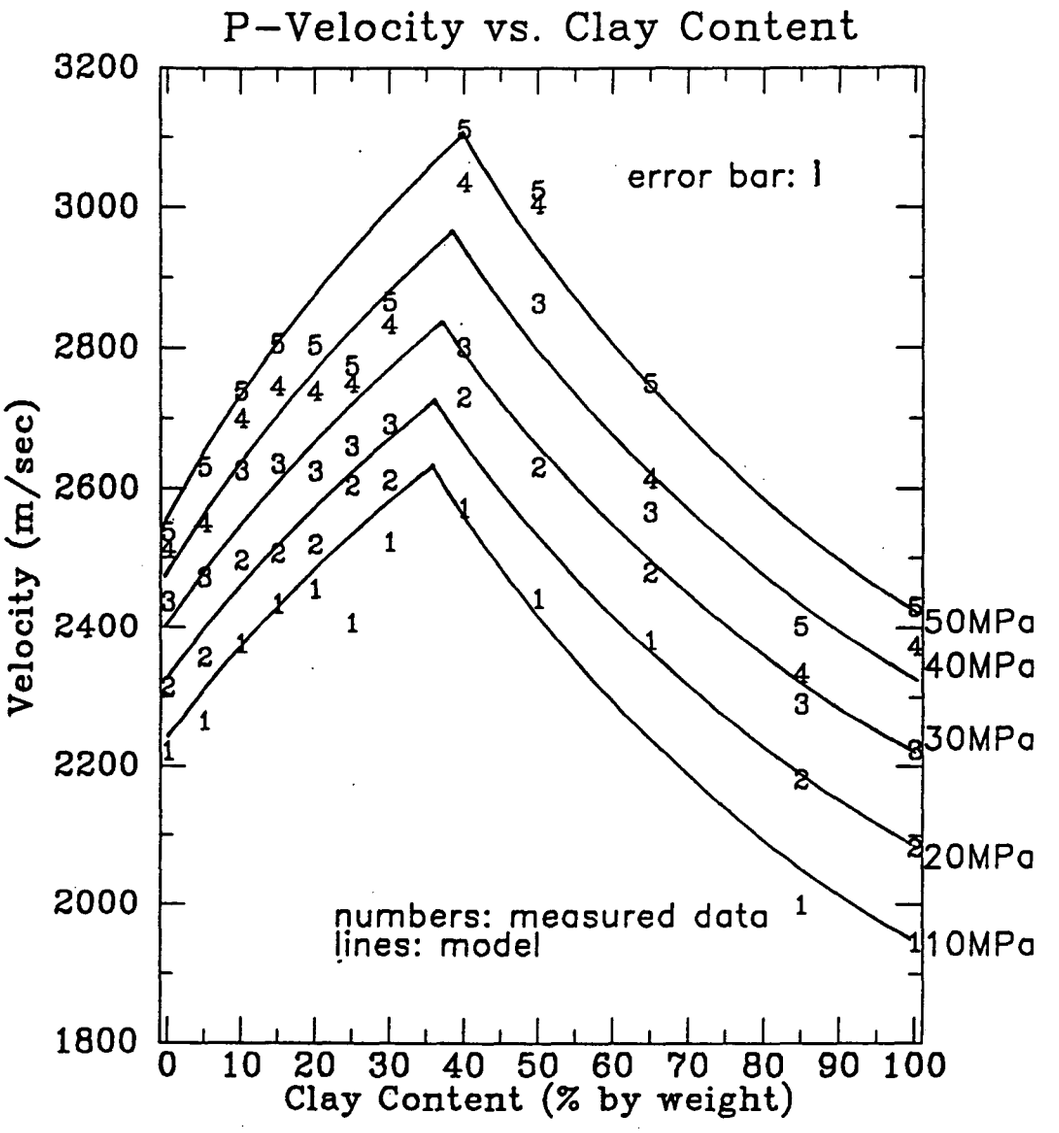

Figure 2.10: P-wave velocity of sand-clay mixture. The modeled velocities (lines) fit the measured data well (numbers) under different confining pressures.

S-wave velocities at various confining pressures and during different loading processes are listed in Table 2.2 for reference.

2.3 Cementation of granular materials

Intergranular cementation may significantly influence the elastic properties and the strength of a rock. A theoretical study of the effect of cementation on the elastic properties of granular materials (Dvorkin et al., 1991) has shown that the elastic stiffness of cemented grains is higher than that of grains with Hertzian contact theory even if the cementation is relatively soft. An experimental study of the problem performed on unconsolidated glass beads with cementation simulated by frozen pore fluid has qualitatively supported the theoretical results (Liu et al., 1991).

In order to quantitatively study the cementation effect on elastic properties of granular materials, I designed a special experiments in which a granular medium was simulated by glass beads with epoxy as cement. I measured P-wave and S-wave velocities at different epoxy saturations, various confining pressures, and different stages of epoxy polymerization. In the experiment, I specified the location of cement in the pore space by observing thin section images of the cemented samples, and quantified the amount of "cement", the epoxy, through the definition of saturation.

2.3.1 Sample preparation and experimental procedure

The samples were prepared from glass beads of 200-300 micron average grain diameter and various proportions of epoxy. Glass beads of each sample weighed 20 gram. The percent of cementation (C_e) was accounted for by the percent of epoxy saturation (S_e), that is the percent of cementation equals to the percent of epoxy saturation. The measured initial porosity of the glass beads is 38 %, and S_e or C_e was varied from 0, 10, 25, 50, to 100 %. Prior to adding the epoxy, the glass beads were washed with carbon tetrachloride (CCl_4) before being mixed with epoxy.

The epoxy used in this experiment was produced by WEST SYSTEM Incorporation. The epoxy was composed of WEST's "Brand 105, Epoxy Resin Group B–part 1", and "Brand 206, Epoxy Hardener Group B–part 2" which provides about 30 minutes of pot life at $21C^{\circ}$, and full curing in about 12 hours to a clear, amber-colored solid state.

Each sample consists of 20 *gram* glass beads mixed with a certain percent of epoxy. After the two constituents were carefully mixed until the epoxy evenly coats the glass beads, then the mixture was immediately packed into a one-inch diameter heat shrink tubing with a metal screen at both ends, and then placed into a specially designed stainless steel tube with a tygon tube liner and ultrasonic transducers at each end. Uniaxial stress was applied to the sample by compressing the load-bearing ultrasonic transducers between the plates of a hydraulic press. Pressures were varied from 5MPa to 20MPa in 5MPa increments for each sample's dynamic acoustic measurement. Then, 20MPa pressure was maintained for acoustic measurements while the epoxy cured. The sample's initial length was $25.5mm$, satisfying the ASTM standard that sample's length is at least 10 times greater than the acoustic wave length. The relative P-wave measurement error is less than 3%, and S-wave error is less than 5%.

2.3.2 Experimental results

Thin section photomicrographs of the samples at epoxy saturations of 10, 25, 50 and 100 % are shown in Figure 2.11 (a), (b), (c) and (d), respectively. At low saturation (10 and 25 %), the epoxy forms distinct cementation regions around grain-to-grain contacts due to the internal capillary forces of the epoxy while curing. As saturation increases, the epoxy begins to fill in the pore spaces among the grains.

Cementation and porosity:

The computed porosity (air-filled pore space) of cemented granular samples versus epoxy saturation is given in Figure 2.12-a. If the porosity of unconsolidated or poorly

consolidated materials depends on the packing of constituent grains, their angularity, shorting, and clay content and type, then, the porosity of consolidated materials may depends maily on the degree of cementation (Figure 2.12-a), no matter the cements are silica, calcium carbonate, or other clay cements.

Epoxy saturation and wave velocities:

In order to quantitatively study the cementation effect, I first measured P-wave and S-wave velocities in pure epoxy. The results are plotted versus time in Figure 2.12-b. The velocities remain unchanged after 24 hours, which indicates that the epoxy had fully cured at that time. Note that S-wave was not observable when the epoxy curing time is less than 6 hours, and P-wave velocity at the time zero is about 1.5 km/sec, around the acoustic velocity in fluid.

Figure 2.13 illustrates the experiments conducted immediately after assembling the samples with the epoxy, therefore, the epoxy remained in its liquid state during these measurements. In Figure 2.13-a, P-wave and S-wave velocities are plotted versus applied stress at various epoxy saturations (S_e=0, 10, 25, 50 and 100 %). As one may expect, P-wave and S-wave velocities systematically increase with increasing stress at all saturations. In Fig. 3.13-b, P-wave and S-wave velocities are plotted versus epoxy saturation at various stresses – 5, 10, 15 and 20MPa. P-wave velocity increases with increasing stress and with increasing epoxy saturation[2]. At the same time, shear velocities tend to decrease with increasing liquid epoxy saturation. Recall that at this measurement time, the epoxy remained a liquid state. Therefore, the acoustic velocities are influenced by fluid-grain interactions (the Biot and the squirt-flow mechanisms) and by the effective density which increases with increasing saturation. The stiffness of the grain-formed skeleton can possibly be described by *Hertz contact theory* which explains the systematic increase in velocities with increasing uniaxial

[2]Except 10MPa and 15MPa pressures when epoxy saturation varied from 25 to 50%.

stress.

Epoxy cementation and wave velocities:

P-wave and S-wave velocities recorded during the process of epoxy polymeriazation under 20MPa uniaxial stress are plotted versus time in Figure 2.14-a. The velocities were measured at different epoxy cementation (C_e) which varied from 0, 10, 25, 50 to 100 %.

Both P-wave and S-wave velocities remain constant in the sample without epoxy ($S_e = 0$), whereas P-wave and S-wave velocities both systematically increase in the epoxy-saturated samples between 0 and 12.5 hours and remain approximately constant afterwards. The plots also indicate that P-wave velocity increased with increasing epoxy saturation, and S-wave velocity decrease with increasing epoxy saturation at time zero.

P-wave velocity increased by a factor of 2, and S-wave velocity increased by a factor of 1.5 with increasing epoxy cementation from 0% to 10% after the epoxy had completely cured (Figure 2.14-b). It is clear from Figure 2.11 that the epoxy is polymerized around the grain-to-grain contacts because of its capillary pressure during the curing process at low epoxy cementation (10% to 25%), and fills the intergranular space at epoxy cementation 25% or higher. These observations supports our conclusion that cementation can dramatically increase the stiffness of a granular material only if the cement is placed around grain-to-grain contacts[3]. The addition of a small amount of cementation—10% epoxy cementation—results in sharp increases of both P-wave and S-wave velocities. Further increase of epoxy cementation results in much less velocity increases.

[3]Would we consider that the bulk material is cemented if this were not true?

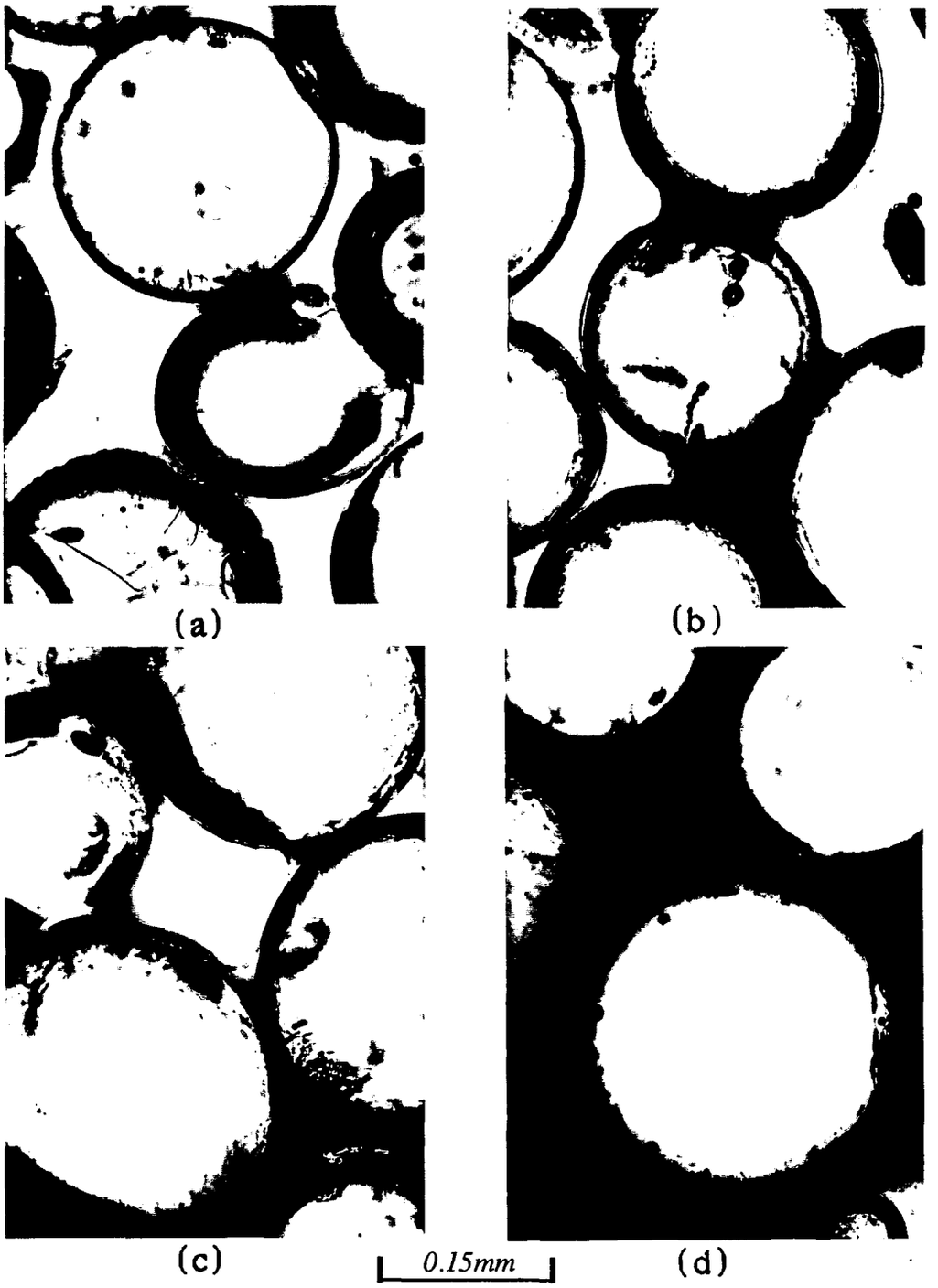

Figure 2.11: Thin sections of glass beads with epoxy cementation (the epoxy is blue-colored): (a) 10, (b) 25, (c) 50 and (d) 100 % epoxy saturation.

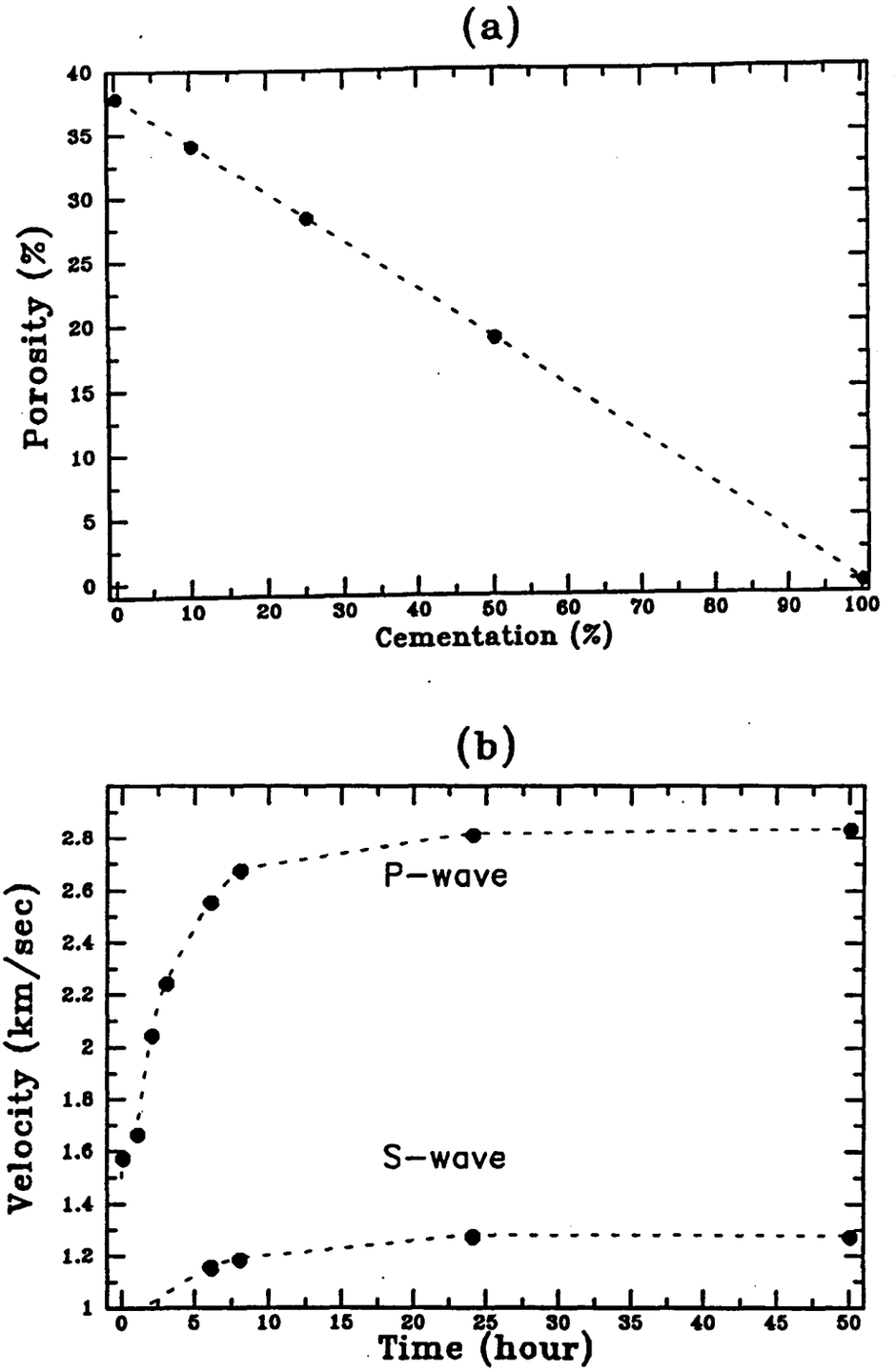

Figure 2.12: (a). Porosity versus epoxy cementation. The dots correspond to epoxy cementation of 0, 10, 25, 50 and 100 %. (b). P and S velocities of pure epoxy vs. curing time. Note velocities remains unchanged after 24 hours.

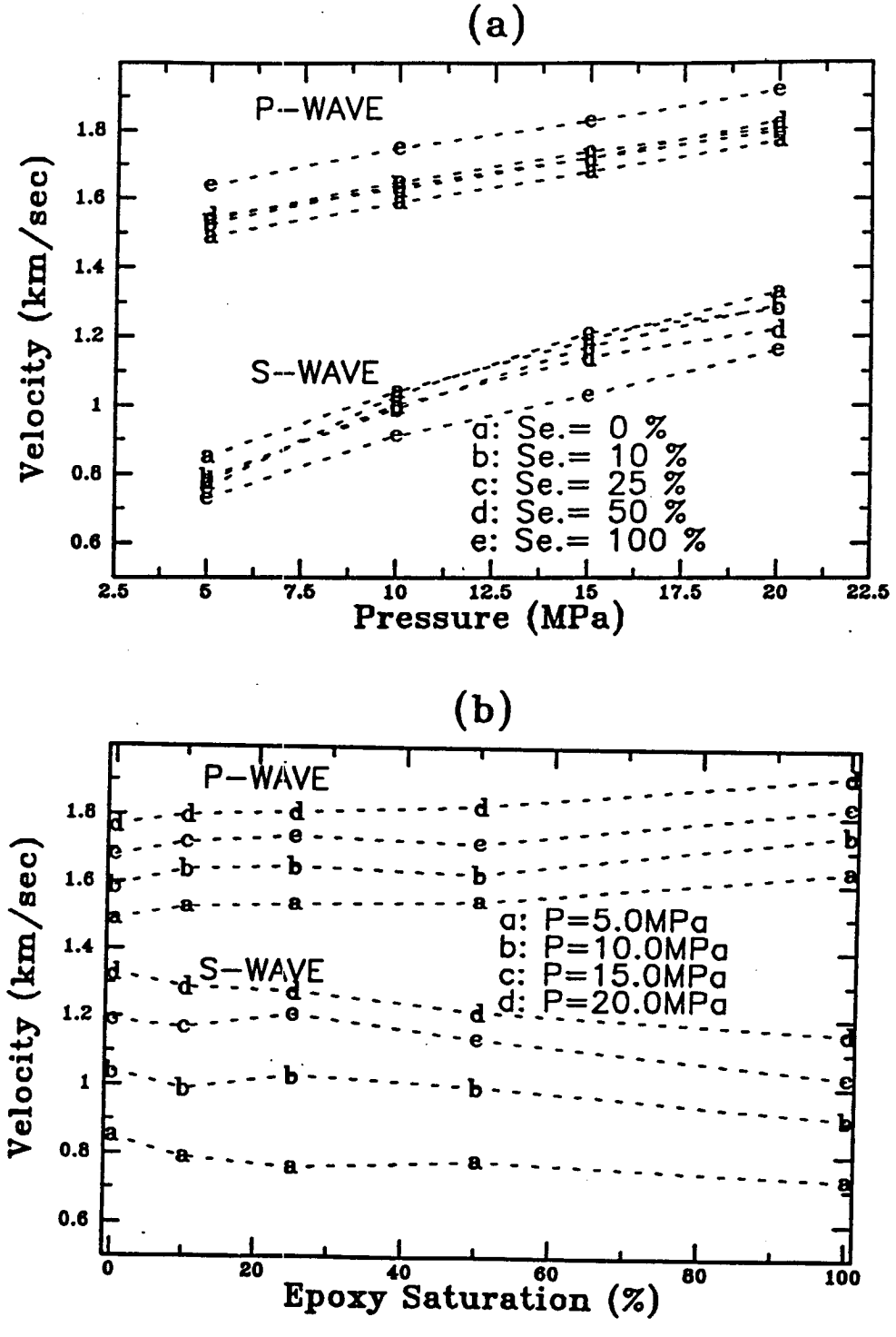

Figure 2.13: P-wave and S-wave velocities measured immediately after sample prepared, e.g., the epoxy was still in fluid state. (a). Velocities versus stress at different epoxy saturations. (b). Velocities versus epoxy saturation at different stresses.

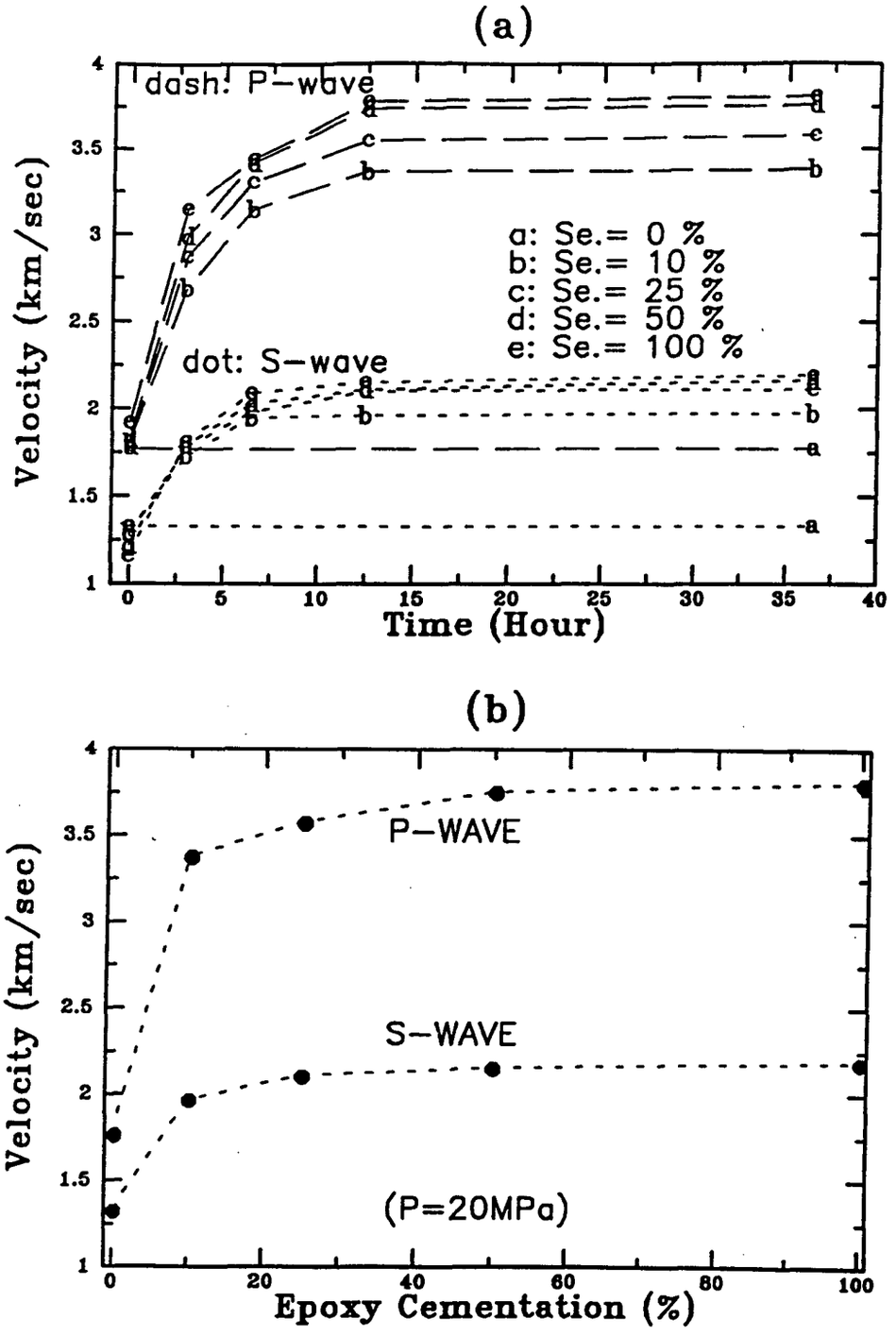

Figure 2.14: (a). P-wave and S-wave velocities versus time with different epoxy saturations under 20MPa stress. Velocities remain constant after the epoxy solidified in 12 hours. (b). P-wave and S-wave velocities vs. epoxy saturations at 20 MPa after 37 hours epoxy curing time.

2.4 Conclusion

The experiments on unconsolidated synthetic sediments revealed a few important but surprisingly simple relations.

From sand to shaly-sand ($V_c < \phi_s$), clay particles fill the sand pore space and act to stiffen the matrix. As a result, porosity decreases and velocity increases with increasing clay content. In contrast, from sandy-shale to shale, ($V_c \geq \phi_s$), sand grains are suspended in the clay matrix. Therefore, porosity increases and velocity decreases with increasing clay-content. The transition of acoustic properties from shaly-sand to sandy-shale is clearly indicated by the Critical Clay-content which equals the sand matrix porosity at a given confining pressure.

Permeability strongly depends on clay-content in shaly sands ($V_c < \phi_s$), and the percolation threshold may be recognized by the value of Critical Clay-content. Below the Critical Clay-content, permeability logarithmically decreases with increasing clay-content; above the Critical Clay-content, permeability changes little with increasing clay-content, but still varies with confining pressure.

The porosity of unconsolidated or poorly consolidated materials depends on the packing of constituent grains, their angularity, shorting, and clay content and types; the porosity of consolidated materials depends mainly on the degree of cementation. Acoustic properties of rock strongly depends on the cementation. The addition of a small amount of cementation—10% epoxy cementation—results in sharp increases of P-wave and S-wave velocities. Further increase in epoxy cementation results in much less velocity increases.

The concept of Critical Clay-content indeed plays the role of characteristic threshold in porous media.

Table 2.1: Porosity vs. Clay-content at various confining pressure.

Porosity vs. Clay-content (up-loading) (P_c: MPa, W_c: % by weight)												
P_c/W_c	0.0	5.0	10.0	15.0	20.0	25.0	30.0	40.0	50.0	65.0	85.0	100.0
0	0.387	0.365	0.345	0.341	0.353	0.364	0.393	0.440	0.486	0.541	0.590	0.621
10	0.360	0.339	0.312	0.288	0.255	0.269	0.273	0.324	0.344	0.392	0.447	0.474
20	0.346	0.321	0.284	0.246	0.217	0.206	0.217	0.236	0.267	0.309	0.356	0.374
30	0.337	0.315	0.273	0.229	0.192	0.187	0.174	0.181	0.220	0.241	0.276	0.300
40	0.329	0.312	0.262	0.212	0.179	0.166	0.153	0.156	0.184	0.212	0.226	0.244
50	0.321	0.299	0.256	0.206	0.169	0.146	0.136	0.128	0.148	0.181	0.196	0.204
Porosity vs. Clay-content (down-loading) (P_c: MPa, W_c: % by weight)												
P_c/W_c	0.0	5.0	10.0	15.0	20.0	25.0	30.0	40.0	50.0	65.0	85.0	100.0
50	0.321	0.299	0.256	0.206	0.169	0.146	0.136	0.128	0.148	0.181	0.196	0.204
30	0.324	0.303	0.265	0.208	0.172	0.148	0.140	0.123	0.149	0.207	0.236	0.301
10	0.331	0.310	0.278	0.215	0.179	0.153	0.147	0.126	0.150	0.221	0.266	0.474

Table 2.2: Velocity list of Sand-Clay mixture.

P_c(MPa)	load #	2.5	5.0	7.5	10.0	15.0	20.0	30.0	40.0	50.0
Pure Ottawa Sand – (dry)										
Vp(km/s)	up-1	0.87	1.09	1.28	1.35	1.48	1.56	1.75	1.87	1.99
Vp(km/s)	down-1	0.89	1.22	1.33	1.45	1.56	1.64	1.83	1.92	1.99
Vp(km/s)	up-2	0.88	1.12	1.29	1.36	1.50	1.59	1.77	1.92	2.03
Vp(km/s)	down-2		1.16	1.34	1.42	1.57	1.65	1.83	1.96	2.03
Vs(km/s)	up-1	0.69	0.69	0.78	0.84	0.89	0.93	1.03	1.11	1.16
Vs(km/s)	down-1	0.69	0.77	0.84	0.89	0.95	0.99	1.08	1.12	1.16
Vs(km/s)	up-2			0.80	0.86	0.92	0.97	1.09	1.16	1.22
Vs(km/s)	down-2	0.59	0.71	0.86	0.92	0.99	1.04	1.13	1.19	1.22
Pure Ottawa Sand – (saturated)										
Vp(km/s)	up-1	2.02	2.06	2.12	2.16	2.26	2.28	2.41	2.48	2.54
Vp(km/s)	down-1	2.05	2.12	2.16	2.22	2.27	2.31	2.44	2.51	2.54
Vp(km/s)	up-2	2.05	2.11	2.16	2.18	2.25	2.30	2.38	2.49	2.55
Vs(km/s)	up-1			0.65	0.71	0.79	0.81	1.05	1.12	1.26
Vs(km/s)	down-1		0.63	0.71	0.76	0.83	0.98	1.07	1.13	1.26
Vs(km/s)	up-2			0.69	0.74	0.80	0.85	1.05	1.12	1.27
Vs(km/s)	down-2		0.63	0.72	0.77	0.94	1.02	1.09	1.14	1.27
95 % Sand +5 %Clay (dry)										
Vp(km/s)	up-1	1.07	1.12	1.26	1.36	1.49	1.59	1.78	1.91	2.00
Vp(km/s)	down-1	1.08	1.10	1.20	1.36	1.49	1.59	1.78	1.92	2.00
Vs(km/s)	up-1	0.56	0.74	0.80	0.85	0.91	0.96	1.14	1.20	1.25
Vs(km/s)	down-1	0.55	0.74	0.81	0.87	0.94	0.99	1.14	1.21	1.25
95 % Sand +5 % Clay (saturated)										
Vp(km/s)	up-1	2.09	2.12	2.18	2.24	2.28	2.30	2.45	2.52	2.63
Vp(km/s)	down-1	2.12	2.18	2.23	2.26	2.31	2.36	2.47	2.55	2.63
Vs(km/s)	up-1					0.74	0.78	0.87	0.93	0.98
Vs(km/s)	down-1		0.59	0.67	0.72	0.78	0.82	0.90	0.94	0.98

TABLE 2.2 (continued)

P_c(MPa)	load #	2.5	5.0	7.5	10.0	15.0	20.0	30.0	40.0	50.0
90 % Sand +10 % Clay (dry)										
Vp(km/s)	up-1	0.88	1.12	1.27	1.38	1.55	1.62	1.81	1.95	2.08
Vp(km/s)	down-1	1.09	1.29	1.33	1.40	1.51	1.65	1.81	1.95	2.08
Vs(km/s)	up-1					0.91	0.96	1.09	1.19	1.28
Vs(km/s)	down-1	0.56	0.65	0.82	0.85	0.97	1.02	1.13	1.20	1.28
90 %Sand +10 % Clay (saturated)										
Vp(km/s)	up-1	2.18	2.25	2.29	2.35	2.38	2.41	2.55	2.66	2.74
Vp(km/s)	down-1	2.21	2.29	2.33	2.38	2.44	2.50	2.62	2.70	2.74
Vs(km/s)	up-1				0.62	0.76	0.78	0.87	0.93	0.98
Vs(km/s)	down-1			0.67	0.74	0.79	0.83	0.91	0.96	0.98
85 % Sand +15 % Clay (dry)										
Vp(km/s)	up-1	1.06	1.16	1.27	1.39	1.52	1.62	1.81	1.97	2.12
Vp(km/s)	down-1		1.08	1.24	1.32	1.50	1.58	1.81	1.97	2.12
Vs(km/s)	up-1		0.57	0.81	0.85	0.91	1.04	1.13	1.21	1.28
Vs(km/s)	down-1		0.77	0.81	0.87	1.02	1.06	1.15	1.22	1.28
85 % Sand +15 % Clay (saturated)										
Vp(km/s)	up-1	2.22	2.28	2.32	2.37	2.42	2.42	2.58	2.67	2.80
Vp(km/s)	down-1	2.24	2.33	2.43	2.43	2.48	2.51	2.63	2.74	2.80
Vs(km/s)	up-1				0.61	0.74	0.79	0.87	0.95	1.02
Vs(km/s)	down-1			0.60	0.74	0.80	0.83	0.93	0.98	1.02
80 % Sand +20 % Clay (dry)										
Vp(km/s)	up-1		1.11	1.33	1.38	1.48	1.54	2.01	2.28	2.44
Vp(km/s)	down-1	1.23	1.28	1.30	1.37	1.97	2.12	2.28	2.38	2.44
Vs(km/s)	up-1		0.64	0.68	0.71	0.78	0.81	1.09	1.21	1.34
Vs(km/s)	down-1	0.68	0.77	0.82	0.90	0.97	1.04	1.14	1.25	1.34
80 % Sand +20 % Clay (saturated)										
Vp(km/s)	up-1	2.08	2.19	2.27	2.34	2.38	2.44	2.56	2.70	2.80
Vp(km/s)	down-1	2.19	2.30	2.40	2.46	2.47	2.52	2.62	2.74	2.80
Vp(km/s)	up-2	2.19	2.26	2.36	2.43	2.48	2.50	2.61	2.74	2.84
Vp(km/s)	down-2		2.31		2.47	2.54	2.53	2.66	2.75	2.84
Vs(km/s)	up-1		0.53	0.66	0.72	0.76	0.82	0.90	0.97	1.02
Vs(km/s)	down-1	0.44	0.58	0.71	0.76	0.81	0.85	0.93	0.99	1.02
Vs(km/s)	up-2	0.44	0.55	0.69	0.75	0.82	0.85	0.93	1.00	1.05
Vs(km/s)	down-2		0.58	0.00	0.77	0.84	0.87	0.95	1.01	1.05

TABLE 2.2 (continued)

P_c(MPa)	load #	2.5	5.0	7.5	10.0	15.0	20.0	30.0	40.0	50.0
75 % Sand +25 % Clay (dry)										
Vp(km/s)	up-1	1.32	1.30	1.36	1.39	1.59	1.70	1.92	2.04	2.26
Vp(km/s)	down-1	1.23	1.24	1.43	1.50	1.90	1.91	2.05	2.17	2.26
Vs(km/s)	up-1			0.68	0.71	0.78	0.83	0.91	0.99	1.08
Vs(km/s)	down-1	0.53	0.62	0.77	0.84	0.94	0.94	0.99	1.04	1.08
75 % Sand +25 % Clay (saturated)										
Vp(km/s)	up-1	2.06	2.14	2.20	2.25	2.29	2.43	2.46	2.64	2.77
Vp(km/s)	down-1	2.15	2.27	2.34	2.41	2.46	2.60	2.66	2.75	2.77
Vs(km/s)	up-1	0.53	0.53	0.59	0.64	0.68	0.74	0.78	0.85	0.91
Vs(km/s)	down-1			0.63	0.68	0.73	0.83	0.86	0.90	0.91
70 % Sand +30 % Clay (dry)										
Vp(km/s)	up-1	1.08	1.07	1.35	1.36	1.52	1.65	1.85	2.02	2.17
Vp(km/s)	down-1	1.01	1.04	1.36	1.45	1.64	1.75	1.95	2.10	2.17
Vs(km/s)	up-1	0.53	0.62	0.67	0.72	0.80	0.85	0.94	1.01	1.06
Vs(km/s)	down-1	0.49	0.67	0.73	0.79	0.88	0.91	0.99	1.05	1.06
70 % Sand +30 % Clay (saturated)										
Vs(km/s)	up-1			0.61	0.66	0.70	0.73	0.92	1.02	1.09
Vs(km/s)	down-1		0.58	0.65	0.71	0.89	0.93	0.99	1.06	1.09
Vs(km/s)	up-2		0.58		0.69	0.88	0.92	0.99	1.06	1.14
Vs(km/s)	down-2		0.48		0.73	0.93	0.96	1.03	1.11	1.14
Vp(km/s)	up-1		2.23	2.28	2.33	2.40	2.41	2.55	2.73	2.86
Vp(km/s)	down-1		2.36	2.42	2.52	2.59	2.61	2.69	2.83	2.86
Vp(km/s)	up-2		2.36		2.49	2.54	2.55	2.68	2.82	2.98
Vp(km/s)	down-2		2.41		2.55	2.62	2.65	2.77	2.92	2.98
60 % Sand +40 % Clay (dry)										
Vp(km/s)	up-1	0.64	1.05	1.21	1.48	1.68	1.78	2.00	2.20	2.38
Vp(km/s)	down-1		1.37	1.53	1.74	1.86	1.98	2.17	2.26	2.38
Vs(km/s)	up-1	1.03	1.31	1.54	1.60	1.80	1.93	1.95	2.25	2.41
Vs(km/s)	down-1	1.22	1.45	1.66	1.78	1.97	2.09	2.26	2.38	2.41
Vs(km/s)	up-1	0.57	0.66	0.74	0.76	0.89	0.94	1.03	1.12	1.19
Vs(km/s)	down-1		0.82	0.89	0.97	1.01	1.04	1.11	1.16	1.19
Vs(km/s)	up-2	0.62	0.71	0.81	0.81	0.94	0.02	0.03	0.04	0.05
Vs(km/s)	down-2	0.76	0.86	0.92	0.96	1.04	1.12	1.14	1.20	1.21

TABLE 2.2 (continued)

P_c(MPa)	load #	2.5	5.0	7.5	10.0	15.0	20.0	30.0	40.0	50.0
60 % Sand +40 % Clay (saturated)										
Vp(km/s)	up-1				2.47	2.51	2.55	2.70	2.94	3.11
Vp(km/s)	down-1	2.29	2.29		2.57		2.73	2.80	3.04	3.11
Vp(km/s)	up-2				0.89	0.93	0.96	1.03	1.13	1.21
Vp(km/s)	down-2		0.88		1.00		1.06	0.03	0.04	0.05
50 % Sand +50 % Clay (dry)										
Vp(km/s)	up-1	1.02	1.19	1.25	1.41	1.61	1.71	1.93	2.09	2.24
Vp(km/s)	down-1	1.09	1.40	1.64	1.71	1.83	1.89	2.06	2.18	2.24
Vs(km/s)	up-1	0.63	0.68	0.72	0.78	0.88	0.93	1.02	1.09	1.17
Vs(km/s)	down-1	0.73	0.84	0.92	0.95	1.01	1.03	1.10	1.14	1.17
50 % Sand +50 % Clay (saturated)										
Vp(km/s)	up-1		2.26		2.36	2.42	2.49	2.67	2.86	2.96
Vp(km/s)	down-1		2.18		2.44	2.57	2.63	2.86	0.04	0.05
Vs(km/s)	up-1				0.79	0.85	0.90	1.02	1.10	1.17
Vs(km/s)	down-1		0.90		0.99	1.03	1.04	1.12	1.18	1.20
35 % Sand +65 % Clay (dry)										
Vp(km/s)	up-1		1.18	1.21	1.41	1.55	1.68	1.90	2.08	2.22
Vp(km/s)	down-1	1.40	1.62	1.72	1.81	1.92	1.97	2.09	2.18	2.22
Vs(km/s)	up-1	0.59	0.68	0.69	0.78	0.86	0.93	1.01	1.10	1.15
Vs(km/s)	down-1	0.85	0.96	1.00	1.03	1.06	1.07	1.11	1.15	1.15
35 % Sand +65 % Clay (saturated)										
Vp(km/s)	up-1	1.51	1.60	1.80	1.91	2.03	2.16	2.23	2.44	2.63
Vp(km/s)	down-1		2.30		2.38	2.47	2.48	2.57	2.61	2.75
Vp(km/s)	up-2		2.30		2.33	2.37	2.37	2.49	2.61	2.73
Vp(km/s)	down-2		2.19		2.38		0.02	0.03	0.04	0.05
Vs(km/s)	up-1						0.77	0.82	0.92	1.03
Vs(km/s)	down-1		0.85		0.89	0.94	0.96	0.99	1.01	1.03
Vs(km/s)	up-2		0.85		0.85	0.87	0.88	0.95	1.01	1.05
Vs(km/s)	down-2		0.87		0.94		1.00	1.02	1.05	1.05

TABLE 2.2 (continued)

P_c(MPa)	load #	2.5	5.0	7.5	10.0	15.0	20.0	30.0	40.0	50.0
15 % Sand +85 % Clay (dry)										
Vp(km/s)	up-1	0.91	0.94	1.12	1.32	1.48	1.59	1.79	1.97	2.11
Vp(km/s)	down-1		1.58		1.76	1.85	1.88	2.00	2.08	2.11
Vs(km/s)	up-1	0.61	0.61	0.67	0.75	0.82	0.89	0.97	1.06	1.11
Vs(km/s)	down-1		0.91		0.99	1.02	1.04	1.07	1.11	1.11
15 % Sand +85 % Clay (saturated)										
Vp(km/s)	up-1		1.46		1.55	1.76	1.82	2.01	2.17	2.40
Vs(km/s)	up-1		0.78		0.84	0.91	0.93	1.00	1.04	1.08
Pure Kaolinite (100 % clay) (dry)										
Vp(km/s)	up-1				0.97	1.37	1.40	1.59	1.76	1.90
Vp(km/s)	down-1	1.09	1.40	1.49	1.60		1.67	1.78	1.87	1.90
Vs(km/s)	up-1				0.77	0.90	0.91	1.01	1.11	1.17
Vs(km/s)	down-1	0.84	0.94	1.02	1.04		1.09	1.12	1.17	1.17
Pure Kaolinite (100 % clay) (saturated)										
Vp(km/s)	up-1	1.64	1.69	1.87	1.94	2.03	2.08	2.22	2.37	2.43
Vs(km/s)	up-1	0.87	0.91	0.97	0.99	1.03	1.06	1.12	1.19	1.22

References

Bear, J., 1972, Dynamics of fluids in porous media, American elsevier publishing company, inc.

Beard, D.C. and Weyl, P.K., 1973, Influence of Texture on Porosity an Permeability of Unconsolidated Sand, AAPG Bul. V.57, No.2, 349-369.

Birch, F., 1960, The velocity of compressional waves in rocks to 10 kilobars, J. G. R., 65, 1083-1102

Bourbie, et al., 1987, Acoustic of porous media, Gulf Publishing Company.

Carcia-Bengochea, et al., 1981, Correlative measurements of pore-size distribution and permeability in soils, Permeability and Ground-water Contaminant Transport, ASTM STP 746, American Society for Testing and Materials, 1981, 137-150.

Clark, R. H., 1979, Reservoir properties of conglomerates and conglomeratic sandstones, AAPG Bull., 63, 799-803

Digby, P.J., 1981, The effective elastic moduli of porous granular rocks, J. Appl. Mech., 48, 803-808.

Domenico, S.N., 1977, Elastic properties of unconsolidated porous granular rocks, Geophysics, 42, 1339-1368.

Dvorkin, J., Mavko, G. and Nur, A., "The Effect of Cementation on the Elastic Properties of Granular Material," 1991, Mechanics of Materials, 12, 207 - 217.

Han, D., et al., 1986, Effect of porosity and clay content on wave velocity in sandstones, Geophysics, 51, 2093-2107.

Heron, M., 1987, Estimating the intrinsic permeability of clastic sediments from geochemical data, SPWLA Symposium, paper HH.

Johnston, D.H., 1987, Physical properties of shale at temperature and pressure: Geophysics, 52, 1391-1401.

Liu, X., Dvorkin, J. and Nur, A., "The Effect of Cementation on Rock Properties: Experimental Study," 1991, abstract, AGU-1991, San Francisco.

Murphy, W., 1982, Effect of micro structure and pore fluid on the acoustic properties of granular sedimentary materials, Ph.D. dissertation, Stanford University.

Neasham, J.W., 1977, The morphology of dispersed clay in sandstones and its effect

on sandstone shaliness, pore space and fluid flow properties: 52nd Annual Fall Technical Conference and Exhibition of Society of Petroleum Engineers of AIME, Denvor, SPE paper 6858.

Nobes, D.C., et al., 1986, Estimation of marine sediments bulk physical properties at depth from sea-floor geophysical measurements, J.G.R., 91, 14033-14043.

Raymer, D.S., Hunt, E.R., and Gardner, J.S., 1980, An improved sonic transit time-to-porosity transform: Presented at 21st Ann. Mtg., Soc. Prof. Well-log Anal., paper P.

Reuss, A., 1929, Berechnung der fliessgrense von mischkristallen auf grund der plastizitatsbedingung fur einkristalle: Zeitschrift fur Angewandte Mathematik and Machanik, **9**, 49-58.

Tosaya, C., 1982, Acoustical properties of clay-bearing rocks, Ph.D. dissertation, Stanford University.

Winkler, K., "Contact Stiffness in Granular Porous Materials: Comparison between Theory and Experiment," 1983, GRL, 10 (11), 1073-1076.

Walls, J.D., 1983, Effects on pore pressure, confining pressure and partial saturation on permeability of sandstones, Ph.D. dissertation, Stanford University.

Wood, A.B., 1941, A Textbook of Sound, Macmillan, New York.

Wyllie, M.R.J., et al., 1956, Elastic wave velocities in heterogeneous and porous media, Geophysics, 21, 41-70.

Voigt, W., 1928, Lehrbuch der Kristallphysik, Teubner, Leipzig. Macmillan, New York.

Yin, H., Han, D. and Nur, A., 1988, Study of velocity and compaction on sand-clay mixtures, Stanford Rock and Borehole Project, Vol. 33.

Chapter 3

Critical Porosity—A physical boundary in poroelasticity

"By definition, porosity is the ratio of the pore volume (V_p) to the total volume (V_t) of the porous media considered... A good model of earth material should be simple and plain, as plain as you could make five-year old kid understand."

— Amos Nur, 1988, "GP262-lecture".

Porosity is one of the most important physical parameters of rock. For decades, researchers have been relating porosity to seismic properties with various methods of analysis. In this chapter, I present a physical model of a solid-fluid two phase composite—the *Critical Porosity Model.* Critical Porosity is a physical boundary between the solid-host and fluid-host porous media, a percolation threshold of qualitative phase transition from the solid-host state to the fluid-host state in poroelasticity. I discuss the physical insight of Critical Porosity and its intuitive mathematics through the concepts of "quantitative change" and "qualitative change" in the transition of elastic properties of porous media. I applied the idea of critical porosity and its consequent logic to correct "clay effect" on velocity with the "isostrain" and "isostress" physical concepts. The results show excellent agreement between the model and measured data.

3.1 Introduction

The elastic properties of fluid-filled porous media encompass a broad and diverse set of physical problems. The relation between elastic properties and porosity has been at issue for more than sixty years ever since Voigt (1928) and Reuss (1929) stated their "isostrain" and "isostress" models, and the Voigt Model and the Reuss Model are recognized for describing the extreme upper and lower bounds of elastic moduli of such a two-phase porous media as function of porosity.

Gassmann (1951) found a relation of fluid saturated elastic modulus as function of mineral bulk modulus, fluid modulus, dry frame bulk modulus, and porosity by considering elementary elasticity. The relation is well known as the Gassmann Equation. With an emphasis on solid-fluid relative motion which causes fluid diffusion, velocity dispersion, and attenuation, Biot (1956) proposed a simple semi-phenomenological theory that treats the average motions of both the solid and the fluid parts separately, as two distinct interpenetrating "effective media". To expand on the qualitative aspects of Biot's theory, Plona (1982) proposed two schemes of a saturated porous medium formed by the interpenetration of two phases, where the fluid phase is either discontinuous in scheme One, or continuous in scheme Two, and the solid phase is continuous in both schemes. He experimentally verified the theory of both a fast and a slow compressional wave, and a shear wave propagating in scheme Two. Schoenberg et al. (1983) used scheme Two to calculate slowness surfaces of those modes for a plexiglas-water system. He also found that there are two distinct compressional modes (one faster than another), and a shear mode.

Hashin and Shtrikman (1963) narrowed the Voigt and Reuss bounds by using a variational principle for stress and strain, and the result was found to provide the best possible bounds for bulk modulus when given the porosity of a medium, and the elastic moduli of its solid and fluid phases.

Toksöz et al. (1976) specified the properties of porous medium in terms of "effective properties" of K^*, μ^*, ρ^* and proposed a relationship between those quantities, and this is known, for arcane reasons, as QCA (Lax, 1951), Kuster-Toksöz (Kuster et al. 1974) approximation, or ATA (Sen et al. 1983). ATA is essentially a dilute-concentration theory.

Johnson (1986) summarized recent developments on the acoustic properties of porous media, in which the "multiple-scattering theory" (Berryman, 1980) was discussed. One of the approximations for a two-phase system is called "self-consistent" approximation, or CPA sometimes by analogy, with a theory of disorder in quantum-mechanical systems (Velickey et al. 1968). From the conventional multiple-scattering theory, one can not derive two distinct compressional modes because the simultaneous connectivity of the two components is not possible. There is one situation in which an "effective-medium" theory gives a good account of the acoustic properties of the fluid-solid system, and that occurs when the solid does not form a percolating cluster (solid suspension), and the host is nonviscous fluid. Then, the result agrees exactly with Wood's formula or Biot theory, provided one makes a substitution of the result of "dilute-concentration" of spherical solids, that is the Biot's high frequency limit for suspension status.

Most recently, Marion (1990) compared experimental data with Wood's relation and Biot's high frequency limit for suspensions, and pointed out the problem of the transition from "suspension" to "compacted" sediment.

All above works and other numerous studies here in SRB on the fluid-solid two phase system tell us that there is a characteristic difference of elastic property between the suspension status and grain contacted solid host status—a sight so familiar to everyone that not much attention has been paid.

What physical parameter can be used to distinguish these states unequivocally? Amos Nur pinpointed out that "a rock will break down and its poroelastic properties

should have a characteristic change when its porosity reaches a certain value, namely critical porosity" (Nur, 1990).

Inspired by Nur's sharp observation, and the similarity between "Critical porosity" and "Critical clay-content" discused in Chapter 2, I developed a new relation between acoustic velocity and porosity in this chapter by analyzing extensive experimental data. I have applied the "isostrain" and "isostress" concepts to "clay-effect" correction and derived a new relation between seismic velocity and clay-content for the consolidated rocks. The key to obtaining these relationships is the critical porosity, ϕ_c, below which the solid is stress-bearing, and above which the pore-fluid is also stress-bearing.

3.2 Physical insight of the critical porosity

Quantification: [1]

> *"Universal" proposition: For all porosities, if porosity is void fraction of porous media, then porosity is void fraction of a two-phase system;*
> $(\phi)\ [P_\phi \supset T_\phi]$;
> *"Instantiation": If porosity is 100% of porous media, then porosity is 100% of a two(?)-phase system. (from "universal" proposition.)*
> $P_{\phi=100\%} \supset T_{\phi=100\%}$ (?) *(Modus Ponens.)*

Analogously, if porosity is zero, then $[P_{\phi=0\%} \supset T_{\phi=0\%}]$ results in a single solid phase. Mathematicians may claim that one phase is a limit of a two phase system as

$$\lim_{\phi \to 100\%} T(\phi) \Rightarrow Fluid, \quad or \quad \lim_{\phi \to 0\%} T(\phi) \Rightarrow Solid. \tag{3.1}$$

But physicists would certainly argue that **solid** and **fluid** are physically different states of matter with qualitatively different physical properties, including elastic properties. Porosity as a physical parameter in poroelasticity may not be used as a continuous variable changing from 0 to 100% when porous media's physical state and properties undergo qualitative leaps.

[1] A theory devised for expressing in symbolic form statements of a general nature in modern logic.

3.2.1 Definition of the Critical Porosity

Porosity, by its definition, can be varied from 0 to 100%. Its use over that entire range may be appropriate only if the material's physical state is not a major concern, such as in the density—porosity linear relationship of a two-phase porous medium (Figure 3.1). However, porosity may not be used as a continuous variable changing from 0 to 100% when porous media's physical state and properties undergo a qualitative change. Figure 3.2. shows that velocity variation as function of porosity in clastic sediments has an apparently complex relationship, but a phase transition from a grain contact solid status to grain suspended fluid host status is rigorously characterized by the velocity data (measured in sand, Yin et al., 1988) with a narrow window of porosity variation.

We define CRITICAL POROSITY, ϕ_c as a certain porosity value when a given porous medium's solid-phase, or grains of clastic rocks, start to loose contacts. More inclusively, CRITICAL POROSITY is the porosity of a porous medium at which its poroelastic nature undergoes a *Qualitative Leap.*

When porosity varies from zero to critical porosity, or from critical porosity to 100%, we describe the variations of the physical characteristics of porous media as a process of *quantitative change*, a continuous change.

Different rocks may have different values of "Critical Porosity". The value of critical porosity in granular rocks may vary with the packing patterns, (cubic, hexagonal, or tetrahedral, etc.), the sorting properties, and grain-angularity (Figure 3.3).

In the plot of experimental velocity data as function of porosity (Figure 3.2), we can see that there is an apparent discontinuity of velocity as function of porosity at about 39% porosity. This is the porosity value of the simple hexagonal packing of spherical grains, and approximately the porosity value of the haphazard packing of natural Ottawa Sand. From this population, we may define the critical porosity for rock packed by spherical grains as 39%. We propose this value of porosity as

the Critical Porosity for similar types of clastic rocks. Such a porosity value may be indeed a boundary of qualitative changes of rocks' elastic properties. This is the implication of the Critical Porosity as well as its physical significance.

3.2.2 Intuitive algebra for applying the Critical Porosity

It seems no matter that Wyllie's time average formula (1956) or Schoenberg's (1983) fluid-solid system have not gone beyond the Voigt's "isostrain" or the Reuss' "isostress" physical assumptions. It has been well documented that the Reuss Model or the Wood Equation gives good account of acoustic properties of the fluid-solid system when the solid is in suspension status, e.g., when porosity is higher than critical porosity. The gaps between theories and measured data seems to have remained within the range of porosity varying from zero to critical porosity (solid-fluid two phase system with a solid host base).

The Voigt model states that elastic moduli have the following linear relationship with porosity,

$$M = (1 - \phi)M_s + \phi M_f \tag{3.2}$$

and the Reuss model has an inverse proportional relationship with porosity,

$$\frac{1}{M} = \frac{(1 - \phi)}{M_s} + \frac{\phi}{M_f} \tag{3.3}$$

where M_s and M_f are elastic moduli of solid and fluid, respectively.

The physical significance of the Voigt and the Reuss models are the "isostrain" and the "isostress" load bearing of solid phase and liquid phase. According to previous studies, we have learned that neither the Voigt model nor the Reuss Model matches real velocity data in the scope of porosity varying from zero to the critical porosity, but the Reuss Model fits data well when porosity greater than Critical porosity and velocity data hardly show any porosity dependency (Figure 3.2).

It is indeed valid to consider a solid host two-phase system by the isostrain physical assumption as Voigt proposed, if and only if the two-phase system is in *solid-host status.* What misdirected the Voigt model was that the isostrain assumption was retained throughout the entire range of porosity from 0 to 100%, without acknowledging that porosity above a certain value would invalidate the isostrain assumption itself. As defined above, the critical porosity can explicitly dilineate the solid-host status from fluid-host status and make the isostrain or isostress assumption valid.

The intuitive algebra asks that we should equate value of the modulus via the Voigt isostrain model with the value of the modulus given by the Reuss isostress model at critical porosity. We have observed that the elastic property of a two-phase system is approximately constant and close to the elastic property given by the Reuss "isostress" model when porosity is equal to or greater than the critical porosity, that is in suspension status in Figure 3.2. Now, the intuitive algebra is that $(1-\phi)$ must be zero, and ϕM_f equals M_f when porosity is equal to the critical porosity in Equation 3.2, the Voigt model. We can get this result by simply defining $\bar{\phi} = \phi/\phi_c$ where ϕ_c is critical porosity, and substitute ϕ in the Voigt model with $\bar{\phi}$ as

$$M = (1 - \bar{\phi})M_s + \bar{\phi}M_{fs}, \quad (0 \leq \phi < \phi_c) \tag{3.4}$$

where M_s and M_{fs} are the modulus of solid grains, and the modulus of grains suspended in fluid, respectively.

To identify M_{fs}, one may use a velocity-porosity plot to find critical porosity, or make an assumption of critical porosity based on the rock type studied, then calculate M_{fs} with the Reuss relation at critical porosity. To have a closer description of elastic moduli at critical porosity, I use M_{fs} here which is modulus resulted from both fluid and solid interpenetration, rather than M_f which is solely the modulus of fluid.

The results of this modified Voigt-average are plotted in Figure 3.4. Note that the bulk modulus drops linearly to the critical porosity, then follows Reuss model in the

fluid saturated case, or drops to zero at critical porosity in the dry case. The shear modulus is linearly changed to zero in both the dry and saturated cases. We may name this physical modeling approach "Critical Porosity Modeling".

I calculated both P-wave and S-wave velocities under both dry and saturated conditions based on above model, and the velocity-moduli relations,

$$\begin{cases} V_p = \sqrt{(K + 4G/3)/\rho}, \\ V_s = \sqrt{G/\rho}, \end{cases} \tag{3.5}$$

where K, G and ρ are the bulk modulus, the shear modulus, and the density of the rocks respectively.

The result in Figure 3.5 shows excellent agreement between measured velocity data in clean sandstones and clean Ottawa sands (Han et al., 1986, and Yin et al., 1988).

This simple critical porosity modeling explicitly describes the *qualitative leap* of the elastic properties from solid host status to suspension status, and also the *quantitative changes* of the elastic properties for porous media where porosity varies on either side of Critical Porosity.

3.3 A new look at Gassmann Equation

Many sedimentary rocks consist of a porous skeleton filled with water. Those special cases where the pore space is filled with oil or gas are of particular interest, so the possible effects of fluid content on seismic velocity and other properties of porous rocks merit detailed attention. To approach this problem with a minimum of simplifying assumptions, Gassmann (1951) supposed that the elastic properties of the skeleton could be measured some way, and he derived an expression for the corresponding properties of the rock when saturated with any fluid of known properties as the following,

$$K - K_o = \frac{(1 - K_o/K_s)^2}{\phi/K_f + (1-\phi)/K_s - K_o/K_s^2} \tag{3.6}$$

where K and K_o are the bulk modulus in saturated and dry conditions respectively, K_s is the bulk modulus of minerals or pure solid part of a porous medium, K_f is the fluid bulk modulus. Note that shear modulus G in saturated-condition is equal to G_o in dry-condition, and shear velocity is only influenced through density by saturation.

The Gassmann Equation appears to be quite compatible with the limiting cases as porosity varied from 0 to 100%. For a pure solid-phase medium corresponding to $\phi = 0$, the right hand side of the Gassmann Equation equals $K_s - K_o$, so $K = K_s$ as one would expect. For a pure fluid-phase medium corresponding to $\phi = 1$ and $K_o = 0$, we can obtain $K = K_f$ from the Gassmann Equation (Bourbie et al., 1987, p. 68). It seems that fluid bulk modulus K_f affects the medium's bulk modulus K through the factor ϕ/K_f, and thus the influence of fluid should decrease with decreasing porosity in the Gassmann Equation. One may even think that the Gassmann Equation can be used to calculate bulk modulus as function of porosity.

We must realize that the Gassmann Equation is totally misrepresented in the discussion above. Gassmann did not solve the relation between modulus and porosity. He supposed that the properties of skeleton with a given porosity in dry condition is known, and he only derived the equation for the corresponding properties of that medium when saturated with known property fluid.

Actually, K_o, the dry modulus of the skeleton of a porous medium varies with porosity, and it may dominate the elastic properties of the porous medium. Now, does the Gassmann Equation predict saturated modulus better than other models when rock's porosity, dry modulus, and saturation fluid modulus are given?

In order to look into how the dry modulus affects the medium's elastic properties with porosity as a variable, and how the Gassmann Equation predicts saturation effect compared with other models, I used the Voigt model, the Reuss Model, and the

Critical Porosity Model to calculate the dry modulus K_o as function of porosity, then predicted the saturated modulus K with the Reuss, Voigt, Critical Porosity models, and the Gassmann Equation. The results were plotted in Figure 3.6. We may learn the following two points from the results.

First, K_o, the dry modulus of the skeleton of a porous medium as function of porosity, dominates the elastic properties of the porous medium. Clearly, the Critical Porosity Model predicts the bulk modulus K_o as a function of porosity much better than does the Voigt (the upper bound) and the Reuss (the lower bound) models.

Second, the Gassmann Equation did not much improve the Voigt average, the Reuss average, or the Critical Porosity Model for predicting saturated modulus K from a given dry modulus K_o, although the Gassmann Equation has been recognized as well-consideration of elementary elasticity. The complicated right-hand side of the Gassmann Equation, $[(1 - K_o/K_s)^2]/[\phi/K_f + (1 - \phi)/K_s - K_o/K_s^2]$, did no better than ϕK_f in the Voigt average, or $\bar{\phi} K_f$ in the Critical Porosity Model for predicting the fluid saturation effect. A plain and simple model of earth material should be more applicable than does a complicated one.

3.4 Modeling clay-effect with the concept of Critical Porosity

Shaly sandstones are among the most common constituents of sedimentary rocks, and they are of foremost relevance to hydrocarbon reservoirs. The acoustic properties of these rocks are thus of great interest in both seismic exploration and acoustic log interpretation.

Tosaya (1982), Kowallis et al. (1984) and Han (1986) summarized their studies on clay effect correction to velocity predictions by least squares regression, which resulted in empirical relationships of velocities as functions of porosity and clay content. Such empirical formulae could not account for the physical locations of clay with respect

to the mineral framework, , that is clay within the pore space or clay wedged into contact zones between mineral grains of higher modulus, as stated by Tosaya. The importance of clay location arises because clays between matrix grains have a far greater effect on skeleton dry modulus than do clays only within pore space. This distinction is even more important for saturated rock samples.

Mathematical modeling, including least squares regression, is a powerful tool for dealing with quantities, magnitudes, their relationships, and quantitative attributes, but a physical approach may reveal nature, changes, interactions and qualitative attributes of matter. A physical model with appropriate reasoning, rather than just a model originated from data fitting, should lead us to a better understanding of the data.

The way that shaliness affects rock elastic properties depends on the amounts of clay, its physical properties, and also on the location of clay in rocks. Clay material can be distributed in rocks by the following four major ways:

1. Sand grain lining or dispersed clay;

2. Laminal or large fracture-filling clay;

3. Pore-filling clay;

4. Pseudomorphous replacement or structural clay.

Clay distributions in the way of (1) and (2) may be modeled by the isostress assumption, while clay distributions such as (3) and (4) may be modeled by isostrain relation.

Sometimes, the amount of detrital (allogenic) clays at sand grain contacts is proportional to the total amount of clay in a given rock, so that as clay content increases, so does the probability that clay is positioned at sand grains' contact (Tosaya 1982, and Jizba 1991). However, it is often observed that small amount of authigenic clay

associated with altered feldspars, very fine detrital clay, and iron (Fe) oxide appear as rims that encapsulate detrital quartz grains and define the edge of quartz grain, even among the mostly siliceous cement. Such a case is quite common among shaly rocks such as Gulf Sandstone and Tight Gas Sandstone, based on the petrophysical description in "Rock Catalog of Stanford Rock Physics". These clay "rims" may be only a few percent or less in terms of its volume fraction, but they may significantly reduce the rigidity of rocks (Han 1986), especially the shear modulus.

We find hardly any correlation between porosity and clay contents in real rocks due to the complexity of mechanical and chemical aspects of diagenesis, though such a correlation was found in binary mechanical packing of spheres when combining sand and clay powders (Yin et al. 1988). Here, we treat clay as a solid part of solid-fluid system, since we may only measure the overall porosity in real rocks.

Based on the analysis above, we may redefine the elastic moduli of solid M_s in Equation 3.4 as

$$M_s^i = (1 - \bar{C})M_q^i + \bar{C}M_{qc}^i \tag{3.7}$$

where $\bar{C}$ is "pseudo clay volume fraction"; M_q is modulus of quartz in the case of shaly-sand or sandy-shale system; M_{qc} is the modulus resulting from quartz grain and clay interaction (except clay volume fraction V_c equals 100%, then it is modulus of pure clay); and $i = +1$, if "isostrain", or $i = -1$, if "isostress". We divide clay volume fraction V_c into three regimes:

1. If $0\% < V_c \leq 5\%$, clay as grain-coating rims, then
   $\bar{C} = V_c$, $i = -1$, "isostress".

2. If $5\% \leq V_c \leq 40\%$, clay as framework, then
   $\bar{C} = (V_c - 0.05)/0.35$, $i = +1$, "isostrain".

3. If $40\% \leq V_c \leq 100\%$, clay as matrix, then

$\bar{C} = (V_c - 0.4)/0.6$, $i = -1$, "isotress".

where c is total clay volume fraction.

Through the above analysis, bulk modulus and shear modulus were calculated as functions of porosity at different clay volume fractions (Figure 3.7), and as function of clay volume fraction at different porosity (Figure 3.8). Velocities are also predicted with the above method, and compared with measured P-wave and S-wave velocity data (Han 1986, and Yin 1988) in Figure 3.9. The results show good agreement between the the clay-effect corrected Critical-Porosity model and the large set of measured data. Figure 3.10 and Figure 3.11 are the three dimensional presentations of bulk and shear moduli, and P-wave and S-wave velocities predicted with our clay-effect corrected Critical Porosity Model.

The choices of dividing clay volume fractions into two or three regimes and setting bounds for those regimes remain a subject of further discussion. Here, my approach is to look for insight with simple physical assumptions and modeling, rather than using numerical analysis as a tool to derive empirical relations.

The critical porosity and the clay volume fraction values used to divide shaly rocks into three regimes in this study may only be valid for the type of rocks we have studied here. Still, I think that the compositions of this clay-effect corrected Critical Porosity approach will shine new light on the variation of P-wave and S-wave velocities as functions of porosity and clay content.

The isostrain or the isostress assumptions may be also applied when modeling interbeded anisotropic porous media with a proper value of critical porosity. A wave propagating parallel to bedding may travel in isostrain status, and a wave propagating perpendicular to bedding may travel in isostress status.

3.5 Conclusion

Critical porosity for different rock types may take on different values, but its physical implication is to distinguish a qualitative leap of rocks' elastic properties in a qualitative way.

Critical porosity is a boundary of characteristic differences between the elastic properties of matrix grains in suspension status and grains compacted together in a solid host status. Critical porosity is a limit of the *quantitative change* in the elastic properties of solid host porous media as function of porosity. Critical porosity marks a *qualitative leap* of the elastic properties of a composite solid-fluid porous system, a phase transition from the frame-supported solid host status to the grain suspension status.

The isostrain and isostress approximations are valid physical assumptions, but the isostrain assumption may be applied if and only if a two-phase system is in solid-host status, and the isostress assumption may be applied if and only if a two-phase system is in fluid-host status. The isostrain approximation may fit real velocity data exclusively when Critical Porosity is applied.

Through extensive experimental data and a physical modeling approach, we have derived rigorous relations between velocities, porosity, and clay-content. The key to obtaining these improved relationships is the critical porosity, ϕ_c, below which the solid is stress-bearing, and above which the pore-fluid and solid grains are equally stress-bearing.

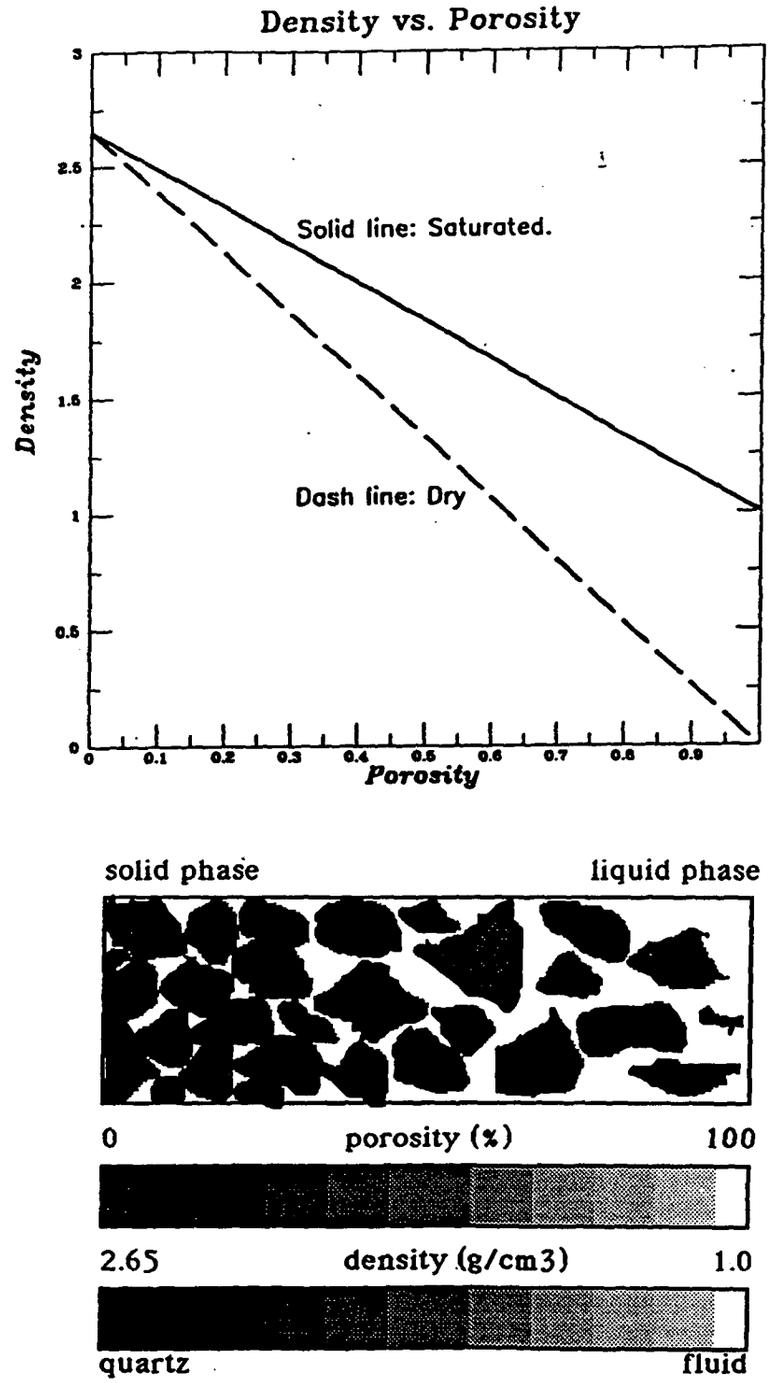

Figure 3.1: Density of a two-phase medium may have a linear and continuous relationship as function of porosity, varying from 0 to 100%, e.g., $\rho = (1 - \phi)\rho_g + \phi\rho_f$.

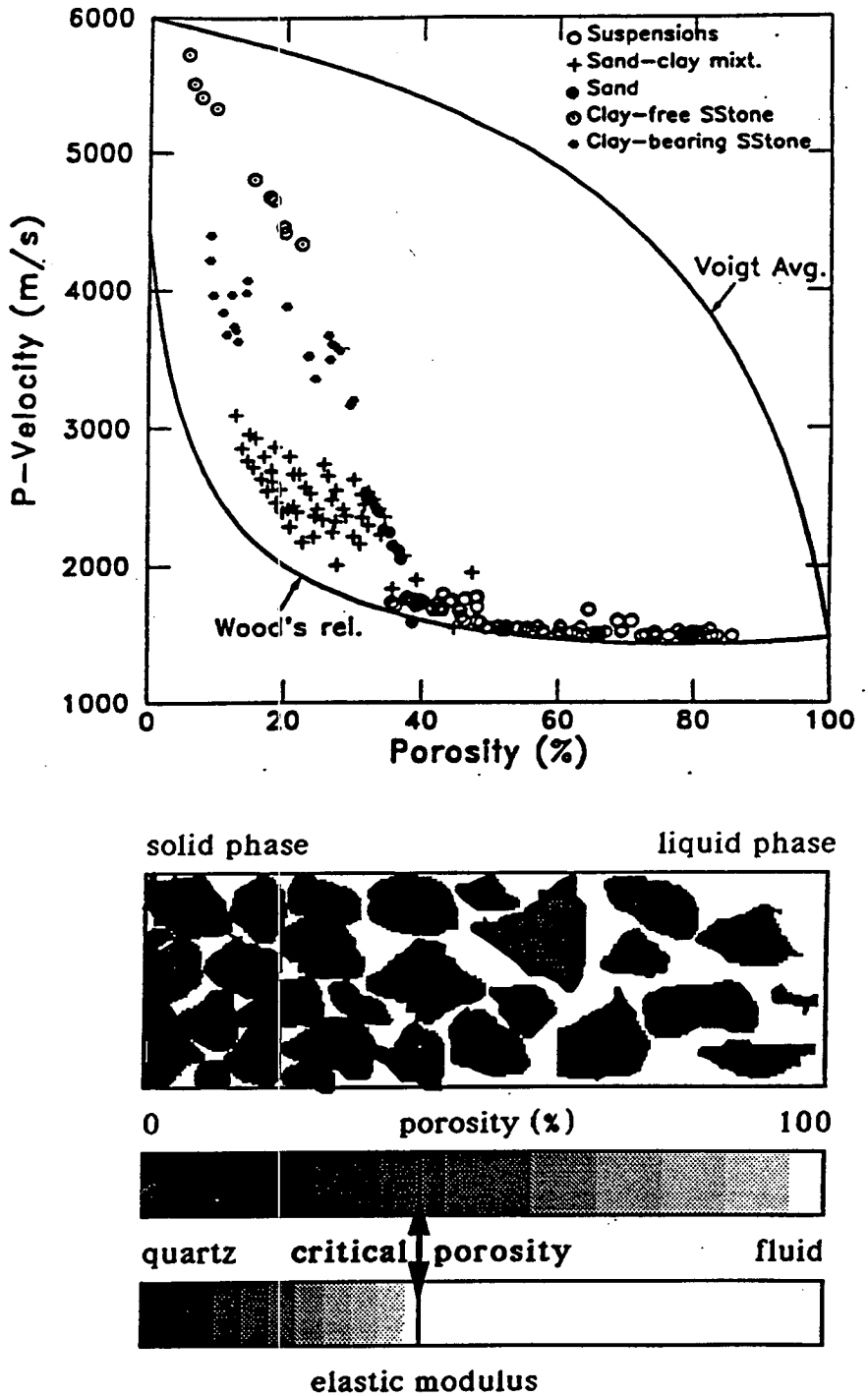

Figure 3.2: Velocity vs. porosity data in clastic sediments show the apparent complexity of the relationship (after Marion 1990). Data are from Hamilton (o), 1956, Han et al., (⊙ and ∗) 1986, and Yin et al., (• and +), 1988. The phase transition from grain contact solid host status to grain suspended fluid host status is rigorously characterized by the Critical Porosity.

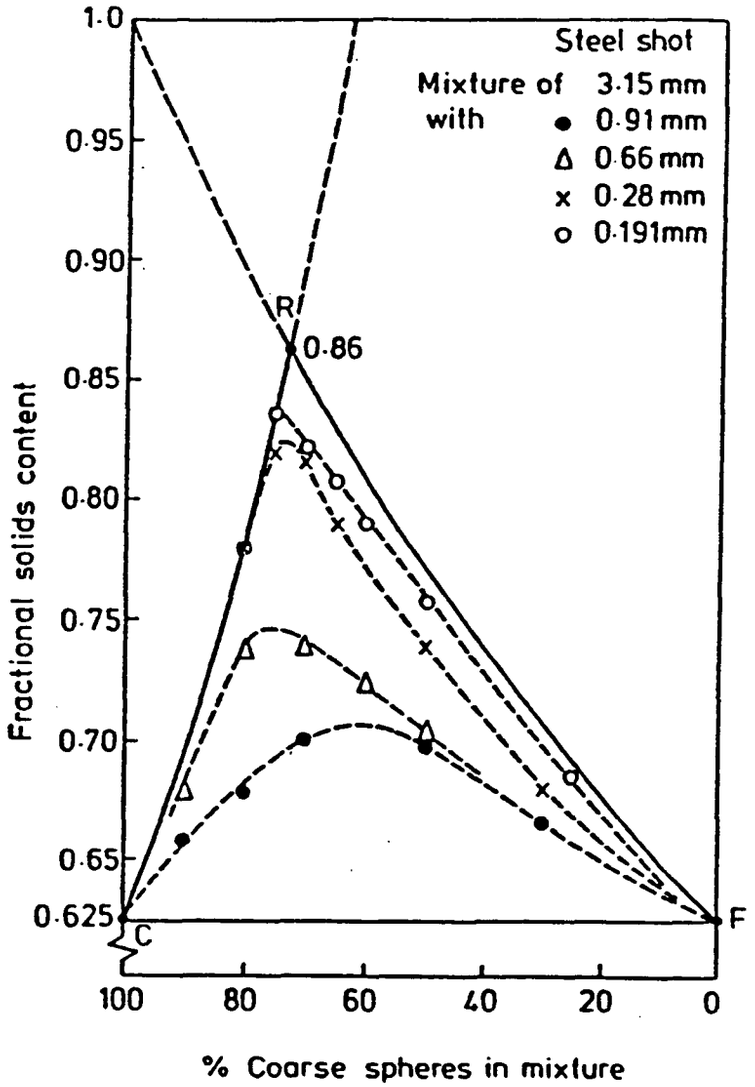

Figure 3.3: Binary mechanical packings of spheres. (after Cumberland et al., 1987)

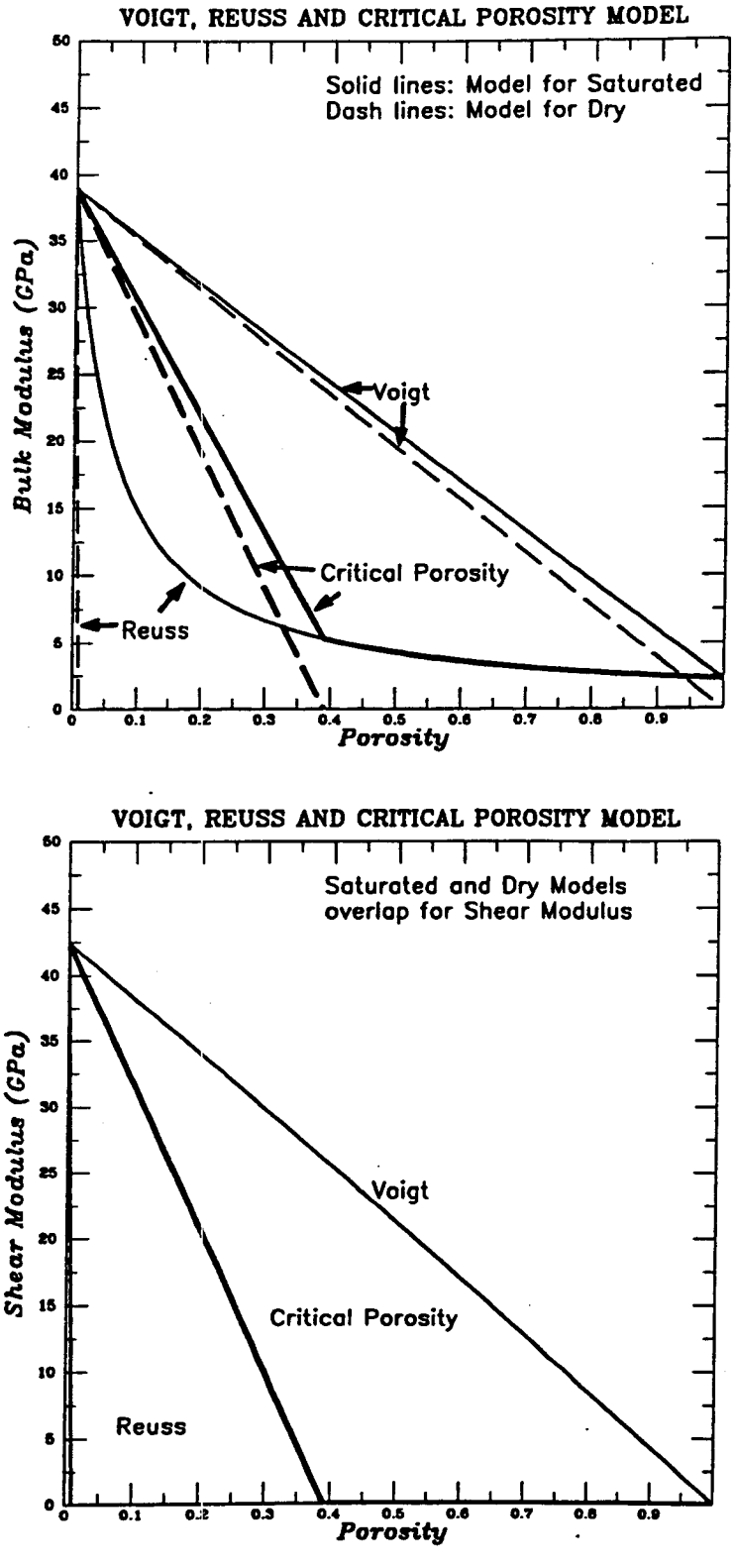

Figure 3.4: Bulk Modulus and Shear modulus as calculated with the Voigt, Reuss and Critical Porosity models, respectively.

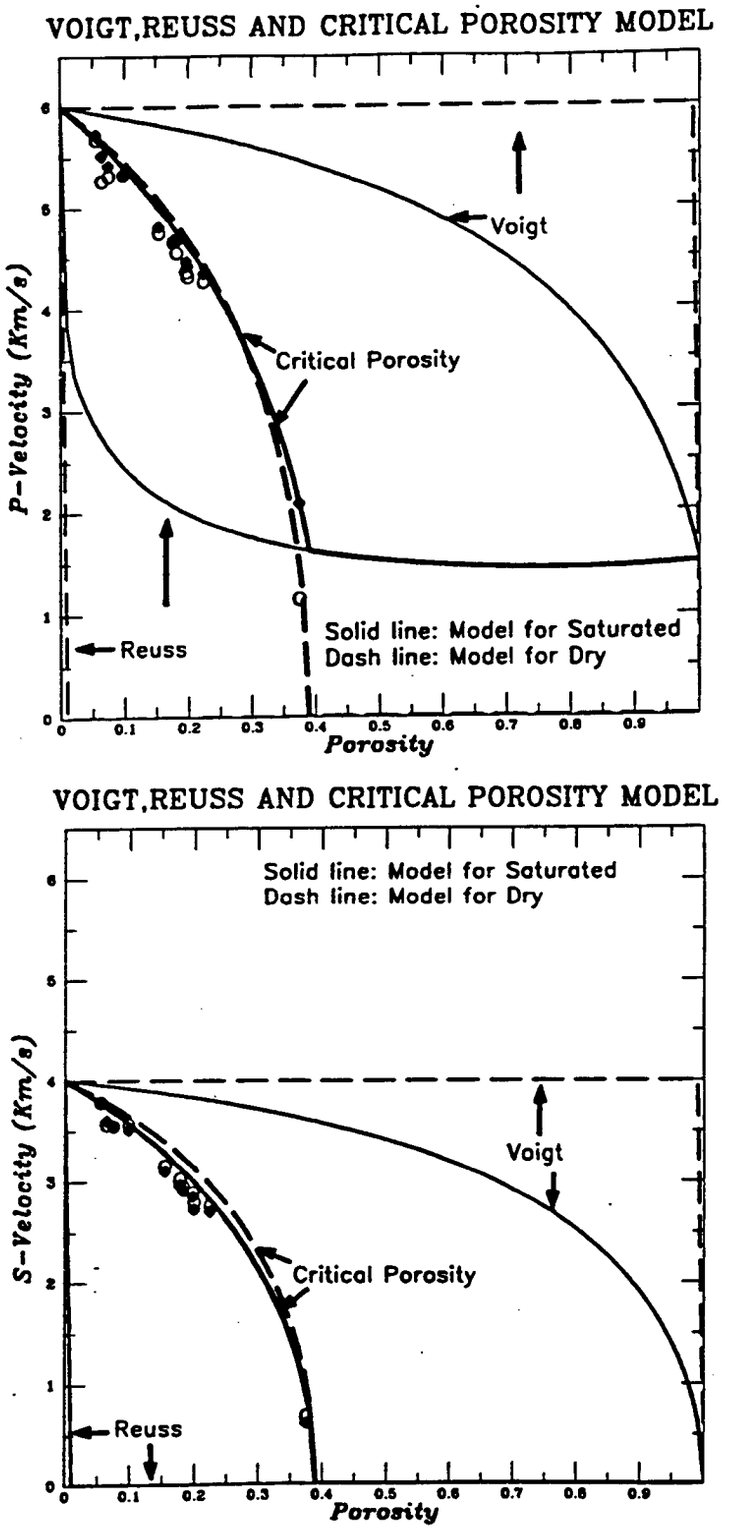

Figure 3.5: P-wave and S-wave velocities were calculated with the Voigt, Reuss and Critical Porosity Models, and compared with the measured data (Han, 1986, and Yin et al., 1988). Both P-wave and S-wave velocities calculated with Critical Porosity Model shows good agreements.

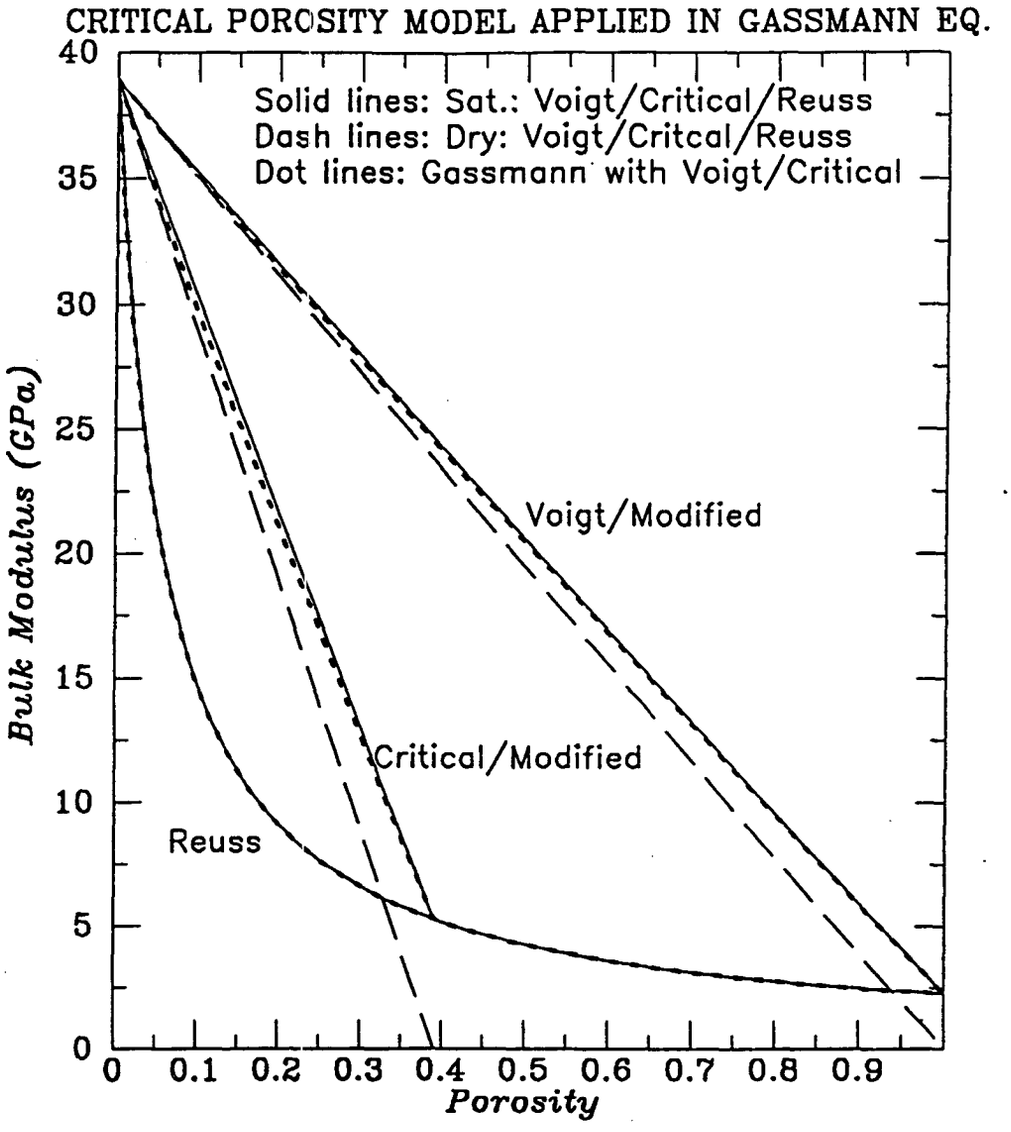

Figure 3.6: The bulk modulus of dry skeleton K_o calculated with the Voigt, Reuss, and Critical Porosity models as function of porosity was used to predict saturated bulk modulus with the Gassmann Eq., Voigt average, Reuss average, and Critical Porosity models. Note that Gassmann Eq. prediction hardly shows any advantage compared with Voigt average and critical porosity model.

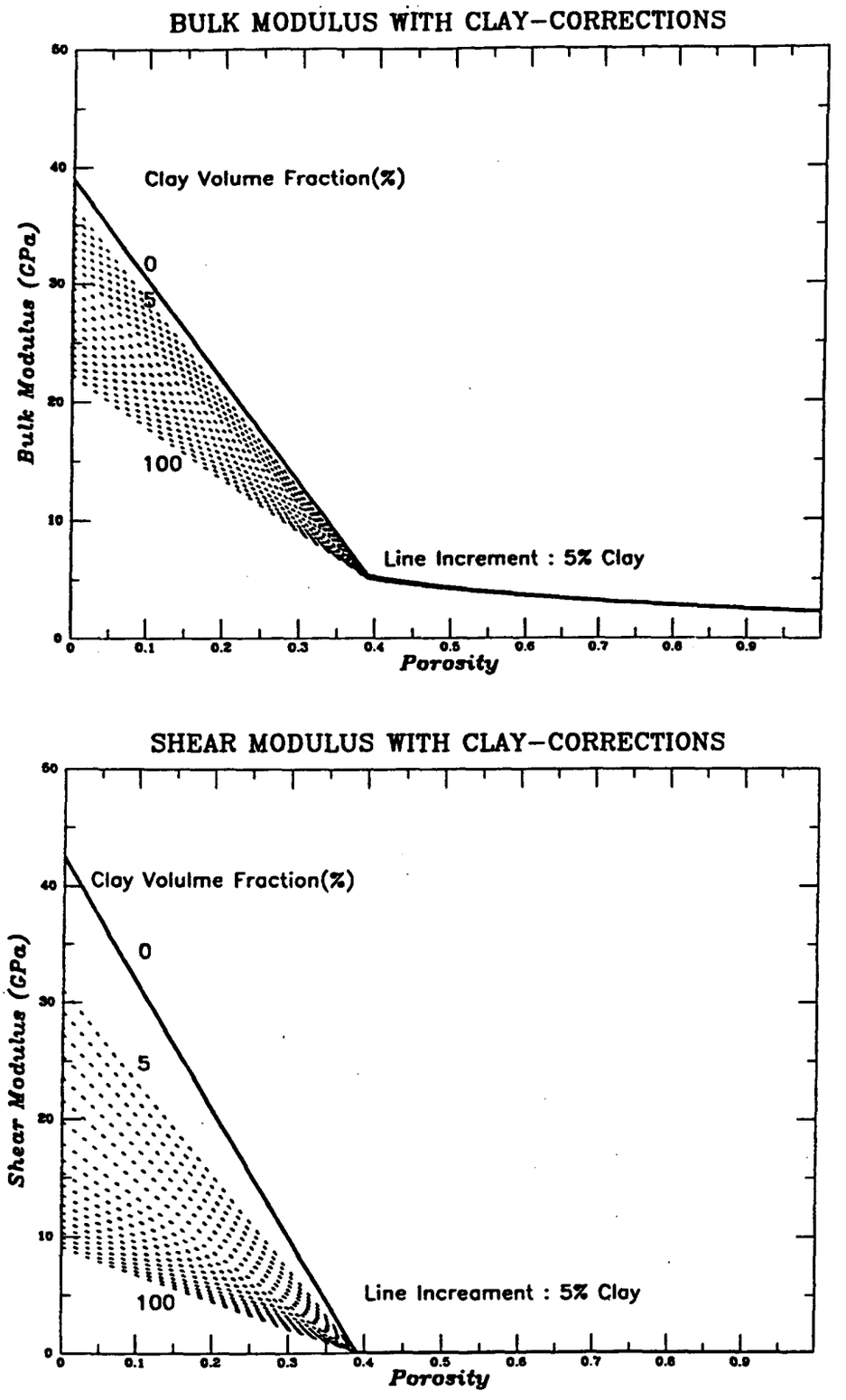

Figure 3.7: Bulk and Shear moduli as function of porosity were calculated with clay effect correction term in Critical Porosity Model.

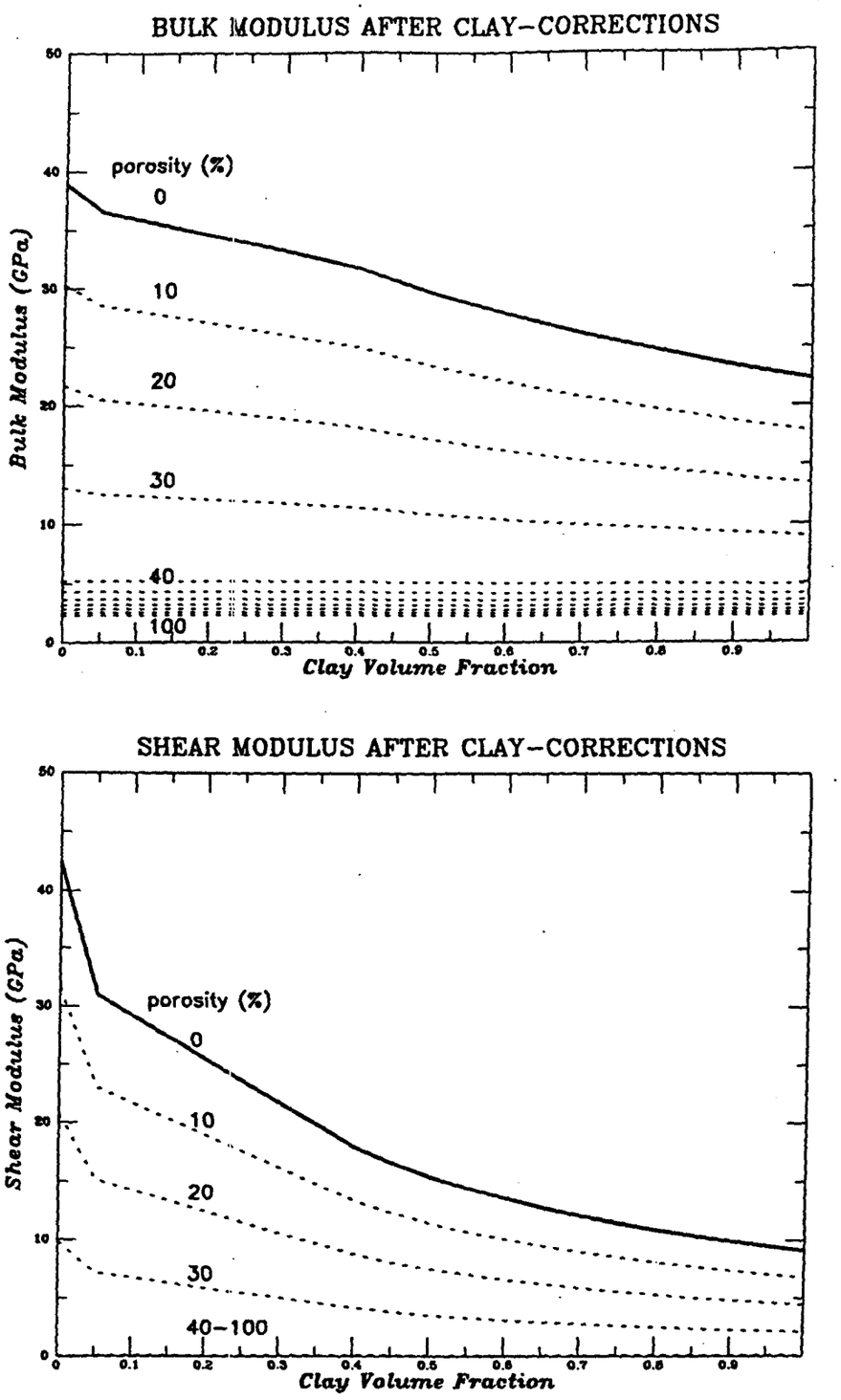

Figure 3.8: Bulk and Shear moduli as function of clay volume fraction were calculated with the clay effect correction term in Critical Porosity Model.

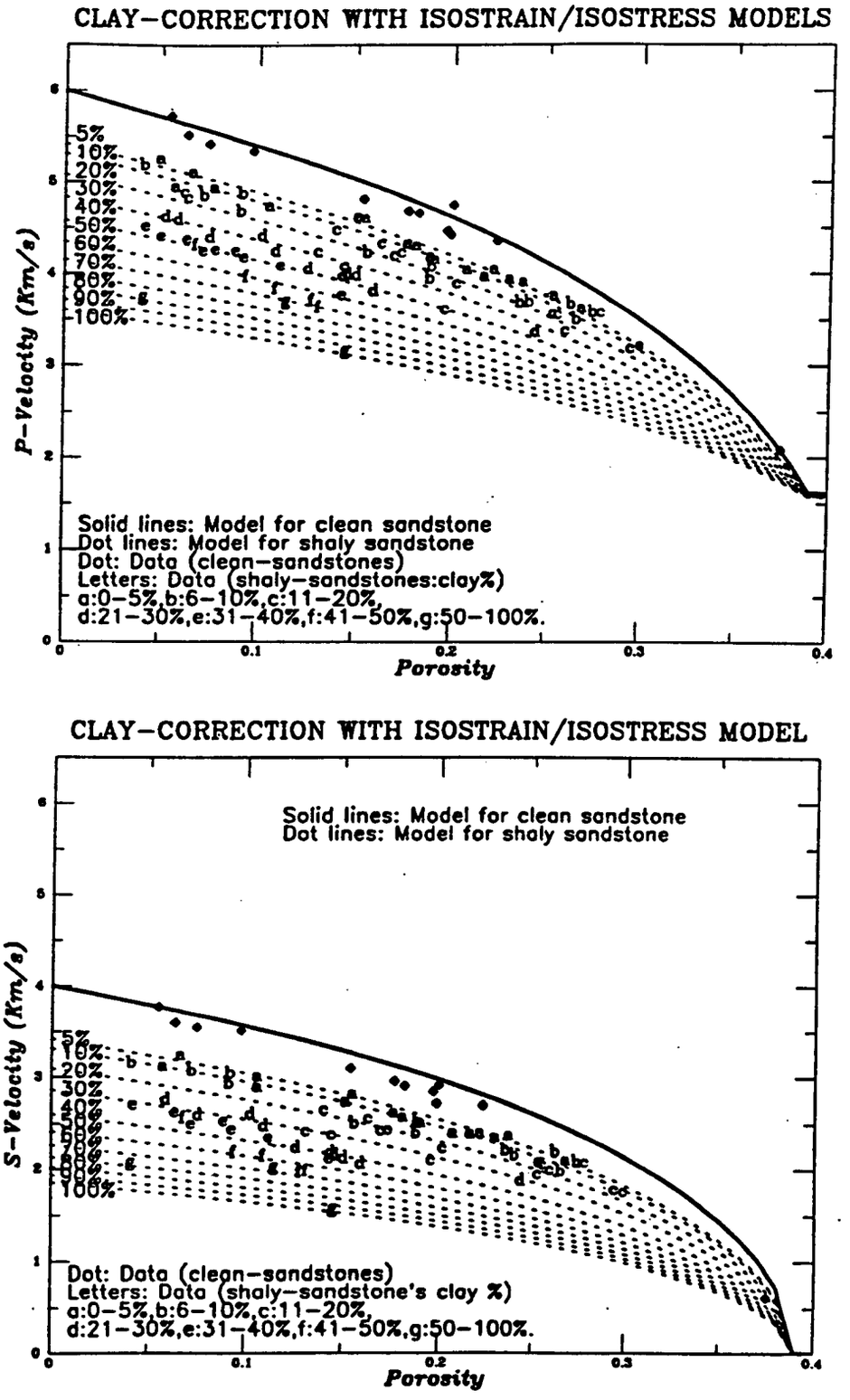

Figure 3.9: Calculated P-wave and S-wave velocities with clay effect corrected Critical Porosity Model, and compared with the measured data (Han, 1986, and Yin et al., 1988). It shows good agreement between the calculation and data.

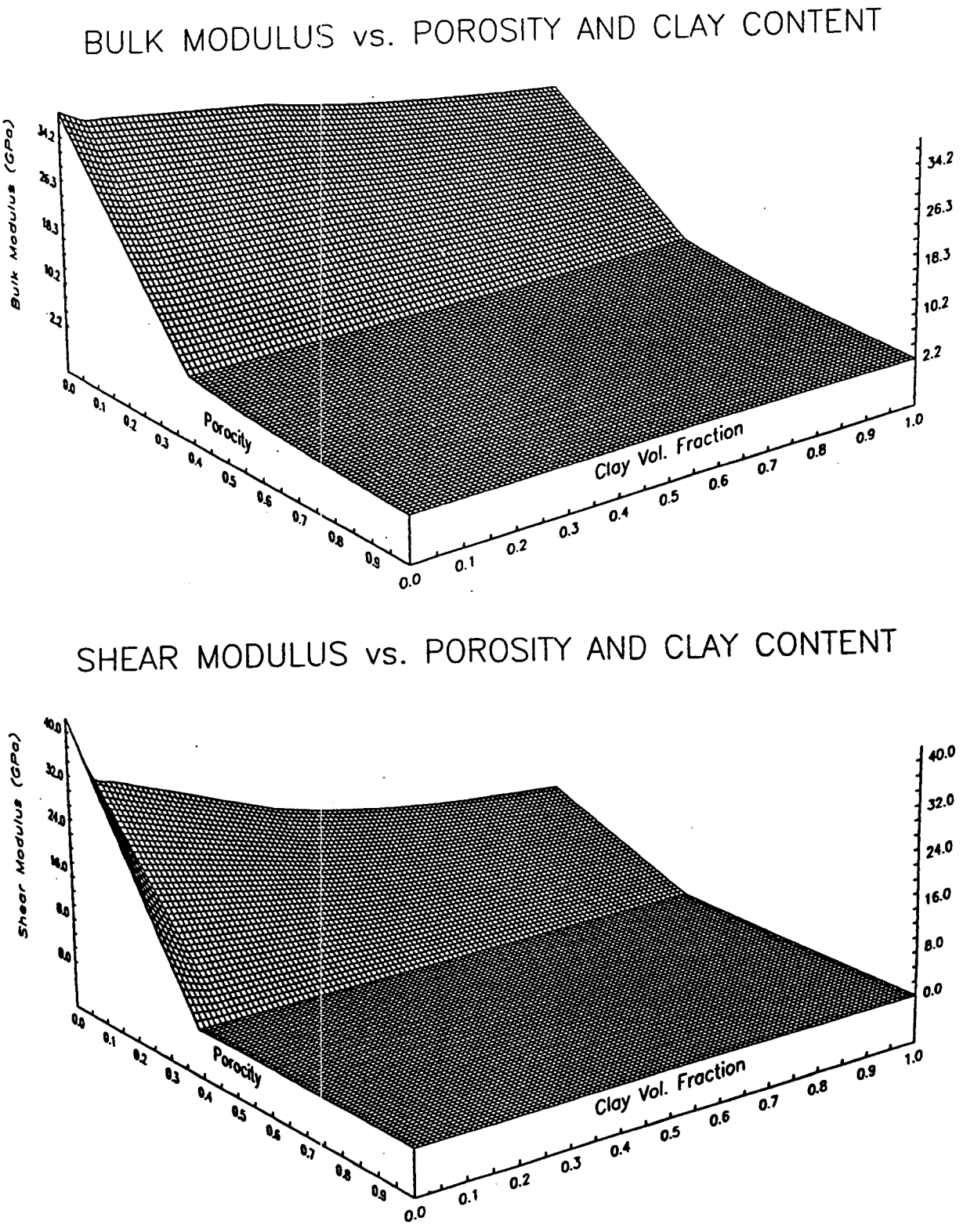

Figure 3.10: 3-D presentation of the relationship of Bulk and Shear moduli as a function of porosity and clay volume fraction by the clay effect corrected Critical Porosity Model.

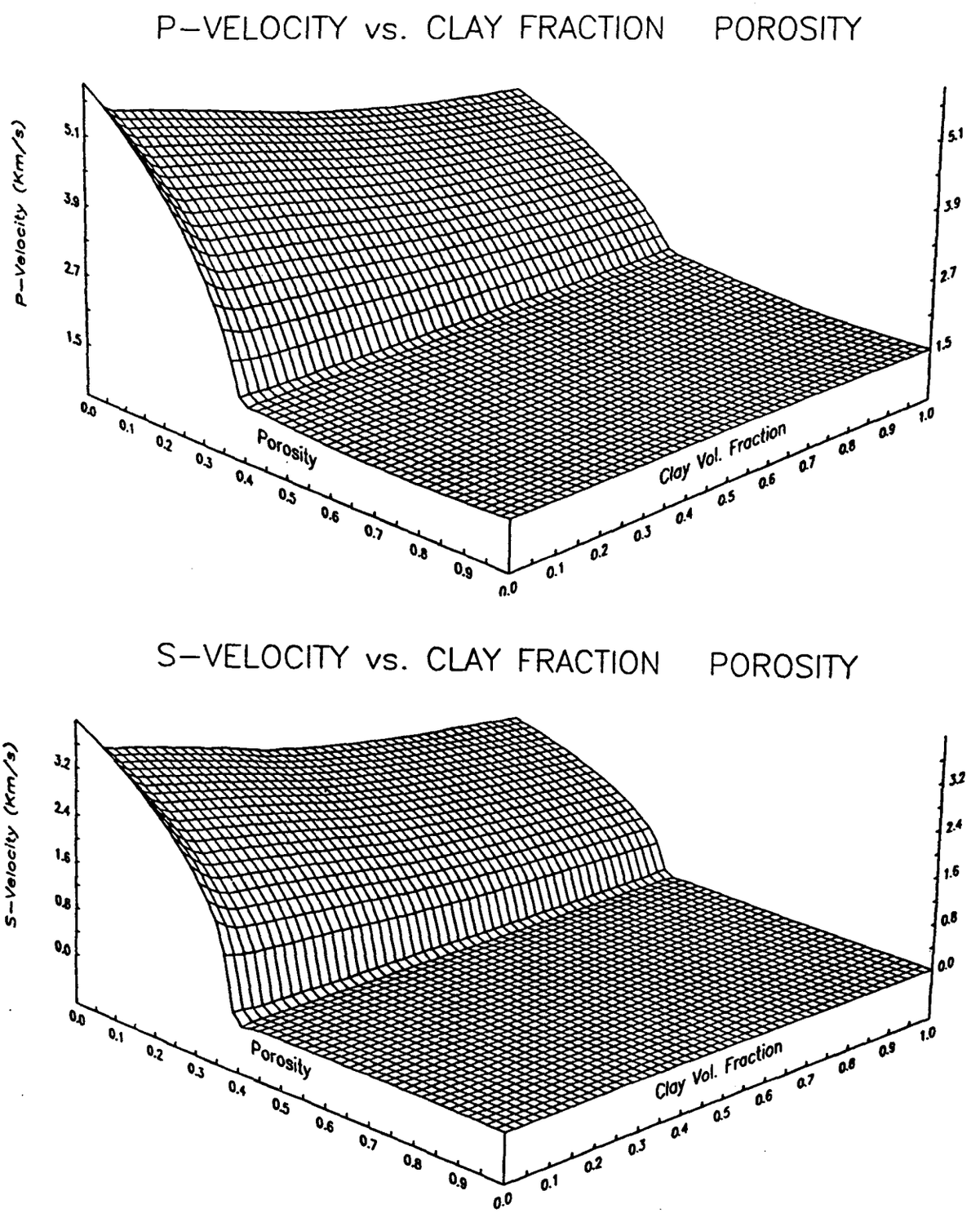

Figure 3.11: 3-D presentation of the relationship of P and S velocities as a function of porosity and clay volume fraction by the clay effect corrected Critical Porosity Model.

References

Biot, M. A., 1956, Theory of propagation of elastic waves in fluid saturated porous solid, 1. Low-frequency range, J Acoust. Soc. Am., 28, 168-178

Biot, M. A., 1956, Theory of propagation of elastic waves in fluid saturated porous solid, 1. Higher-frequency range, J Acoust. Soc. Am., 28, 179-191

Cumberland, D. J. and Crawford, R. J., 1987, The packing of particles, Elsevier, Amsterdam - Oxford - New York - Tokyo.

Gassmann, F., 1951, Elastic waves through a packing of spheres: Geophysics, Vol. 16, 673-685

Han, D., Nur, A. and Morgan, D., 1986, Effect of porosity and clay content on wave velocity in sandstones, Geophysics, Vol. 51, 2093-2107

Hamilton, E. L., 1956, Low sound velocities in high porosity sediments: J. Acoust. Soc. Am., 28, p. 16-19.

Hashin, Z. and Shtrikman, S., 1963, A variational approach to the elastic behavior of multiphase materials, J. Mech. Phys. Solid, Vol. 11, 127-140.

Jizba, D. L., 1991, Mechanical and acoustical properties of sandstones and shales, Ph.D dissertation, Stanford University.

Johnson, D. L., 1986, Recent developments in the acoustic properties of porous media, Proceedings of the International school of Physics, Course XCIII, Frontiers in Physical Acoustics, edited by D. Sette, North-Holland.

Kuster, G. T., and Toksoz, M. N., 1974, Geophysics, 39, p. 587-607

Lax, M., 1951, Rev. Mod. Phys., 23, p. 287

Marion, D. P., 1990, Acoustical, mechanical and transport properties of sediments and granular materials, Ph.D dissertation, Stanford University.

Nur, A. and Simmons, G., 1969, The origin of small crack in igneous rocks, Int. J. Rock Mech. Sci. Vol. 7 307-314

Nur, A., Summer, 1990, Personal Communication.

Plona, T., Acoustic of fluid-saturated porous media, Ultrasonic Symp. IEEE, 2, 1044-1048.

Reuss, A., 1929, Berechnung der dliessgrense von mischkristallen auf frund der plastizitatsbedingung fur einkeristalle, Zeitschrift fur Angewandte Mathematik and Mechanik, Vol. 9, 49-58.

Sandstone Diagenesis Application to hydrocarbon exploration and Production, 1981, Compiled by Ali, Syed. A., Geology and International Department, Department Report No. 4231R006, Gulf Science and Technology Company.

Schoenberg, M., 1983, Appl. Phys. Lett., Vol. 42, 350.

Sen, P. N., and Johnson, D. L., 1983, Phys. Rev. B, 27, p. 3113

Stanford Rock Physics Rock Catalog, 1984, Vol. 1 Compiled by Leslie B. Yale.

Stanford Rock Physics Rock Catalog, 1985, Vol. 2 Compiled by Katherine K. Velasco.

Stanford Rock Physics Rock Catalog, 1986, Vol. 3 Compiled by Katherine K. Velasco.

Toksoz, M. N., Cheng, C. H. and Timur A., 1976, Velocities of seismic waves in porous rocks, Geophysics, Vol. 40, No. 4, 621-645.

Tosaya, C. and Nur, A., 1982, Effects of diagenesis and clays on compressional velocities in rocks, Geophys. Res. Letters, Vol. 9, No. 1 5-8.

Velicky, B. Kirkpatrick, S., and Ehrenreich, H., 1968, Phys. Rev., 175, p. 747

Visher, G. S., 1969, Grain size distributions and depositional processes, Jour. Sed. Petrology, Vol. 39 1074-1106.

Voigt, W., 1928, Lehrbuch der Kristallphysik, Teubner, Leipzig.

Wood, A. B., 1941, A textbook of Sound, Macmillan, New York.

Wyllie, M. R. J., Gregory, A. R., and Gardner, G. H. F., 1956, Elastic wave velocities in heterogeneous and porous media, Geophysics, 21, p. 41-70.

Yin, H., Han, D. and Nur, A., 1988, Study of velocity and compaction on sand-clay mixtures, Stanford Rock and Borehole Project, Vol. 33.

Chapter 4

Velocity and attenuation of shales: intrinsic anisotropy

$V_p(\phi, c, p_c, s_w)$ is about C_{11}, $V_s(\phi, c, p_c, s_w)$ is about C_{44}, and... is that it?
"Don't count your chickens before they're hatched".

—Anonymous

Compressional and shear wave velocity anisotropy of Freeman Jewett Shale [1] has been investigated in this chapter. An extensive laboratory ultrasonic measurement was carried out under both "dry" and "saturated" conditions as confining pressure varied from 5 MPa to 50 MPa. Three sets of samples were measured to identify the anisotropic properties of these samples. Not only intrinsic anisotropic properties, but also time-dependent velocity and attenuation were observed. Monitoring the pore-pressure equilibrium process permits the inference of permeability through dynamic acoustic measurement. The experimental results show that velocity and attenuation anisotropy are indeed intrinsic properties of the poorly consolidated Freeman Jewett Shale. The causes of these shale samples' acoustic anisotropy may be attributed

[1]Shale is historically accepted class name for the group of silica clastic sedimentary rocks and the mudrocks, composed of fine particles of silt and clay (Tourtelot, 1960), although some authors restrict the usage of shale to mudrocks that show lamination. The fine particle size of shale of mudrocks is defined less than about 0.06mm (Udden-Wentworth scale, 1922).

to mineral grain preferential orientation and matrix supported bedding clay. The magnitude of anisotropy decreases with increasing confining pressure.

4.1 Introduction

4.1.1 Is anisotropy worth trying to measure?

Recent trends in seismic exploration prove that yes, anisotropy is worth quantifying. Natural rocks are far more diverse than do our synthetically made sand-clay mixtures from Chapter 2. Among the many other interesting properties of natural rocks, anisotropy has become particularly important following the development of vertical multi-component seismic, VSP, and cross-well seismic methods (Banick, 1984, Lynn et al., 1986, Winterstein, 1990). Recent work shows that even seemingly homogeneous sandstone, such as Berea Sandstone, has about 10% of intrinsic velocity anisotropy (Sayers, 1990). These anisotropic properties may be one of the major causes of scattering in Han's (1986) data fitting.

"If anisotropy is such a big deal, why NMO[2] worked as the basis for time-depth conversion for 50 years" (F. Muir, 1985)? Seismologists have realized why and how anisotropy has been successfully ignored—to the near complete satisfaction of seismologists—before the 1980's. I will try to answer a simpler question in this and the next chapter through laboratory ultrasonic measurement: What *causes* anisotropy and how much of it *is* there?

4.1.2 Why shales?

Why study the seismic properties of *shales*—the fine grained clastic rocks? In general, each of the following may be considered as part of the overall reason for this study.

- Shales constitute approximately 75% of clastic basin fill,
- Shales contain the organic matter from which hydrocarbons are generated,

[2]For non-Geophysical readers: NMO stands for "Normal Move Out" (Sheriff, 1984).

- Shales form the top and bottom seals in clastic traps,
- Shales contain the fluids that, when expelled by compaction, carry hydrocarbons to available traps,
- Shales' expelled fluids carry the dissolved ions that destroy reservoir porosity by cementation ...

For years, shaly formations in association with petroleum reservoirs have posed numerous problems for both seismologists and reservoir engineers. Specifically, the detailed and accurate knowledge about the seismic properties of shaly formations has been needed to deploy and develop high resolution seismic processing. These high resolution seismic processing techniques provide crucial information for locating and evaluating seals of petroleum reservoirs and subsurfaces stratigraphic traps. Such a challenge has attracted many seismologists and rockphysicists over the years. The bulk of their work on rock anisotropy, however, has focused on theoretical and numerical analysis of wave propagation in anisotropic media, and most have eschewed direct study of wave velocity and attenuation anisotropy in actual reservoir rocks, like shales. We may find only a few anisotropy measurement of shales and shaly rocks in literature, and most of those experiments were carried under "room dry" or "vacuum dry" conditions, although velocity and attenuation anisotropy of shales and clay-bearing rocks under saturated condition, and high pore-pressure associated time-dependent velocity and attenuation variations have been crucial for studying reservoir and sedimentary basin development through seismic methods. Many reasons have been invoked to explain this avoidance of dominant in-situ, the saturated condition, but principally the issue is cost. Apparently, to measure shales' anisotropic properties under saturated condition itself will take a very long time for the low permeability shales to reach equilibrium at a given effective-stress state, and extreme delicacy is required to measure the acoustic anisotropy at the equilibrated state.

We have hardly any alternative if we are to gain an understanding of shaly rocks. By strictly controlling measurement conditions in the laboratory, like fluid saturation and pore pressure under a simulated in-situ condition, and propagation and polarization directions of ultrasonic waves, we may obtain highly useful data that contribute to direct understanding of the anisotropic properties of shaly rocks.

4.1.3 Previous work

It is well known that treatment of the earth's crust as an elastically isotropic medium yields incorrect results when evaluating media that are not isotropic on the wave length scales of seismics or acoustic well-logging. Several examples in the literature (Banik, 1984, among others) showed how anisotropy of wave velocity, if neglected, can lead to serious errors in time-depth conversion in the presence of shales and other shaly formations. In these cases, the shale fraction of the rock column exhibits an intrinsic velocity anisotropy caused by the preferential alignment of grains and cracks. Such an intrinsic anisotropy has been recognized as hexagonal anisotropy, or transverse isotropy, in several studies (Tosaya, 1982; White, 1983; Banik, 1984 and 1987; Lo et al., 1986; Rai et al., 1988). In all these studies, however, either the samples were unsaturated, or the sample pore pressures were not controlled—leaving unconstrained key parameters of in-situ conditions. Thus, those data may provide an incomplete foundation upon which to build a convincing model for the interpretation of sophisticated seismic exploration data sets. Considering that shales comprise about three quarters of clastic basin fill, we have devoted remarkably little study to predicting shale's in-situ seismic properties.

4.2 Laboratory Measurement technique

4.2.1 Fundamentals

Hook's law states that strain is linearly proportional to stress, or conversely, that the stress (T) is linearly proportional to the strain (S). In general, then,

$$T_{i,j} = c_{ijkl} S_{kl}, \tag{4.1}$$

$$i, j, k, l, = x, y, z$$

with summation over the repeated subscripts k and l. The "microscopic spring constants" c_{ijkl} are called *elastic stiffness constants* and they have the dimensions of stress ($Newton/m^2$).

Material's symmetry further reduces the number of independent stiffness constants. A transversely isotropic or hexagonally symmetric medium, like shale, may contain one axis of rotational symmetry—say Z, oriented such that material properties do not vary in those directions perpendicular to it. This orthogonal plane of circular symmetry would then be defined by the X and Y axes.

In the transversely isotropic (TI) case, it has been well documented that there are only five independent, nonzero constants with $c_{12} = c_{11} - 2c_{66}$. In concise notation, the strain and stress relations, and the associated stiffness constants matrix for transversely isotropic media take the form:

$$\begin{pmatrix} T_1 \\ T_2 \\ T_3 \\ T_4 \\ T_5 \\ T_6 \end{pmatrix} = \begin{pmatrix} c_{11} & c_{12} & c_{13} & 0 & 0 & 0 \\ c_{12} & c_{11} & c_{13} & 0 & 0 & 0 \\ c_{13} & c_{13} & c_{33} & 0 & 0 & 0 \\ 0 & 0 & 0 & c_{44} & 0 & 0 \\ 0 & 0 & 0 & 0 & c_{44} & 0 \\ 0 & 0 & 0 & 0 & 0 & c_{66} \end{pmatrix} \begin{pmatrix} S_1 \\ S_2 \\ S_3 \\ S_4 \\ S_5 \\ S_6 \end{pmatrix} \tag{4.2}$$

The *Christoffel equations* deduced from wave equations are convenient for describing waves in anisotropic media (Refer *Appendix B* for details).

In general, shales—devoid of cracks or fractures oriented across their bedding planes—can be considered transversely isotropic with the symmetry axis normal to the beddingplane, or lamination plane. The following five independent elastic stiffness constants are sufficient for the complete description of these rocks:

$$\begin{cases} c_{11} = \rho V^2_{P(\|)} \\ c_{33} = \rho V^2_{P(\perp)} \\ c_{44} = \rho V^2_{SV(\|)} \\ c_{66} = \rho V^2_{SH(\|)} \\ c_{13} = \sqrt{4\rho^2 V^4_{P(45^0)} - 2\rho V^2_{P(45^0)}(c_{11} + c_{33} + 2c_{44}) + (c_{11} + c_{44})(c_{33} + c_{44})} - c_{44} \end{cases} \tag{4.3}$$

with $c_{12} = c_{11} - 2c_{66}$. Referring to the orientation of axes with respect to the symmetry of transversely isotropic medium, we have

$$\begin{cases} V_{P(\|)} = V_{xx} = V_{yy} = V_{P-0^o} \\ V_{P(\perp)} = V_{zz} = V_{P-90^0} \\ V_{SH(\|)} = V_{xy} = V_{yx} \\ V_{SV(\|)} = V_{xz} = V_{yz} = V_{SH(\perp)} = V_{zx} = V_{zy} \end{cases}$$

By measuring five different velocities on three sample plugs as a set cut from a single core in three different orientations, we may estimate all five elastic stiffness constants using Equation 4.3 to study transversely isotropic medium (Figure 4.1 and Figure 4.2).

In this study, I have adapted the pulse-transmission method. The P-wave transducer central frequency is close to one megahertz, and the S-wave transducer central frequency is close to 0.6 megahertz. I chose this method not only because the method is widely used and accepted for accurate velocity measurement, but also because it is an efficient method for measuring highly attenuating rock samples, such as shales. For details of the ultrasonic pulse-transmission method, please refer to *Appendix A*.

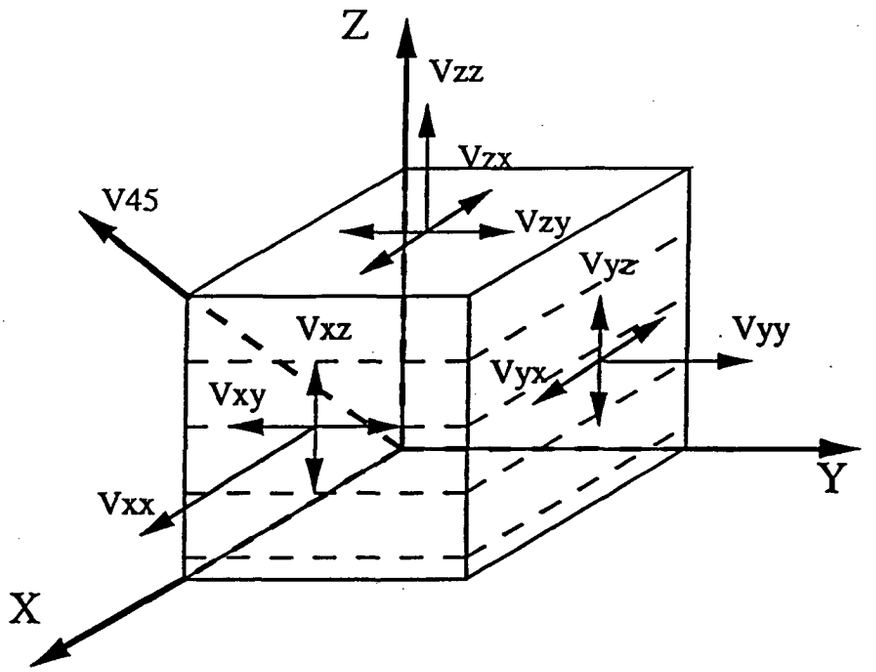

Figure 4.1: Orientation of axes with respect to symmetry of hexagonal, or transversely isotropic medium. Velocity notation: first subscript refers to direction of wave propagation, second subscript denotes direction of "particle" polarization". For example, V_{zy} refers the wave propagating along the Z–axis and polarized along the Y–axis, hence, it is a pure S-wave.

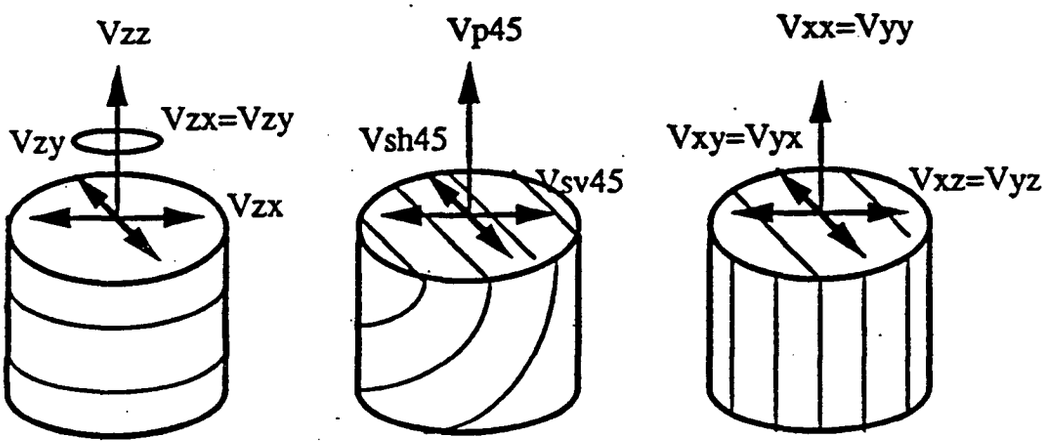

Figure 4.2: A schematic diagram of the three samples cut for velocity measurements. Thin line indicates bedding plane or lamination. Arrows show the directions of wave propagation and polarization.

4.2.2 Sample preparations

To obtain the most accurate results from the ultrasonic pulse-transmission experiments, one must minimize pulse wave energy dissipation by diffraction, scattering, and reflection. These effects can be significantly reduced by optimizing the transient pulses with respect to the range of variation in physical characteristics of the samples.

Sample dimensions were designed not only to satisfy the constraints described in *Appendix A* for accurate ultrasonic measurement, but also to consider that smaller sample dimensions can lessen the times required to equilibrate pore pressure when changing confining pressures, due to shale samples' low permeabilities. All sample plugs were drilled at 2.54 cm diameter and 3.0 cm length, through three different angles with respect to the bedding plane. Three plugs were taken at a particular depth of borehole core to estimate the five independent elastic constants through ultrasonic velocity measurement. The three plugs' axial orientations are parallel, perpendicular, and 45^0 relative to the bedding plane (Figure 4.2).

4.2.3 Petrographic analysis of the samples

The cores chosen in this study are from ARCO's Round Mountain Oilfield, Well No.1, 14 miles northeast of Bakersfield, in the southeastern San Joaquin Basin. The stratigraphy of these Oligocene to Miocene deposits has been studied for over 100 years, beginning with the Union Pacific Railroad survey in 1855. Traditionally, these Temblor equivalents have been defined as the following units: Vedder Sand, Jewett Sand (including the Pyramid Hill Sand, members of the Jewett Sand), Freeman Jewett Shale, Olcese Sand and Round Mountain Silt. Lithologic, electrical and acoustic log characteristics of these units are well known from many oil fields reports, including California Division of Oil and Gas Report.

The Oligocene marine Vedder Sand overlies and interfingers with the bed of the Walker Formation, and is unconformably overlain by the Jewett Sand-Pyramid Hill.

Table 4.1: Petrographic analysis of Freeman Siltstone.

FREEMAN SILTSTONE		
TEXTURES	grain size:	less than 0.05m (silt)
	sorting:	poor
	particle form:	low sphericity, angular-subangular, grain orientation parallel to bedding
COMPOSITION	quartz:	65%
	feldspar:	5%
Fragments-	mica:	17% - 20%
	others:	10% - 13%
Cements-	clay and calcite:	(mud rich)
DIAGENESIS	compaction:	loose, some crushed grains, and bent mica
	support:	matrix support-90%, clastic support-10%
	structure:	bioturbid, intense burrowing
POROSITY	helium: 24.3%	saturation: 23.1%
DENSITY	(bulk):	1.84 g/cm^3 (dry)

Vedder Sand is conformably overlain by the Freeman silt (Figure 4.3).

The Vedder Sand formation is the principal reservoir in this area, and the Pyramid Hill is the next most productive formation. Fossiliferous, calcareous siltstones, fish scales, and carbonaceous material are common in the Jewett Sand. The Freeman Silt in its subsurface type section consists of grey, micaceous shales with interfingering silty sands. Megafossils, fish scales and carbonaceous material are also common in Freeman Silt (after Olsen, 1988). The Freeman Silt may be a good seal and "source rock" for the Vedder Sand, and the lithological difference between these two can be a characteristic "reflector" in a seismic profile.

The cores were carefully drilled and kept frozen. Typically, the cores appeared homogeneous to visual inspection, but some fractures with random orientations were identified. To study intrinsic anisotropy, and to avoid fractures induced by drilling

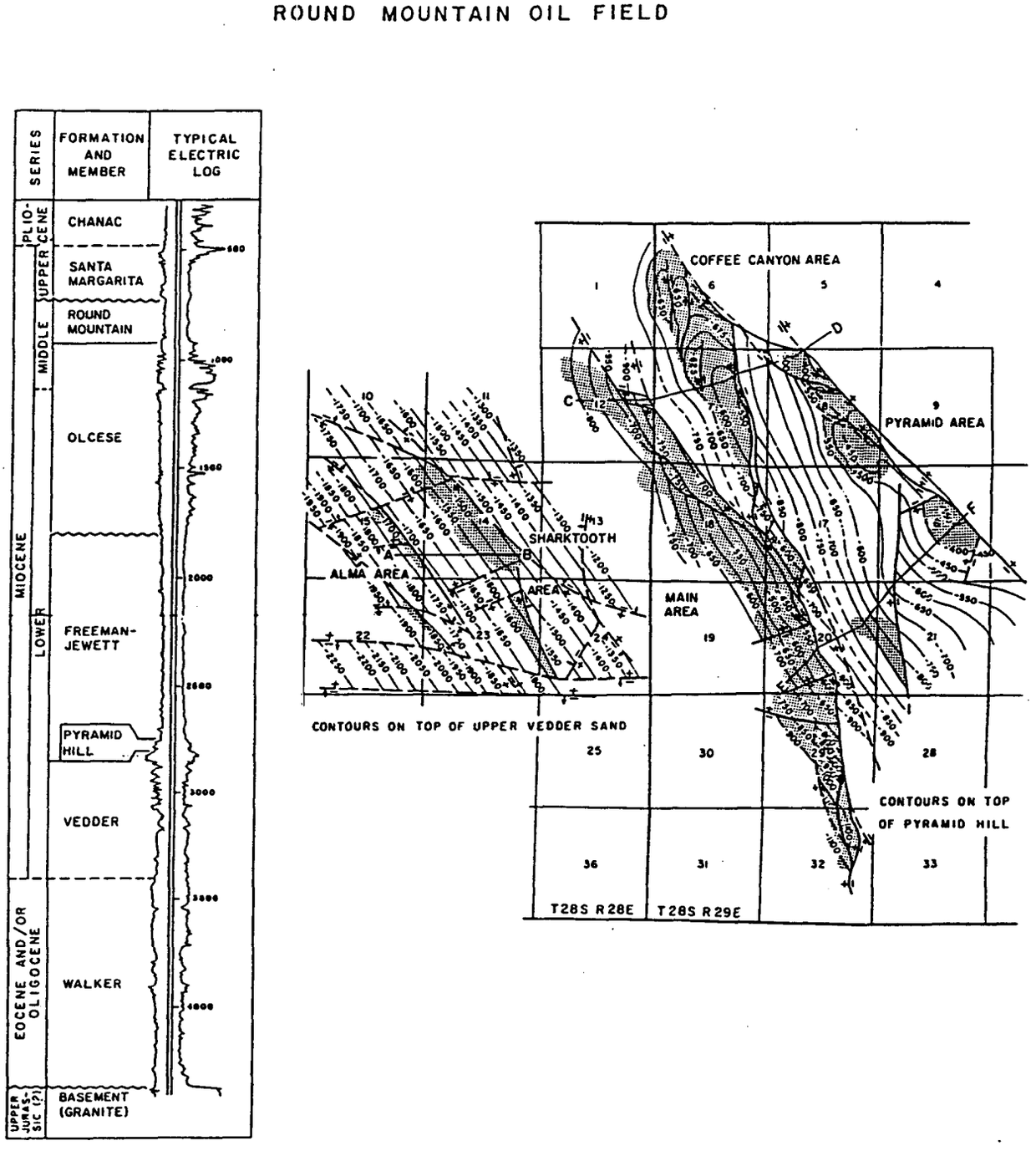

Figure 4.3: Formation members, typical electric log, and contour map of Round Mountain Oil Field (California Division of Oil and Gas).

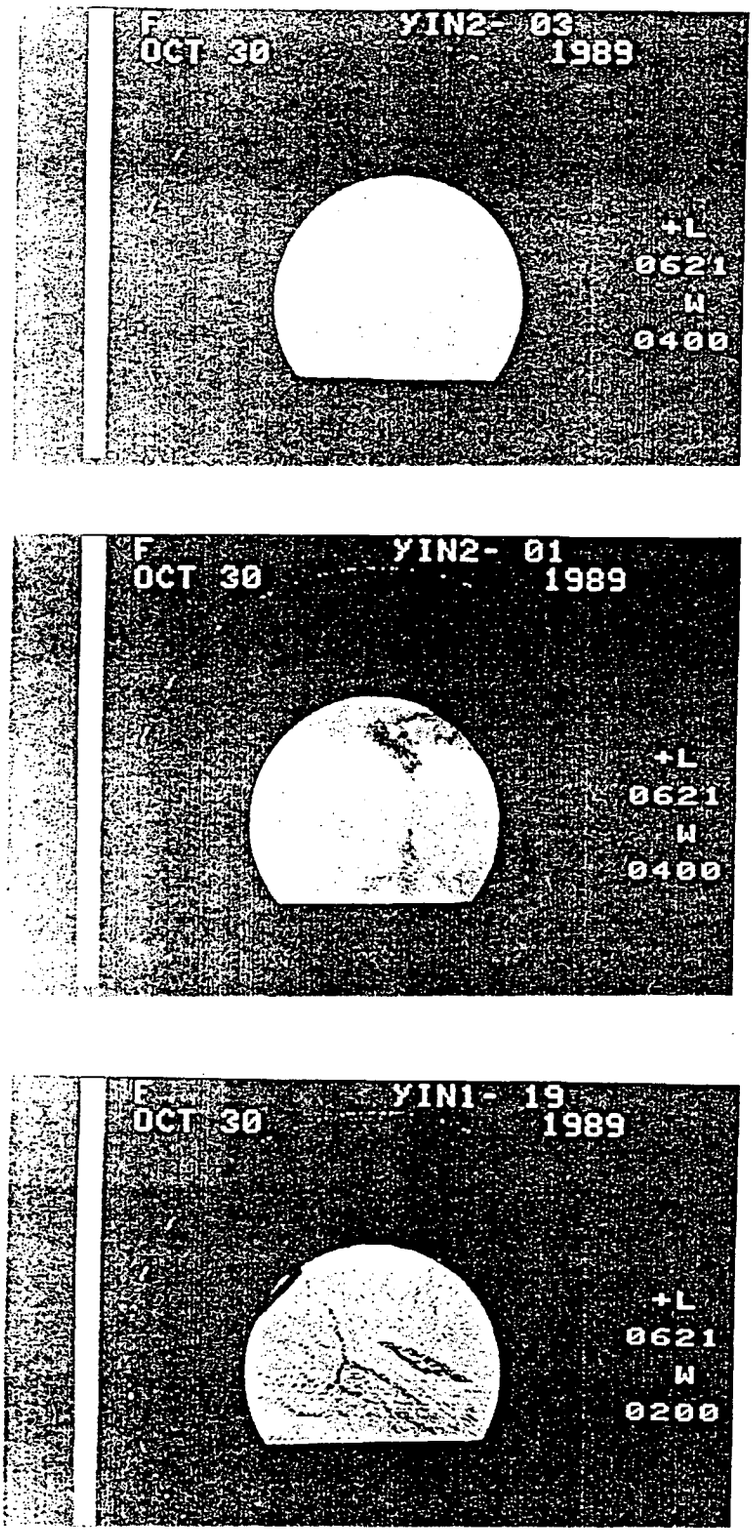

Figure 4.4: CAT-Scanning images of the Freeman Jewett Shale borehole cores. Top: homogeneous; Middle: fractures perpendicular to the core axis; Bottom: fractures parallel to the core axis.

in-situ, I examined the frozen cores with X-ray CAT-Scanning to avoid sample plugs were drilled through fractures (Figure 4.4).

In order to make a petrographic analysis, I prepared thin sections from the core taken at a depth of 2458 ft both parallel and perpendicular to the core axis. I assumed that the bedding plane was perpendicular to the borehole core axis, since I could not clearly distinguish the lamination plane visually.

By studying these thin-sections under a microscope, I found that there is an apparent trend of preferential grain orientation. The long axes of grains are parallel to the bedding plane with laminated clay layers as the support-matrix.

4.3 Results

Three sets of samples were measured and the velocities were plotted in Figures 4.5, 4.6, and 4.7. Pore pressure was kept constant at 0 MPa, while the confining pressure was varied from 0-50 MPa in the measurements. After each variation of confining pressure, pore pressure equilibration took from 48 to 72 hours depending on the orientation of the sample plug.

4.3.1 Velocity anisotropy

By verifying that horizontally propagated and vertically polarized shear waves (Vxz, or Vyz) travel at the same velocity as do the vertically propagated and horizontally polarized shear waves (Vzx or Vzy), we can confirm whether a medium has at least a transversely isotropic symmetry. With our specially designed 3-component transducer, we can confirm the above by measuring one sample plug drilled parallel to its bedding plane, and other drilled perpendicular to its bedding plane.

In Figures 4.5, 4.6, and 4.7, we can observe that Vzx approximately equals Vzy, and they approximately equal Vyz or Vxz, too. These waves may be called V_{sv}. The discrepancy among them may be caused by the discrepancy between the sample

plugs' axes and anisotropic symmetry axis. The discrepancy may also caused by great attenuation in these waves which result in large experimental error. We can also observe that V_{sh} (Vxy, or Vyx) is always higher than V_{sv}. We may conclude that Freeman Silt is probably transversely isotropic with respect to the vertical symmetry axis—the axis perpendicular to bedding. P-waves propagating parallel to bedding have higher velocity than those propagating perpendicular to bedding plane, Vzz < Vxx or Vyy.

Recalling the thin sections analyses of the samples, we have seen that the sample grains have preferential orientations along the bedding plane, and laminated clay layers act as the support-matrix. These features might be the causes of the observed elastic anisotropy.

We can also observe, as a rule, that velocities increase with increasing effective pressure under both dry and saturated conditions, but the changes ($\partial V_{ij}/\partial P_c$) are different for the velocities measured in different orientations, particularly in sample sets 1 and 2. Examination of the data plots reveals that the velocity rate change for P-waves measured perpendicular to the bedding (V_{p-90} or Vzz) is about 15 $m/sec/MPa$ in both dry and saturated conditions. The slope for P-waves measured parallel to the bedding (V_{p-0}, Vxx, or Vyy) is only about 6 $m/sec/MPa$ under dry condition, but the same, 15 $m/sec/MPa$ under saturated conditions. The velocity rate change for P-waves measured 45° (V_{45^o}) to the bedding plane remained relatively unchanged at 10 $m/sec/MPa$ under both dry and saturated conditions. The relatively rapid pressure rate of change of V_{p-90} under both dry and saturated conditions reflects progressive closure of pores and cracks under pressure, as well as improved alignment of grains in the plane of low shear resistance—the bedding plane. The low slope of V_{p-0} under dry condition may be due to higher shear resistance among the grains along the bedding plane than under saturated condition, where V_{p-0}, has about the same slope as do V_{p-90} and V_{p-45}. We may note how P-wave velocities increased

almost linearly with increasing confining pressure, or if modeled as an exponential increase, than with an index much less the 1/3 predicted by Hertzian contact theory. This character may result from the samples' poorly consolidated state, particularly its load-bearing soft matrix-support clay layers.

We can observe that P-wave velocities in all three directions are higher under saturated than under dry conditions, and S-wave velocities in all directions are lower under saturated than under dry conditions. These responses may be due to fluid saturation increasing bulk modulus, but reducing shear modulus.

I calculated all five independent elastic stiffness constants based on Equation 4.3, substituting all measured velocities. I also calculated anisotropic factors, following the measures of the degree of anisotropy for a weekly transverse isotropic medium given by Thomsen in 1986.

$$\begin{cases} \epsilon = (c_{11} - c_{33})/2c_{33} \\ \gamma = (c_{66} - c_{44})/2c_{44} \\ \delta = [2(c_{13} + c_{44})^2 - (c_{33} - c_{44})(c_{11} + c_{33} - 2c_{44})]/2c_{33}^2 \end{cases} \tag{4.4}$$

The results are plotted in Figures 4.8 for sample set 1, 4.9 for set 2, and 4.10 for set 3. We can observe that all five independent elastic stiffness constants increase with increasing confining pressure. P-wave related elastic stiffnesses show stronger confining pressure dependence than do pure S-wave related elastic stiffnesses. P-wave related elastic stiffnesses under saturated condition show stronger stress-dependence than do those stiffnesses under dry condition. All stiffness constants calculated from the three sample sets satisfy the physical strain energy constraint bounds, $c_{11} > (c_{11} - c_{12}) > c_{44} > 0$ and $c_{11} > c_{33}$. We note that the S-wave anisotropic factor γ remained relatively constant under both dry (about 20%) and saturated (about 24%) conditions in all three sample sets even when they were subjected to increasing confining pressure. The P-wave anisotropic factor ϵ decreased with increasing confining pressure from about 52% to 20% in dry condition and from about 41% to 22% in saturated condition.

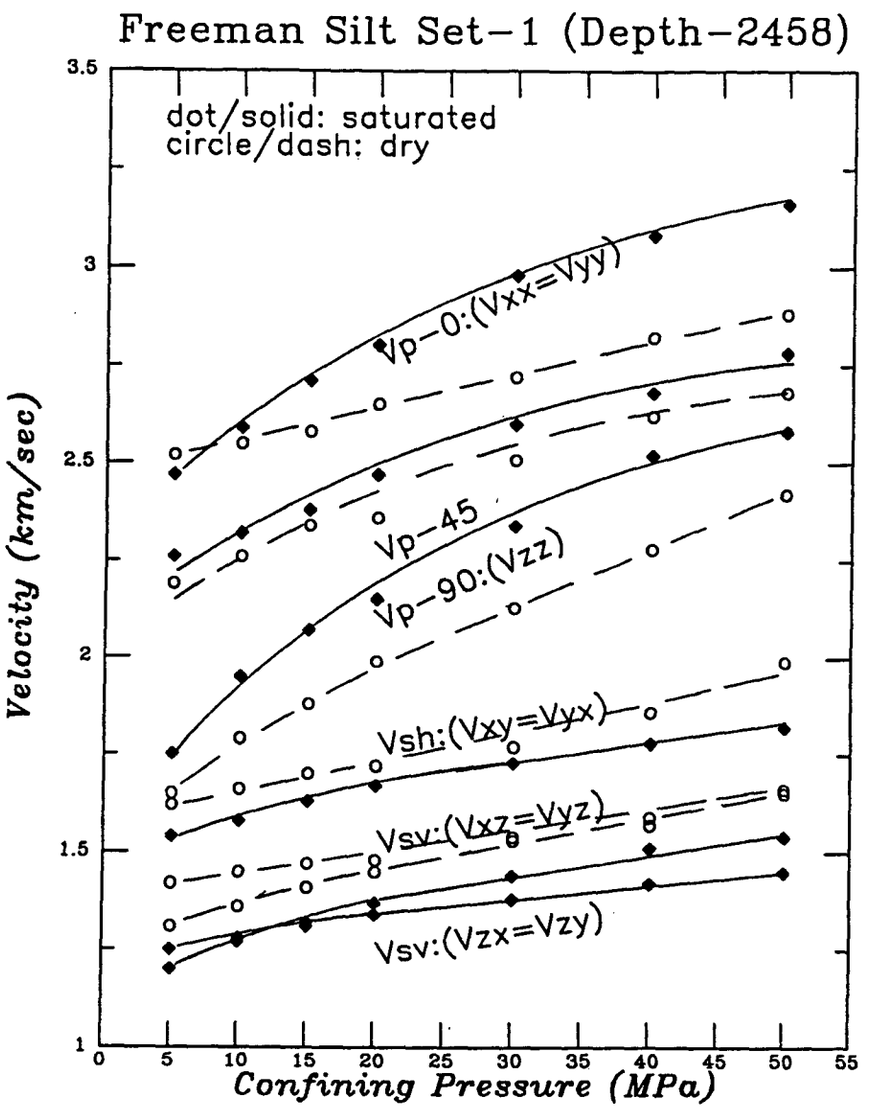

Figure 4.5: Velocity vs. confining pressure of sample set 1 under both dry (dashed lines) and saturated (solid lines) conditions.

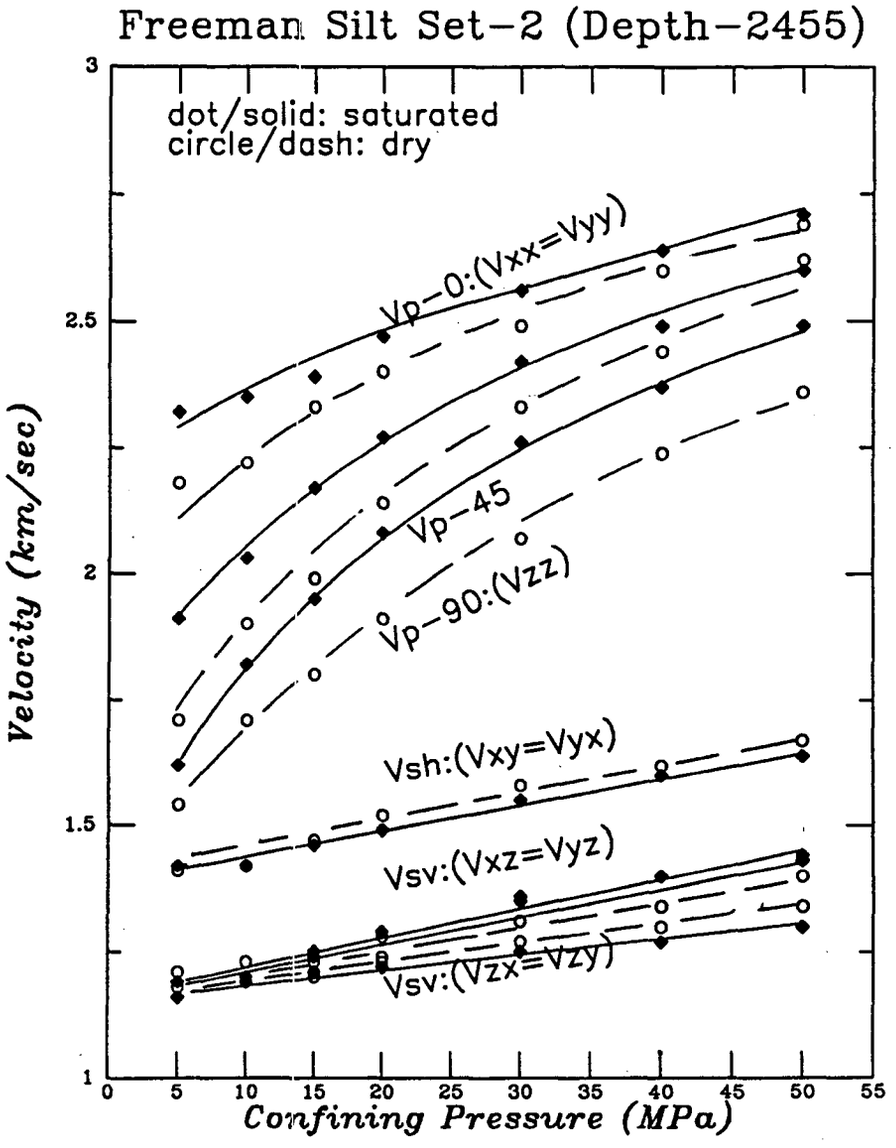

Figure 4.6: Velocity vs. confining pressure of sample set 2 under both dry (dashed lines) and saturated (solid lines) conditions.

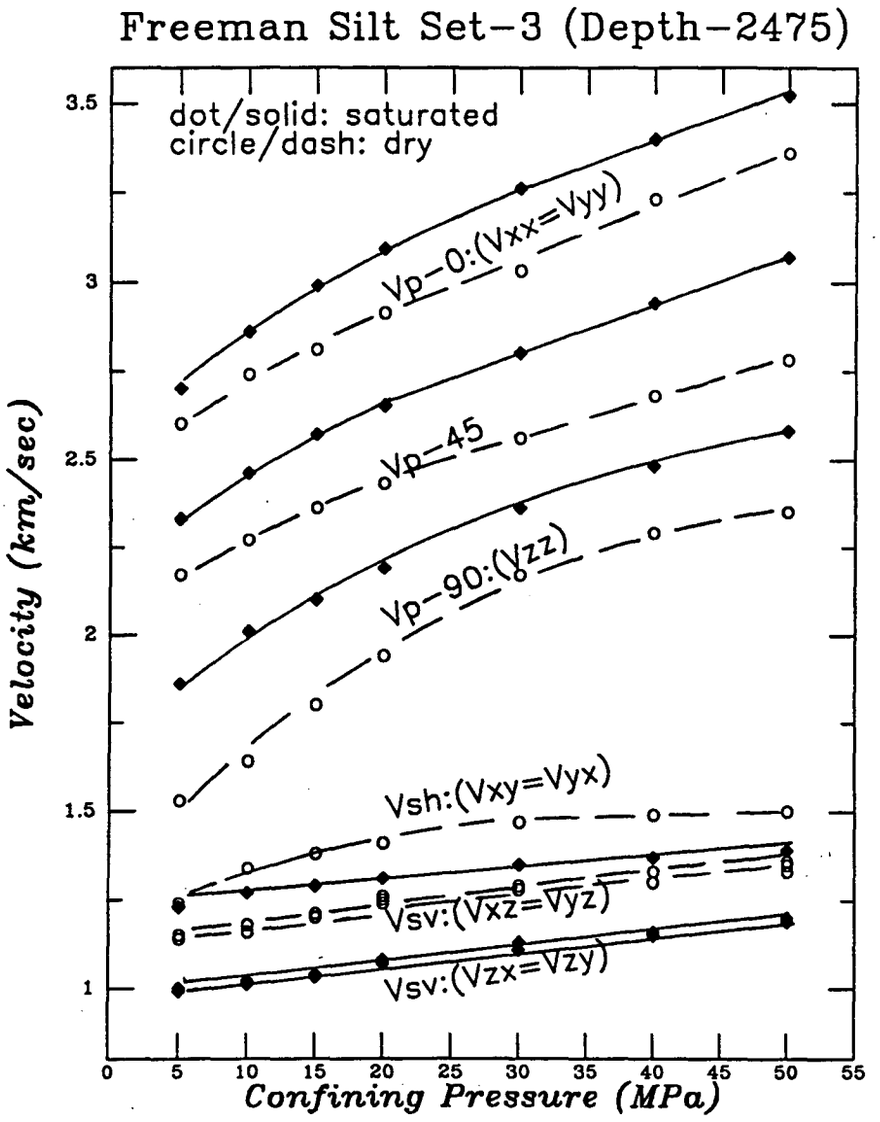

Figure 4.7: Velocity vs. confining pressure of sample set 3 under both dry (dashed lines) and saturated (solid lines) conditions.

The last factor, δ, in which "error could be same order as δ itself", (Thomsen 1986) varied from 80% to 25% in dry condition and 75% to 9% in saturated condition as confining pressure varied from 5 to 50MPa in samples set 1 (Figure 4.8).

4.3.2 Attenuation anisotropy

I measured attenuation anisotropy by the spectral ratio method as described in *Appendix A*, and I calculated the attenuation coefficients after correcting for the transmitter-sample and sample-receiver reflection coefficients. The results are presented in Figure 4.11 through Figure 4.14.

In general, the results show that P-wave attenuation varies with changes of wave propagation direction, confining pressure, the saturation.

P-wave spectral amplitude varies with confining pressure. Higher confining pressure causes higher spectral amplitude, indicating a lower attenuation coefficient. In dry condition, the P-wave spectral amplitude measured from the sample parallel to bedding plane around central frequency was about 35% higher than the amplitude measured from the sample perpendicular to the bedding plane at all observed confining pressures, 30MPa, 40MPa, and 50MPa. Less attenuation anisotropy can be observed in saturated samples. The spectral amplitude of P-wave propagating along bedding than is about 12% higher than the spectral amplitude of P-wave propagating perpendicular to bedding at all observed confining pressures.

4.4 Permeability and time-dependent velocity

Must we wait three to five days to equilibrate pore-pressure state between each dynamic measurement in shales? If the above results that we obtained through this exhausting experimental effort should seem mundane, I trust that the following results by monitoring the time-dependent variations in velocity and attenuation associated with pore pressure equilibrium process will help to stir some new thoughts on

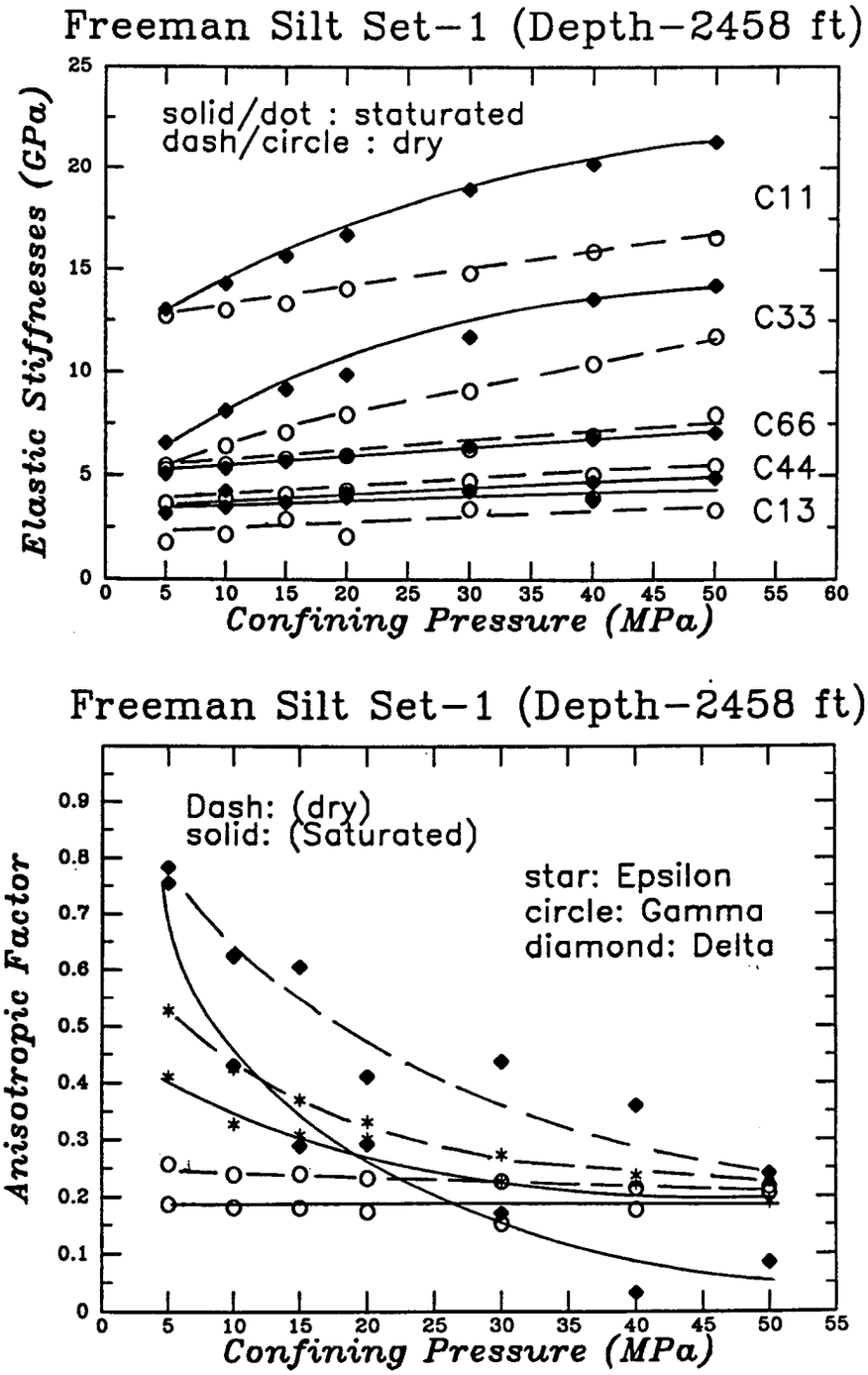

Figure 4.8: Five independent elastic constants and velocity anisotropic factors vs. confining pressure, based on the weak transverse isotropic assumption, Set 1.

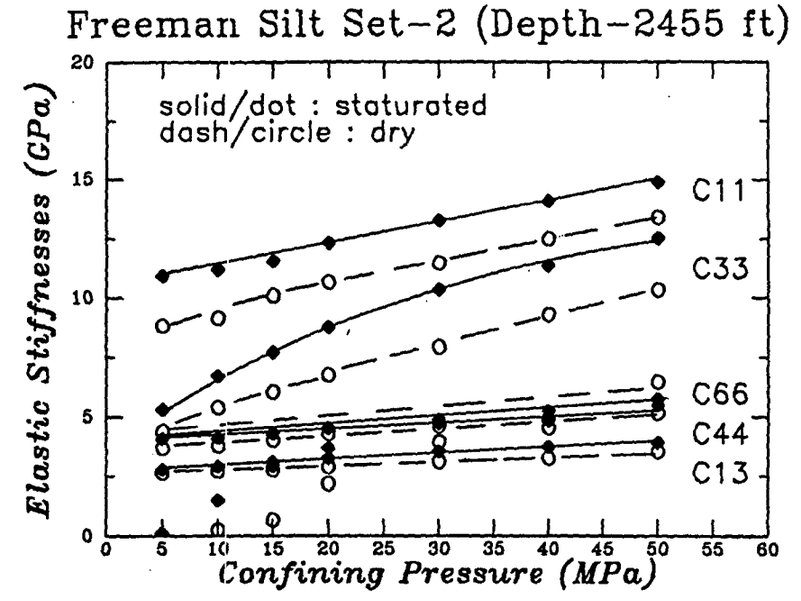

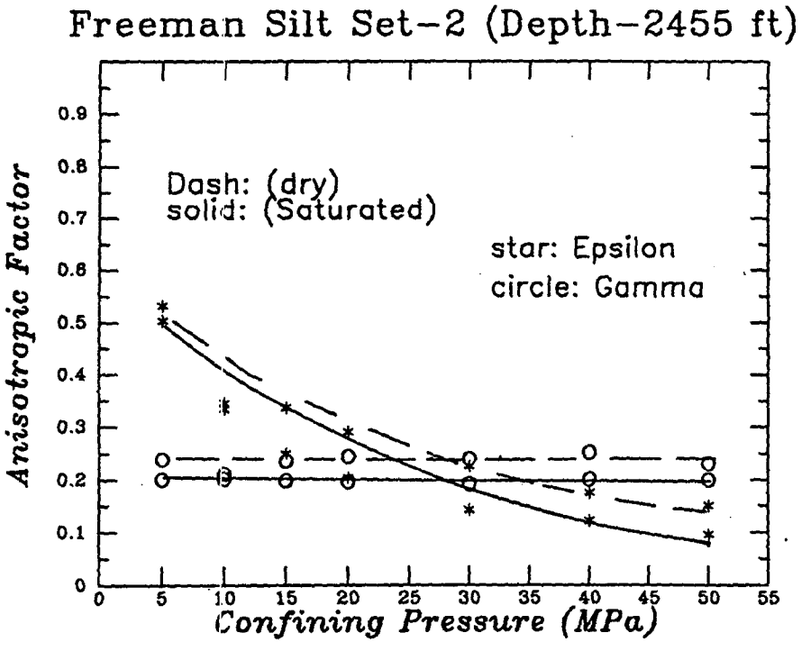

Figure 4.9: Five independent elastic constants and velocity anisotropic factors vs. confining pressure, based on the weak transverse isotropic assumption, Set 2.

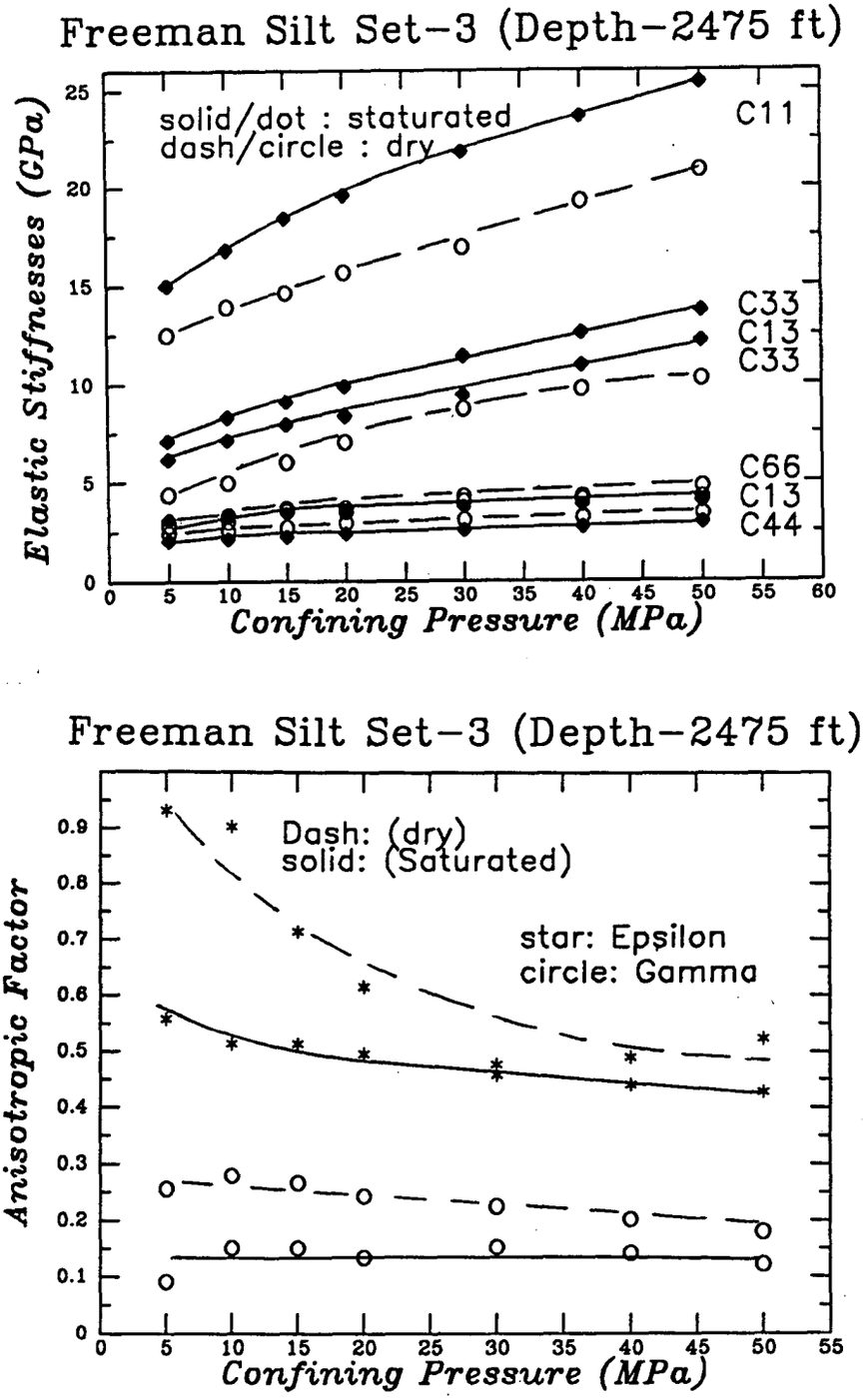

Figure 4.10: Five independent elastic constants and velocity anisotropic factors vs. confining pressure, based on the weak transverse isotropic assumption, Set 3.

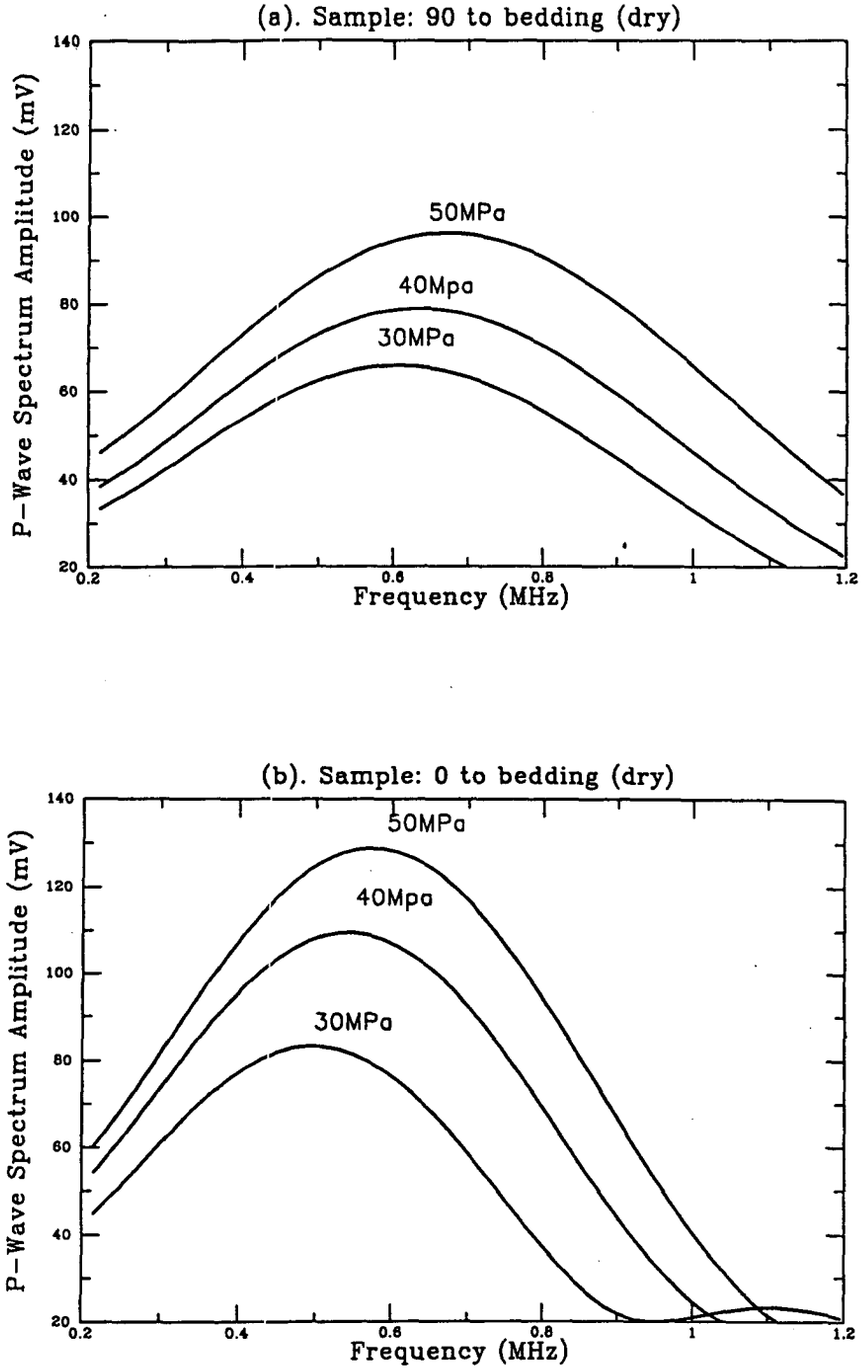

Figure 4.11: Spectral amplitude under dry condition. (a) sample perpendicular to bedding, (b) sample parallel to bedding.

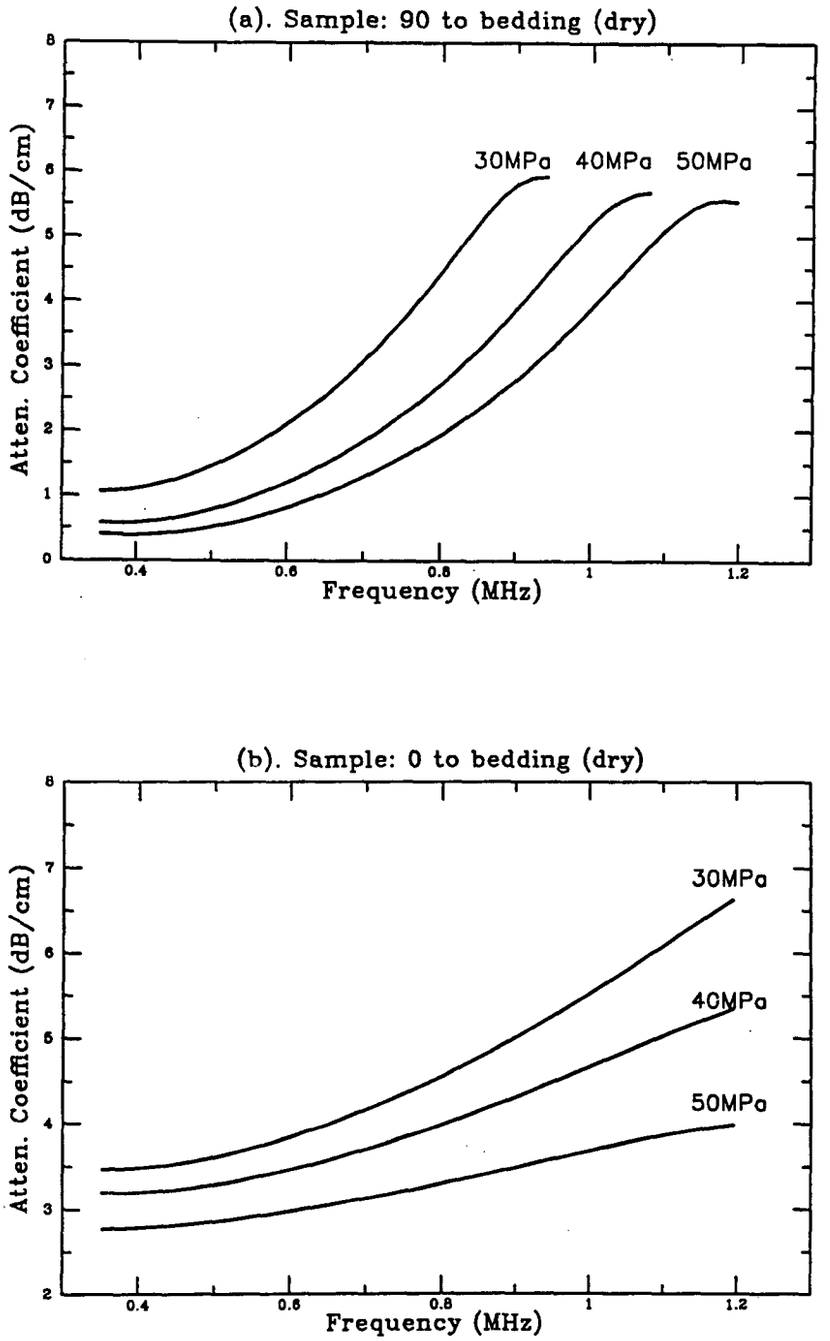

Figure 4.12: Attenuation coefficient under dry condition. (a) sample perpendicular to bedding, (b) sample parallel to bedding.

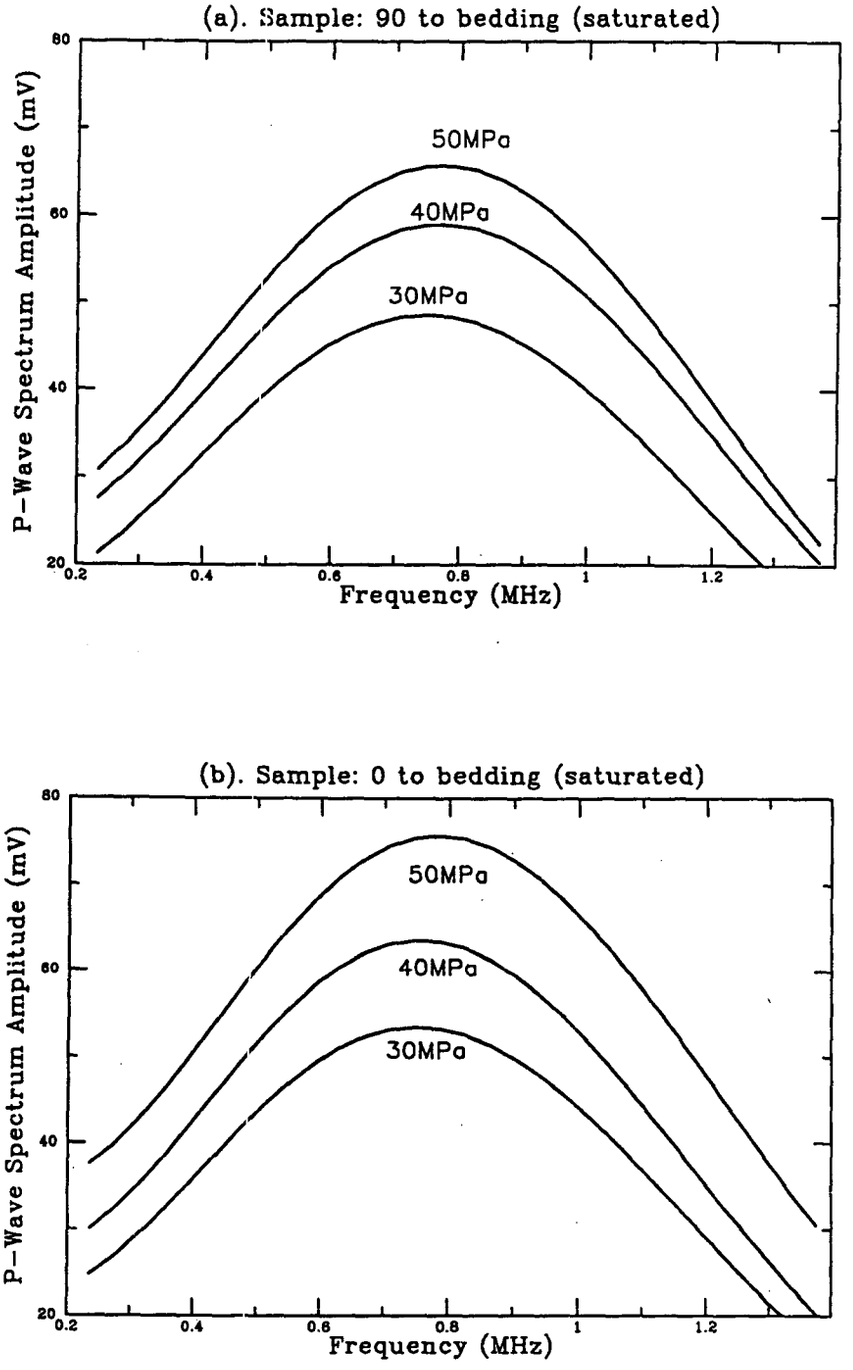

Figure 4.13: Spectral amplitude under saturated condition. (a) sample perpendicular to bedding, (b) sample parallel to bedding.

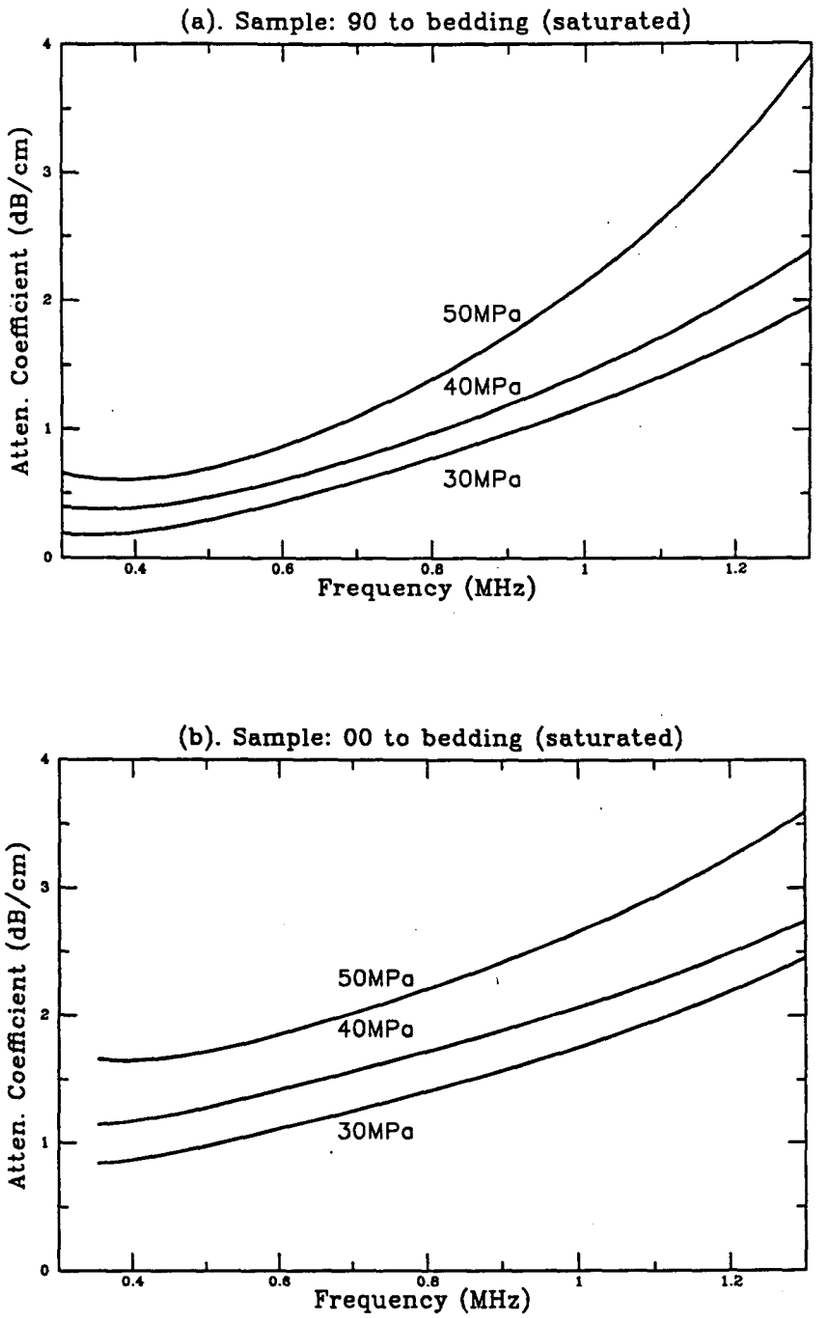

Figure 4.14: Attenuation coefficient under saturated condition. (a) sample perpendicular to bedding, (b) sample parallel to bedding.

laboratory measurement techniques for shaly rocks.

4.4.1 Time-dependent velocity and effective stress

I observed time-dependent velocity variations in these Freeman Jewett Shales during the pore pressure equilibrium process due to their low permeability. The variations are especially noticeable for P-waves. For the P-waves propagating parallel to the bedding, the velocity changed from 2.62 km/sec to 2.71 km/sec (about 3%) in 54 hours, and for P-waves traveling perpendicular to bedding, the velocity changed from 2.38 km/sec to 2.49 km/sec (about 5%) in 80 hours, when confining pressure varied from 40 MPa to 50 MPa. These are shown in Figure 4.15 and Figure 4.16. Note that velocity variation was not significant until 42 hours in sample parallel to bedding and 60 hours in sample perpendicular to bedding after confining pressure increased at time $t = +0$.

Assume that P-wave velocity is a function of the combination of confining pressure P_c and pore pressure P_p in the following way,

$$V_P = F(P_c + \alpha P_p), \tag{4.5}$$

and that an undrained close system, a constant fluid mass, should obey the following equation as given by Rice (1975),

$$\frac{\phi_0 P_p}{K_f} - (P_c - P_p)(1/K_d - 1/K_s) - \frac{\phi_0 P_p}{K_s} = 0 \tag{4.6}$$

where ϕ_0 is initial porosity, K_f is fluid bulk modulus, K_s is solid or grain bulk modulus, K_d is bulk modulus of the sample measured under drained condition (Rice 1975).

We may rearrange above equation into the form of

$$P_p = \{(1/K_d - 1/K_s)/[\phi_0(1/K_f - 1/K_s) + (1/K_d - 1/K_s)]\} \cdot P_c = k \cdot P_c \tag{4.7}$$

Now, we have

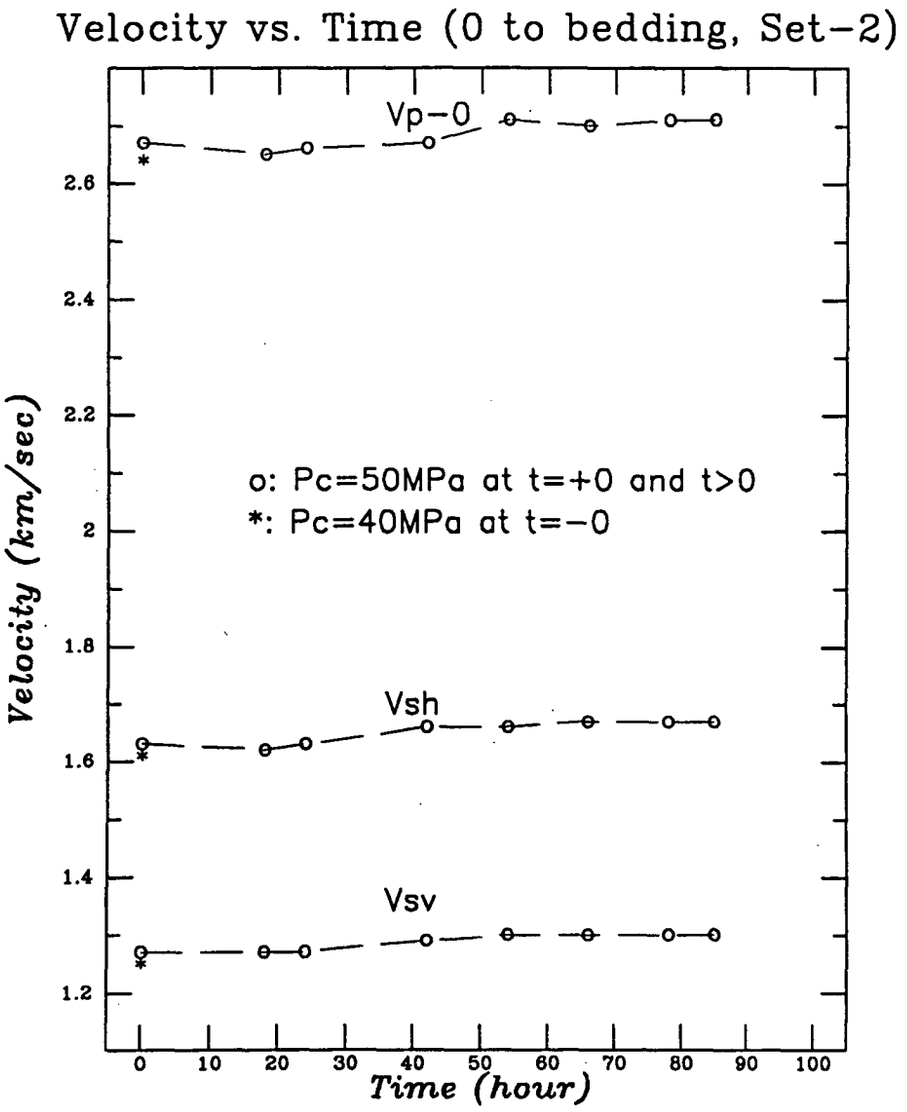

Figure 4.15: Velocity variation with time in the sample parallel to bedding.

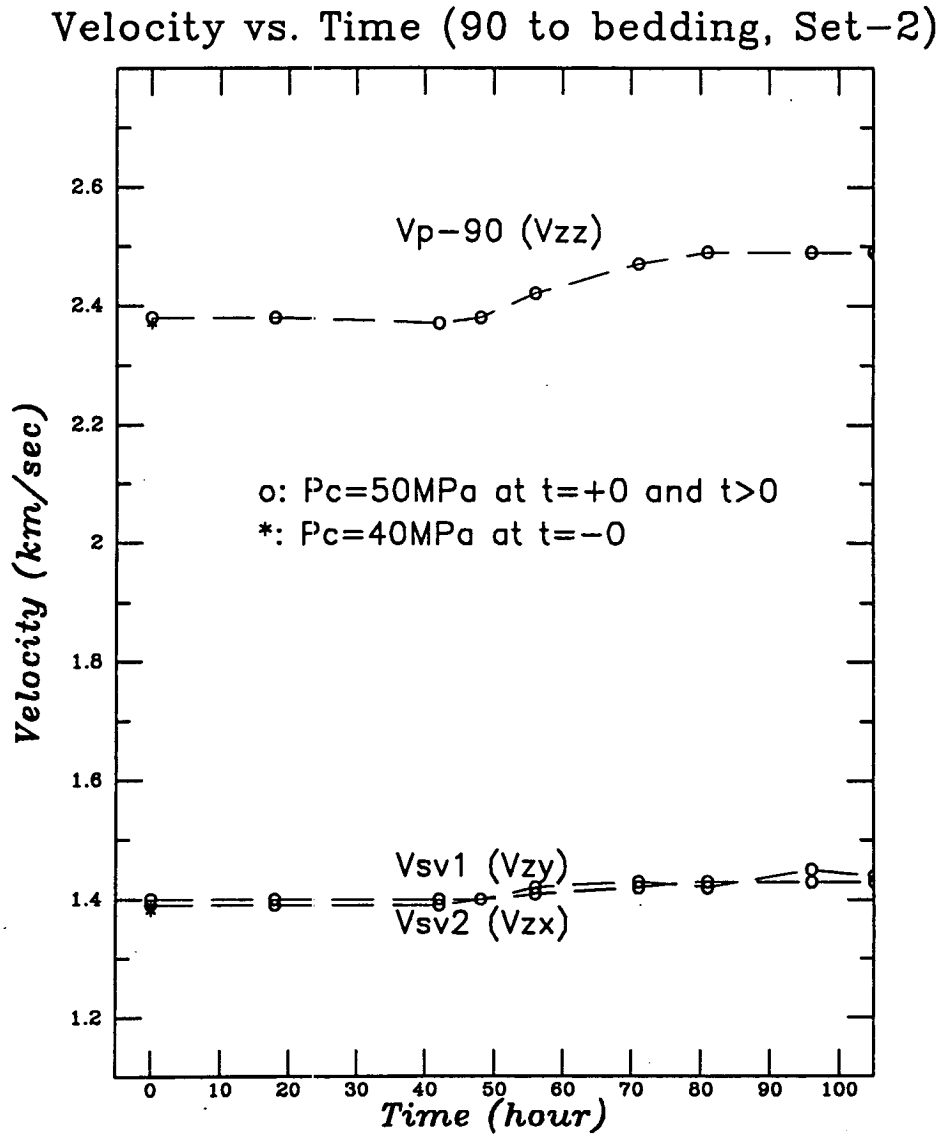

Figure 4.16: Velocity variation with time in the sample perpendicular to bedding.

$$P_c + \alpha P_p = P_c(1 + \alpha k) \tag{4.8}$$

We may deduce a function $F[P_c(1+\alpha k)]$ through a sequence of undrained experiments. And we may also find α and k through a single drained experiment, and then plot $V_p = F(Pc + \alpha P_p)$ as function of $P_c(1 + \alpha k)$, instead of P_c.

For simplicity, I assumed a linear relation between V_p and P_c based on the observations in Figure 4.5 through 4.7, and found that

$$V_P = 2.277 + 0.00867(P_c - \alpha P_p). \tag{4.9}$$

In practice, one might construct the V_p and P_c relation through least squares fitting of the undrained data, then get the relation of $V_p = F(Pc + \alpha P_p)$ as function of $P_c(1+\alpha k)$. This simple approach may save months of time spent waiting for pore-pressure equilibrium in a saturated shale sample, and free up laboratory apparatus for the next sample measurement (Dvorkin, 1991).

4.4.2 Time-dependent velocity and permeability

The very slow pore-pressure equilibrium process in Freemann Jewett shales are caused by the low permeability of these samples. By monitoring pore-pressure changes with time, we may be able to estimate the samples' permeability.

The volumetric rate q at which fluid flows due to a pressure gradient is related by Darcy's law to the conduit cross-sectional area A, the fluid viscosity μ, and the permeability k.

$$q = -(kA/\mu)(\partial P/\partial x) \tag{4.10}$$

In one dimension, the transient flow of a compressible fluid through a compressible porous medium may be described by combining Darcy's law with the one-dimensional diffusion equation,

diffusion equation,

$$\frac{\partial^2 P}{\partial x^2} = \left(\frac{\mu\beta_f}{k}\right)\left[\frac{\beta_{eff} - \beta_s}{\beta_f} + \phi\left(1 - \frac{\beta_s}{\beta_f}\right)\right]\frac{\partial P}{\partial t} \tag{4.11}$$

where μ is fluid viscosity, ϕ is porosity, β_f, β_s and β_{eff} are the fluid compressibility, the mineral compressibility of the rock, and effective compressibility of the rock as jacketed, respectively, and x is distance from the upgradient end of the sample plug (after Brace, 1968).

Assuming that the term $(\beta_{eff} - \beta_s)/\beta_f$ inside the square brackets is nearly zero in this experiment, and that the term $\phi(1 - \beta_s/\beta_f) \approx \phi$, because $\beta_f >> \beta_s$ or β_{eff}, then, we may reduce the expression to

$$\frac{\partial^2 P}{\partial x^2} \approx \left(\frac{\mu\beta_f\phi}{k}\right)\frac{\partial P}{\partial t} \tag{4.12}$$

or

$$\frac{\partial P}{\partial x} \approx \frac{P(t)}{C} \tag{4.13}$$

where $C = (\mu\beta_f\phi)/k$, and $P(t)$ is a linear function of time.

Thus, the pressure gradient in the sample is constant along its length, although it will decay exponentially with time (Figure 4.17).

In the experiment, we placed the sample in a pressure vessel and assumed that the confining pressure was increased stepwise at time $t = t_0$, and held constant with the pore-system closed. Over time, the pore-pressure builds up due to the sample compressibility, and becomes constant just before time $t = t_1$. This process is analogous to the voltage across a resistor-capacitor circuit, where the capacitor (pore pipe system as a reservoir) is charged and discharged through the resistor (the rock sample) as described in "pressure-pulse" method (Brace et al. 1968). It is a simple matter to show that the pressure gradient at one end of the sample decays

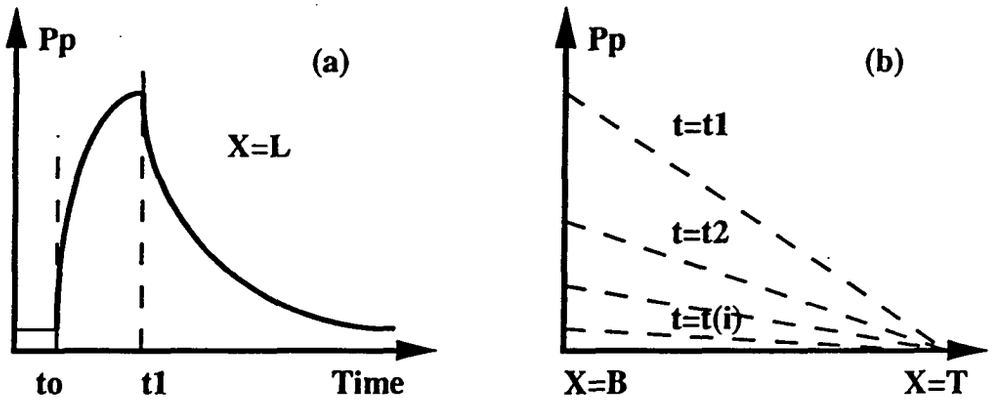

Figure 4.17: Schematic diagram of pore-pressure variation with time (a), and with the position (b), modeled by one-dimensional diffusion equation.

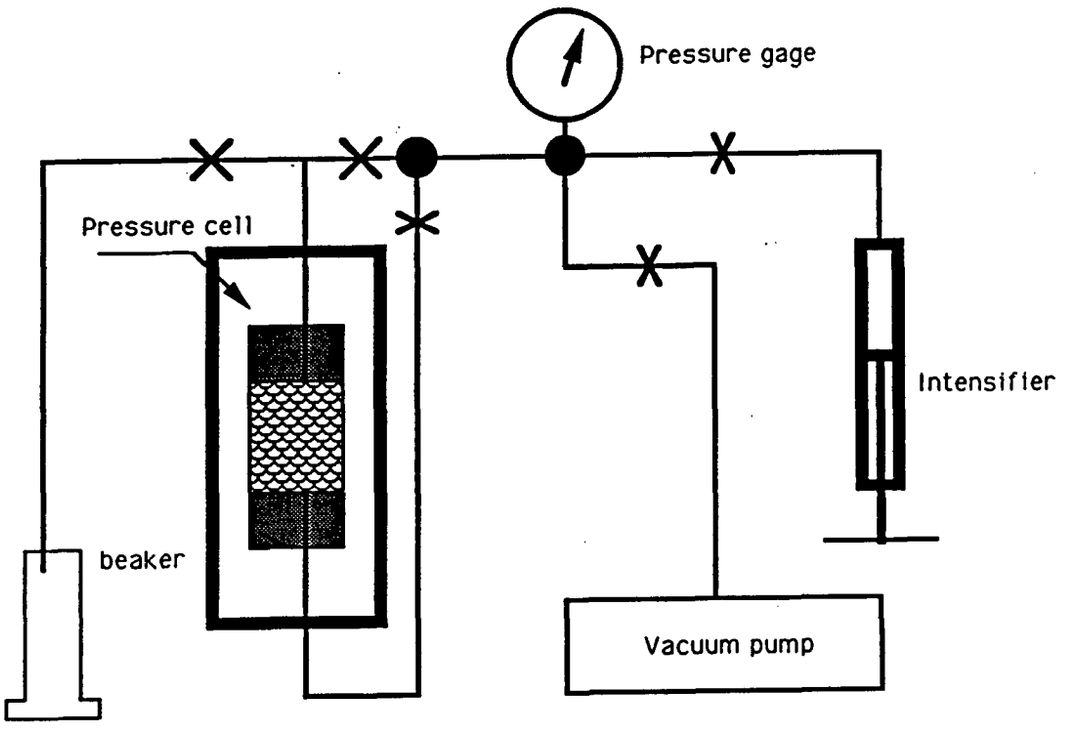

Figure 4.18: Schematic diagram of the pore-pipe connections and pore-pressure controlling system.

exponentially to zero when we open the other end of the sample just after time $t = t_1$ to a beaker at atmosphere pressure. The equation may then be expressed as

$$P_p(t) = \Delta P V e^{-\alpha t} \tag{4.14}$$

where $P_p(t)$ is the time dependent pore-pressure, ΔP is the pore-pressure built up at time just before $t = t_1$, V is the capacity of the pore-pipe system which can be calibrated by the relation of the pore pressure and the compressibility of the pore fluid and pore-pipe system, and α is hydraulic diffusivity. The hydraulic diffusivity may be expressed as

$$\alpha = \frac{kA}{\mu\beta LV} \tag{4.15}$$

where A is the cross-sectional area of sample, L is length of sample, and k is the permeability, the unknown which we may calculate through the above equations.

By plotting the pressure decay of $P_p(t)$ on a semi-log scale, the sample hydraulic diffusivity α can be found from the resulting slope. Then, the permeability can be estimated with Equation 4.15. Figure 4.19 is the initial observation, and Figure 4.20 is the semi-log plot, from which we can estimate the hydraulic diffusivity.

Using the method above, I calculated the permeability for sample set 2 assuming the viscosity of the pore fluid as 0.99 x 10^{-2} $dyne \cdot sec/cm^2$, the compressibility of the pore-fluid as 0.42 x 10^{-10} $cm^2/dyne$, the length of the sample as 3 cm, the sample cross-sectional area as $5.07cm^2$, and the calibrated pore-system volume of the as $0.125cm^3$. permeability with above method for sample set 2. The calculated permeabilities are 8.71x10^{-6} md for the sample cut perpendicular to bedding and 7.01x10^{-6} md for the sample cut parallel to bedding, respectively. These values are 10^6 times less than the gas permeability measured on above samples. Gas-permeability testing of the same samples produced 8.05 md parallel to bedding and 3.16 md perpendicular to bedding. Note how the small anisotropy of the brine-permeability in the above

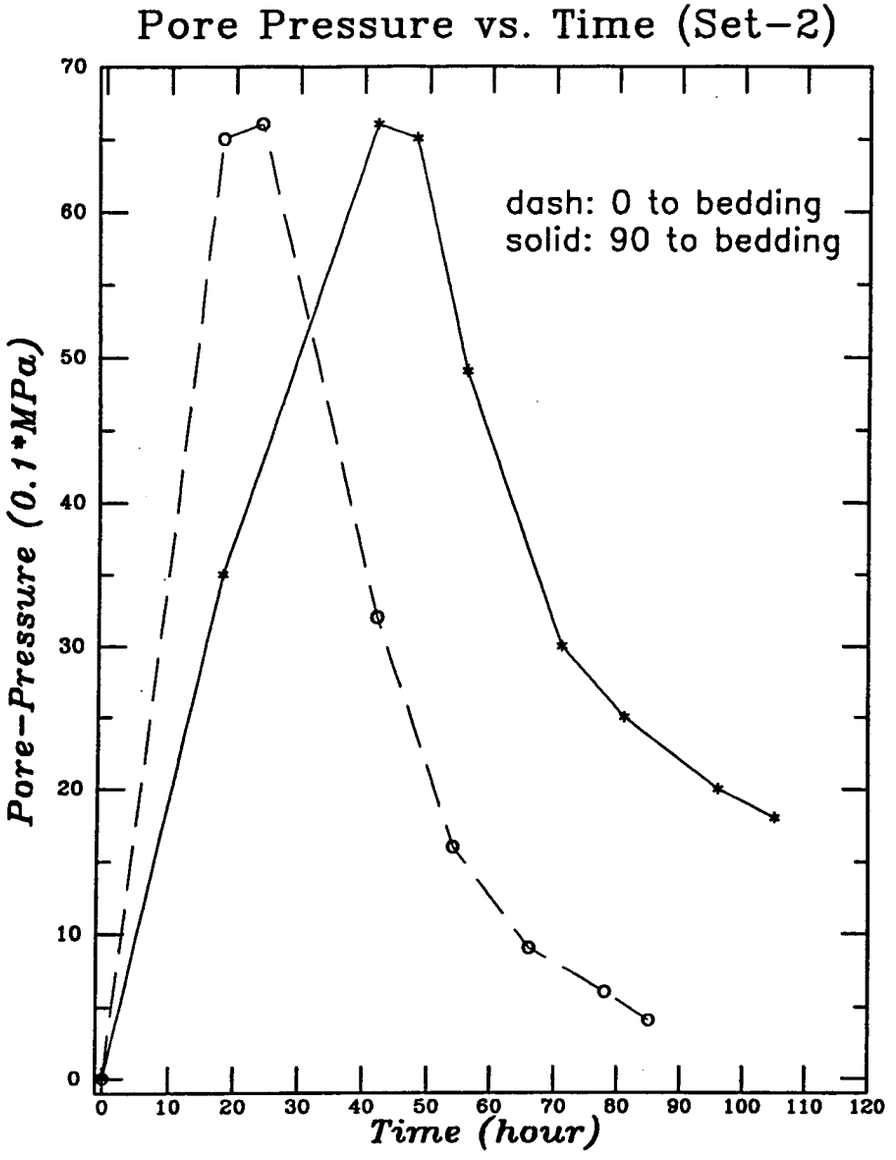

Figure 4.19: Pore-pressure variation with time in linear scale, where t_1 is 24 hours for the sample parallel to bedding, and 48 hours for the sample perpendicular bedding.

causes tremendous time differences in the pore-pressure equilibrium process (Figure 4.19).

The time-dependent velocity variation may also be used to estimate the permeability through a similar procedure. An empirical relation may be found by plotting velocity variations as a function of pore-pressure in log scale as shown in Figure 4.21, and it may take the form

$$V_p(t) = V_p(\infty)e^{(P_p(t)-c)} \tag{4.16}$$

where $V_p(\infty)$ is the velocity that would be measured at infinite time, when the pore pressure had dropped to zero, and c is an empirical constant which can be determined from experimental data.

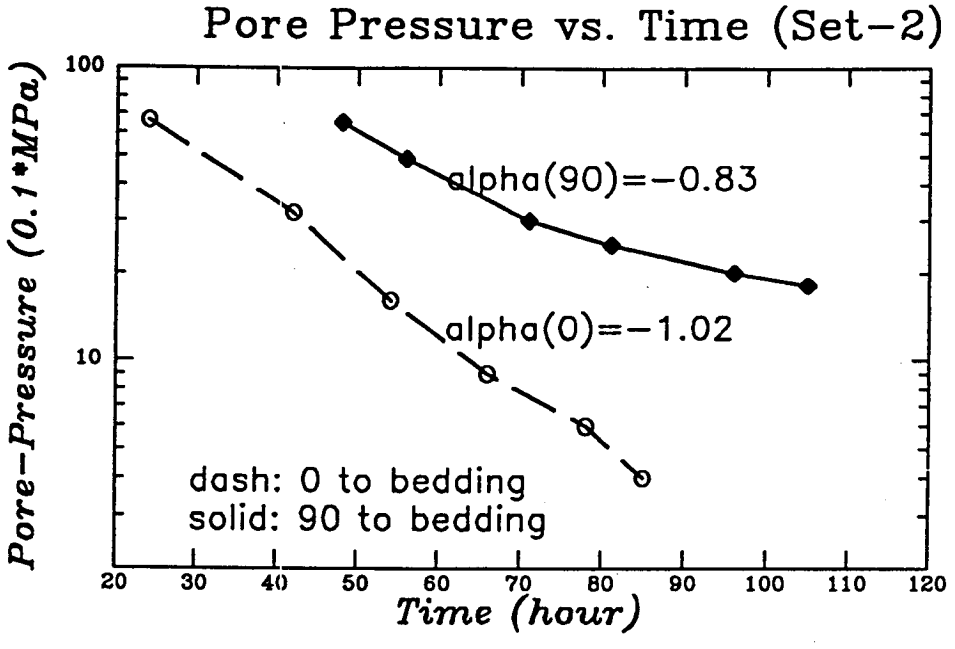

Figure 4.20: Observed pore-pressure variation with time in log scale. The slope is hydraulic diffusivity which is proportional to permeability.

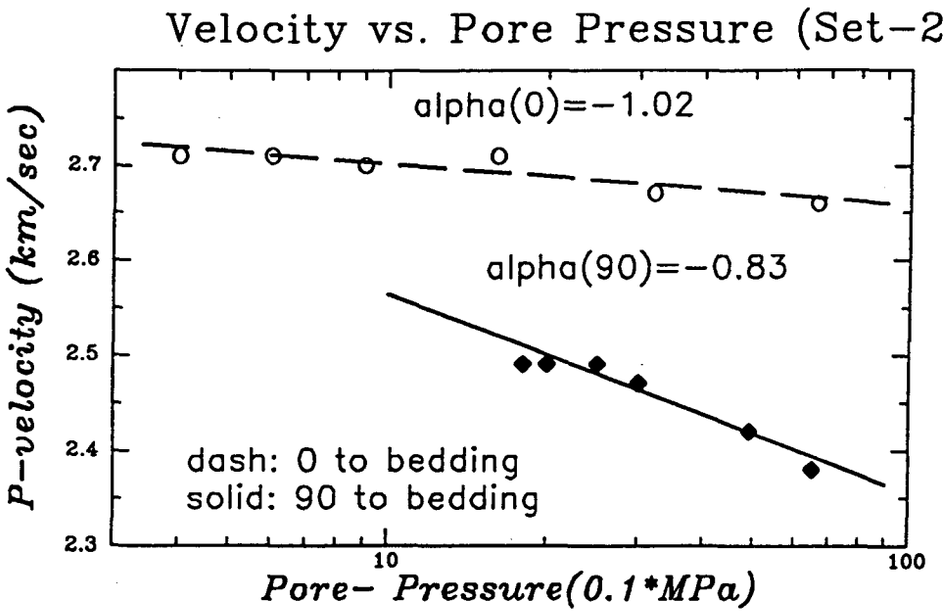

Figure 4.21: Velocity variation as a function of pore-pressure in log scale, the slope is proportional to "hydraulic diffusivity".

4.5 Velocity and attenuation under high pore pressure

It seems remarkable that we can observe "over-pressure" in shale formation in-situ, and at the same time retain doubts about the applicability of poroelastic theory to low permeability shaly rocks. To verify the applicability of this theory, I measured velocity and attenuation under high pore pressure.

4.5.1 Velocity and high pore pressure

To study effective pressure theory, I carried out an experiment by increasing pore pressure while the confining pressure was kept constant at 30 MPa. After pore-pressure was increased at a given time, I recorded the velocities a few days later when velocity and pore pressure variations are nearly zero.

The result is plotted in Figure 4.22. Note that velocity decreased about 0.45

km/s as pore pressure increased to about 25 MPa. Clearly, the effective pressure theory discussed in Section **4.4.1** also agrees with the results here, because we have waited long enough for pore pressure equilibrated. Effective pressure theory suggests that the velocity should remain the same for any level of total external pressure, the confining pressure P_c, as long as the pore pressure P_p changes accordingly, to maintain a constant pressure difference P_d, the effective pressure. The few experimental work in the literature that use data obtained by controlling pore pressure have also shown this characteristic (Hick et al., 1956, Wyllie et al., 1958, Tosaya, 1982).

A simple exercise using our limited experimental data to map velocity variations as a function of effective pressure may help us to explain the mystery of velocity changes as a function of pore pressure or effective pressure in anisotropic medium.

Through a regression of our drained up-loading velocity data at different confining pressures, we can obtain the following expression for P-wave velocity V_p as a function of confining pressure P_c,

$$V_p = A + BP_c^a \tag{4.17}$$

where A, B and k are constant at a given pore pressure.

First, we assume that the curvature of the velocity variation as function of confining pressure a will remain unchanged for different pore pressures, and velocity as a function of confining pressure is nearly constant if the effective pressure remains zero, as other studies cited above have shown. After that, we may interpolate to predict velocity as a function of both confining and pore pressures with our limited data of high pore pressure measurement presented in Figure 4.19, and with the following procedure:

1. Find the constant curvature parameter a by regression of the drained velocity data (P_p=0) (Figure 4.6);

2. Apply the above regressed velocity and confining pressure relation to estimated velocity at zero confining pressure and zero pore pressure;

3. Require that velocity as function of confining pressure must agree with both the velocity at zero differential pressure (nearly a constant), and the velocity data measured with varying pore pressures at a constant confining pressure of 30 MPa, to find constants A and B in Equation 4.17 under every measured high pore pressure;

4. Calculate velocity as a function of confining pressure under every measured high pore pressure.

The result of this interpolation is plotted in Figure 4.23. Note the wide range of velocity values possible at various differential pressures.

From the results of this study, it appears that uncontrolled pore pressure of shaly rocks are sufficient to cause very significant changes of wave velocity by varying effective pressure. We suggest that problems in predicting wave velocities in shaly rocks are the result of the inadequate constraints on the pore pressure, rather than a failure of effective pressure theory to shaly rocks.

4.5.2 Attenuation and high pore pressure

The attenuation variations associated with the high pore pressure were also measured by the spectral ratio method as described in Appendix A.

In general, we have observed that the spectral amplitude decreases as the pore pressure increases at a constant confining pressure. In other words, the spectral amplitude decreases as the effective pressure decreases (Figure 4.24). The attenuation coefficients resulting from the spectral ratio method, after corrected for transducer-sample reflection coefficients, are presented in Figure 4.25. Note that attenuation coefficients increased significantly as the pore pressure increased.

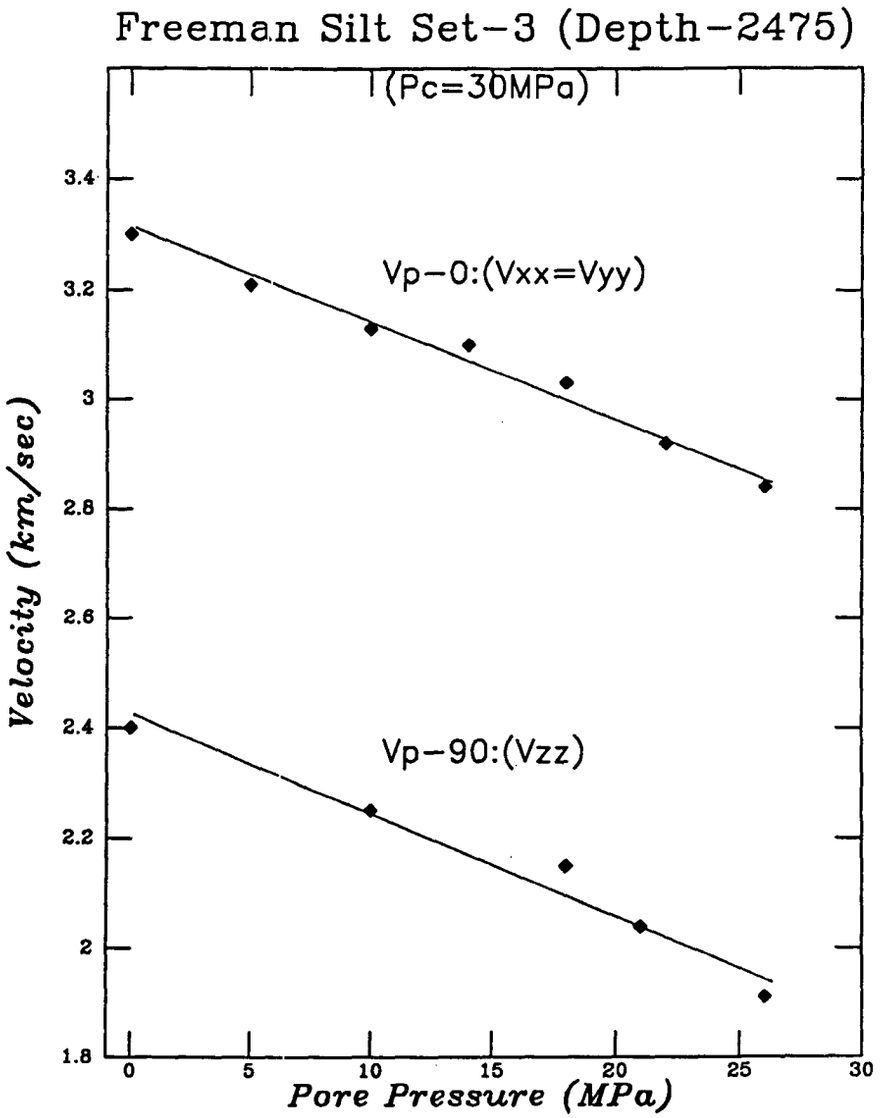

Figure 4.22: Velocity variation as function of high pore pressure. Note that the velocity decreased about 0.45 km/sec in both samples as pore pressure increased to about 25 MPa.

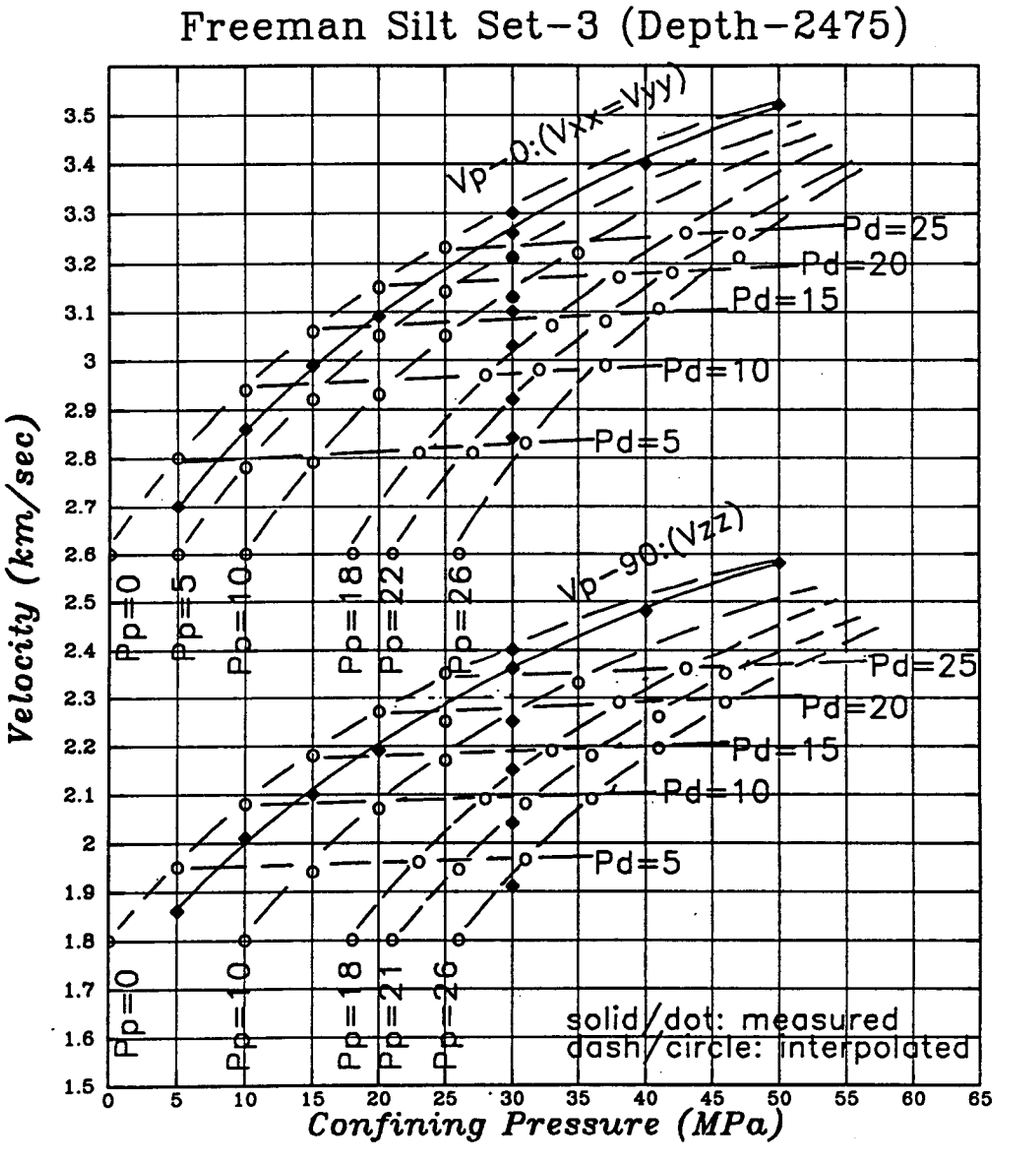

Figure 4.23: Velocity variation as function of effective pressure. Note that not only does the anisotropy of shale samples make a drastic velocity difference, but also the different pore pressures induce a wide range of velocity variations.

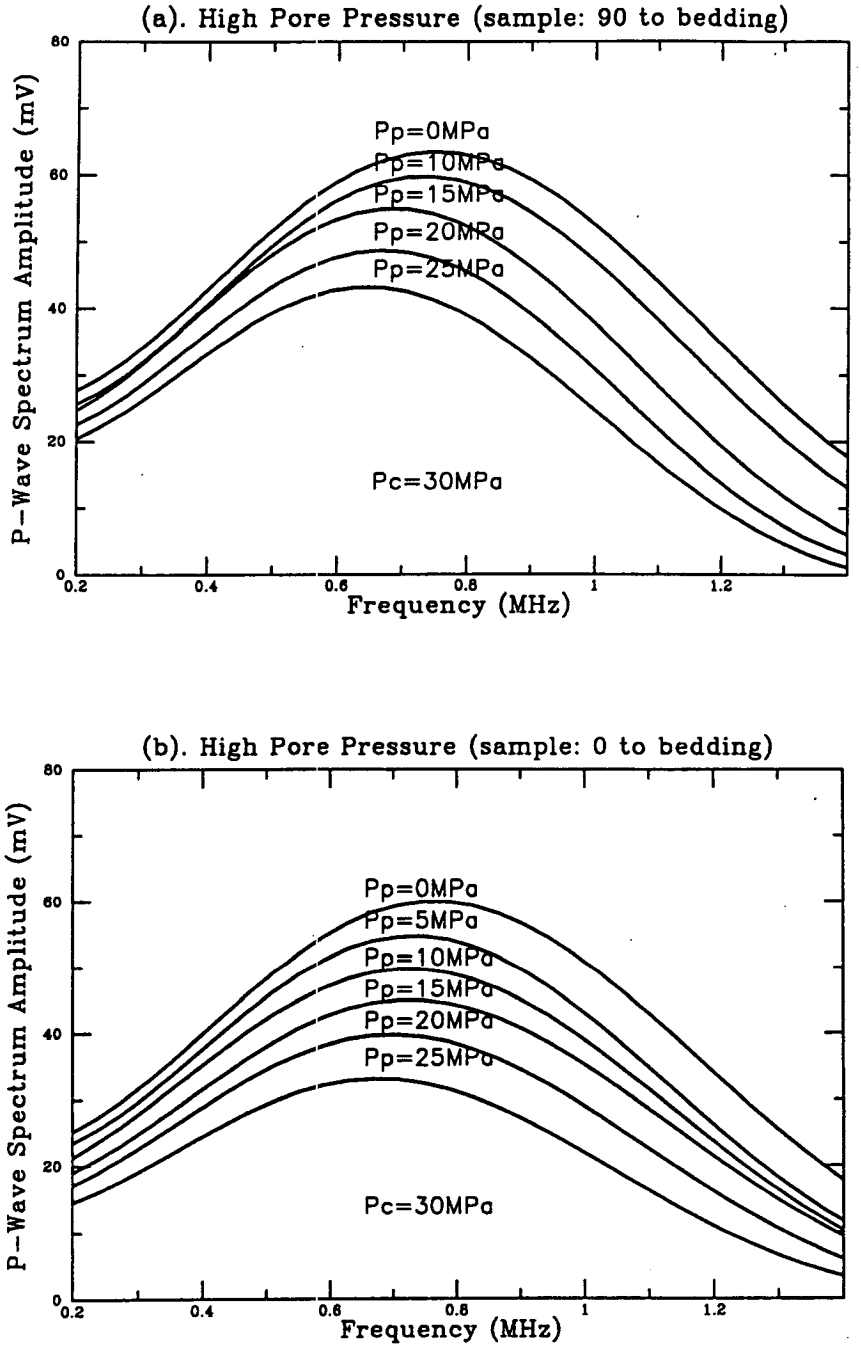

Figure 4.24: P-wave spectral amplitude at different pore pressures. (a). sample perpendicular to bedding, (b). sample parallel to bedding.

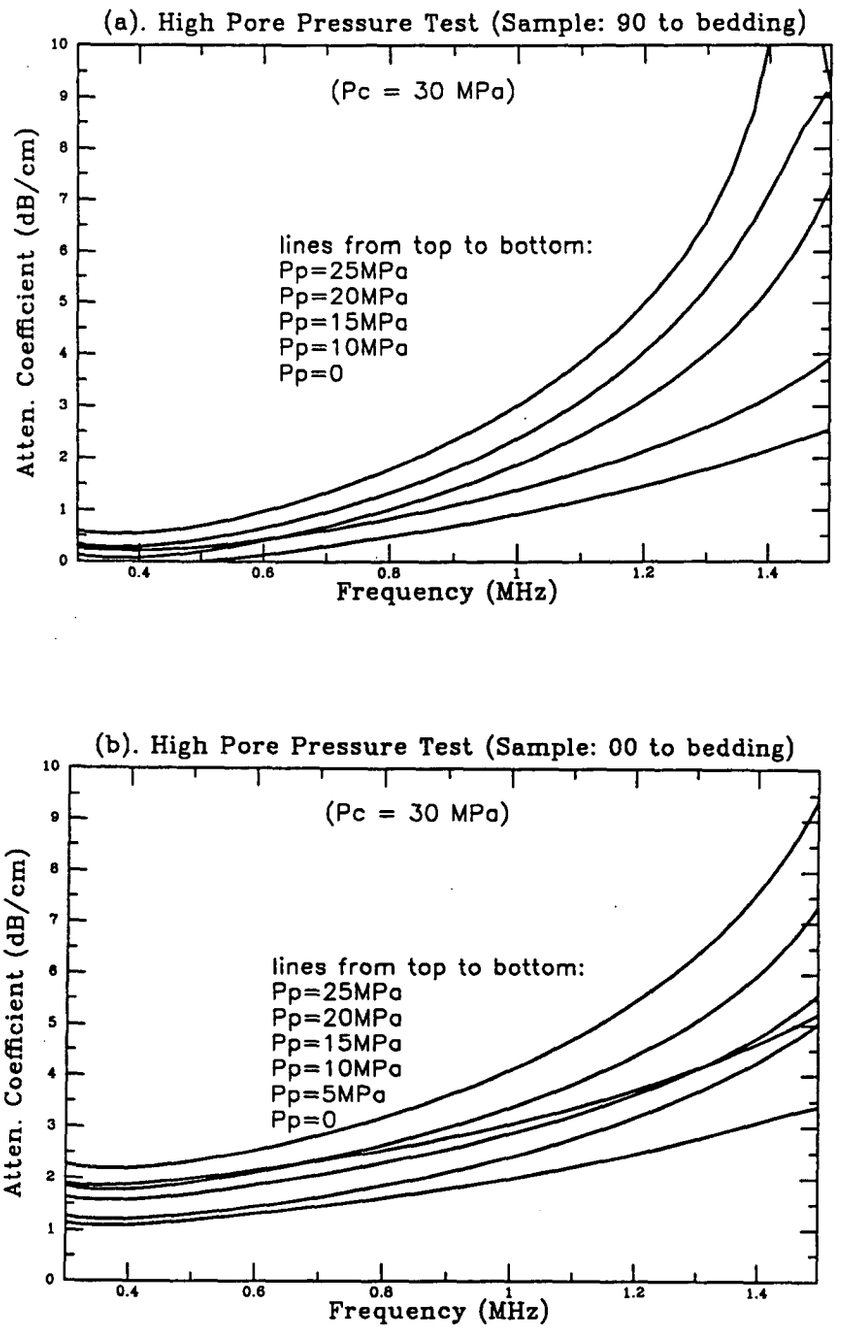

Figure 4.25: Spectral attenuation coefficient at different pore pressures. (a). sample perpendicular to bedding, (b). sample parallel to bedding.

4.6 Conclusion

I draw the following conclusions from the experimental observations in this chapter.

The P-wave velocity of brine saturated Freeman Jewett shale is higher than the P-wave velocity when dried. The S-wave velocities, in general, are lower under saturated than under dry conditions.

Petrographic analysis of the samples suggests that the intrinsic velocity anisotropy of the Freeman Jewett shale samples results from preferential orientation of mineral grains, and laminated clay layers acting as support matrix. The anisotropy factors decrease as the confining pressures were increased, due to the closing of pores and cracks which may have formed along the low shear resistant bedding plane during field coring and sample plug preparation. The anisotropic factors observed at high confining pressure may represent the intrinsic anisotropy of the samples.

The time-dependent velocity changes that we have observed can be used to estimate permeability. If such a time-dependent velocity variation is measurable in-situ as pore pressure is released, it may possibly be exploited to estimate in-situ permeability, and used to study the "reservoir recovery status " through VSP and cross-well seismic logging.

High pore pressure caused by low formation permeability can alter the effective stress enough to foil attempts to predict wave velocities with poroelastic theory. As long as the pore pressure is a known, the effective pressure theory may work well in a shaly formation. But in most laboratory observations, people have been either unable to maintain control of the pore pressure, or the phenomenon was neglected.

Attenuation of shaly samples, like wave velocities, varies as a function of pore pressure, confining pressure, or effective pressure. Understanding of this effect in a particular formation may help to predict the seismic properties of overpressured shaly formation. The details of the experimental techniques in-situ may require some refinement to develop this method into a diagnostic tool.

References

Auld, B. A., 1973, Acoustic Fields and Waves in Solids, Vol. 1, New York: John Wiley & Sons, Inc.

Backus, S., 1962, Long-Wave elastic anisotropy produced by horizontal layering, J. Geophysics. Res., Vol. 67, p.4427-4440.

Banick, N., 1984, Velocity anisotropy of shales and depth estimation in the North Sea basin, Geophysics, Vol. 49, p 1411-1419.

Banick, N., 1987, An effective anisotropy parameter in transversely isotropic media, Geophysic, Vol. 44, p 910.

Brace, W.F., Walsh, J.B., and Frangos, W.T. 1968, Permeability of Granite under High Pressure, J.G.R., Vol. 73, No.6, pp. 2225-2236

Dvorkin, J., 1991, Personal Communication.

Hicks, W.G. and Berry, J.E., 1956, Application of continuous velocity logs to determination of fluid saturation of reservoir rocks. Geophysics, 21, 739-754

Hosten, B., Deschamps, M. and Tittmann, B.R., 1987, Inhomogeneous wave generation and propagation in lossy anisotropic solids. Application to the characterization of viscoelastic composite materials, J. Acoust. Soc. Am., Vol. 82, No. 5, p 1763-1770.

Lynn, H. B., and Thomsen, L. A., 1986, Reflection shear-wave data along the principal axes of anisotropy, 56th Ann. Internat. Mtg., Soc. Expl. Geophysics, Expanded Abstracts, 473-476.

Lo, T., Coyner, K., and Toksoz, N., 1986, Experimental determination of elastic anisotropy of Berea sandstone, Chicopee Shale, and Chelmsford granite, Geophysics, 51, 164-171

Olson, H.C., 1988, Middle tertiary stratigraphy, depositional environments, paleoecology and tectonic history of the southeastern San Joaquin Basin, California, Ph.D thesis, Stanford.

Rai, C. S. and Hanson, K. E., 1988, Shear-wave velocity anisotropy in sedimentary rocks: A laboratory study, Geophysics, 53, 800-806

Rice, J. R., and Cleary, M. P., 1976, Some Basic Stress Diffusion Solution for Fluid-Saturated Elastic Porous Media With Compressible Constituents, Review of Geophysics and Space Physics, Vol. 14, No. 2, May, 1976.

Sayers, C. M., 1988, Stress-induced elastic wave anisotropy in fractured rock, Ultrasonics, 26, 311-317.

Shefiff, R. E., 1984, Encyclopedic Dictionary of Exploration Geophysics, Society of Exploration Geophysics, p. 152, Library of Congress Catalog Card No. 72-94565.

Thomsen, L., 1986, Week elastic anisotropy, Geophysics, 51, p 1954-1966

Tosaya, C., 1982, Acoustical properties of clay-bearing rocks, Ph.D thesis, Stanford University.

Winterstein, D. F., and Paulsson, B. N. P., 1990, Velocity anisotropy in shale determined from cross-hole seismic and vertical seismic profile, Geophysics, Vol. 55, No.4, 470-479.

Wodlett, R. S., 1970, Ultrasonic Transducers: Part 2, Underwater Sound Transducers, Ultrasonics, Vol. 3, pp. 243-253.

Wyllie, M.R.J., Gregory, A.R., and Gardner, G.H.F., 1958, An experimental investigation of factors affecting elastic wave velocity in porous media, Geophysic, 23, 459-493

Chapter 5

Stress-induced velocity and attenuation anisotropy of rocks

I call the fastest wave P, and the next S, and the slowest T, for primary, secondary, and tertiary.

— Francis Muir, 1988.

This chapter investigated acoustic velocity and attenuation anisotropy of rocks induced by applied anisotropic stresses. Cubic rock samples were probed by ultrasonic waves passing between a pair of three-component piezoelectric transducers, and three pairs of the transducers are disposed on all six faces of the cube sample. With our specially designed apparatus, one compressional wave and two orthogonally polarized shear waves were transmitted along each of the three principal directions of the cubic rock sample under "general triaxial loading"[1]. Eight rock samples (granite, dolomite, sandstones, shales, and Ottawa sand) have been tested under these conditions. Distinct P-wave velocity anisotropy, S-wave splitting, and attenuation anisotropic patterns have been observed under the polyaxial loading process. A particular physical

[1]In Rock Mechanics, this loading is also called polyaxial loading (Jaeger and Cook, 1979). In this chapter, I use "polyaxial loading" to mean the homogeneous true triaxial stresses, e.g., $P_{zz} \neq P_{xx} \neq P_{yy}$. This can be obtained, in principle, by loading a cube across its three pair of mutually perpendicular surfaces. I use "triaxial loading" to mean that only one of three principal stresses is different with the other two, e.g., $P_{zz} \neq (P_{yy} = P_{xx})$.

model—orthorhombic anisotropy of both velocity and attenuation—was observed under polyaxial loading.

5.1 Introduction

Anisotropic properties of rocks and shear-wave splitting phenomena are being studied more frequently by researchers worldwide as part of the ongoing effort to enhance seismic data interpretation and reservoir exploitation. Parallel cracks, cracks with co-planar normals, repeated sequences of fine layers, and aligned grains in rocks all produce transverse isotropy with a vertical symmetry axis or hexagonal symmetry as demonstrated through both laboratory and in-situ measurements (Kaarsberg 1968, Tosaya 1982, Lo et al. 1986, Rai et al. 1988, Berge et al. 1991). Consequently, vertical cracks with a horizontal axis of symmetry, periodic thin-layers with a horizontal axis of symmetry, or aligned orthorhombic olivine crystals may cause "azimuthal anisotropy" not only in hydrocarbon-bearing sedimentary basins, but also in the upper mantle of the earth (Hess 1964, Alford 1986, Lynn and Thomsen 1986).

5.1.1 Why three types of faults in the earth crust?

The existence of three types of faults: normal, strike-slip, and thrust, has been posited as evidence for three-dimensional stress fields in the crust. Underground rocks may never have been subjected to three equal principal stresses. Isotropic three dimensional stresses, if measured in-situ, may only be a transitory feature in a dynamic equilibrium state. Even in the near-surface, observed in-situ stresses show remarkable differences between the maximum and minimum horizontal stresses (Engelder et al. 1984).

Depending on the value of the vertical stress in relation to the two other horizontal principal stresses, three type of common faulting are discussed by Zobzck et al., 1989 in the review paper article—"Global pattern of tectonic stress" (Figure 5.1). They

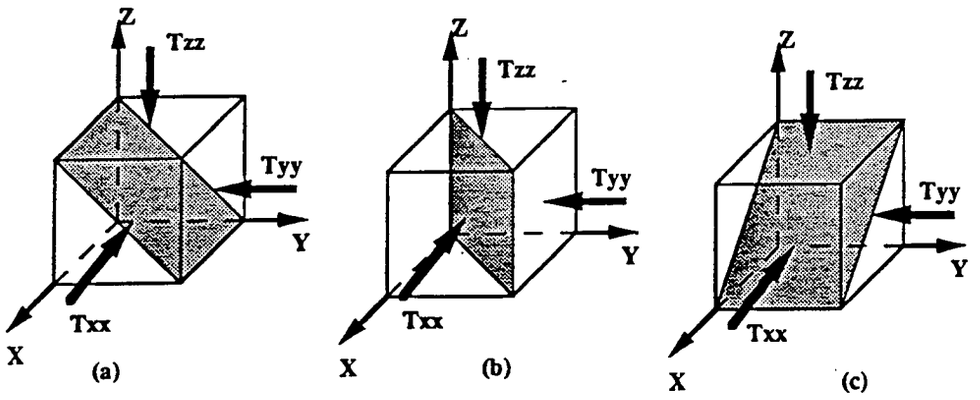

Figure 5.1: The principal shear stresses (shaded) generated by three principal compressional stresses. (a) $T_{zz} > T_{xx} > T_{yy}$: Normal faulting, (b) $T_{xx} > T_{zz} > T_{yy}$: Strike-slip faulting, (c) $T_{xx} > T_{yy} > T_{zz}$: Trust or reverse faulting.

summarized that

- $T_{Hmax.} > T_{hmin.} > T_{zz}$ results in thrust or reverse faulting,
- $T_{zz} > T_{Hmax.} > T_{hmin.}$ produces normal faulting,
- $T_{Hmax.} > T_{zz} > T_{hmin.}$ yields strike-slip faulting,

5.1.2 Does stress induce anisotropy?

Over twenty-two years have elapsed since Nur and Simmons published a substantiating stress-induced wave velocity anisotropy in rocks (1969). Field data did not observe the predicted emanations until recent equipment and techniques improved in vertical seismic profiling (VSP), multi-component 3-D surface reflections seismics, and cross borehole seismic surveying. With these new seismic equipments and techniques now, we have routinely observed the anisotropic indicator—seismic wave birefringence—commonly known as shear wave splitting this decade. Workers have found reason to

interpret this wave velocity birefringence as detection of structural stress anisotropy and subparallel microcrack planes as across the axis of an anticline (Lynn 1989, Winterstein et al. 1990).

In this chapter, I address the following three concerns:

1. Can we generalize stress-induced wave velocity anisotropy from one or two dimensions into three?

2. What might occur if we could measure wave attenuation anisotropy?

3. Must three-dimensional wave phenomena be studied under three dimensional stresses?

I seek to broaden our knowledge of both the intrinsic and stress-induced anisotropic properties of rocks through a three-dimensional experiment using both triaxial and polyaxial loading processes. I simultaneously measured acoustic velocities and attenuations in three mutually orthogonal principal axes X, Y and Z, and also along 45^{o} diagonals in three symmetry planes. Orthogonal anisotropy is the initial assumption behind this experiment. The polyaxial loading process is designed to observe all possible combinations of unconstrained horizontal and vertical stresses (Brown et al., 1978).

5.2 Fundamentals of acoustic anisotropy

5.2.1 Orthorhombic anisotropy

Orthorhombic symmetry has three mutually orthogonal planes of symmetry. In such a case, it has been proven that there are only nine independent, nonzero constants (Auld, 1973). In compressed notation, the matrix of strain (S_i) and stress (T_i) relation and their associated stiffness constants (c_{ij}) for orthorhombic symmetry may be expressed as

$$\begin{pmatrix} T_1 \\ T_2 \\ T_3 \\ T_4 \\ T_5 \\ T_6 \end{pmatrix} = \begin{pmatrix} c_{11} & c_{12} & c_{13} & 0 & 0 & 0 \\ c_{21} & c_{22} & c_{23} & 0 & 0 & 0 \\ c_{31} & c_{32} & c_{33} & 0 & 0 & 0 \\ 0 & 0 & 0 & c_{44} & 0 & 0 \\ 0 & 0 & 0 & 0 & c_{55} & 0 \\ 0 & 0 & 0 & 0 & 0 & c_{66} \end{pmatrix} \begin{pmatrix} S_1 \\ S_2 \\ S_3 \\ S_4 \\ S_5 \\ S_6 \end{pmatrix} \tag{5.1}$$

5.2.2 Velocity and elastic constants

In-situ, a plane wave propagating through anisotropic media may not have its particle motion polarized either parallel or normal to the wave vector. In the laboratory, however, the wave vector directions can be aligned with certain symmetry directions (pure mode directions) of the media.

If the wave vector directions and polarizing directions of particle motion are aligned with *Cartesian coordinate* axes X, Y, or Z in some sense, then we can deduce the following general expressions for stiffness constants as functions of group or ray velocity under orthorhombic symmetry as

$$\begin{cases} c_{11} = \rho v_{xx}^2 \\ c_{22} = \rho v_{yy}^2 \\ c_{33} = \rho v_{zz}^2 \\ c_{44} = \rho v_{yz}^2 = \rho v_{zy}^2 \\ c_{55} = \rho v_{xz}^2 = \rho v_{zx}^2 \\ c_{66} = \rho v_{xy}^2 = \rho v_{yx}^2 \\ c_{12} = \frac{\rho}{l_x l_y}\sqrt{[\frac{1}{2}(l_x+l_y)^2 v_{45-xy}^2 - l_x^2 v_{xy}^2 - l_y^2 v_{yy}^2][\frac{1}{2}(l_x+l_y)^2 v_{45-xy}^2 - l_x^2 v_{xx}^2 - l_y^2 v_{xy}^2]} - \rho v_{xy}^2 \\ c_{13} = \frac{\rho}{l_x l_z}\sqrt{[\frac{1}{2}(l_x+l_z)^2 v_{45-xz}^2 - l_z^2 v_{zx}^2 - l_x^2 v_{xx}^2][\frac{1}{2}(l_x+l_z)^2 v_{45-xz}^2 - l_z^2 v_{zz}^2 - l_x^2 v_{zx}^2]} - \rho v_{zx}^2 \\ c_{23} = \frac{\rho}{l_y l_z}\sqrt{[\frac{1}{2}(l_y+l_z)^2 v_{45-yz}^2 - l_y^2 v_{yz}^2 - l_z^2 v_{zz}^2][\frac{1}{2}(l_y+l_z)^2 v_{45-yz}^2 - l_y^2 v_{yy}^2 - l_z^2 v_{yz}^2]} - \rho v_{yz}^2 \end{cases} \tag{5.2}$$

where c_{ij} is stiffness constant, v_{ij} is group velocity measured in a particular direction, ρ is rock sample density, and l_i is directional cosine between group and phase velocities. Refer to *Appendix B* for details.

In the velocity and elastic constant relations above, the first subscript of group velocities, $v_{i,j}$ ($i = x, y, z$ and $j = x, y, z$), stands for the propagation direction of the

wave, while the second subscript stands for the wave's particle polarization direction. Those velocities with nonequal first and second subscripts are shear waves, and those with equal subscripts are longitudinal waves. Those velocities with subscripts like $45 - ij$ are also longitudinal waves. They propagate on the ij planes and their propagation direction is 45^o to one of the adjacent principal axis on that plane (Figure. 5.2-a and 5.2-b).

If we could observe a sample's wave velocities along its three principal axes, recording one P-mode and two mutually orthogonal S-mode, plus three diagonal P-modes—then we could deduce whether the sample has anisotropy with three axes of two-fold symmetry. To confirm this symmetry, we can compare v_{xy} with v_{yx}, v_{xz} with v_{zx}, and v_{xy} with v_{yx}. Only if all three of these comparisons are equal have we satisfied the conditions for orthorhombic symmetry. If we have this symmetry together with the full set of data described above, then we may infer all nine elastic stiffness constants for orthorhombic anisotropic medium (Figure 5.2-(a)).

5.2.3 Attenuation and Viscoelastic constants

The inhomogeneity and large acoustic wave absorption of most rocks, especially soft shale samples, have precluded applications of many high precision wave measurement techniques employed in solid state physics and nondestructive evaluation. Still, the pressing need for attenuation parameters in quantitative seismic interpretation keeps the heat on for improved attenuation measurement in both the field and the laboratory. Attenuation measurement techniques have rapidly been developed for rock sample measurement, and theory for geometrical diffraction correction in lossy anisotropic media has also been advanced from Papadakis (1966) to Tang et al., (1990).

I have adopted the spectral ratio method of estimating attenuation as developed by Papadakis (1966) and modified by Winkler (1982). Assuming the intrinsic attenuation of our reference aluminum cube $\alpha_r(\omega)$ is close to zero compared with the attenuation

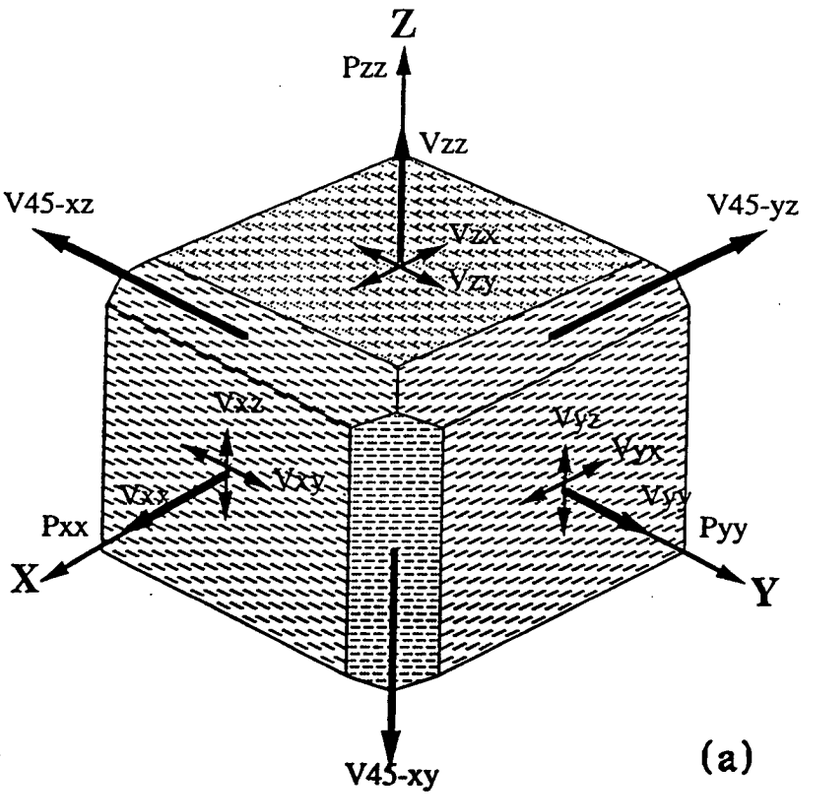

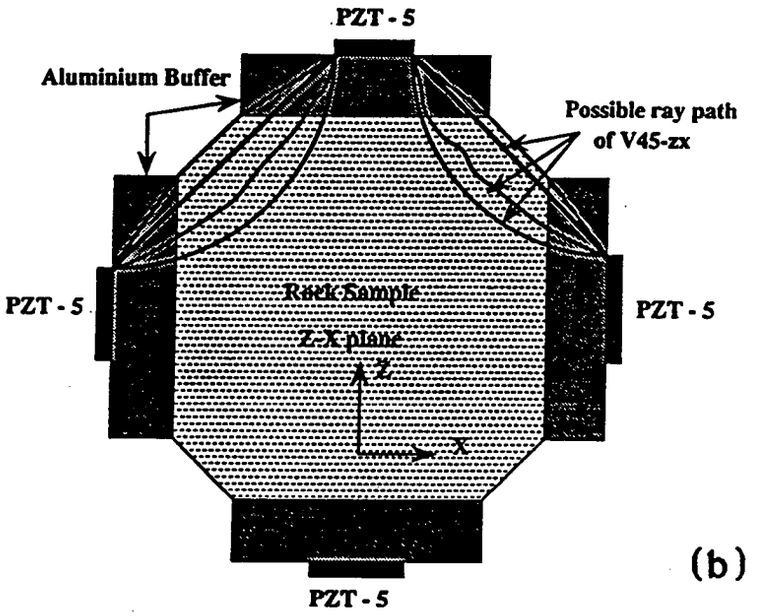

Figure 5.2: (a). A schematic diagram of sample shape, wave propagation directions, and particle polarization directions, (b). A profile view of possible ray-paths of the wave, V_{45-zx} in $Z - X$ plane.

of rocks, we have:

$$\alpha_s(\omega) = \frac{20}{L}\log_{10}\left[\frac{A_r(\omega)}{A_s(\omega)}(1-R^2)\right] - \frac{20}{L}\log_{10}\left[\frac{G_r(\lambda_r,a,L)}{G_s(\lambda_s,a,L)}\right] \tag{5.3}$$

where $\alpha_s(\omega)$ is attenuation coefficient of the measured sample in dB/cm; $A_r(\omega)$ is the reference cube amplitude spectrum measured, $A_s(\omega)$ is the amplitude spectrum of the sample measured; and R is reflection coefficient between the aluminum platen of the transducers and the measured sample.

If we assume that the geometric diffraction term of the reference cube $G_r(\lambda_r, a, L)$ is same as in the sample $G_s(\lambda_s, a, L)$ because of the identical geometries of both the rock and the reference cubes, then the last term in Equation 5.3 is zero. This method is strictly valid only for plane waves transmitted through perfectly bonded plane and parallel interfaces from transmitter to sample and sample to receiver.

We may deduce the visco-elastic stiffness constants $\hat{c}_{ij}$ and study attenuation anisotropy of rocks, if we can measure the attenuation coefficients along different directions. Wave propagation in a viscoelastic medium can be described by introducing complex stiffness constants:

$$\hat{c}_{ij} = c_{ij}(1 + iQ_{ij}^{-1}) \tag{5.4}$$

where $\hat{c} = [\hat{c}_{ij}]$ are the complex stiffness matrix; $c = [c_{ij}]$ is its real part, $[c_{ij}Q_{ij}] = \hat{c}$ is its imaginary part, and Q_{ij} is the anisotropic quality factor, which may take the form with directional attenuation coefficients α_{ij} as

$$\frac{100}{Q_{ij}(f)} = \frac{\alpha_{ij}(f)V_{ij}}{8.686\pi f} \tag{5.5}$$

where α_{ij} is the attenuation in dB/cm, V_{ij} is the phase velocity in m/s, and f is the frequency in *hertz* (Winkler 1982).

5.3 Experiment and set-up

5.3.1 Rock samples

The rocks measured in this experiment were Sierra White Granite, Colorado Shaly Sandstone, Colorado Oil Shale (dolomite), Berea Sandstone, Massillon Sandstone, two Freeman Jewett Silt, and Ottawa Sand. We consider the first three samples to be "hard rocks" because of their near zero porosity and high density, and the rest of the samples to be "soft rocks" because of their high porosity and the lower level of their consolidation. The samples were cut into cubes and the six surfaces were carefully ground, except for the Ottawa Sand. The dimension of all the cube samples[2] is about $71.1mm$ x $71.1mm$ x $71.1mm$.

Thin-sections were cut from all samples, and for those samples with apparent bedding planes, thin-sections were made from cuts both parallel and perpendicular to the bedding plane.

Figures 5.3 to 5.5 show the micro texture of the rock samples chosen in this study through thin-section photomicrographs. The apparent bedding plane and preferred grain orientation can be observed in the shale samples. X-Ray Diffraction or Micro-probe analyses were used for the mineral composition studies. The petrophysical descriptions are summarized in Table 5.1

All samples were kept in a heated oven for at least 72 hours at 80 C^o before any dynamic measurement. All dynamic measurements were made under room-dry conditions.

5.3.2 Experimental set-up

I have constructed two orthogonally welded square reaction frames with broad-flanged steel beams. The frames are designed for a working capacity of 200 kN in each of the three directions. The loading set in each of the three directions consists of two

[2]In detail, actual samples were cut into an octadecahedral shape (18 faces), and the area of the 12 diagonal faces are $14.4mm$ x $71.12mm$, much smaller than the 6 principal faces (Figure 5.2).

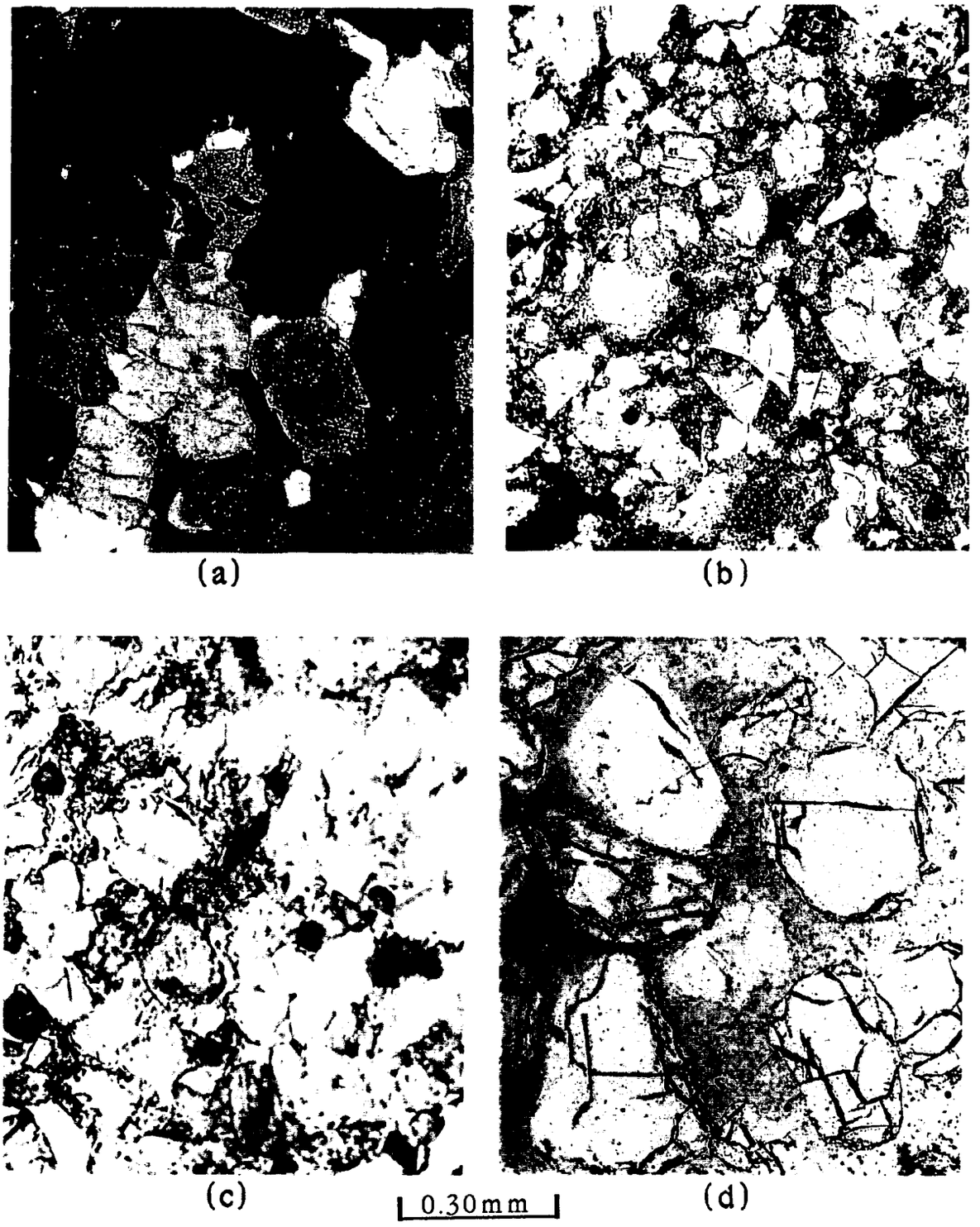

Figure 5.3: Thin-section photomicrographs. (a) Sierra White Granite, (b) Berea 200 Sandstone, (c) Massillon Sandstone, (d) Ottawwa Sand.

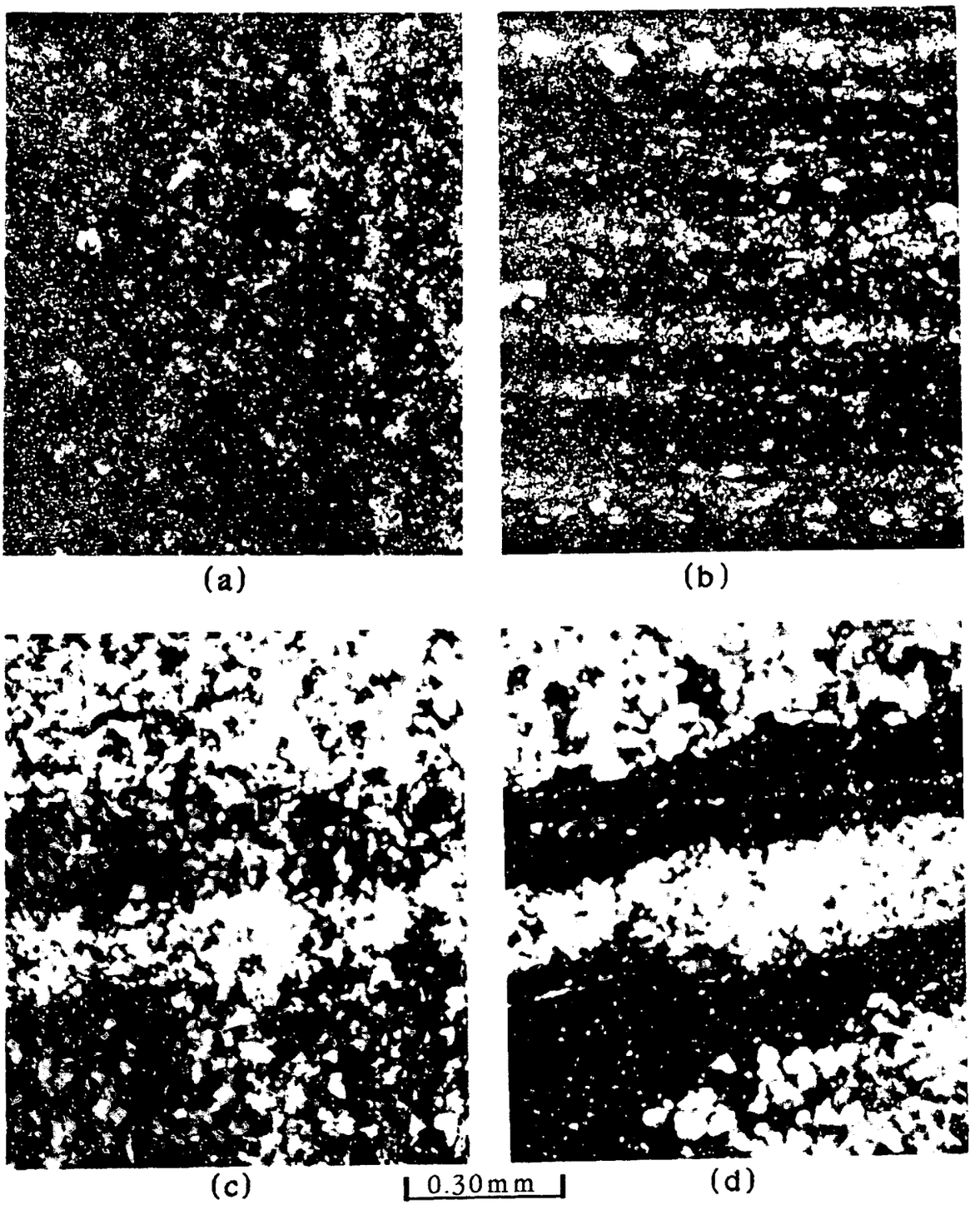

Figure 5.4: Thin-section photomicrographs. (a) Colorado Oil Shale parallel to bedding, (b) Colorado Oil Shale perpendicular to bedding, (c) Colorado Shaly Sandstone parallel to bedding, (d) Colorado Shaly Sandstone perpendicular to bedding.

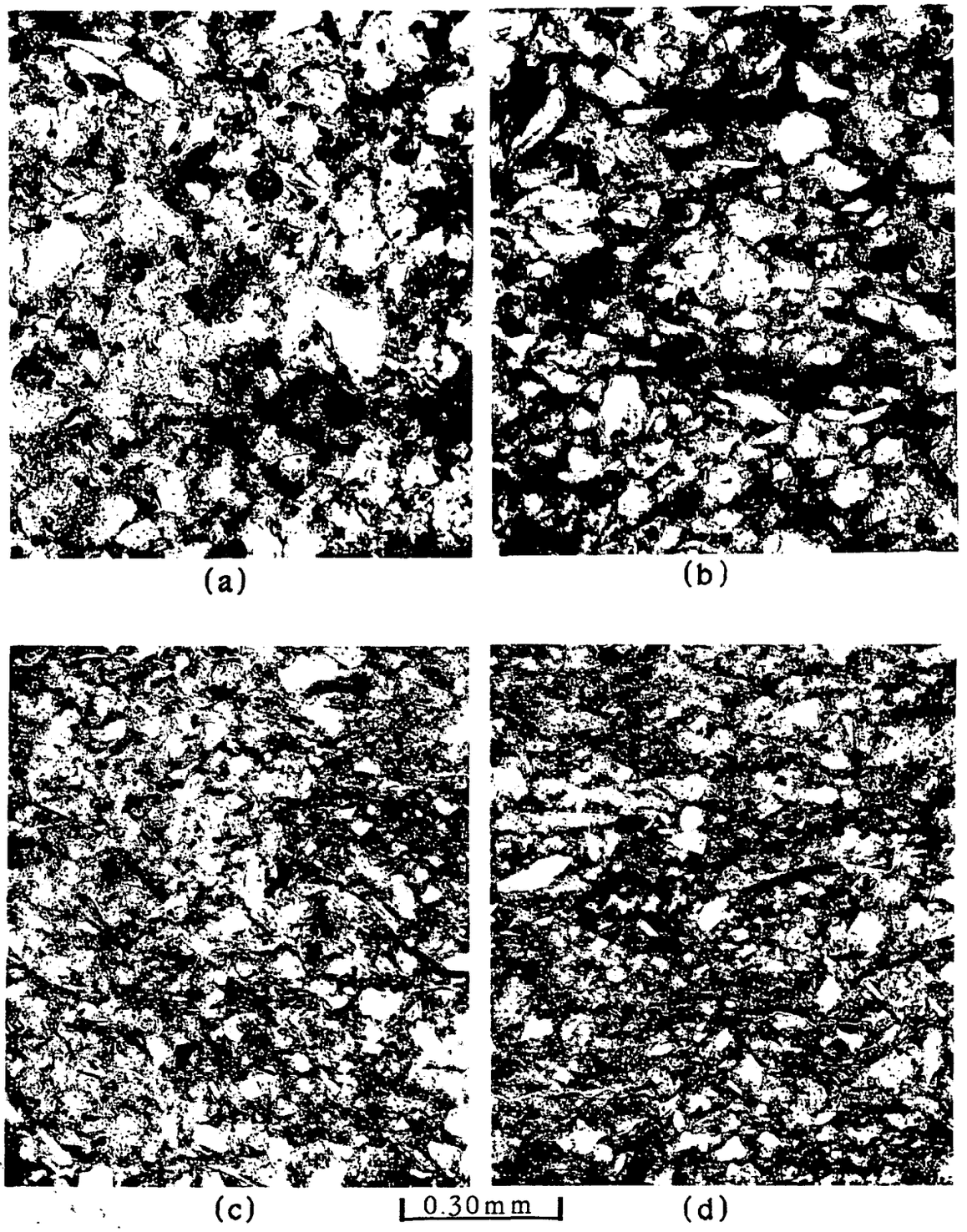

Figure 5.5: Thin-section photomicrographs. (a) Freeman Jewett Silt-A parallel to bedding, (b) Freeman Jewett Silt-A perpendicular to bedding, (c) Freeman Jewett Silt-B parallel to bedding, (d) Freeman Jewett Silt-B perpendicular to bedding.

one-inch diameter standard bolts opposite each other inside the reaction frames and co-axial across the center of the frames. A thrust bearing with a semi-spherical surface cap is mounted at the end of each loading bolt to align each pair of loading platens. Three pair of ultrasonic transducers are held in flat contact with the surface of the sample cube. The bearing caps correct for any slight non-parallelism of the sample's faces. Stressing the rock sample in this way has the advantage that additional shear stresses in the loading components are minimized and the rock sample can be kept centered in the rig during the loading process. The sample loading was performed by manually turning the loading bolts with a torque wrench. The torque force and stress were calibrated with an electronic load cell. Figure 5.6 is an overview of the set-up.

The samples were jacketed in a specially designed hard cell with six square inlets[3]. The sample's six faces directly contact the aluminum load-bearing platens of the transducers, and the back side of each transducer case is in direct contact with each thrust bearing cap. Inside each transducer, one P-mode and two S-mode PZT-5 crystals were mosaicked. The central frequency of the P-mode crystal is about 1 MHz, while the S-mode is about 0.6MHz, corresponding to wavelengths about 10 times greater than the grain diameter of the measured samples, conforming to ASTM-D-2845-90 measurement standards. At each pressure setting during a loading process, a certain ultrasonic pulse mode triggered in sending transducer travels through the sample and is sensed by either a receiving transducer directly opposite the emitting transducer, or one of the adjacent—perpendicular to the transmitter in three principal planes for the V_{45-ij} measurement. Figure 5.7 is a schematic profile of the sample cell, transducer array, and loading bolts in $X-Y$ plane.

A Velonex-345 high power pulse-generator is used to apply an electric pulse to one of transmitting transducers through a multi-channel switch board. A 600 Volt, 50

[3]The sample cell was designed to seal the rock sample inside and make saturated sample measurements possible.

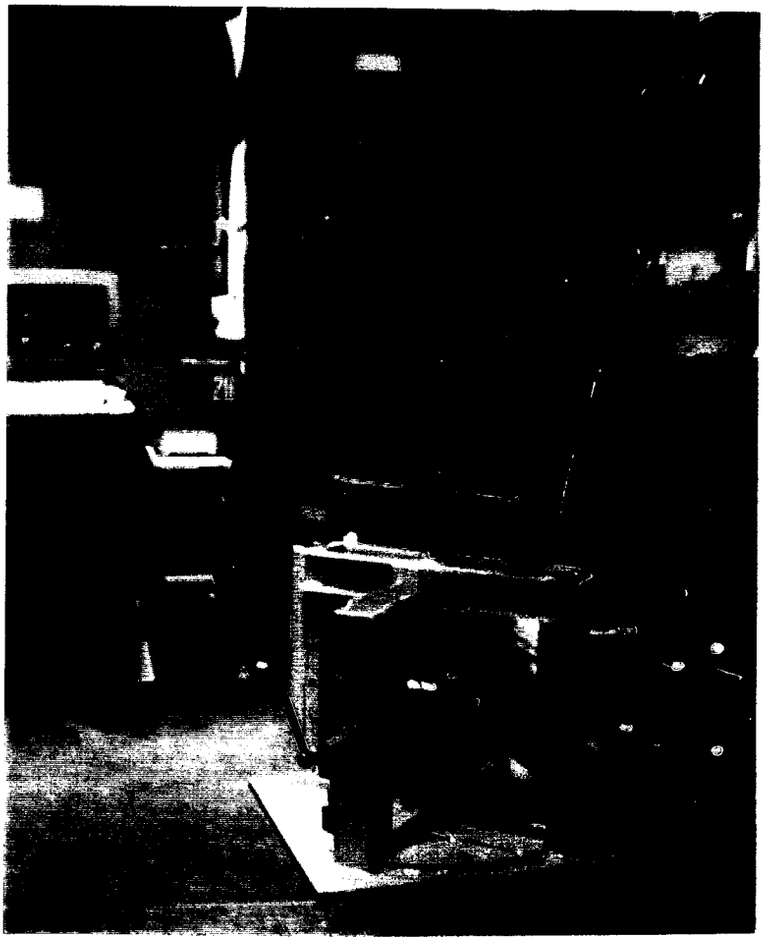

Figure 5.6: Overview of the experimental set-up and the polyaxial loading frame. Rock sample is jacked in the center of the frame.

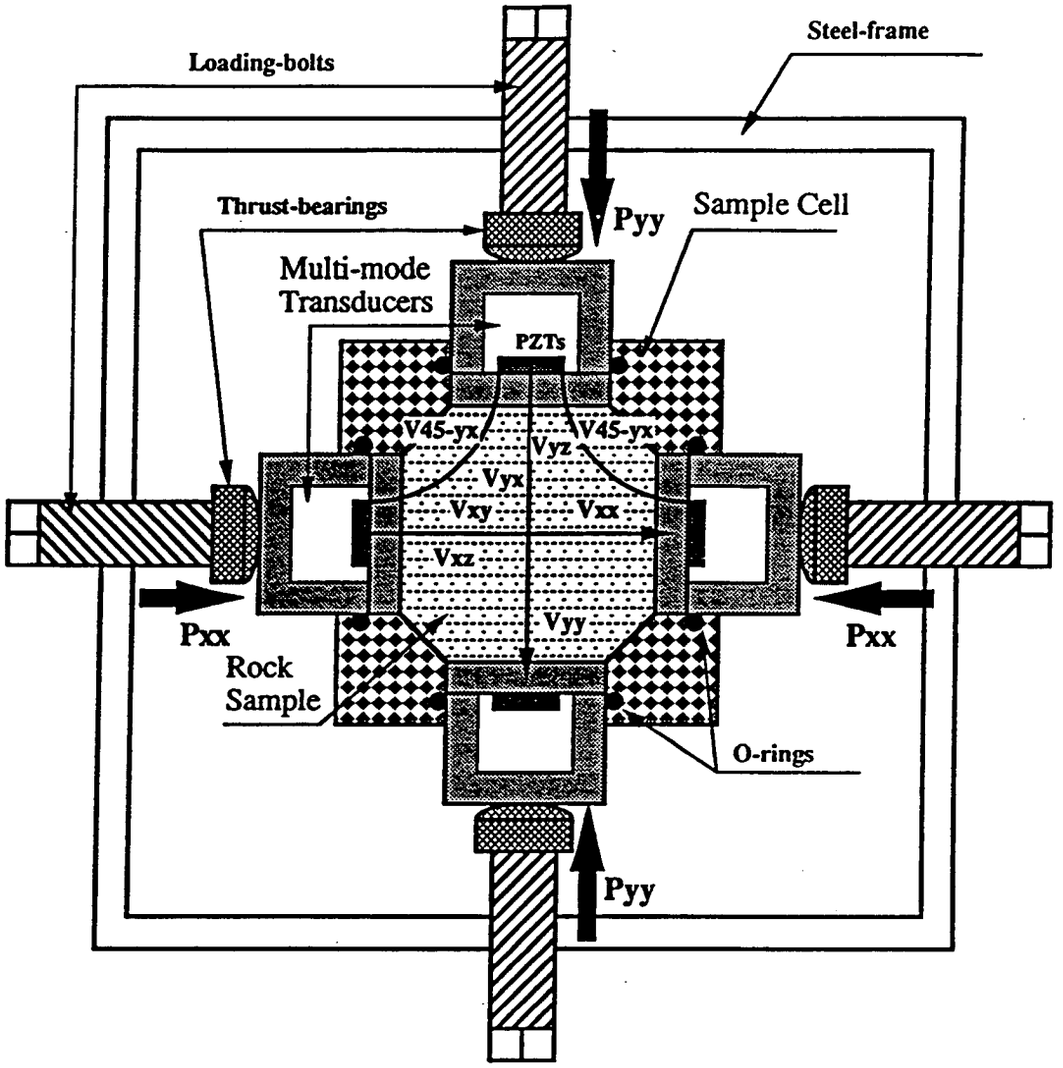

Figure 5.7: Profile view of the test jig in the X-Z plane.

nanosecond duration pulse is applied with a repetition rate of about 100 Hz. An *HP*-465A pre-amplifier was used for the highly attenuating Freeman Jewett Silt and unconsolidated Ottawa sand samples measurement. A Nicolet 2090 digital oscilloscope with a sampling rate of 50 nanosecond (20 MHz) was used to record the detected electrical pulse from the receiving transducers, and an *HP* Vectra RS/20 PC was linked to the oscilloscope to collect the data and process wavelets. The electrical pulses (to transmitters and from receivers) were switched manually for the 12 wave-mode measurements at each stress point through a multi-channel switch board. Panametrics acoustic couplant SWC-I02 was carefully applied between the transducers and rock samples to insure consistent amplitude measurement.

5.3.3 Loading procedure

The real world seems so complicated that we still have no inclusive theory to account for the wide range of observed in-situ stress patterns. Nevertheless, we may design a loading process to represent published empirical relationships of vertical versus horizontal stresses. These relationships may apply throughout a regional or subcontinental basis.

The state of stress in the crust at many different locations throughout the world have been studied by Brown and Hoek (1978). The measured vertical stresses follow the trend of lithostatic stress, $P_{zz} = \rho g z$, so when taking $\rho = 2.7 g/cm^3$, $g = 10 m/sec^2$, the vertical stress may expressed as

$$P_{zz} = 0.027 Z \tag{5.6}$$

where P_{zz} is vertical stress in MPa, Z is depth in meters.

The ratio k, average horizontal stress P_{xx} or P_{yy} to vertical stress P_{zz}, generally lies within limits defined by

$$100/Z + 0.30 \leq k \leq 1500/Z + 0.50 \tag{5.7}$$

Substitution of $P_{zz} = 0.027Z$ into this relation yields the upper and lower bounds for average horizontal stress

$$2.7 + 0.008Z \leq P_{xx} \leq 40.5 + 0.0135Z \tag{5.8}$$

These upper and lower bounds were used to design our loadings.

We aplly the term "triaxial" to identify the type of test in which two equal principal stresses applied to a sample, like $P_{xx} = P_{yy}$, and the term "polyaxial" to describe loading values of the three principal stress all differ from one another, $P_{zz} \neq P_{xx} \neq P_{yy}$, as commonly used in rock mechanics literature.

For triaxial loading, we first set $P_{xx} = P_{yy} = P_{zz}$ to ensure good acoustic coupling between the transducers and rock sample, then increased P_{zz} alone. For polyaxial loading, we kept P_{xx} and P_{zz} at different constant values, and only increased P_{yy} to a certain value based on Equation 5.8.

5.4 Results

5.4.1 Velocities and Stiffness Constants

Wave velocities were determined by measuring the time taken for an ultrasonic pulse to traverse the rock sample. The total time delay was measured by picking the first arrival from each wave-mode, and a time correction was applied based on the transducers' delays measured from each transmitter and receiver pair in face-to-face contact. The corrected time delay and sample length were then used to calculate the ultrasonic velocities of a rock sample by $V_{ij} = L/[t_m(ij) - t_c(ij)]$. The absolute error ΔV in the wave velocity measurement may be estimated by partial differentiation,

$$\Delta V = \left|\frac{\partial V}{\partial L}\Delta L\right| + \left|\frac{\partial V}{\partial t_m(ij)}\Delta t_m(ij)\right| + \left|\frac{\partial V}{\partial t_c(ij)}\Delta t_c(ij)\right| \tag{5.9}$$

and the relative error may be evaluated by

$$\frac{\Delta V}{V} = \frac{\Delta L}{L} + \frac{\Delta t_m(ij)}{t_m(ij) - t_c(ij)} + \frac{\Delta t_c(ij)}{t_m(ij) - t_c(ij)} \tag{5.10}$$

For $\Delta L = 0.025mm$, $\Delta t_m(ij) = \Delta t_c(ij) = 50ns$, the estimated maximum absolute error ΔV in our measurement is about 30 m/sec for P-waves, and 15 m/sec for S-waves. This estimate is only valid for the P and S velocities along the principal directions (a less pessimistic error may be obtained by *rms* errors).

For the P-waves measured along the diagonal directions in a principal plane, V_{45-ij}, we found that the amplitude was about 10 times smaller than in the principal directions, and consequently it had a much poorer signal to noise ratio. This observation may be subject to an interpretation of the actual "ray-path". To obtain a first-order estimate of anisotropy, we estimated the ray path length along diagonal directions with the P-velocity measured in principal directions under isotropic stress status, and assumed a constant ray path length under various anisotropic stress states. Despite these efforts, velocity estimates along the diagonal directions may remain experimental at this stage due to the difference between the group and phase velocities.

Table 2 is a list of velocity data for all samples studied, including measurements along all principal directions and three 45° diagonal directions under the triaxial and polyaxial loading processes. In the table, we may observe that all V_{ij} are near or equal to V_{ji}, within experimental error. To study elastic anisotropy, the elastic stiffness constants on the diagonal of the stiffness matrix were calculated with the following equations based on orthorhombic symmetry.

$$\begin{cases} c_{11} = \rho v_{xx}^2 \\ c_{22} = \rho v_{yy}^2 \\ c_{33} = \rho v_{zz}^2 \\ c_{44} = \rho[(v_{yz} + v_{zy})/2]^2 \\ c_{55} = \rho[(v_{xz} + v_{zx})/2]^2 \\ c_{66} = \rho[(v_{xy} + v_{yx})/2]^2 \end{cases} \tag{5.11}$$

Figures 5.8 to 5.11 show anisotropic patterns of elastic stiffnesses associated with

the triaxial and polyaxial loading processes.

Colorado oil shale and Colorado shaly sandstone:

Colorado oil shale (dolomite) and Colorado shaly sandstone are both from Well-22-12, at depth over 10,000 ft, Wildcat Field, Colorado. Velocities are almost independent of stresses, over a range of 1 to 10 MPa, except in the Z direction (perpendicular to bedding) of the Colorado Shaly Sandstone. The dramatic increase of V_{zz} with increasing stress P_{zz} of Z direction in Colorado Shaly Sandstone may represent microcrack closure response to the stress in the Z direction. The cracks may have developed in sample's thin clay layers parallel to the bedding plane, either at the time the core were drilled or during the time the core was dried. These two fine clastic rocks with apparent preferential grain orientation and interbeded clay layers show strong intrinsic transverse isotropy.

Sierra white granite:

Velocity variation associated with stress changes in Sierra white granite (Figure 5.9) show that Sierra white granite may have a weak intrinsic orthorhombic symmetry. Quarries tell us that most rocks have a "hard-way", a "mid-way", and an "easy-way" to cut along. Micro-cracks may be better developed on the "easy-way" (rift plane), and secondary micro-cracks may also exist along the "mid-way" (grain plane). The easy-way may cut along a plane of fractures that might be called the right plane, while the mid-way may cut along grain orientations, the grain plane. Whether or not our applied stress directions were aligned to the sample's principal directions of anisotropic symmetry could not be determined since we prepared only one thin-section of the granite sample. Stress-induced anisotropy was only detected in P-waves, at about 7%.

Berea 200 sandstone:

The Berea sample was measured with its Z direction normal to its bedding plane. It has weak intrinsic anisotropy, at about 6%. Its intrinsic anisotropy did not dominate its anisotropic pattern under triaxial and polyaxial loading. Triaxial loading resulted in the disappearance of its intrinsic anisotropy when P_{zz} increased to 4MPa, and polyaxial loading lead to a near azimuthally transverse isotropic symmetry (Figure 5.9).

Massillon sandstone and Ottawa sand

Velocity changes in Massillon Sandstone and Ottawa Sand under triaxial and polyaxial loading, shown in Figure 5.10, were close to the changes predicted by Nur and Simmon in 1970. The effect of directional stress on velocity anisotropy in these two *isotropic and homogeneous* samples closely follows the stress pattern. Triaxial loading to these two samples causes transversely isotropic symmetry, polyaxial loading causes orthorhombic symmetry. The stress-induced velocity anisotropy may result from cracks closing normal to the increased stress direction, and better grain contact along the higher stress direction.

Freeman Jewett Silts

The Freeman Jewett Silt samples were from Well No.1, Round Mountain Oil field, ARCO Oil and Gas Co., Bakersfield, California. Sample A was taken from depth 2,798 ft, and sample B was taken from depth 2493 ft. Both samples have a preferred grain orientation and are clay matrix supported. Sample B was completely fractured along its bedding plane, because of clay swelling during the defrosting and drying processes. Figure 5.11 shows that both Sample A and Sample B initially have the transversely isotropic symmetry with the symmetry axis perpendicular to each sample's bedding plane. While the intrinsic anisotropy disappeared as the stress P_{zz}

increased to 3.5MPa along its symmetry axis in Sample A, and finally developed an azimuthally transverse isotropic symmetry under triaxial loading. Under the polyaxial loading process, the samples showed orthorhombic symmetry, if not monoclinic symmetry.

5.4.2 Elastic Anisotropic Factors

Elastic anisotropic factors for orthorhombic symmetry are hard to define. To estimate the stress-induced orthorhombic anisotropy, we have defined P-wave anisotropy and S-wave anisotropy with the following equations.

$$\begin{cases} P.A.(xx-yy) = |(c_{11}-c_{22})/(c_{11}+c_{22})| \\ P.A.(xx-zz) = |(c_{11}-c_{33})/(c_{11}+c_{33})| \\ P.A.(yy-zz) = |(c_{22}-c_{33})/(c_{22}+c_{33})| \\ S.A.(xy-xz) = |(c_{55}-c_{66})/(c_{55}+c_{66})| \\ S.A.(yx-yz) = |(c_{44}-c_{66})/(c_{44}+c_{66})| \\ S.A.(zx-zy) = |(c_{44}-c_{55})/(c_{44}+c_{55})| \end{cases} \tag{5.12}$$

In the above equation set, $P.A.(xx-yy)$ means an anisotropic factor which measures the P-wave propagating in the X-direction over the P-wave propagating in the Y-direction. $S.A.(xy-xz)$ describes an anisotropic factor which compares an S-wave propagating in the X-direction and polarized in the Y-direction to another S-wave propagating in the same direction, but polarized in Z-direction, and so on. These simple definitions of anisotropic factors may be sufficient to correlate our laboratory measurements with in-situ VSP, vertical multi-component survey, and cross-well anisotropy measurements. The results are shown in Figure 5.12 through 5.15.

In summary, *stress-induced anisotropy is more significant in soft rocks than in hard rock.* This should be expected in static measurement since soft rocks have higher Poisson's ratio than do hard rocks, and also have higher strain ratio than hard rocks under a given stress. We have observed that soft rocks in their wave velocity anisotropy are also more stress-dependent than hard rocks.

For the intrinsically anisotropic hard rocks, like Colorado oil shale and Colorado

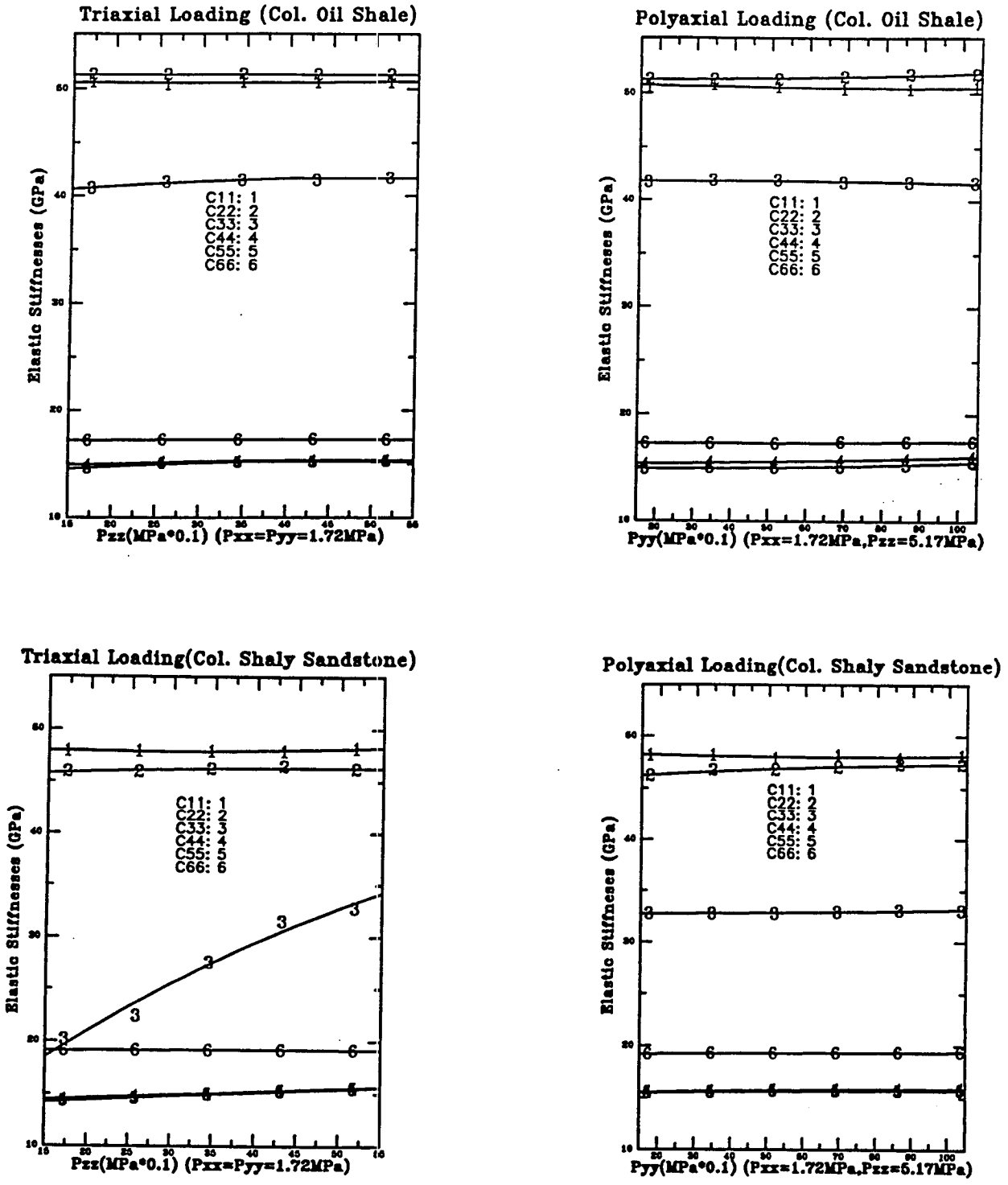

Figure 5.8: Elastic stiffness Constants of Colorado Oil Shale and Colorado Shaly Sandstone as function of loading stresses. The left column shows triaxial loading process, and right column shows polyaxial loading process.

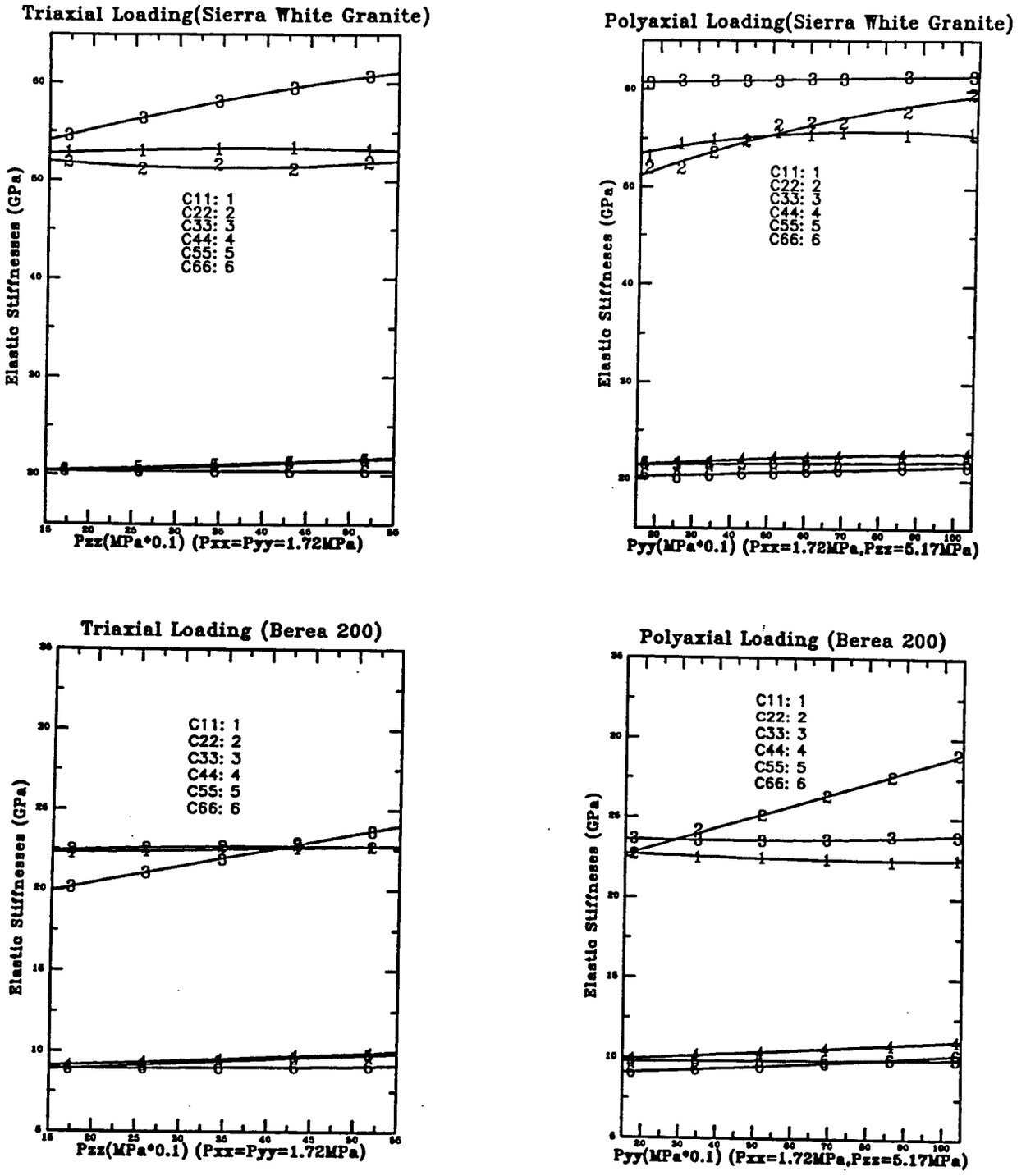

Figure 5.9: Elastic stiffness constants of Sierra White Granite and Berea 200 Sandstone as function of loading stresses. The left column shows triaxial loading process, and right column shows polyaxial loading process.

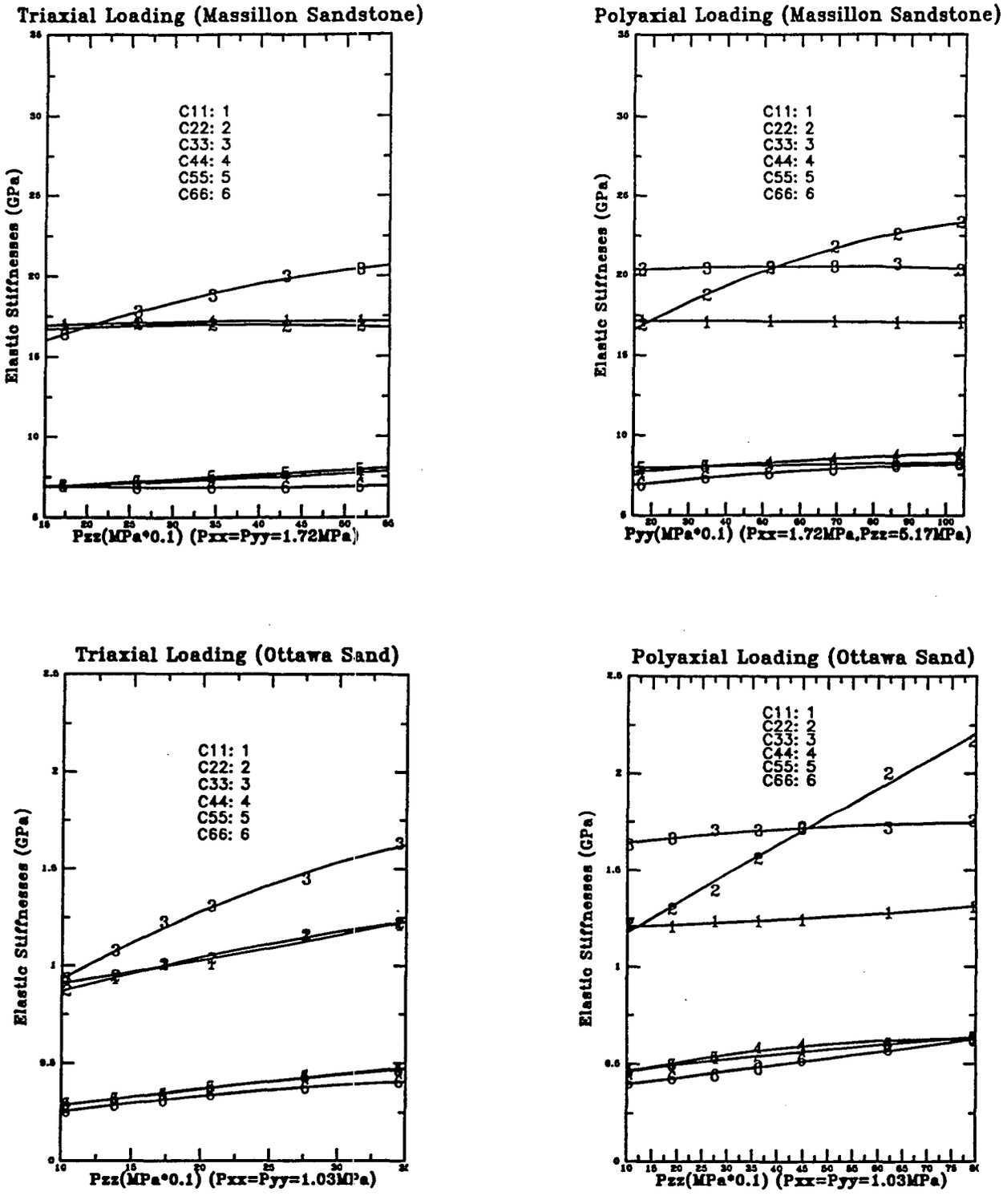

Figure 5.10: Elastic stiffness constants of Massillon Sandstone and Ottawa Sand as function of loading stresses. The left column shows triaxial loading process, and right column shows polyaxial loading process.

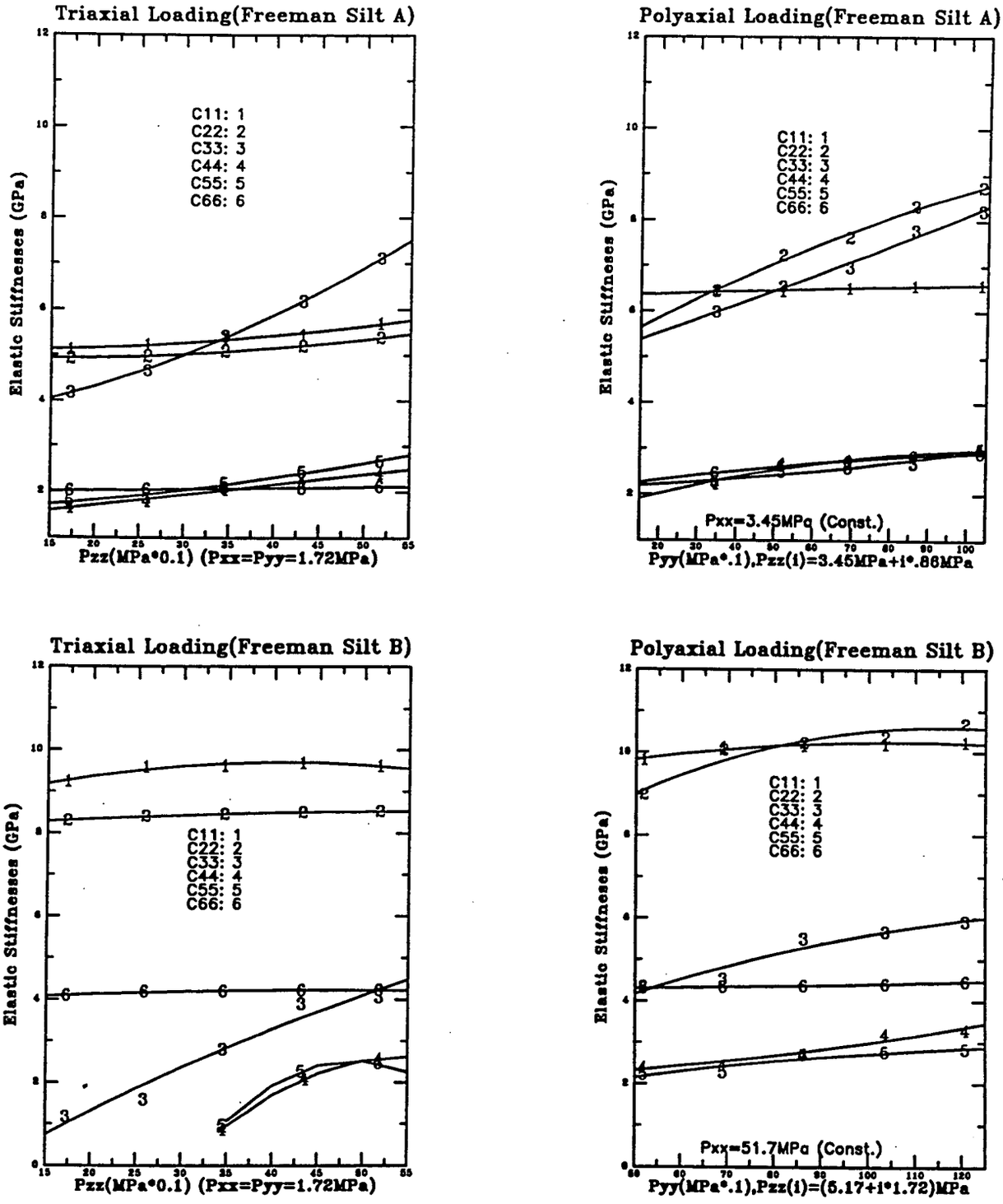

Figure 5.11: Elastic stiffness constants of Freeman Jewett Shale A and B as function of loading stresses. The left column shows triaxial loading process, and right column shows polyaxial loading process.

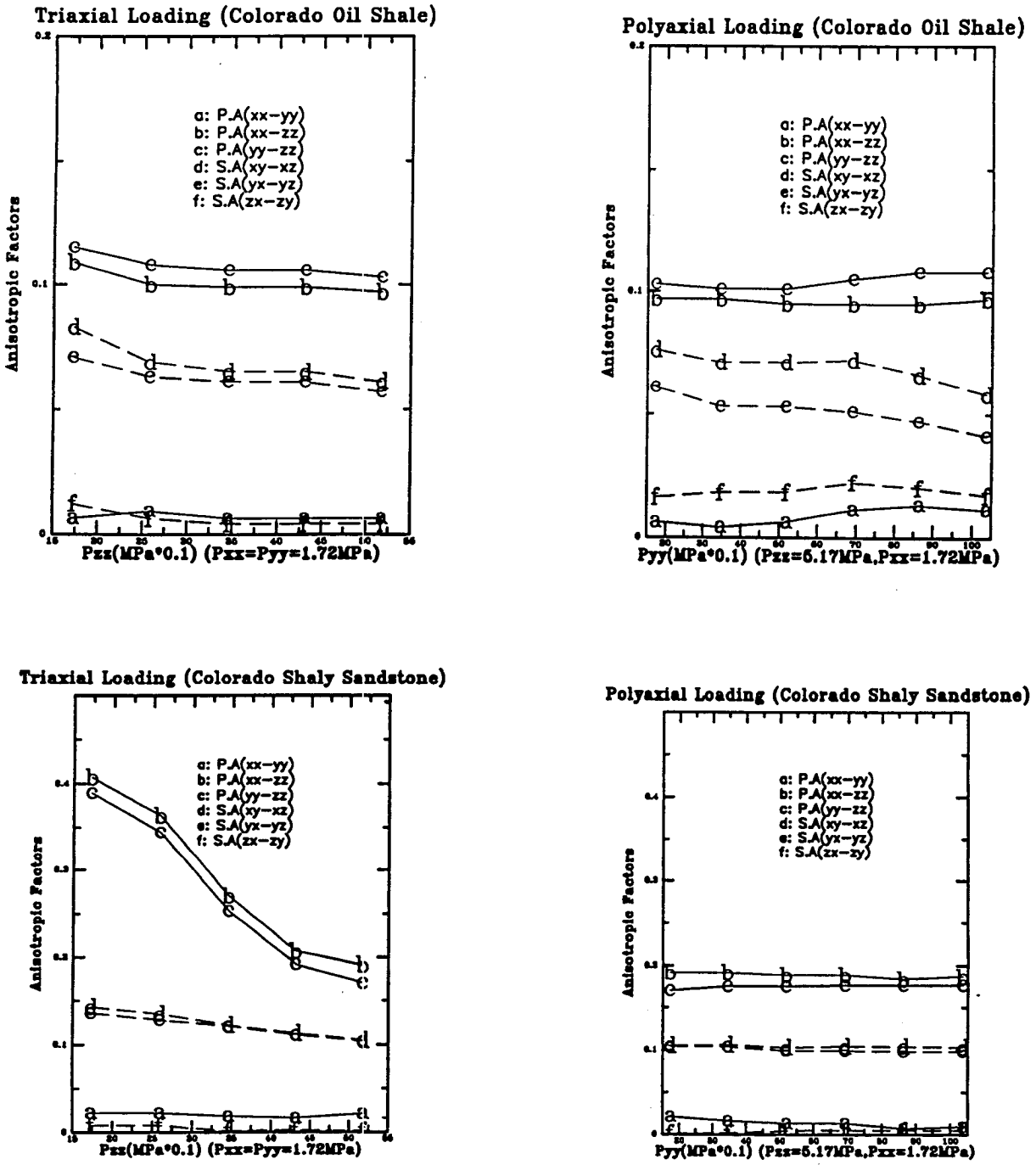

Figure 5.12: Anisotropic Factors of Colorado Oil Shale and Colorado Shaly Sandstone. The left column shows triaxial loading process, and the right column shows polyaxial loading process.

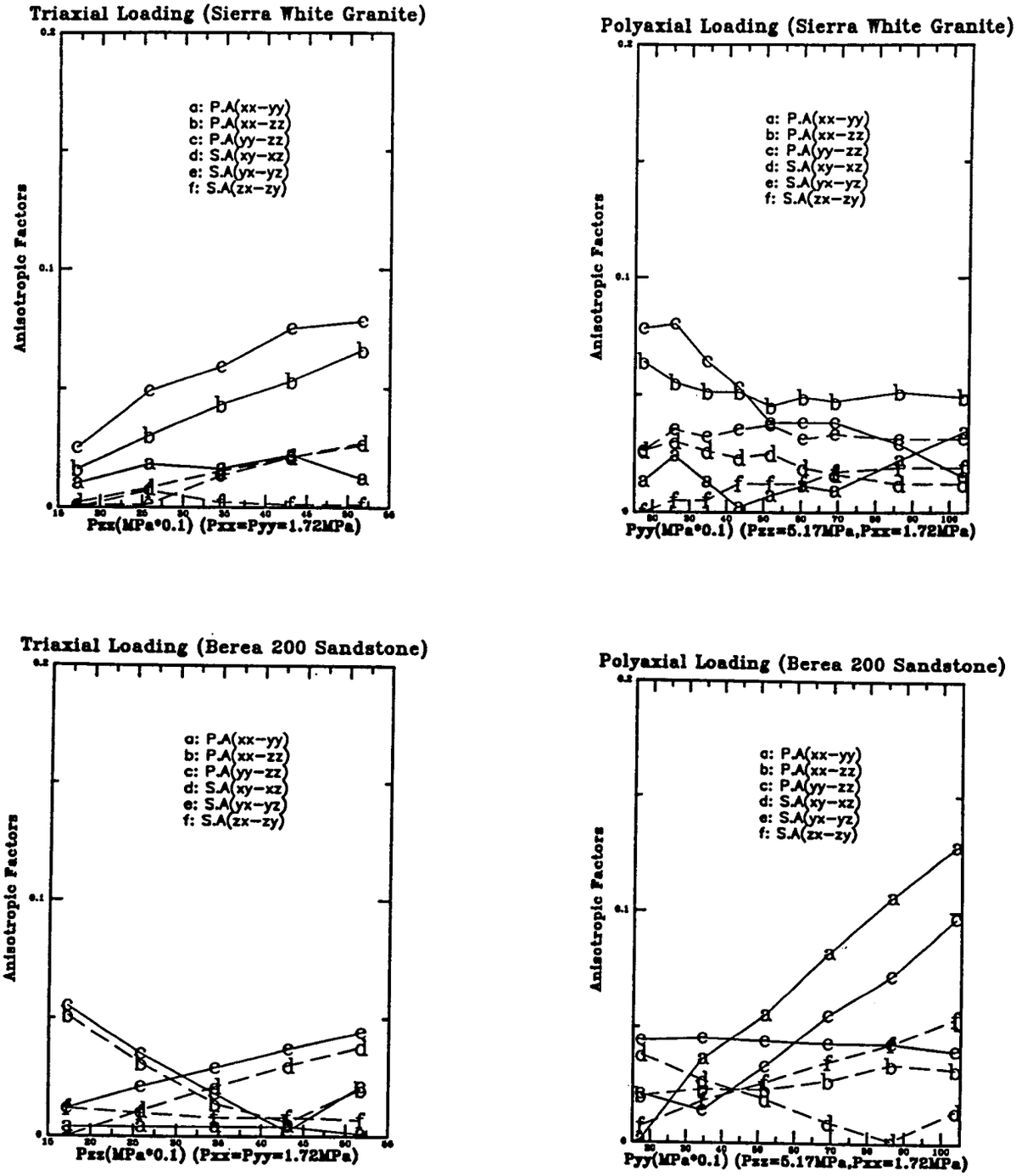

Figure 5.13: Anisotropic Factors of Sierra White Granite and Berea 200 Sandstone. The left column shows triaxial loading process, and the right column shows polyaxial loading process.

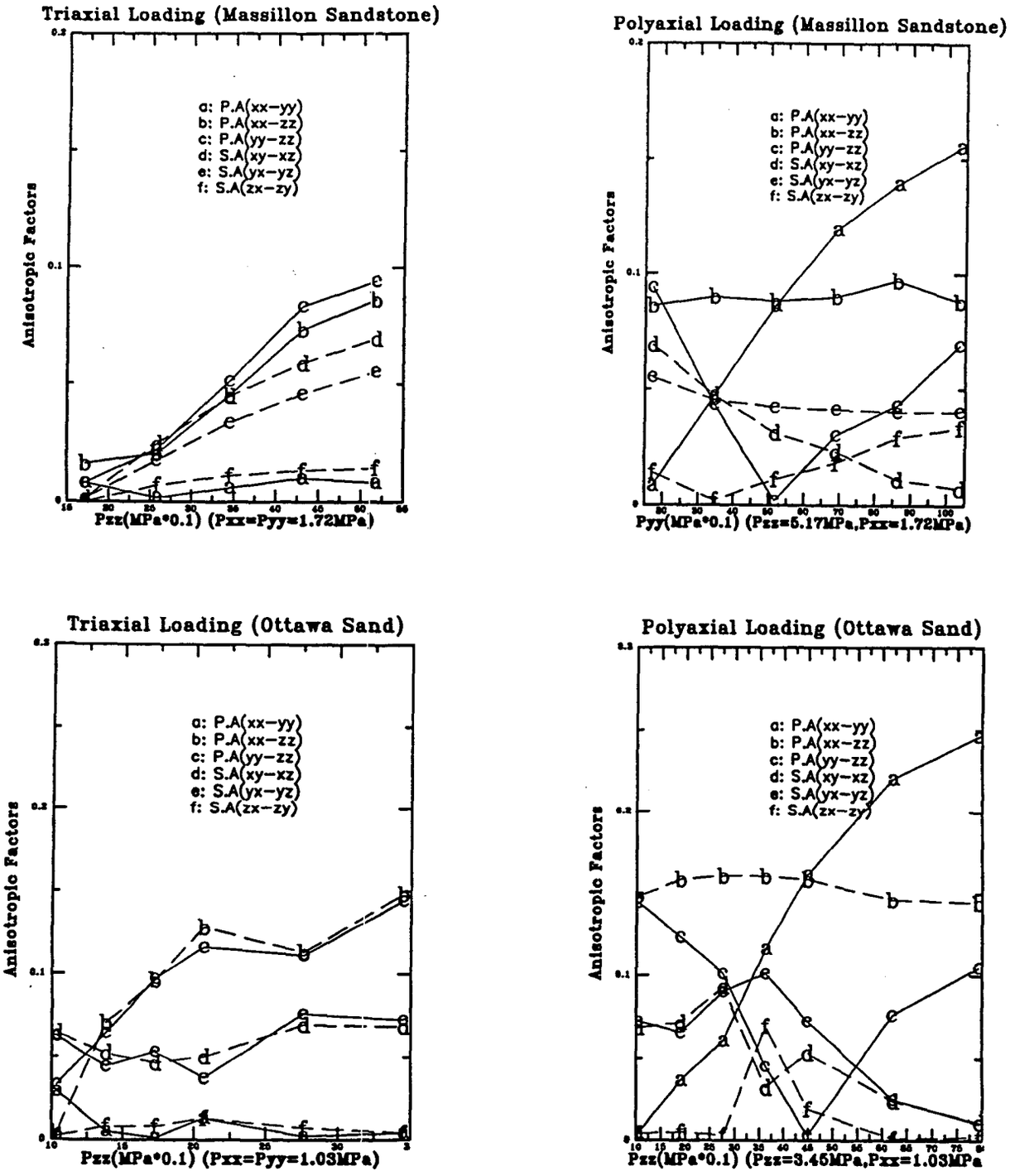

Figure 5.14: Anisotropic Factors of Massillon Sandstone and Ottawa Sand. The left column shows triaxial loading process, and the right column shows polyaxial loading process.

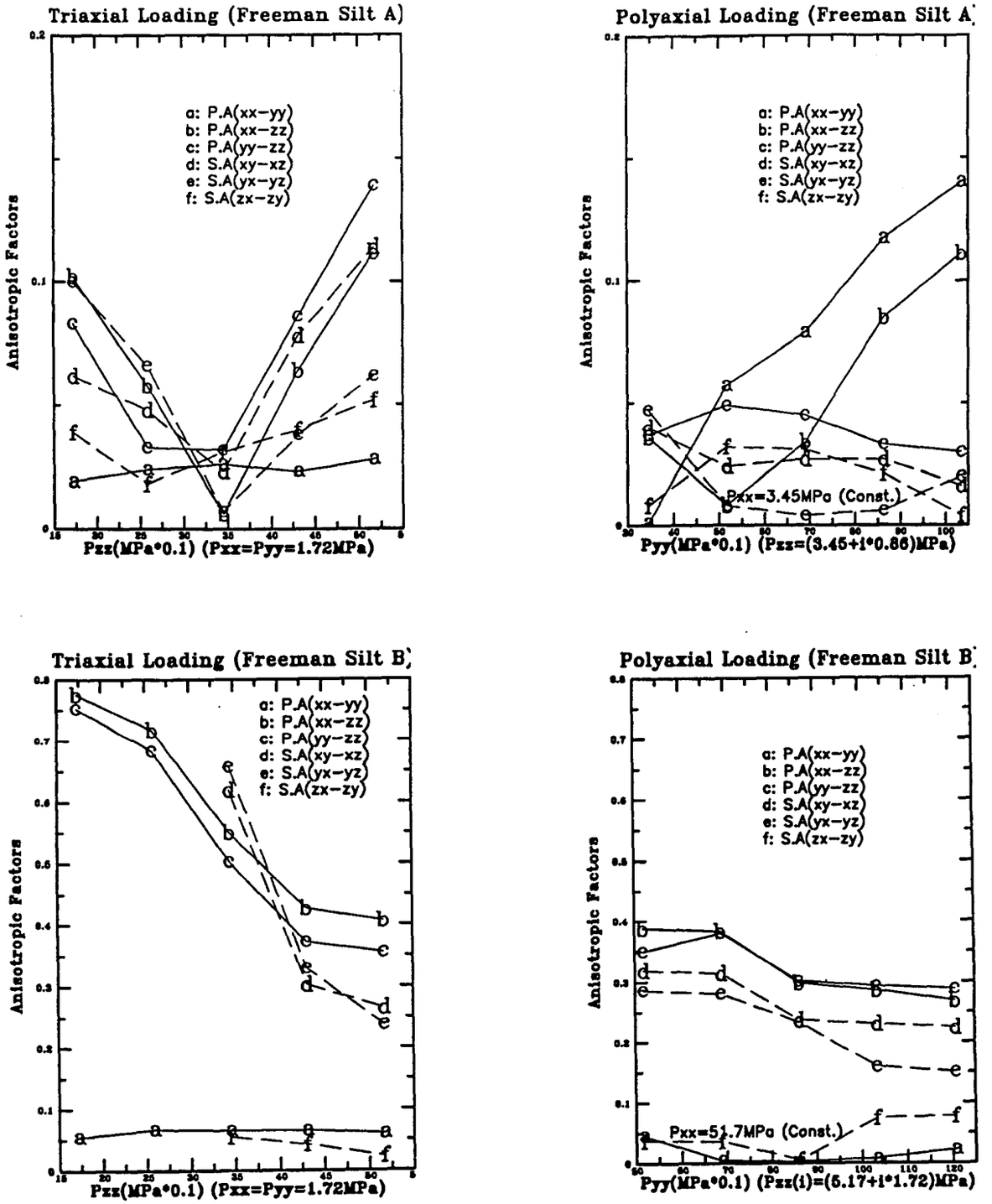

Figure 5.15: Anisotropic Factors of Freeman Silt A and B. The left column shows triaxial loading process, and the right column shows polyaxial loading process.

shaly sandstone, intrinsic anisotropy remains the dominant anisotropic nature over our limited range of loading stresses (Figure 5.12). For the intrinsically isotropic hard rocks, such as Sierra white granite, the stress may only introduce a few percent of anisotropy within the scope of our experiments' loading (Figure 5.13). Most granites have been considered as isotropic rocks, but recent work has shown that granite has a few percent anisotropy with orthorhombic symmetry (Sano et al., 1992). Such a week orthorhombic anisotropy was not clearly observed in our velocity measurement, but quite apparent in the amplitude domain as we will see.

For the intrinsically isotropic soft rocks, the stress-induced anisotropy ideally follows the stress patterns. Triaxially loaded stresses result in transverse isotropy, and polyaxially loaded stresses result in orthorhombic anisotropy (Figure 5.14). For the intrinsically transverse-isotropic soft rocks, the stresses may induce isotropy, reversed transverse isotropy, and orthorhombic anisotropy (Figure 5.15). These four type of rocks' anisotropic patterns are summarized in Figures 5.16 and 5.17.

5.4.3 Stress-induced and Intrinsic Attenuation Anisotropy

Several side-effects may cause failure of an attenuation measurement. The source of serious measurement errors may be one or more of the following.

- dispersion and diffraction within the sample,
- reflection and refraction within the boundaries of bedding layers,
- mode conversion and phase cancellation within the sample,
- coupling problems between sample and transducers,
- windowing effects on the time series prior to the frequency domain conversion.

The first three side effects, should they occur, result from the nature of the rock samples themselves. These effects are present to varying degrees in many different

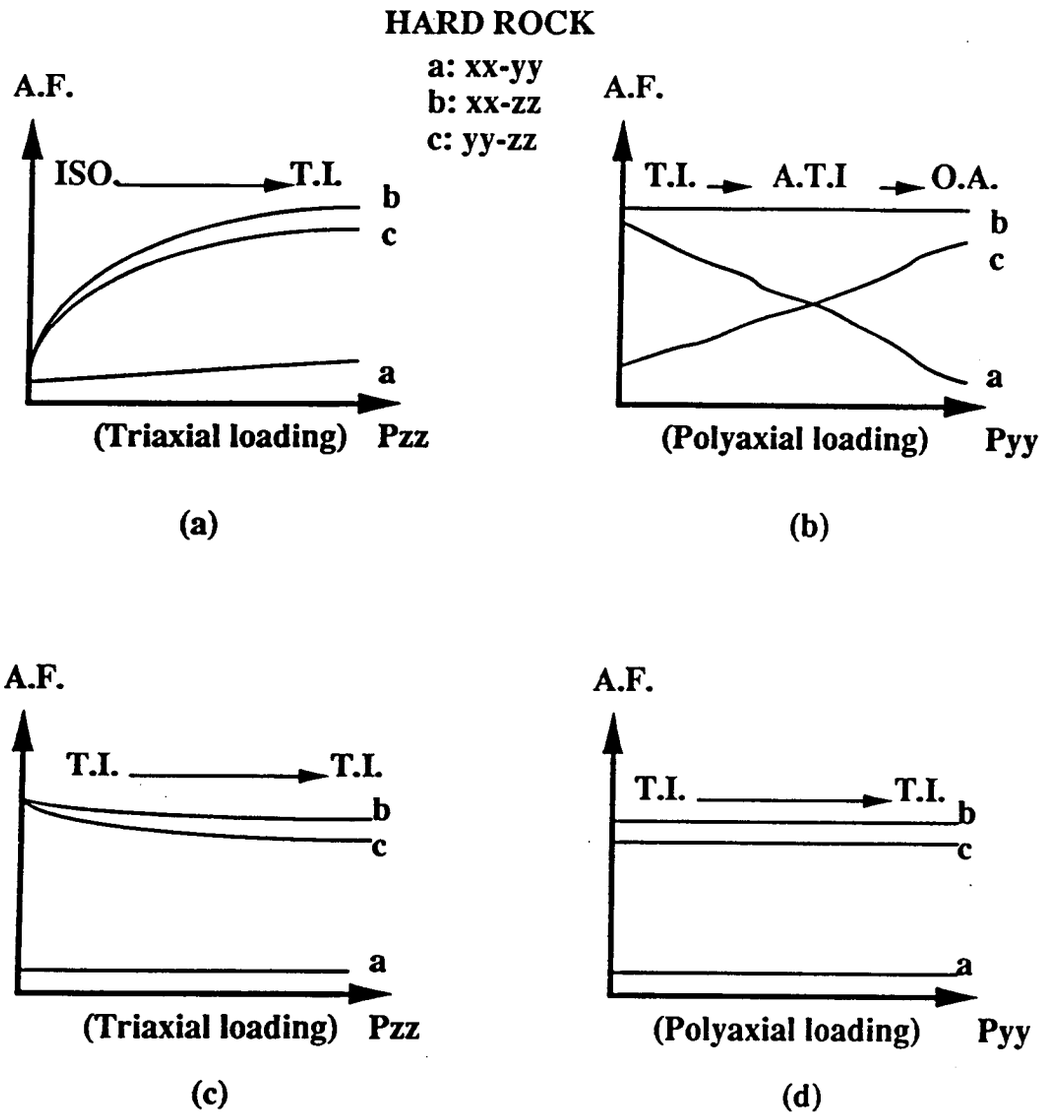

Figure 5.16: A summary of anisotropic factors of "hard rocks" associated with the stress state. The left column shows triaxial loading, and right column shows polyaxial loading.

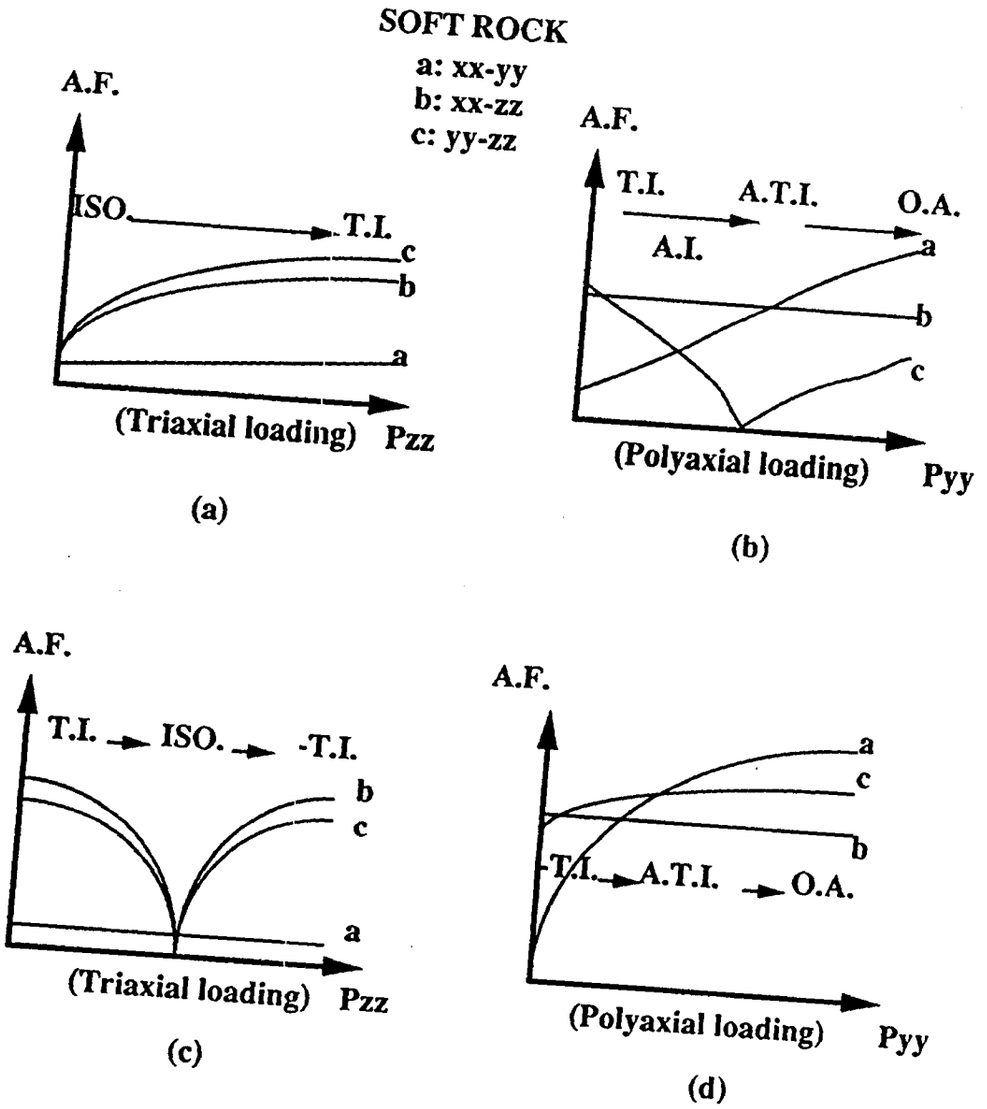

Figure 5.17: A summary of anisotropic factors of "soft rocks" associated with the stress state. The left column shows triaxial loading, and right column shows polyaxial loading.

rocks. Overall, these effects tend to become part of a rock's estimated intrinsic attenuation. The last two side-effects derive from the experiment, and can be minimized with proper design and consistent operation during the experiment.

We kept our experiment as consistent as possible throughout the eight samples measurements. The results of the Q_{ij} measurement show the differences among rocks, and the variations associated with the stress status may possess a certain significance.

A thin-layer couplant was carefully applied between sample and transducers. By measuring a reference aluminum cube with the same dimension as the rock samples, we found that wavelet amplitude was invariant with coupling force above 1.0 MPa. The wavelets recorded in the reference measurement were used in the spectral ratio calculation to minimize the geometric diffraction effect. Figure 5.18 shows the wavelets recorded during the reference measurement.

For each wavelet, the first two subscripts stand for the transmitter's wave propagation direction and polarization direction, and the last two subscripts stand for the receiver's wave receiving direction and polarization direction. For example, zz-zz stands for both transmitter and receiver aligned in the Z-direction observing a propagating wave polarized in the Z-direction, implying a compressional or P-wave. Waves transmitted in one polarization and received in another, like zx-zy etc. are "cross talks". We see that the energy of the cross talk is much smaller than the energy of the matched polarization wavelets, especially the mode conversions between P-wave and S-wave.

Attenuation Anisotropy in Time-domain

I have deliberately decided to present the results of attenuation here without any speculations upon the mechanism involved, since attenuation measurements are far more variable and a few actual mechanism involved are mostly subject to considerable debate.

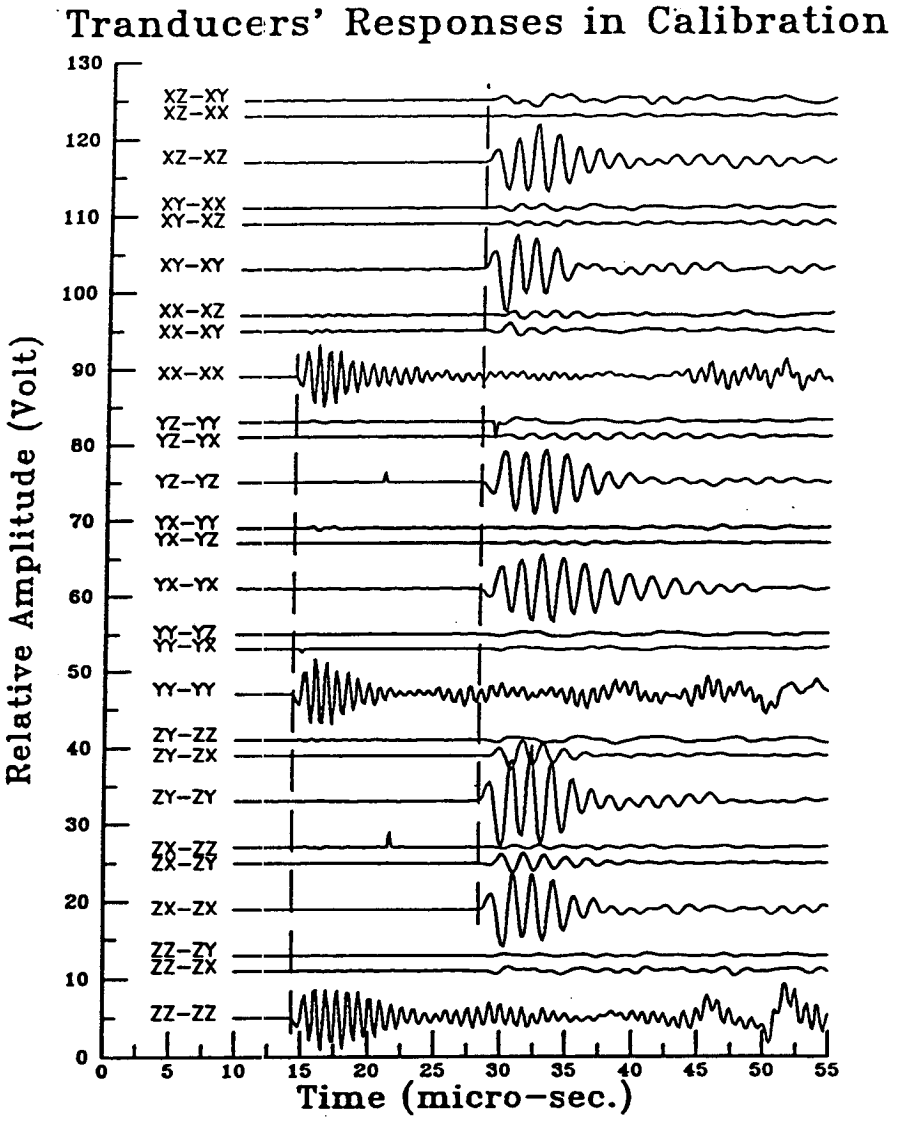

Figure 5.18: Time domain responses of the three pair of transducers. Wavelets were taken by measuring an aluminum cube block for the geometric diffraction corrections. Note that the "cross talks" have small energy compared with polarization-aligned wavelets.

Figures 5.19 and 5.20 show the wavelets in time domain at three-state of stresses, strong *wave-splitting* in the amplitude domain can be easily observed.

For Colorado Oil Shale and Colorado Shaly Sandstone, the sharp wave splitting in both the time and amplitude domains is strongly depended on the samples' intrinsic anisotropic properties. All wave amplitudes, either those propagating along or polarized toward the z-direction normal to bedding plane, show significant increases under triaxial loading. The velocity of waves traveling along the bedding planes, as in the $X - Y$ plane, is almost independent of stress. Stress-induced amplitude changes can be much more readily observed than do the stress-induced arrival time changes, the stress-induced velocity changes. The amplitudes of these waves show far greater sensitivity to stress applied, perhaps due to crack closure with increased pressure. Attenuation estimate may be a more sensitive measure to detect cracks in rocks (Figure 5.19-a and 5.19-b).

For the Massillon sandstone (Figure 5.20-a), we can see the amplitude of the wavelets increasing as a directional stress increased—whether the waves propagating along or the waves polarized toward the direction of stress increased all raised considerably. Wave amplitude variations associated with the stress state closely follow triaxial and polyaxial loading.

For the Berea 200 sandstone and Sierra white granite samples, wavelet amplitudes show that these two rock may have intrinsic orthorhombic attenuation anisotropy. Small cracks in the $Y - Z$ plane, and the cracks in $X - Z$ plane in the Sierra white granite sample are observed by different pair of transducers in two principal directions. Similarly, not only the crack and bedding layer in the $X-Y$ plane, but also crack in the $X-Z$ plane are observed by different pair of transducers in different directions (Figure 5.19-c and Figure 5.20-a). This is strong evidence that such amplitude differences in the experiments are due to the sample's intrinsic attenuation nature, rather than experimental error, such as coupling differences.

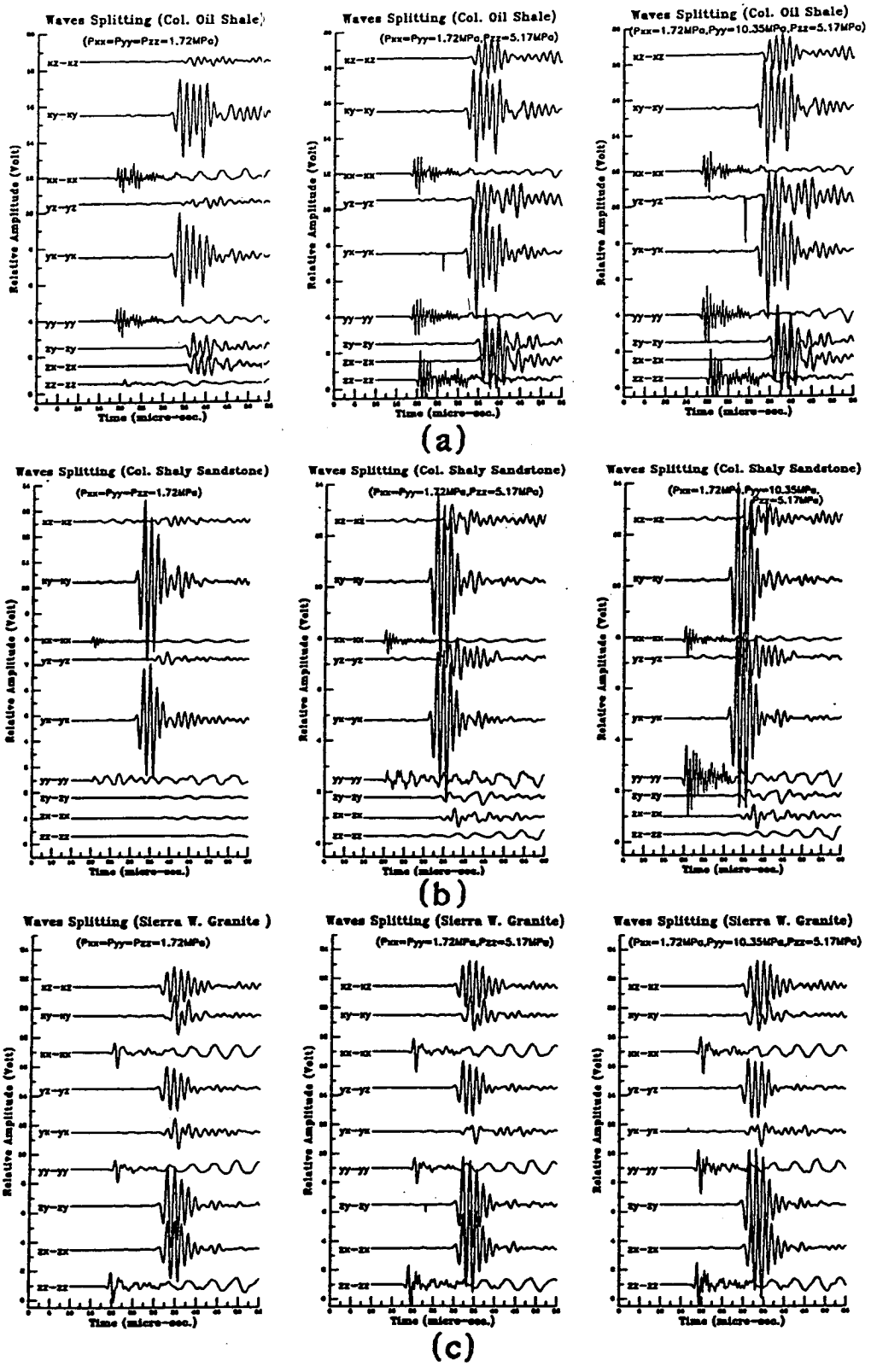

Figure 5.19: Time domain responses of the Colorado Oil Shale, Colorado Shaly Sandstone and Sierra White Granite. Striking shear wave splitting in the bedding plane (X-Y plane) can be clearly observed in (a) and (b). Stress-induced amplitude variations are only observable in the ZZ direction while its time lag or velocity stress-dependence may be neglected.

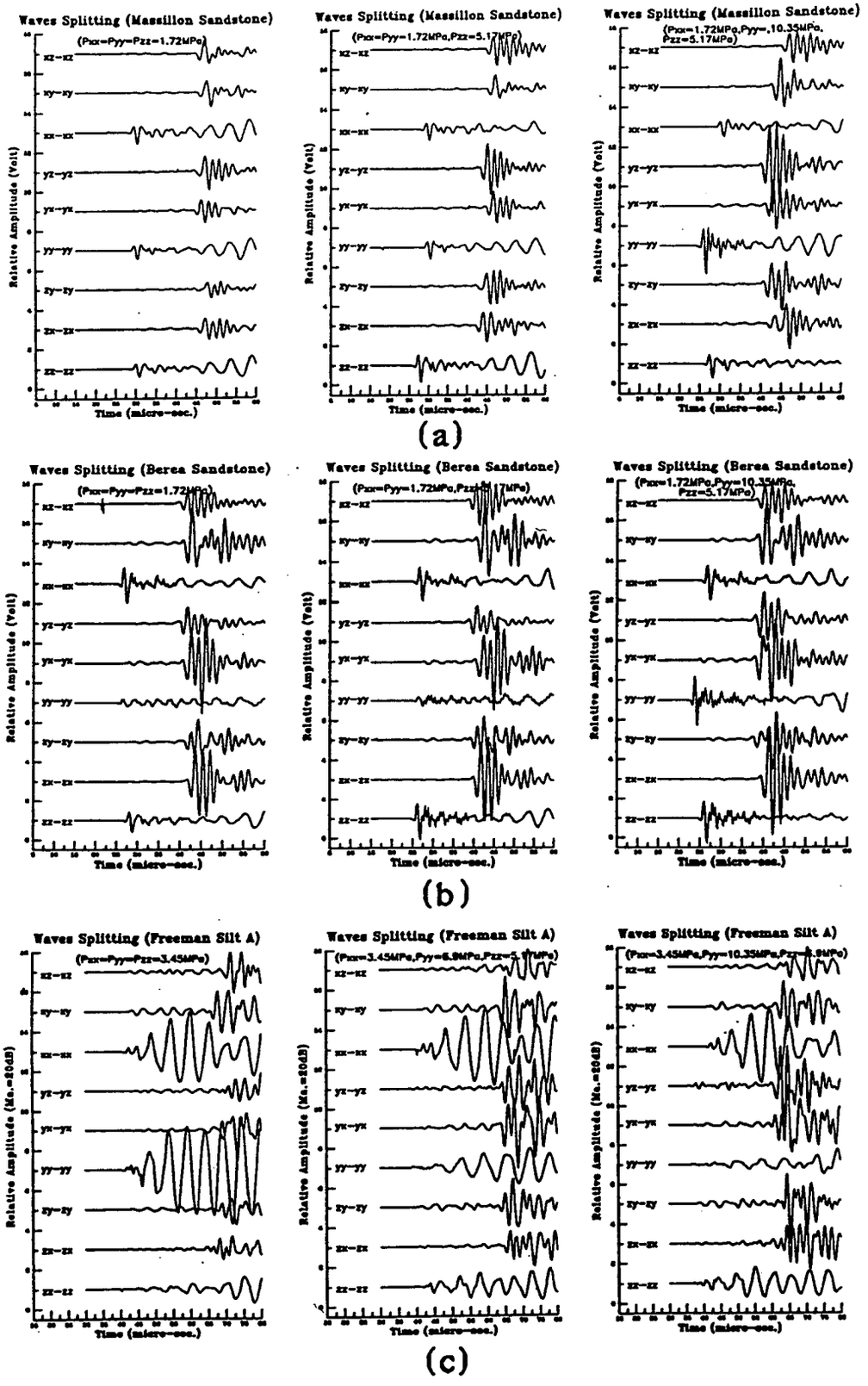

Figure 5.20: Time domain responses of the Massillon Sandstone, Berea 200, and Freeman Jewett Silt-A. Wave amplitude splitting associated with stress states can be clearly observed.

For the Freeman Shale samples, the amplitude information may be not valid because of severe mode-conversion and diffraction.

Attenuation Anisotropy in Frequency Domain—α_{ij} and Q_{ij}

We made the reflection coefficient correction as those have been done for the pulse-echo method in nondestructive evaluation (Papadakis, 1990). This correction may be significant to our low velocity samples. The reflection coefficient could be calculated from the acoustic impedance of aluminum end-platens and the impedance of sample under a certain state of stress.

Windowing in time domain can have an important effect on the computed values of the attenuation coefficient. If $A_r(\omega)$ and $A_s(\omega)$ are the Fourier spectrum of the wavelets by reference measurement and sample measurement respectively, and $W(\omega)$ is the Fourier spectrum of the windowing function, then, the time domain windowing may be expressed as frequency domain convolution.

$$\frac{|A_r(\omega) * W(\omega)|}{|A_s(\omega) * W(\omega)|} = \frac{A_r(\omega)}{A_s(\omega)} \frac{\left|[S(\omega)e^{i\phi(\omega)}] * [e^{-\alpha_s(\omega)L}W(\omega)]\right|}{|S(\omega) * W(\omega)|} \tag{5.13}$$

where $S(\omega)$ is Fourier spectrum of the transducer. Windowing makes the attenuation coefficient take the form

$$\alpha_s(\omega) = \frac{20}{L}\log_{10}\left[\frac{A_r(\omega)}{A_s(\omega)}(1-R^2)\right] + \frac{20}{L}\log_{10}\frac{\left|[S(\omega)e^{i\phi(\omega)}] * [e^{-\alpha_s(\omega)L}W(\omega)\right|}{|S(\omega) * W(\omega)|}. \tag{5.14}$$

The last term in this equation may be considered to be the windowing effect. Three types of windows were tested. The results are shown in Figure 5.21. I used a rectangular window throughout our data processing because it is easy to apply, and I chose one and half cycle as the window width, because the theoretical pulse response of the transducers was designed to vibrate only one and half cycles.

Figure 5.22 shows an example of the wave attenuation spectra via reference calibration measurement and Massillon Sandstone measurement. Note how the attenuation

coefficients vary with the stress status (Figure 5.22-c).

With the assumption of constant Q, Q_{ij} were calculated by linear square fitting to the slopes of the attenuation coefficients, and the estimates of α_{ij} from each fit were limited to within $\pm 0.2MHz$ of the peak frequency in its spectrum. The results are given in Table 5.3.

The stress normal to the Colorado Oil Shale's bedding plane has significant effects in changing its intrinsic attenuation anisotropic patterns. This implies that attenuation may be more sensitive to the closing of cracks than to elastic stiffness. The sample's attenuation anisotropic pattern seems to have the same symmetry as its elastic constants c_{ij}. The Q_{ij} variation along with the loading pattern changed in Massillon Sandstone is clear evidence of stress-induced attenuation anisotropy. The triaxial loading induced a transversely isotropic attenuation symmetry, and polyaxial loading of the sample induced an orthorhombic attenuation symmetry (Figure 5.23).

5.5 Discussion

5.5.1 Stress and Velocity Anisotropy

Dynamic acoustic or seismic measurement has been widely used as a means of estimating in-situ stress. Multi-component acoustic logging, VSP, and cross-well logging techniques all are used in studies of in-situ stresses, regardless of stress distribution complexity in the borehole environment (Barton and Zoback, 1988). We limit here our discussion only to laboratory measurements. The possibilities for flied use are subject to individual interpretation and imagination.

From Roesler (1979), shear wave velocity depends on stresses as

$$V_{ij} = cP_i^a P_j^b P_k^0;\ (i \neq j \neq k) \tag{5.15}$$

where the stress component, P_i^a is in the direction of S-wave propagation, P_j^b is in the direction of S-wave polarization, and P_k^0 is orthogonal to P_i^a and P_j^b, and V_{ij} is

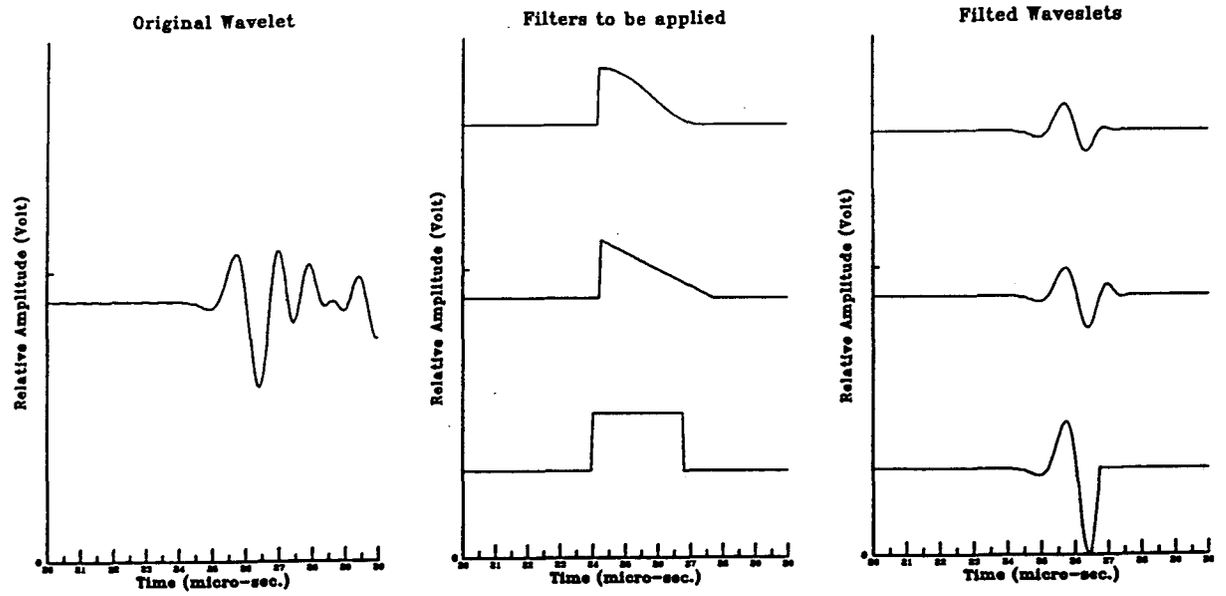

(a)

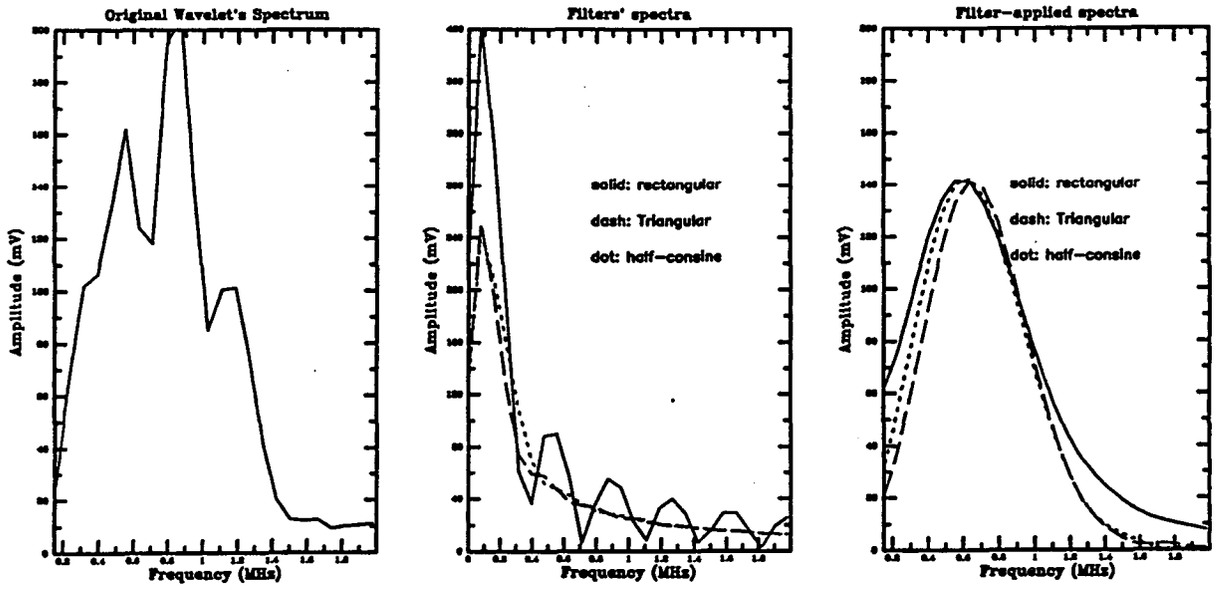

(b)

Figure 5.21: (a) Windows tested in time domain, (b) Frequency domain responses. Time domain applied window has a convolution relation in frequency domain.

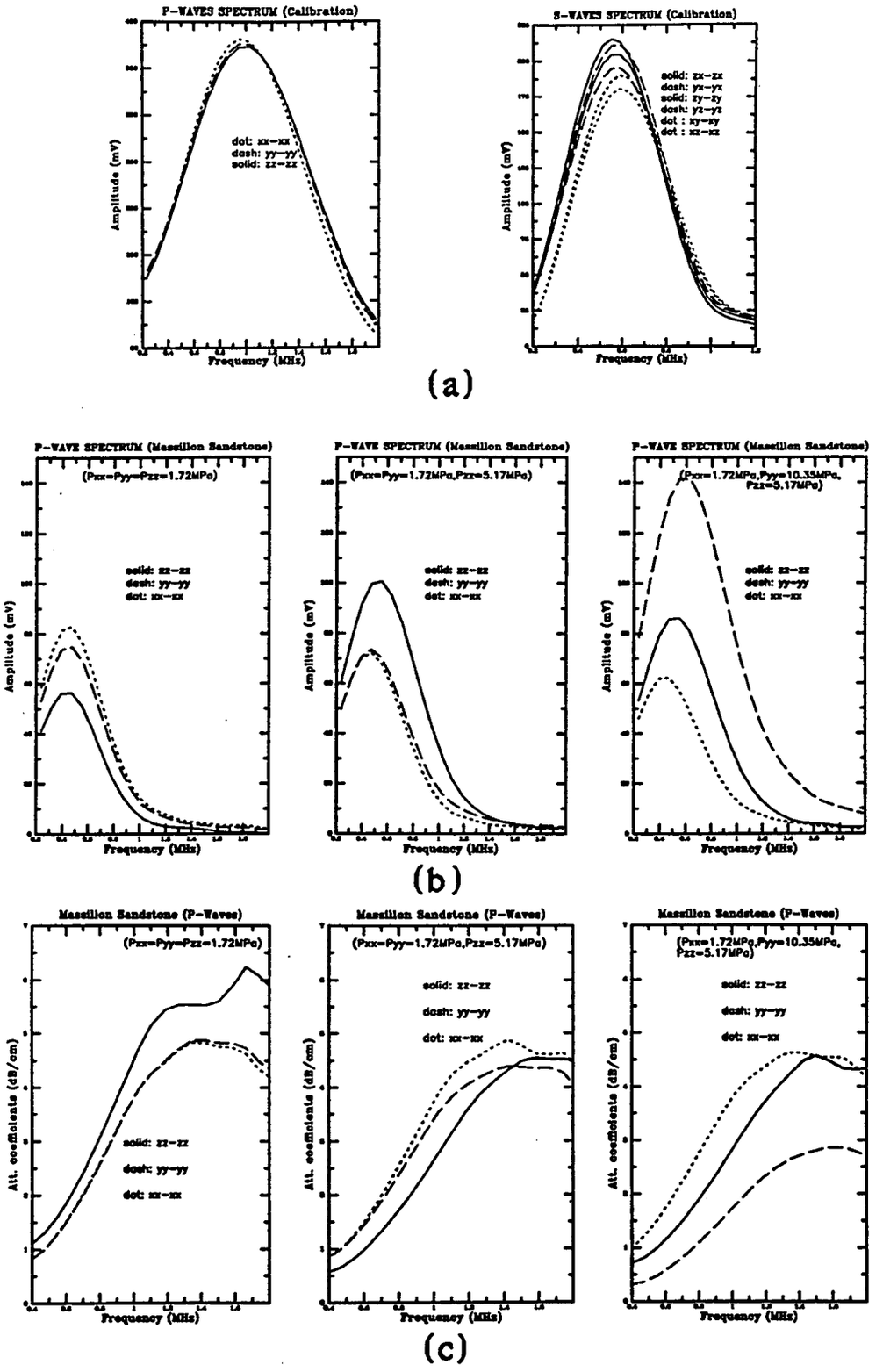

Figure 5.22: (a) Frequency spectra of three pair of transmitter and receiver under aluminum cube calibration measurement, (b) P-wave frequency spectra of Massillon sandstone, (c) Attenuation coefficients calculated.

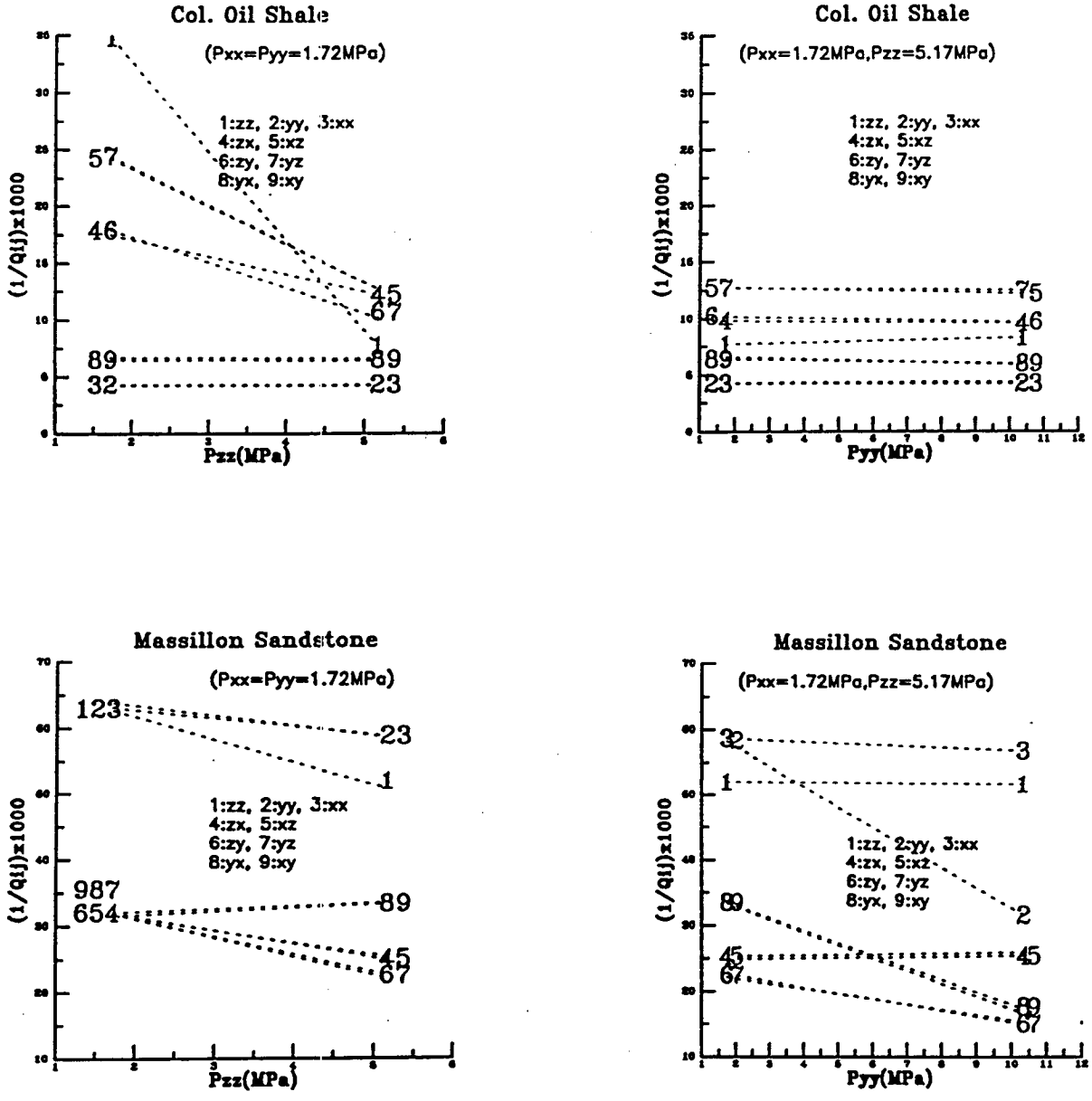

Figure 5.23: $1000/Q_{ij}$ with constant Q assumption. The left column shows triaxial loading process, and right column shows polyaxial loading process.

shear waves propagating to i–direction and polarizing to j–direction.

Data from this experiment show that S-wave velocity depends about equally on the principal effective stresses in the directions of wave propagation and of particle polarization, and very little on the third principal stress component. The magnitude of stress-induced S-wave anisotropy is less than the magnitude of stress-induced P-wave anisotropy. Therefore, P-wave anisotropy may be a more dependable indicator of underground stress patterns than S-wave anisotropy.

Our loading process may be analytically expressed as

$$\begin{cases} P_{xx} = c_{11}\varepsilon_{xx} + c_{12}\varepsilon_{yy} + c_{13}\varepsilon_{zz} \\ P_{yy} = c_{12}\varepsilon_{xx} + c_{22}\varepsilon_{yy} + c_{23}\varepsilon_{zz} \\ P_{zz} = c_{13}\varepsilon_{xx} + c_{23}\varepsilon_{yy} + c_{33}\varepsilon_{zz} \end{cases} \tag{5.16}$$

where ε_{ij} are the compressional strains.

If we may neglect the isotropic initial stress-induced strains, e.g. $\varepsilon_{xx} = \varepsilon_{yy} = 0$, we have the following simple relations between "vertical stress" P_{zz} and "horizontal stress" P_{xx} (or P_{yy}), and stiffness constants c_{ij} as

$$\begin{cases} P_{zz}/P_{xx} = c_{33}/c_{13} \\ P_{zz}/P_{yy} = c_{33}/c_{23} \end{cases} \tag{5.17}$$

Under these conditions, our loading may be modeled as a "uniaxial strain test". At the triaxial loading, we have stress ratio $P_{zz}/P_{xx} = P_{zz}/P_{yy} = 5.17MPa/1.72MPa = 3.01$, and we found that $c_{33}/c_{13} = 4.8$ from Massillon Sandstone. This suggests a relative error of stress prediction via dynamic moduli of some 35%. The error may result from errors in c_{13} estimation, but more likely it is the result of neglecting the horizontal strain as zero, $\varepsilon_{xx} = \varepsilon_{yy} = 0$. Under the polyaxial loading state, P_{yy}/P_{xx} is higher than P_{zz}/P_{xx}, and the resulting value of c_{33}/c_{13} is much closer to the actual applied stress ratio.

Despite the inescapable difference between static and dynamic moduli, we may retain the technique of the stress states from dynamic moduli estimates as a means of estimating the ratio of horizontal stress to vertical, or the ratio of the two orthogonal

horizontal stresses, if only we can measure ε_{xx}, ε_{yy}, and ε_{zz} with LVDT or other sensors, rather than assuming that the horizontal strains are identically zero. The results may enhance a possibility that P-wave anisotropy may someday predict the in-situ stress ratios that control hydrofracturing.

5.5.2 Attenuation Anisotropy and Stress States

Is Q_{ij} really such a big deal? The absolute value of attenuation factor Q may be totally neglected in seismic modeling, however, the anisotropic attenuation factors Q_{ij} may deserve a special attention. Considering this experiment's amplitude domain, we did see striking examples of wave splitting caused by both intrinsically anisotropic rocks and by anisotropic stresses. Why, with this, have seismologists successfully ignored wave splitting in amplitude domain for so long? Again, I limit my discussion here to analysis of our laboratory observations rather than including commonly observed wave-splitting in amplitudes through VSP or cross-well surveys nowdays.

I tested a "pseudo-hodogram" method to visualize wave amplitude splitting. The pseudo nature of our hodograms stems both from a shifting of the time lags between any two wavelets that are plotted against each other, and also from a focus on visualization of the wave amplitude ratio associated with the stress ratio, not the particle polarization direction[4] alone.

The tangent of the angle in the "pseudo-hodogram", after a time lag shift, is a measure of amplitude ratio, $\theta = tan^{-1}(A_1/A_2)$. The time lag between two wavelets was caused by velocity anisotropy. Figures 5.24 and Figure 5.26 display these hodograms. We clearly observe the angle changes associated with stress state changes in Massillon Sandstone samples. In Colorado oil shale samples, the angles show no stress dependency except in the Z-direction, which is the direction perpendicular the shale bedding plane.

[4]The particle polarization direction of each P-wave and S-wave was set by the configuration of the transducers, ignoring mode conversion.

Each pair of wavelets plotted against each other may be expressed as $A_1 = A_o e^{-\alpha_1 L} sin(\omega - \phi_o)$ and $A_2 = A_o e^{-\alpha_2 L} sin(\omega - \phi_j)$. If we neglect the phase difference after the time lag shift, and take the natural log of the ratio $A_1/A2$, then we have

$$\ln\left(\frac{A_1}{A_2}\right) = \ln\left(\frac{e^{-\alpha_1 L}}{e^{-\alpha_2 L}}\right) = (\alpha_2 - \alpha 1)L \tag{5.18}$$

We calculated this amplitude ratio for P-waves in three principal directions, A_{yy}/A_{xx}, A_{zz}/A_{xx}, and A_{yy}/A_{zz}, and also for each pair of orthogonally polarized S-waves in three principal directions, A_{xy}/A_{xz}, A_{yz}/A_{yx}, and A_{zy}/A_{zx}.

We found that the natural log amplitude ratio has a valid relation to the applied anisotropic stress states for the isotropic Massillon Sandstone, and the relation has the following from.

$$\ln\left(\frac{A_1}{A_2}\right) = 0.64 \ln\left(\frac{P_1}{P_2}\right). \tag{5.19}$$

We found that this form is valid for both the triaxial and the polyaxial loading states with an absolute error less than 0.1 (Figure 5.26).

For rock with intrinsic anisotropic attenuation, like Colorado oil shale, we find that the relation between the amplitude ratio and stress ratio looks like

$$\ln\left(\frac{A_1}{A_2}\right) = 1.94 \ln\left(\frac{P_1}{P_2}\right) + 2.1 \tag{5.20}$$

for P-waves, and

$$\ln\left(\frac{A_1}{A_2}\right) = \ln\left(\frac{P_1}{P_2}\right) + 2.1 \tag{5.21}$$

for S-waves (Figure 5.26).

In general, the relation between wave amplitude ratio and stress ratio may be expressed as

$$a \ln\left(\frac{A_1}{A_2}\right) = b \ln\left(\frac{P_1}{P_2}\right) + c \tag{5.22}$$

where a, b and c are constants that depend on the rock's intrinsic anisotropy.

The simplicity of these relations implies that accurate field estimates of wave attenuation could be used to quantitatively infer the in-situ stress anisotropy. Wave amplitudes may provide a more sensitive and potentially reliable measure of intrinsic anisotropy and stress-induced anisotropy than does wave velocity alone.

5.6 Conclusion

We have observed and modeled several examples of wave velocity anisotropy in rock samples. The soft rocks exhibited stress-induced anisotropy, while the hard rocks had such a state frozen into them, and they exhibited intrinsic transverse isotropy even under polyaxial loading. From our laboratory observations, we think that crack closure along the direction of increasing stress is the primary cause of this effect. We believe that intrinsic wave velocity anisotropy results mostly from preferred grain orientations, systems of micro-cracks in parallel planes, and interbeded fine clay layers.

Among rocks with anisotropic stress-induced wave velocity anisotropy, the observations of P-waves are more diagnostic than the observations of S-waves. This responsiveness and larger magnitude variation with changes in stress results from the sensitivities of P-wave mainly to longitudinal compressional stress (along the wavefront path). S-waves depend about equally on the longitudinal and transverse compressional stresses in the sense of wave propagation and polarization, and so show a convolved response to anisotropic stresses. A third principal stress parallel neither to an S-wave propagation direction nor to its polarization direction has only a negligible effect on the S-wave.

Soft rocks display greater sensitivity to anisotropic stresses than do hard rocks. Anisotropic factors of soft rocks are more stress-dependent than those of hard rock.

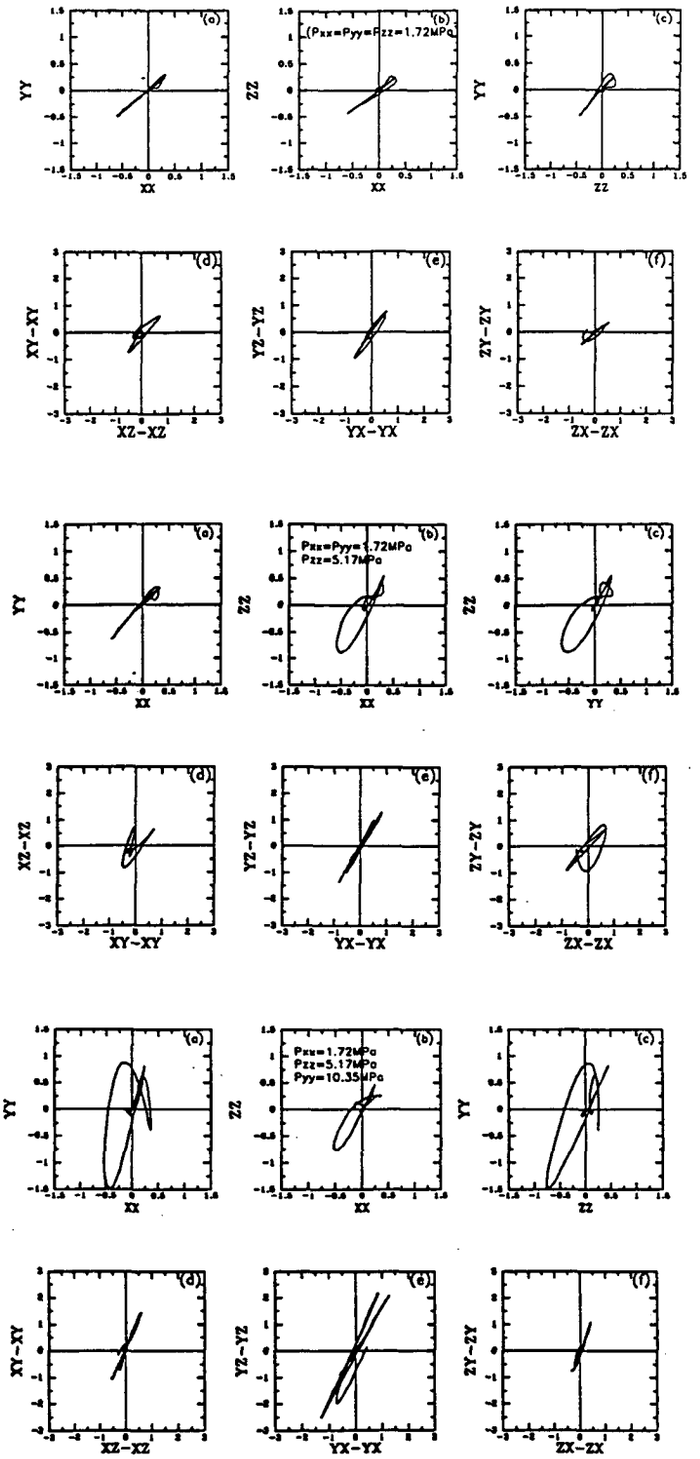

Figure 5.24: "Pseudo-hodogram" from Massillon Sandstone measurements. The top six "hodograms" are from isotropic loading, the mid-six are from triaxial loading, and the bottom-six are from polyaxial loading.

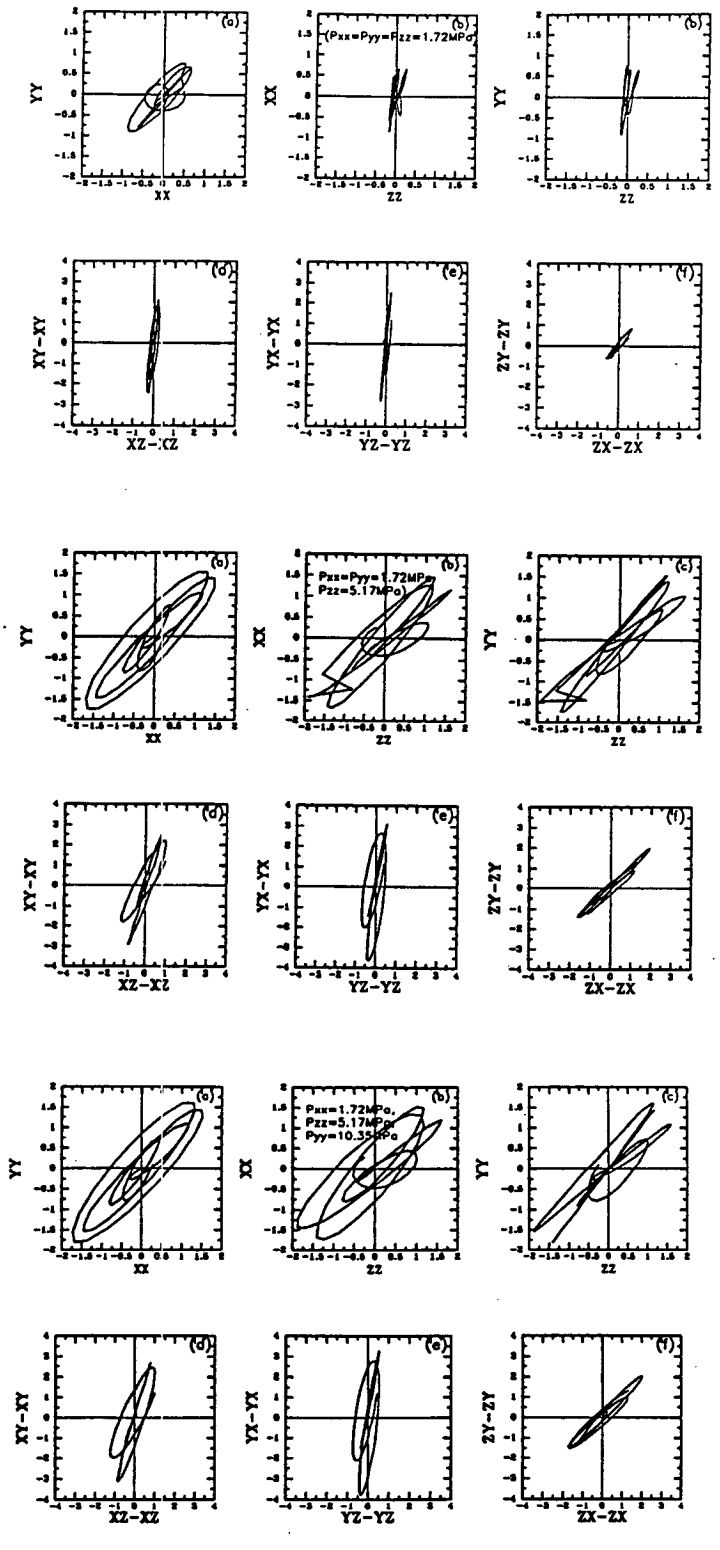

Figure 5.25: "Pseudo-hodogram" from Colorado Oil Shale measurements. The top six "hodograms" are from isotropic loading, the mid-six are from triaxial loading, and the bottom-six are from polyaxial loading.

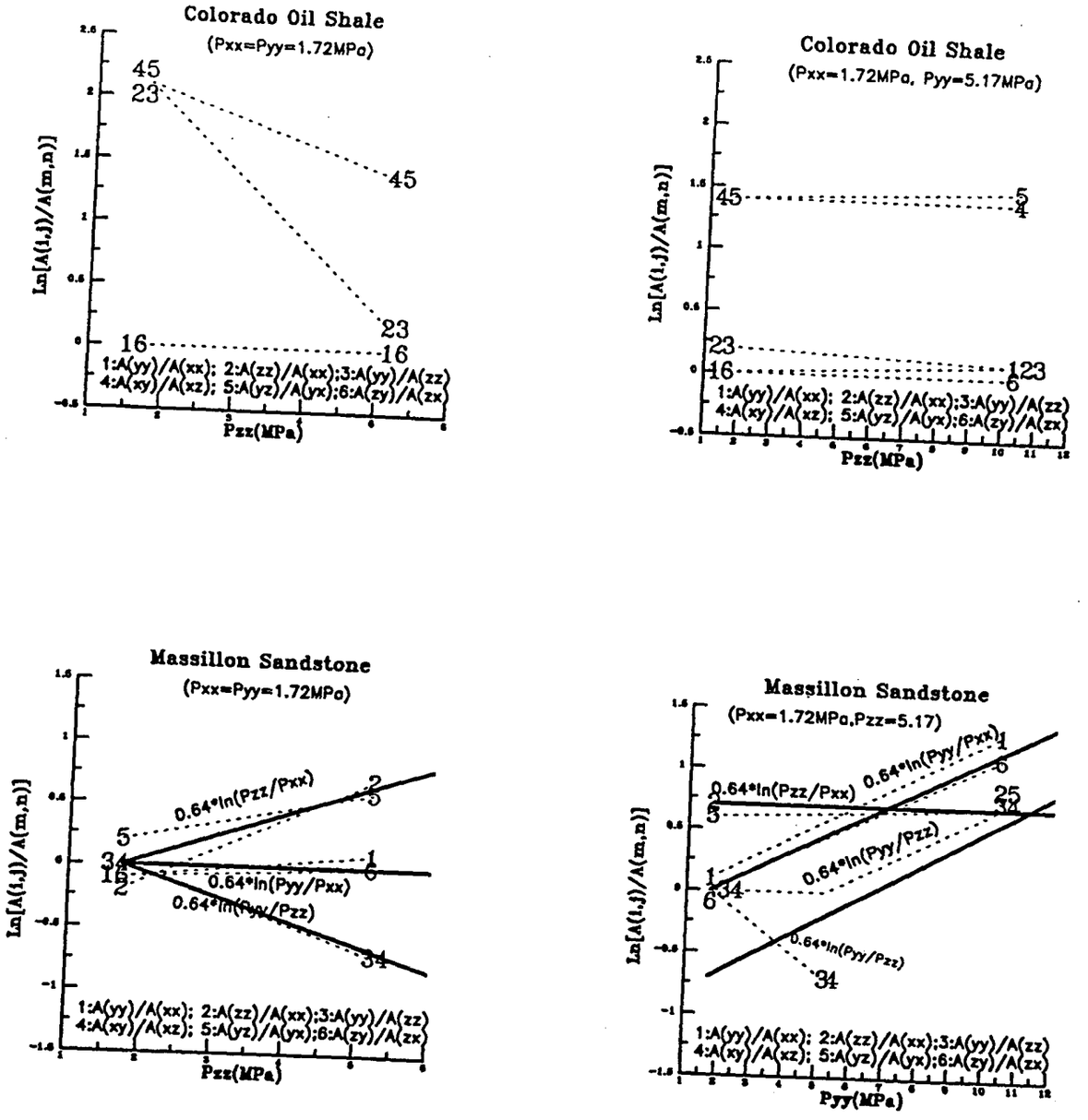

Figure 5.26: Hodogram logarithmic amplitude ratio. The left column displays the triaxial loading, and right column displays polyaxial loading.

This result is theoretically expected because soft rocks have higher Poisson's ratio than do hard rocks. They are also more compressible than hard rocks, and the resulting strain can be expected to rearrange grain contacts. Hence, at a shallow depth of burial, the stress-induced wave anisotropy may be more a characteristic of soil and soft rock than it is in well consolidated outcrops.

Wave attenuation anisotropy appears to reflect the symmetries of wave velocity anisotropy. Patterns of attenuation anisotropy in Colorado Oil Shale and Massillon Sandstone show that attenuation quality factors Q_{ij} have the same anisotropic symmetry as do these sample's elastic stiffnesses c_{ij}. Some important differences may be found between the magnitudes of viscoelastic attenuation anisotropy (Q_{ij}) and elastic wave velocity anisotropy (c_{ij}). Attenuation anisotropy may be more sensitive to cracks and stress than does wave velocity anisotropy—thus we may expect that shear wave splitting may be more readily observed in the amplitude domain than in the velocity domain. The results of this empirical effort suggests that amplitude information may become an important tool for estimates of in-situ stress anisotropy. If data acquisition techniques permit, amplitude anisotropy observation may some day soon become a preferred technique for field estimates of anisotropic stress states. The The absolute value of wave attenuation, Q^{-1} may be neglected in seismic modeling, however, the anisotropic attenuation factors Q_{ij}^{-1} should be considered as serious factors in anisotropic seismic wave modeling.

Several important questions remain to challenge investigators, particularly the nature or the mechanism of attenuation anisotropy. Truly, anisotropy requires further research—it should be fruitful.

Reference

Alford, R. M., 1986, Shear data in the presence of azimuthal anisotropy, 56th Ann. Internat. Mtg., Soc. Expl. Geophysics, Expanded abstracts, 476-479

Banick, N., 1987, An effective anisotropy parameter in transversely isotropic media, Geophysic, Vol. 44, 910

Benson, G. C., and Kiyohara, O., 1973, Tabulation of some integral functions describing diffraction effects in the ultrasonic field of a circular piston source, J. Acoust. Soc. Am., Vol. 55, No. 1, 184-185

Birch, F., and Bancroft, D., 1938, Elasticity and internal friction in a long column of granite, Bull. Seism. Soc. Am., 38, 243-254

Breckels, I. M. and Eekelen, H. A. M., 1982, Relationship between horizontal stress and depth in sedimentary basin, J. Pet. Tech., 2,191-2,199

Breazeale, M. A., Cantrell J. H. and Heyman J. S., 1981, Ultrasonic wave velocity and attenuation measurements, Method of Experimental Physics, Vol. 19, (Ultrasonic), Edited by Edmonds, P. D., Academic Press, Inc. 67-137

Brown, E. T. and Hoek, E., 1978, Trend in relationships between measured in-situ stresses and depth, Int. J. Rock. Mech. Min. Sci. and Geomech. ABstr. Vol. 15, 211-215

Crampin, S., 1984, An introduction to wave propagation in anisotropic media, Geophys. J. R. astr. Soc., 76, 17-28

Gordon, R. B., and Davis, L. A., 1968, Velocity and attenuation of seismic waves in imperfectly elastic rock, J. Geophys Res., v.73, 3917-3935

Engelder, T. and Sbar, M., 1984 Near-Surface in Situ Stress, JGR, Vol. 89, No. B11, 9321-9370

Hess, H., 1964, Seismic anisotropy of the uppermost mantler under ocean, Nature, 203, 629-631

Hosten, B., Deschamps, M. and Tittmann, B.R., 1987, Inhomogeneous wave generation and propagation in lossy anisotropic solids. Application to the characterization of viscoelastic composite materials, J. Acoust. Soc. Am., Vol. 82, No. 5, 1763-1770.

Hudson, J. A., 1981, Wave speeds and attenuation of elastic waves in material containing cracks, Geophys. J. R. Astron. Soc. 64, 133-150

Jaeger, J. C. and Cook, N. G. W., 1979, Fundamentals of Rock Mechanics, 3rd ed., Chapman and Hall

Kaarsberg, E. A., 1968, Elastic studies of isotropic and anisotropic rock samples, Trans. Am. Inst. Min. Metallurg. Eng., 241

Klimentos, T., Geometric corrections in attenuation measurement, Geophysical Prospecting, **39**, 193-218

Lo, T. W., Coyner, K. B. and Toksöz, 1986, Experimental determination of elastic anisotropy of Berea sandstone, Chicopee shale, and Chelmsford granite, Geophysics, 51, 164-171

Lynn, H. B., and Thomsen, L. A., 1986, Reflection shear-wave data along the principal axes of anisotropy, 56th Ann. Internat. Mtg., Soc. Expl. Geophysics, Expanded abstracts, 473-476

McGarr, A., 1988, On the state of lithospheric stress in the absence of applied tectonic forces, J. Geophys. Res., Vol. 93, No. B11, 13,609-13,617

Musgrave, M. J. P., 1980, On an elastodynamic classification of orthorhombic media, Proc. R. Soc. Lond. A, 374, 401-429

Norris, A. N., 1989, On the acoustic determination of the elastic moduli of anisotropic solids and acoustic conditions for the existence of symmetry planes, Q. J. Mech. Appl. Math., Vol. 42, Pt.3, 413-426

Nur, A., and Simmons, G., 1969, Stress-induced velocity anisotropy in rocks: An experimental study, J. Geophys. Res., 74, No.27, 6667-6674

Nur, A., 1971, Effects of stress on velocity anisotropy in rocks with cracks, J. Geophys. Res., Vol. 76, No. 8, 2022-2034

Papadakis, E. P., 1990, The measurement of ultrasonic Velocity, in *Ultrasonic Measurement Methods*, edited by R. N. Thurston and A. D. Pierce, Physical Acoustics, Vol. XIX, 81-107

Papadakis, E. P., 1990, The measurement of ultrasonic Attenuation, in *Ultrasonic Measurement Methods*, edited by R. N. Thurston and A. D. Pierce, Physical Acoustics, Vol. XIX, 108-156

Pyrak-Nolte, L., Myer, L. R. and Cook, N. G. W., 1990, Anisotropy in seismic velocities and amplitudes from multiple parallel fractures, J. Geophys. Res., Vol. 95. No. B/, 11,345-11,358

Sano, O., Kudo, Y., and Mizuta, Y., 1992, Experimental Determination of Elastic Constants of Oshima Granite, Barre Granite, and Chelmsford Granite, JGR, Vol. 97, No. B3, p. 3367-3379, Mar. 10, 1992.

Sayers C. M., 1988, Stress-induced elastic wave anisotropy in fractured rock, Ultrasonics, 26, 311-317 (1988)

Roesler, S.K., 1979, Anisotropic shear modulus due to stress anisotropy, J. Geotech. Eng. Div., Proc. of the Am. Soc. Civ. Eng., 105, GT7 871-880

Sayers C. M., 1990, Stress-induced ultrasonic anisotropy in Berea Sandstone, Int. J. Rock Mech. Min. Sci. and Geomech. Abstr. Vol. 27, No. 5, 429-436

Thomsen, L., 1986, Week elastic anisotropy, Geophysics, 51, 1954-1966

Thomsen, L., 1988, Reflection seismology over azimuthally anisotropic media, Geophysics, 53, 304-313

Toksöz, M. N., Johnston, D. H., and Timur, A., 1979, Attenuation of seismic waves in dry and saturated rocks: I. Laboratory measurements, Geophysics, Vol. 44, No. 4, 681-690

Winkler, K. and Plona, T. J., 1982, Technique for measuring ultrasonic velocity and attenuation spectra in rocks under pressure, J. Geophys. Res. Vol. 87. No. B13, 10,776-10,780

Winkler, K., 1983, Frequency dependent ultrasonic properties of high-porosity sandstone, J. Geophys. Res. Vol. 88. No. B11, 9,493-9,499

Winterstein, D. F. and Paulsson, B. N. P., Velocity anisotropy in shale determined from crosshole seismic and vertical seismic profile data, Geophysics, Vo. 55, No. 4, 470-479

Winterstein, D. F., 1990, Velocity anisotropy terminology for Geophysicists, Geophysics, Vol. 55, No.8, 1070-1088

Zamora, M. and Poirier, J. P., 1990, Experimental study of acoustic anisotropy and birefringence in dry and saturated Fountainbleau sandstone, Geophysics, Vol. 55, No.11

Zoback, M. L., Zoback, M. D., et al., 1989, Global patterns of tectonic stress, Nature, Vol. 341, 28, 291-298

Table 5.1: Petrographic description and micro-probe composition analyses from the thin-sections of the rock samples in this chapter's experiments.

SIERRA WHITE GRANITE		
TEXTURES	grain size:	1-2mm, very coarse
COMPOSITION	quartz:	20%–30%
	feldspar:	zonations, plagioclase ,10%
	biotite:	trace
	amphibole:	trace
POROSITY	helium:	0.1%
DENSITY	(bulk):	2.64 g/cm^3 (dry)
COLORADO OIL SHALE		
COMPOSITION	quartz:	detrital, fine grains, 7-10%
	carbonate:	muddy-dolomite with clear lamination, 90%
DIAGENESIS		chemical
POROSITY	helium:	0.1%
DENSITY	(bulk):	2.35g/cm^3 (dry)
COLORADO SHALY SANDSTONE		
TEXTURES	grain size:	0.05-0.1mm,
	sorting:	moderate
	particle:	angular,
COMPOSITION	quartz:	70%,
	feldspar:	10%,
Fragments-	mica:	trace
Cements-	clay:	rich organic matter clay-70%, calcite-30%
DIAGENESIS	compaction:	good
	support:	matrix – 90%, clastic – 10%
	structure:	very fine sand with clay lamination
	others:	strongly bioturbated, vertical & horizontal burrows
POROSITY	helium:	0.1%
DENSITY	(bulk):	2.51 g/cm^3 (dry)

Table 1. (continued)

BEREA 200 SANDSTONE		
TEXTURES	grain size:	0.1mm-0.2mm
	sorting:	well
	particle:	mod. sphericity,
COMPOSITION	quartz:	58%
	feldspar:	7%
	Lithics:	8%
	others:	heavy mineral, muscovite - 1%
Cements-		quartz-10%, clay and calcite-2%
DIAGENESIS	compaction:	well, some crushed grains
	support:	grain-90%, matrix-10%
	structure:	well sorted fine grains, clay beddings
POROSITY	helium:	19.2%
DENSITY	(bulk):	2.14 g/cm^3 (dry)

MASSILLON SANDSTONE		
TEXTURES	grain size:	0.2m
	sorting:	poor
	particle:	high sphericity
COMPOSITION	quartz:	69%
	feldspar:	1%
	Chert:	1%
	others:	muscovite - tr.
Cements-		quartz-4%, clay rimming-3%, chert-4%
DIAGENESIS	compaction:	mod.
	support:	grain-60%, matrix-40%
	structure:	$cc = sut > long > tan$
POROSITY	helium:	22.1%
DENSITY	(bulk):	2.06 g/cm^3 (dry)

Table 1. (continued)

FREEMAN SILTSTONE		
TEXTURES	grain size:	less than 0.05m (silt)
	sorting:	poor
	particle form:	lower sphericity, angular-subangular, grain orientation parallel to bedding
COMPOSITION	quartz:	65%
	feldspar:	5%
Fragments-	mica:	15% - 20%
	others:	7% - 10%
Cements-	clay and calcite:	(mud rich)
DIAGENESIS	compaction:	loose, some crushed grains and bended mica
	support:	matrix support - 90%, clastic support - 10%
	structure:	high burrow intensity
POROSITY	helium: 24.3%	saturation: 23.1%
DENSITY	(bulk):	1.84 g/cm^3 (dry)

Table 5.2: Velocity list

Sierra White Granite (Triaxial Loading, Pxx=Pyy=17.2bar)

Pzz (bar)	Vzz	Vzx	Vzy	Vyy	Vyx	Vyz	Vxx	Vxy	Vxz	V_{45-zx}	V_{45-zy}	V_{45-xy}
	Velocity(KM/Second)											
17.2	4.57	2.77	2.78	4.45	2.78	2.81	4.49	2.80	2.82	4.12	4.11	4.06
25.8	4.64	2.80	2.81	4.42	2.78	2.78	4.50	2.80	2.83	4.15	4.15	4.09
34.5	4.71	2.82	2.83	4.44	2.78	2.83	4.51	2.81	2.85	4.18	4.18	4.09
43.1	4.76	2.84	2.85	4.42	2.78	2.85	4.52	2.80	2.86	4.25	4.21	4.12
51.7	4.81	2.86	2.87	4.45	2.78	2.87	4.51	2.81	2.88	4.32	4.26	4.12

Sierra White Granite (Polyaxial Loading, Pxx=17.2bar, Pyy=51.7bar)

Pyy (bar)	Vzz	Vzx	Vzy	Vyy	Vyx	Vyz	Vxx	Vxy	Vxz	V_{45-zx}	V_{45-zy}	V_{45-xy}
	Velocity(KM/Second)											
17.2	4.81	2.86	2.87	4.45	2.78	2.87	4.51	2.81	2.88	4.34	4.21	4.12
25.8	4.82	2.84	2.86	4.45	2.79	2.89	4.56	2.76	2.88	4.51	4.44	4.24
34.5	4.82	2.85	2.87	4.52	2.82	2.90	4.58	2.77	2.89	4.59	4.37	4.15
43.1	4.82	2.85	2.89	4.57	2.83	2.92	4.58	2.78	2.89	4.66	4.41	4.18
51.7	4.82	2.86	2.90	4.64	2.83	2.93	4.61	2.79	2.90	4.62	4.37	4.31
60.4	4.83	2.86	2.90	4.65	2.85	2.93	4.60	2.80	2.90	4.66	4.82	4.59
69.0	4.83	2.86	2.91	4.65	2.86	2.95	4.61	2.81	2.90	4.78	4.83	4.59
86.2	4.84	2.86	2.92	4.70	2.88	2.96	4.60	2.82	2.91	4.74	4.85	4.70
103.5	4.84	2.87	2.93	4.77	2.89	2.97	4.61	2.83	2.92	4.74	4.86	4.72

Colorado Oil Shale (Triaxial loading, Pxx=Pyy=17.2bar)

Pzz (bar)	Vzz	Vzx	Vzy	Vyy	Vyx	Vyz	Vxx	Vxy	Vxz	V_{45-zx}	V_{45-zy}	V_{45-xy}
	Velocity(KM/Second)											
17.2	4.16	2.48	2.50	4.67	2.70	2.54	4.64	2.71	2.50	4.14	4.16	4.68
25.8	4.19	2.49	2.51	4.67	2.71	2.58	4.63	2.71	2.57	4.16	4.16	4.65
34.5	4.20	2.50	2.52	4.67	2.71	2.58	4.64	2.71	2.58	4.14	4.16	4.68
43.1	4.20	2.50	2.52	4.67	2.71	2.59	4.64	2.72	2.59	4.14	4.14	4.68
51.7	4.21	2.50	2.52	4.67	2.71	2.60	4.64	2.71	2.60	4.14	4.16	4.65

Colorado Oil Shale (Polyaxial loading, Pxx=17.2bar, Pzz=51.7bar)

Pyy (bar)	Vzz	Vzx	Vzy	Vyy	Vyx	Vyz	Vxx	Vxy	Vxz	V_{45-zx}	V_{45-zy}	V_{45-xy}
	Velocity(KM/Second)											
17.2	4.21	2.50	2.52	4.67	2.71	2.58	4.64	2.71	2.52	4.12	4.12	4.65
34.5	4.22	2.51	2.54	4.67	2.71	2.60	4.65	2.71	2.54	4.12	4.19	4.68
51.7	4.22	2.50	2.55	4.67	2.71	2.59	4.64	2.71	2.55	4.14	4.15	4.66
69.0	4.21	2.49	2.57	4.68	2.72	2.60	4.63	2.72	2.57	4.12	4.12	4.68
86.2	4.21	2.50	2.59	4.69	2.72	2.60	4.63	2.72	2.59	4.12	4.14	4.67
103.5	4.21	2.52	2.62	4.69	2.73	2.61	4.64	2.72	2.62	4.12	4.12	4.68

Table 2. (continued)

Colorado Shaly Sandstone (Triaxial Loading, Pxx=Pyy=17.2bar)

Pzz (bar)	Vzz	Vzx	Vzy	Vyy	Vyx	Vyz	Vxx	Vxy	Vxz	V_{45-zx}	V_{45-zy}	V_{45-xy}
	Velocity(KM/Second)											
17.2	2.81	2.37	2.36	4.23	2.74	2.40	4.33	2.72	2.36	3.42	3.44	4.23
25.8	2.96	2.40	2.39	4.23	2.74	2.42	4.33	2.73	2.37	3.48	3.49	4.26
34.5	3.28	2.43	2.42	4.25	2.74	2.43	4.33	2.73	2.41	3.53	3.52	4.29
43.1	3.51	2.46	2.45	4.26	2.74	2.44	4.33	2.73	2.42	3.59	3.62	4.29
51.7	3.58	2.49	2.47	4.25	2.74	2.46	4.34	2.73	2.44	3.74	3.77	4.29

Colorado Shaly Sandstone (Polyaxial Loading, Pxx=17.2bar, Pzz=51.7bar)

Pyy (bar)	Vzz	Vzx	Vzy	Vyy	Vyx	Vyz	Vxx	Vxy	Vxz	V_{45-zx}	V_{45-zy}	V_{45-xy}
	Velocity(KM/Second)											
17.2	3.58	2.49	2.47	4.25	2.74	2.46	4.34	2.73	2.44	3.74	3.77	4.29
34.5	3.58	2.49	2.47	4.27	2.74	2.46	4.34	2.74	2.44	3.84	3.86	4.29
51.7	3.58	2.50	2.49	4.27	2.74	2.47	4.33	2.74	2.45	3.86	3.91	4.32
69.0	3.59	2.50	2.49	4.28	2.75	2.48	4.34	2.74	2.45	3.91	4.08	4.32
86.2	3.60	2.50	2.49	4.30	2.75	2.48	4.33	2.74	2.45	4.16	4.28	4.31
103.5	3.60	2.51	2.50	4.30	2.75	2.49	4.34	2.74	2.45	3.66	3.81	4.55

Berea 200 Sandstone (Triaxial Loading, Pxx=Pyy=17.2bar)

Pzz (bar)	Vzz	Vzx	Vzy	Vyy	Vyx	Vyz	Vxx	Vxy	Vxz	V_{45-zx}	V_{45-zy}	V_{45-xy}
	Velocity(KM/Second)											
17.2	3.04	1.97	2.02	3.21	2.03	2.08	3.20	2.02	2.08	3.17	3.16	3.20
25.8	3.11	2.01	2.05	3.22	2.03	2.09	3.20	2.03	2.10	3.25	3.18	3.21
34.5	3.17	2.03	2.07	3.22	2.03	2.11	3.21	2.03	2.12	3.26	3.25	3.22
43.1	3.24	2.06	2.10	3.23	2.04	2.13	3.22	2.03	2.14	3.29	3.28	3.22
51.7	3.29	2.08	2.13	3.22	2.05	2.14	3.23	2.03	2.15	3.34	3.32	3.25

Berea 200 Sandstone (Polyaxial Loading, Pxx=17.2bar, Pzz=51.7bar)

Pyy (bar)	Vzz	Vzx	Vzy	Vyy	Vyx	Vyz	Vxx	Vxy	Vxz	V_{45-zx}	V_{45-zy}	V_{45-xy}
	Velocity(KM/Second)											
17.2	3.29	2.08	2.13	3.22	2.05	2.14	3.23	2.03	2.15	3.34	3.32	3.25
34.5	3.29	2.09	2.14	3.33	2.07	2.18	3.21	2.06	2.15	3.32	3.38	3.31
51.7	3.29	2.09	2.16	3.39	2.09	2.20	3.21	2.08	2.16	3.26	3.43	3.35
69.0	3.29	2.10	2.18	3.48	2.13	2.23	3.20	2.09	2.16	3.28	3.45	3.37
86.2	3.31	2.10	2.20	3.56	2.15	2.26	3.20	2.12	2.17	3.25	3.47	3.40
103.5	3.31	2.11	2.23	3.65	2.19	2.29	3.20	2.15	2.17	3.27	3.51	3.42

Table 2. (continued)

Massillon Sandstone (Triaxial Loading, Pxx=Pyy=17.2bar)

Pzz (bar)	Vzz	Vzx	Vzy	Vyy	Vyx	Vyz	Vxx	Vxy	Vxz	V_{45-zx}	V_{45-zy}	V_{45-xy}
	Velocity(KM/Second)											
17.2	2.81	1.82	1.83	2.83	1.84	1.83	2.86	1.81	1.84	2.85	2.84	2.82
25.8	2.93	1.86	1.86	2.86	1.83	1.83	2.87	1.80	1.86	2.91	2.88	2.84
34.5	3.01	1.91	1.90	2.86	1.83	1.86	2.87	1.80	1.89	2.99	2.94	2.83
43.1	3.10	1.94	1.92	2.85	1.82	1.88	2.88	1.82	1.92	3.05	3.01	2.85
51.7	3.13	1.97	1.95	2.85	1.83	1.90	2.87	1.82	1.94	3.06	3.03	2.84

Massillon Sandstone (Polyaxial Loading, Pxx=17.2bar,Pzz=51.7bar)

Pyy (bar)	Vzz	Vzx	Vzy	Vyy	Vyx	Vyz	Vxx	Vxy	Vxz	V_{45-zx}	V_{45-zy}	V_{45-xy}
	Velocity(KM/Second)											
17.2	3.13	1.97	1.95	2.85	1.83	1.90	2.87	1.82	1.94	3.06	3.03	2.84
34.5	3.13	1.98	1.97	3.00	1.90	1.96	2.86	1.85	1.95	3.02	3.06	2.95
51.7	3.14	1.98	1.98	3.13	1.94	2.00	2.87	1.88	1.96	3.05	3.14	3.03
69.0	3.14	1.99	2.01	3.23	1.97	2.03	2.87	1.91	1.98	3.07	3.16	3.09
86.2	3.15	2.00	2.03	3.29	2.00	2.07	2.86	1.93	1.97	3.03	3.17	3.13
103.5	3.13	2.02	2.04	3.35	2.02	2.08	2.86	1.94	1.98	3.07	3.19	3.15

Ottawa Sand (Triaxial Loading Pxx=Pyy=1.72bar)

Pzz (bar)	Vzz	Vzx	Vzy	Vyy	Vyx	Vyz	Vxx	Vxy	Vxz	V_{45-zx}	V_{45-zy}	V_{45-xy}
	Velocity(KM/Second)											
10.3	0.76	0.43	0.42	0.74	0.40	0.43	0.76	0.40	0.42			
13.8	0.82	0.44	0.44	0.77	0.42	0.44	0.76	0.43	0.44			
17.2	0.87	0.46	0.46	0.79	0.44	0.47	0.79	0.44	0.46			
20.7	0.90	0.48	0.48	0.80	0.46	0.47	0.79	0.46	0.49			
27.6	0.95	0.52	0.52	0.85	0.48	0.52	0.85	0.48	0.51			
34.5	1.01	0.54	0.54	0.87	0.50	0.54	0.87	0.50	0.53			

Ottawa Sand (Polyaxial Loading, Pxx=17.2 bar, Pzz=34.5 bar)

Pyy (bar)	Vzz	Vzx	Vzy	Vyy	Vyx	Vyz	Vxx	Vxy	Vxz	V_{45-zx}	V_{45-zy}	V_{45-xy}
	Velocity(KM/Second)											
10.3	1.01	0.54	0.54	0.87	0.50	0.54	0.87	0.50	0.53			
19.0	1.02	0.55	0.55	0.90	0.52	0.55	0.87	0.51	0.56			
27.6	1.03	0.58	0.58	0.93	0.53	0.57	0.88	0.52	0.57			
36.2	1.03	0.61	0.58	0.98	0.55	0.62	0.88	0.54	0.51			
44.8	1.03	0.62	0.60	1.03	0.57	0.62	0.88	0.56	0.58			
62.1	1.03	0.63	0.59	1.12	0.60	0.63	0.89	0.59	0.59			
79.3	1.04	0.65	0.60	1.16	0.62	0.65	0.90	0.62	0.61			

Table 2. (continued)

Freeman Siltstone A (Triaxial Loading, Pxx=Pyy=1.72bar)

Pzz (bar)	Vzz	Vzx	Vzy	Vyy	Vyx	Vyz	Vxx	Vxy	Vxz	V_{45zx}	V_{45zy}	V_{45xy}
	Velocity(KM/Second)											
17.2	1.52	0.99	0.96	1.65	1.05	0.95	1.68	1.06	0.99	1.57	1.53	1.67
25.8	1.60	1.01	0.99	1.66	1.05	1.00	1.70	1.07	1.02	1.68	1.57	1.62
34.5	1.73	1.09	1.07	1.67	1.07	1.06	1.72	1.08	1.10	1.72	1.66	1.66
43.1	1.85	1.15	1.11	1.69	1.08	1.11	1.73	1.07	1.16	1.75	1.70	1.68
51.7	1.98	1.20	1.16	1.72	1.09	1.14	1.77	1.08	1.22	1.78	1.73	1.69

Freeman Siltstone A (Polyaxial Loading, Pxx=34.5bar)

Pzz/Pyy (bar)	Vzz	Vzx	Vzy	Vyy	Vyx	Vyz	Vxx	Vxy	Vxz	V_{45zx}	V_{45zy}	V_{45xy}
	Velocity(KM/Second)											
34.5/34.5	1.82	1.11	1.10	1.89	1.14	1.12	1.88	1.19	1.12	1.84	1.83	1.89
43.1/51.7	1.90	1.17	1.19	2.00	1.18	1.23	1.89	1.22	1.18	1.87	1.97	1.92
51.7/69.0	1.96	1.19	1.22	2.05	1.22	1.24	1.90	1.24	1.20	1.91	2.04	1.95
60.4/86.2	2.07	1.22	1.24	2.14	1.25	1.25	1.90	1.25	1.22	1.96	2.05	1.96
69.0/104	2.13	1.27	1.29	2.20	1.27	1.29	1.91	1.26	1.30	2.03	2.15	2.01

Freeman Siltstone B (Triaxial Loading, Pxx=Pyy=1.72bar)

Pzz (bar)	Vzz	Vzx	Vzy	Vyy	Vyx	Vyz	Vxx	Vxy	Vxz	V_{45zx}	V_{45zy}	V_{45xy}
	Velocity(KM/Second)											
17.2	0.83			2.20	1.56		2.32	1.53				
25.8	0.96			2.21	1.56		2.36	1.55				
34.5	1.27	0.75	0.71	2.23	1.57		2.37	1.56				
43.1	1.51	1.14	1.10	2.22	1.57	1.09	2.37	1.56	1.15	1.86	1.76	2.28
51.7	1.54	1.18	1.23	2.23	1.57	1.22	2.37	1.57	1.21	1.92	1.82	2.29

Freeman Siltstone B (Polyaxial Loading, Pxx=51.7bar)

Pzz/Pyy (bar)	Vzz	Vzx	Vzy	Vyy	Vyx	Vyz	Vxx	Vxy	Vxz	V_{45zx}	V_{45zy}	V_{45xy}
	Velocity(KM/Second)											
51.7/51.7	1.59	1.13	1.17	2.28	1.58	1.19	2.39	1.58	1.14	2.04	1.97	2.35
60.4/69.0	1.62	1.15	1.18	2.42	1.59	1.20	2.43	1.59	1.15	2.01	2.04	2.41
69.0/86.2	1.79	1.34	1.33	2.44	1.59	1.18	2.43	1.60	1.16	2.09	2.03	2.42
77.6/103	1.82	1.36	1.35	2.45	1.60	1.38	2.43	1.60	1.17	2.16	2.06	2.43
86.2/120	1.85	1.39	1.39	2.49	1.61	1.38	2.44	1.61	1.18	2.23	2.18	2.44

Table 5.3: Tabulation of experimentally observed quality factors matrix for Colorado oil shale and Massillon sandstone ($1000/Q_{ij}$). The isometric stress case (Iso.) had $P_{xx} = P_{yy} = P_{zz} = 1.72MPa$; The triaxial loading case (Tri.) had $P_{xx} = P_{yy} = 1.72MPa$, and $P_{zz} = 5.17MPa$; The polyaxial loading case (Poly.) was measured at $P_{xx} = 1.72MPa$, $P_{yy} = 10.35MPa$, $P_{zz} = 5.17MPa$.

Col. Oil Shale

	zz	yy	xx	zx	xz	zy	yz	yx	xy
Iso.	34.8	4.30	4.20	17.5	24.2	17.9	24.4	6.50	6.70
Tri.	7.70	4.30	4.20	9.80	12.7	10.2	12.7	6.40	6.60
Poly.	8.30	4.40	4.20	9.60	12.2	9.70	12.5	6.00	5.90

Missillon Sandstone

	zz	yy	xx	zx	xz	zy	yz	yx	xy
Iso.	62.7	63.1	63.8	31.7	32.0	31.9	31.8	32.0	31.5
Tri.	52.0	58.3	58.7	25.3	24.9	22.6	22.1	33.5	33.3
Poly.	52.0	31.6	56.8	25.9	25.4	14.9	15.3	17.3	16.6

Appendix A

Laboratory ultrasonic technique

A.1 Introduction

If we want to assess the influence of subsurface environmental conditions on the physical properties of rocks, like shales, then we must exert strict control over certain key laboratory parameters in order to detect interesting seismic responses in the rocks. Because of the relative ease by which diverse ultrasonic waves may be generated, the simultaneous measurement of a confined rock sample's directional elastic or viscoelastic wave transmission characteristics has been recognized as the most accurate means available for determining porous media elastic moduli.

Typical ultrasonic experiments at Stanford Rock and Borehole Physics Laboratory use pulse transmission technique with a central frequency close to one megahertz (10^6 Hz). This technique is widely recognized and accepted in both mechanical nondestructive evaluation and rockphysics testing. Efficient piezoelectric transducers combined with electrical impedance matched pulse generator, millivolt sensitivity pre-amplifier and oscilloscope allow the pulse transmission technique for an accurate velocity estimation in rockphysics testing, even in those of higher attenuation rocks, such as shales and soil. I have adopted this technique to all experiments described in this thesis. In this chapter, I intend to help fill in some of the background material in basic laboratory ultrasonic measurement technique.

A.2 Rock sample preparation

Considering all significant parameters in the pulse transmission experiments, we must minimize pulse-wave energy dissipation caused by diffraction, scattering, mode conversion, and reflective phenomena. In the pulse-transmission experiments, we hope to reduce the deleterious effect by these phenomena through judicious optimization of the transient pulses, in view of all that is known of a given rock sample's relevant physical characteristics. We may wisely consider the following parameters when preparing rock and soil samples for laboratory ultrasonic measurements.

1. To avoid waveguide effect, the geometric diffraction, the sample radius r should exceed the wavelength λ of the ultrasonic pulse wave that is transmitted along the sample. When $r < \lambda$, the waveguide effect attenuates and slows the propagating waves, which causes the waves travel at a reduced velocity— bar velocity—as r become smaller and smaller with respect to λ (Schreiber, Anderson and Soga, 1973).

2. To assure that the ultrasonic pulse waves transmmited through a sample rather than displacing the sample uniformly, the path of the pulse wave from the source to receiver, usually the rocks sample's length L, should be greater than one wavelength of the pulse wave, $L/\lambda > 1$ (Kolsky, 1953).

3. To avoid scattering of the ultrasonic wave by the pores or grains in rock sample, The wavelength of the transmitted pulse should be at least three times longer than the largest grain size d_s or pore size in the sample, $\lambda_s/d_s > 3$ (Plona and Tsang, 1979).

4. To avoid cancellation of the direct first arrival amplitude by interference with waves reflecting off of the sample sidewalls, the sample length should be less than five times sample diameter d, $L < 5d$, to assure a more distinct first arrival for an accurate velocity estimation.

5. The time required for pore pressure changes to diffuse the pore fluid throughout the sample and equilibrate depends on fluid pressure wave diffusion velocity which drastically decreases with sample permeability decreased. Thus, pore fluid pressure in a smaller low-permeability sample equilibrate faster than in a larger sample. Satisfying the above constraints, but minimizing sample dimension, should speed research concerned with pore pressure effects, like measurements in shale samples (Yin et al. 1991).

A.3 Pressure vessel and electronic system

In order to carry out simultaneous $V_{P(\|)}$, $V_{SH(\|)}$ and $V_{SV(\perp)}$ measurement with multi-component ultrasonic transducers to study anisotropic rocks, I modulated the pulse transmission ultrasonic apparatus in the SRB laboratory. The pressure vessel now contains more than 12 electrical signal output lines.

A Nicolet Digital Oscilloscope 2090 was used to detect wavelets from the ultrasonic transducers and to estimate time-of-flight for the wave velocity calculation. The oscilloscope samples at 20 MHz for time-base resolution, and 0.05 mv for amplitude resolution.

An IBM-PC based data acquisition and signal processing system were developed to make the attenuation measurements and transfer data to any main frame computer. Figure A.1 illustrates the system set-up.

A.4 Velocity measurement

In the ultrasonic pulse transmission experiment, we do not measure wave velocity directly. Rather, we record the travel time of a ultrasonic transient pulse wave. Then, we calculate velocities with the following equation.

$$V_{ij} = \frac{L}{t_M - t_T} \tag{A.1}$$

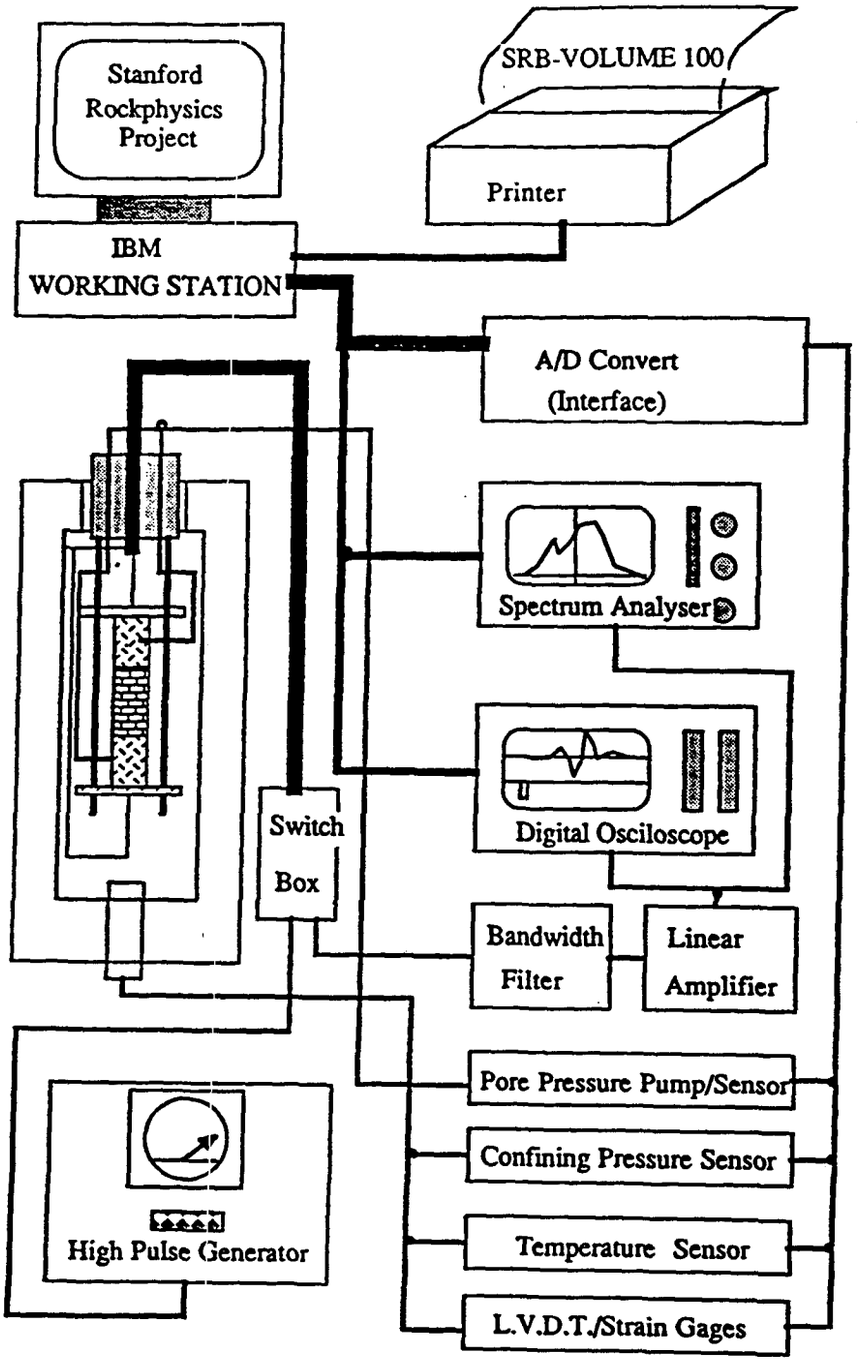

Figure A.1: Schematic diagram of the system set-up.

where V_{ij} is either P-velocity or S-velocity; L is the length of the sample; t_M and t_T are pulse wave travel times with the sample under measurement in place and without the sample in place (the transmitter in direct contact with the receiver), respectively. Then, the error may be analyzed by partial differentiation,

$$\Delta V = \frac{\partial V}{\partial L}\Delta L + \frac{\partial V}{\partial t_M}\Delta t_M + \frac{\partial V}{\partial t_T}\Delta t_T \tag{A.2}$$

and the absolute error can be evaluated as

$$\Delta V = \Delta L\left|\frac{1}{t_M - t_T}\right| + \Delta L\left|\frac{\Delta t_M}{(t_M - t_T)^2}\right| + \Delta L\left|\frac{\Delta t_T}{(t_M - t_T)^2}\right| \tag{A.3}$$

where Δt_T and Δt_M are the oscilloscope's time resolution, and ΔL is the absolute error in sample length measurement, it can be less than $0.05mm$.

Since $t_M - t_T$ is usually larger than $10\mu s$ and typically near $15\mu s$, the second and third terms in the above equation may be neglected. Then, the maximum absolute error ΔV could be less than $50m/sec$, and the corresponding relative error could be less than 3% in P-velocity estimation and 5% in S-velocity estimation.

A.5 Attenuation measurement

Inhomogeneity and large absorption of wave energy in rock samples (especially soft rocks, like shales) have precluded application of many high precision techniques used in solid state physics and nondestructive evaluation. Still the need for better estimates of attenuation parameters in quantitative seismic interpretation keeps the heat on attenuation measurement, both in laboratories and in the field. Techniques have been developed rapidly for rock sample measurement. Theory for the geometrical diffraction correction in lossy anisotropic media measurement has also advanced from Papadakis (1966) to Tang et al. (1990).

Some basic methods for the attenuation measurement in rock samples are:

- Resonant bar (Birch 1938, Winkler 1982, Lucet et al. 1990),

- Slow stress—strain cycling (Gordon et al. 1968, McKavanagh et al. 1974),
- Ultrasonic pulse rise time (Gladwin 1974, Blair 1982, Tarif et al. 1987),
- Ultrasonic pulse-echo (Papadakis 1975, Winkler 1983, Klimentos 1990),
- Ultrasonic pulse transmission (Toksöz et al. 1979, Pyrak-Nolte 1990).

Some other minor methods, like ultrasonic lens technique and "panoramic" receivers technique in water tank have also been used for rock attenuation measurements.

We assume a plane pressure wave $S(\omega)$ propagating in sample placed in between the end-plugs of a PZT transmitter and receiver. The wave power spectrum $A_r(\omega)$ received at the end-plug of the receiver, when measuring an aluminum cube as a reference geometric diffraction correction, may be expressed as:

$$A_r(\omega) = S(\omega)e^{-\alpha_r(\omega)L}G_r(\lambda_r, a, L) \tag{A.4}$$

where $\alpha_r(\omega)$ is the attenuation coefficient of the reference cube aluminum, L is the length of the reference cube, and $G_r(\lambda_r, a, L)$ is geometric diffraction correction term. This term is function of the wave length $\lambda_r = v_r/f_c$, radius of the sample a, and the length of the sample L. Since the reference cube was made of aluminum, the same material as the end-plugs of the transducers, we assume that this arrangement has no reflection losses among the transducers and reference cube interfaces.

When measuring a rock sample, the received wave spectrum $A_s(\omega)$ may be expressed as

$$A_s(\omega) = S(\omega)e^{-\alpha_s(\omega)L}T_1T_2G_s(\lambda_s, a, L) \tag{A.5}$$

where $S(\omega)$ is the power spectrum of the source wave, $\alpha_s(\omega)$ is the attenuation coefficient of the measured rock sample, L is the length of the sample, T_1, T_2 are the

transmission coefficients from the transmitter's plug to the rock sample and from the rock sample to the receiver's plug respectively, and $G_s(\lambda_s, a, L)$ is geometric diffraction loss.

Since $T_1 = 1 - R_1, T_2 = 1 - R_2$ and $R_1 = -R_2$ in our case, the ratio of the two power spectra, after taking the logarithm and eliminating the intrinsic attenuation of the reference cube, ($\alpha_r(\omega) \approx 0$, reasonable compared with rock's attenuation), is

$$\alpha_s(\omega) = \frac{20}{L}\log_{10}\left[\frac{A_r(\omega)}{A_s(\omega)}(1 - R^2)\right] - \frac{20}{L}\log_{10}\left[\frac{G_r(\lambda_r, a, L)}{G_s(\lambda_s, a, L)}\right] \tag{A.6}$$

where $\alpha_s(\omega)$ is the observed attenuation coefficient of the rock sample in dB/cm, $A_r(\omega)$ is the amplitude spectrum measured through the reference cube, $A_s(\omega)$ is the amplitude spectrum measured through the rock sample, and R is reflection coefficient between the transducer's aluminum platen and the rock sample, $G_r(\lambda_r, a, L)$ and $G_s(\lambda_s, a, L)$ are the geometric diffraction losses in rock sample and reference, respectively.

If we assume that the geometric diffraction loss in reference cube $G_r(\lambda_r, a, L)$ is same as in rock sample $G_s(\lambda_s, a, L)$ because the rock sample cube and the reference cube have the same dimensions, then the last term in above equation is zero. Equation A.6 above is strictly valid only for plane waves transmitted through perfectly bounded plane and parallel interfaces from transmitter to sample and sample to receiver.

If we can estimate attenuation coefficients in different directions, then we may infer the visco-elastic stiffness constants $\hat{c}_{ij}$ and examine rock attenuation anisotropy. Wave propagation in a visco-elastic medium can be described by introducing complex stiffness constants:

$$\hat{c}_{ij} = c_{ij}(1 + iQ_{ij}^{-1}) \tag{A.7}$$

where $\hat{c} = [\hat{c}_{ij}]$ are the complex stiffness matrix; $c = [c_{ij}]$ is its real part, $\acute{c} = [c_{ij}Q_{ij}]$ is its imaginary part and Q_{ij} is anisotropic quality factor, which may take form with

directional attenuation coefficients α_{ij} as

$$\frac{100}{Q_{ij}(f)} = \frac{\alpha_{ij}(f)V_{ij}}{8.686\pi f} \tag{A.8}$$

where α_{ij} is the wave attenuation in dB/cm, V_{ij} is the phase velocity in m/s, and f is the frequency in *hertz* (Winkler, 1983).

A.6 Transducer array design for shear wave splitting measurement

PZT[1]-transducer design is a branch of applied acoustics, rich with theories developed for over more than 40 years. Many books and papers have been published in this area. By learning the current state-of-the art of ultrasonic transducer design, I have fabricated two pair of three-components ultrasonic transducers for the experiments of Chapter 4 in high pressure vessel, and three pair of three-components transducers for the experiments of Chapter 5.

PZT crystals are widely used to convert electric energy into mechanical energy and vice versa. A simple liquid-backed P-wave and torsional S-wave transducer has been used in SRB laboratory for more than ten years. It is easy to construct such transducers. They have been sufficiently used to pick first arrivals, which are converted from time delay into wave velocity estimates (Tosaya, 1982). She also designed another type of transducer with one shear wave polarized in a particular direction for anisotropic measurement, but it is still not sufficient in measuring shear wave splitting, since you have to either measure two different samples for c_{44} and c_{66}, or to change the sample's orientation for c_{66} after the c_{44} measurement (or c_{66} first, then c_{44}), and compare the measurement at the same confining pressure conditions. Such measurements might drastically decrease the accuracy of the experiments due to the presence of visco-hysteresis in any rock samples. Therefore, designing three-

[1]PZT stands for piezoelectric transducer

component transducers was critical for decreasing cost and increasing measurement accuracy in the experiments of Chapter 4 and Chapter 5 With the KLM (Krimholtz, Leedom and Matthaei, 1970) model as a theoretical guide, I have designed a new type of crystal mosaic which is shown in Figure A.2.

The KLM model is represented by a three-port network shown in Figure A.3. It was developed from transmission line theory and retains the closest ties to the actual physical process in an acoustic transducer than any other models.

To design a broad-band and high efficiency acoustic transducer and simplify the model, we assumed that we can make $Z_c = Z_b = Z_p = Z_t$. Then, we have insertion loss at electric port $A - A'$:

$$L = -10 \log_{10} \frac{4\alpha\omega_o C_o R_s \varphi/\pi}{(\omega_o C_o R_s \varphi/\pi + \alpha)^2 + \beta^2} \tag{A.9}$$

where

$$\alpha^2 = k_T^2 \sin^2(\varphi/2)/(\varphi/2)$$
$$\beta = 1 - k_T^2 \sin\varphi/\varphi$$

It's been proved that L has minimum value when

$$\omega_o C_o R_s = \sqrt{\alpha^2 + \beta^2}/(\varphi/\pi) \tag{A.10}$$

and L_{min} has the form:

$$L_{min} = -10 \log_{10} \frac{2}{1 + \sqrt{1 + (\beta/\alpha)^2}} \tag{A.11}$$

The resonant frequency is usually chosen at the natural frequency of the PZT crystal, f_o, then,

$$\omega_o C_o R_s = \sqrt{1 + (2k_T^2/\pi^2)^2} \approx 1 \tag{A.12}$$

It should be clear now how we should design the most efficient transducer.

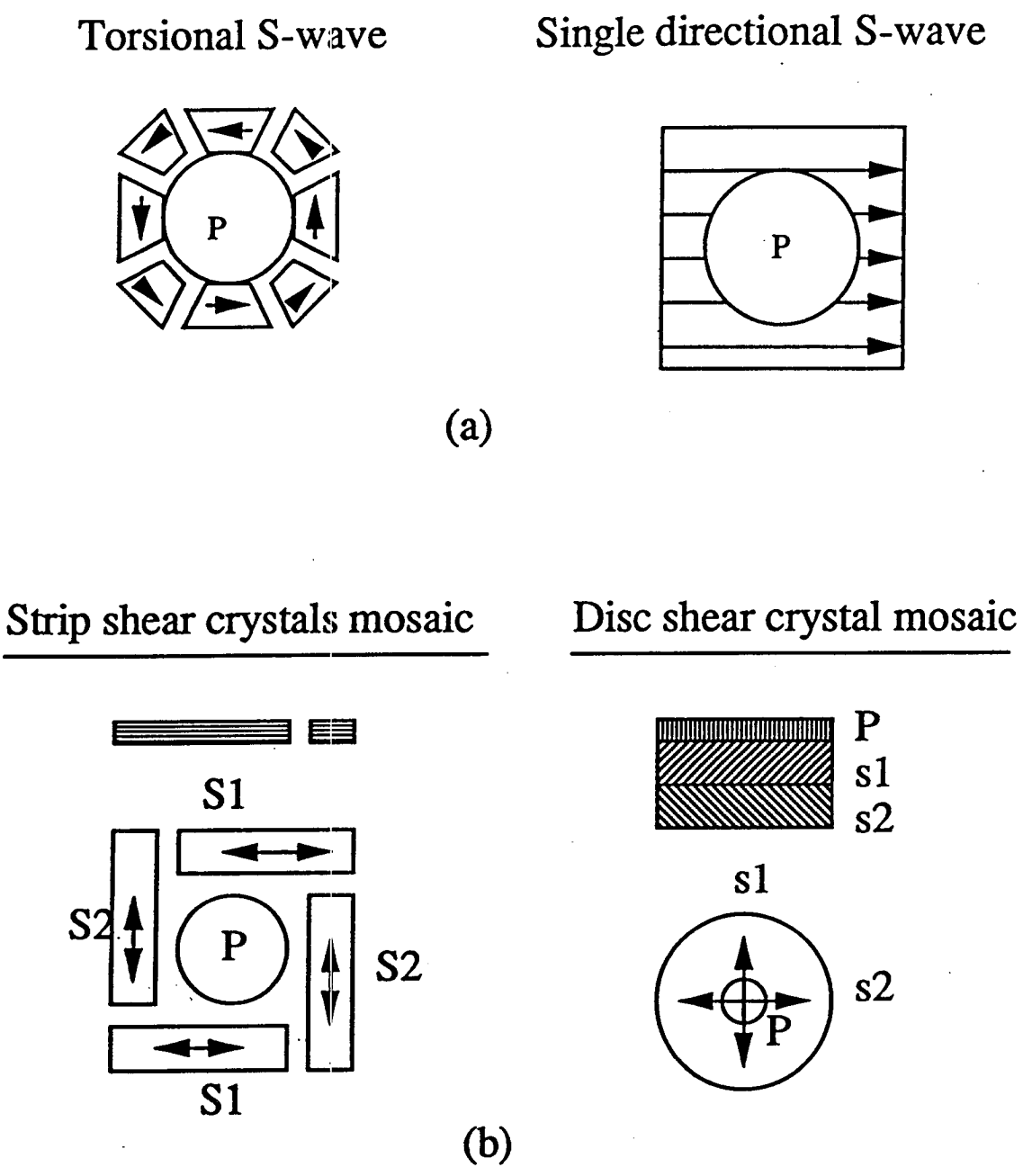

Figure A.2: PZT crystal configurations for three-components transducers. (a) Torsional S-wave and single directional S-wave mosaic (after Tosaya, 1982), (b) newly designed three-component mosaics for shear wave splitting measurement.

1. Choose the resonant frequency of PZT crystal ω_o.

2. Find the output equivalent resistance R_s of the pulse generator which to drive the transducers in experiment.

3. Find out what the surface area **A** of PZT crystal should be based on $C_o = (\varepsilon^s A)/l$, then make $\omega_o C_o R_s \approx 1$.

Such transducer's pulse response can be theoretically modeled by the following equation,

$$T_F\left(\frac{l}{2}\right) = \frac{jhI_3}{\omega A}\frac{1 - e^{-j\bar{\beta}_a l}}{2} \tag{A.13}$$

where $T_F(\frac{l}{2})$ is acoustic stress induced by an input current I which may be expressed by delta function $\delta(\omega_o)$ in the transient pulse excitement case, h is *transmission constant* ($h = e/\varepsilon^s$), and $\bar{\beta}_a$ is called propagation constant, ($\bar{\beta}_a = \omega/V_a$, in which V_a is the acoustic velocity.)

Based on the above theoretical consideration, five pairs of transducers were built for experiments of Chapter 4. Each transducer has one P-mode and two orthogonal S-modes. Two differenct PZT mosaics have been tested, one is PZT stack-mosaic with impedance matched back, the other is PZT parallel-strips mosaic without impedance matched back, confining fluid as back. The transducers were constructed with PZT4-crystals. Typical waveforms of the stack-mosaic transducers designed for high hydraulic pressure uses in both the time and frequency domains are shown in Figure A.4. The end-platens of transducers have a diameter of 2.54 cm and length of 3.5 cm to assure the "plane" wave front and to avoid "Fresnel" zone effects (Kino, 1987). The waveforms of the other three pairs of three-component transducers have been presented in Chapter 5, Figure 5.18.

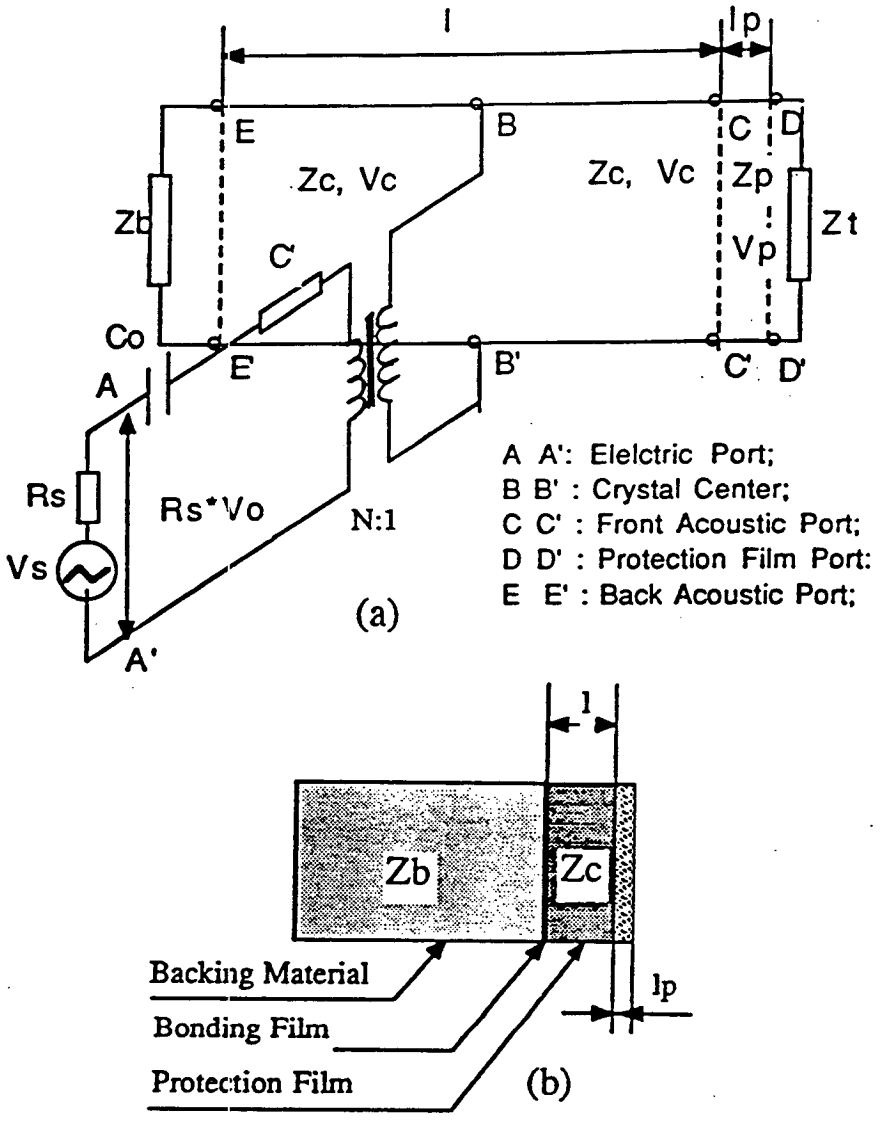

Figure A.3: (a) is the equivalent circuit of KLM model; (b) is the scheme of the brief structure of a PZT transducer. In (a),

$N =$ $k_T\sqrt{\pi/(\omega_o C_o Z_c)}sinc(\omega/2\omega_o)$

$C' =$ $-C_o/[k_T^2 sinc(\omega/\omega_o)]$

k_T is piezoelectric coupling coefficient of PZT crystal;

l is crystal thickness;

V_a is acoustic velocity of crystal;

C_o is natural capacitance of crystal;

ω_o is natural angular frequency of crystal;

l_p is protection film thickness;

Z is acoustic impedance, and the subscripts *c,b,t, and p* refer to crystal, backing material, tested material, and protection film.

R_s is equivalent output resistance of pulse-generator.

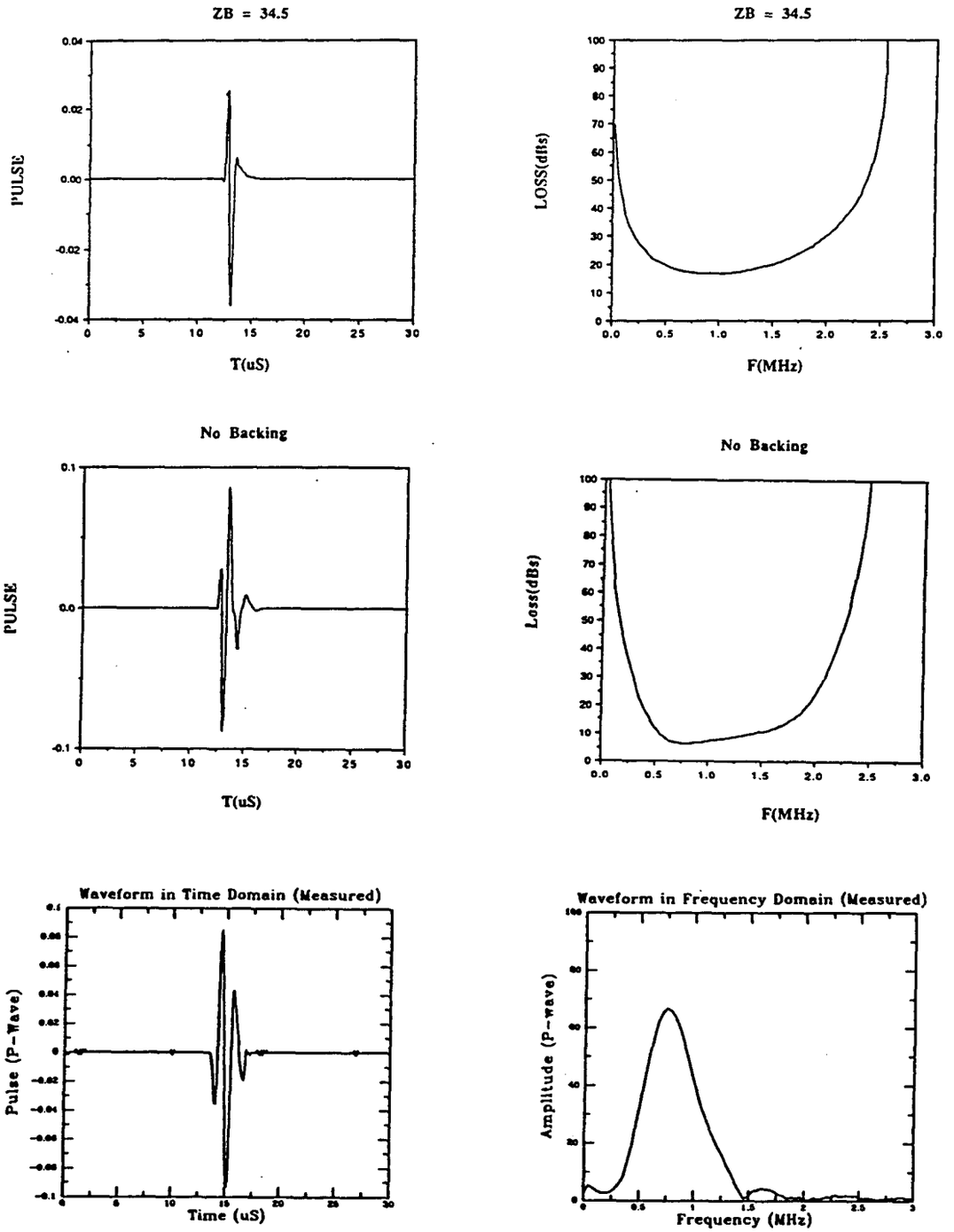

Figure A.4: Modeled wavelets of the High Efficiency, Broad-band Transducers: (a). matched backing; (b) unmatched backing; (c) real measured wavelet.

References

Auld, B. A., 1973, Acoustic Fields and Waves in Solids, Vol. 1, New York: John Wiley & Sons, Inc.

Berlincourt, D. A., Cursan, D. R. and Jaffe, H., 1964, Piezoelectric and Piezomagnetic Materials and Their Function in Transducers, in Physical Acoustics, Vol. I, W. P. Mason, ed., New York: Academic Press, Inc., Part A, Chapter 3, pp. 169-270.

Breazeale, M. A., Cantrell J. H. and Heyman J. S., 1981, Ultrasonic wave velocity and attenuation measurements, Method of Experimental Physics, Vol. 19, (Ultrasonic), Edited by Edmonds, P. D., Academic Press, Inc. 67-137

Hamonic, B., and Decarpigny, J.N., 1988, Power Sonic and Ultrasonic Transducers Design, Springer-Verlag Berlin Heideberg.

Kino, G. S., 1987, Acoustic Waves - Devices, Imaging and Analog Signal Processing, Prentice-Hall Signal Processing Series, Prentice - Hall, Inc.

Klimentos, T., Geometric corrections in attenuation measurement, Geophysical Prospecting, **39**, 193-218

Kolsky, H., 1953, Stress waves in Solids, Clarendon Press, Great Britain.

Lucet, N., et al., 1990, Sonic properties of rocks under confining pressure using the resonant bar technique, J. Acoust. Soc. Am. **89** (3), 980-990

Musgrave, M. J. P., 1970, Crystal Acoustics, Holden-Day, Inc.

Papadakis, E. P., Fowler, K. A., and Lynnworth, L. C., 1973, Ultrasonic attenuation by spectrum analysis of pulses in buffer rods: Method and diffraction correction, J. Acoust. Soc. Am., 53, 1336-1343

Papadakis, E. P., 1990, The measurement of ultrasonic Velocity, in *Ultrasonic Measurement Methods*, edited by R. N. Thurston and A. D. Pierce, Physical Acoustics, Vol. XIX, 81-107

Papadakis, E. P., 1990, The measurement of ultrasonic Attenuation, in *Ultrasonic Measurement Methods*, edited by R. N. Thurston and A. D. Pierce, Physical Acoustics, Vol. XIX, 108-156

Plona, T.J., and Tsang, L.,1979, Determination of the average microscopic dimension in granular media using ultrasonic pulses: theory and experiments. Presented at SEG 1979 Annual Convention, New Orleans, LA.

Schreiber, E., 1973, Elastic Constants and Their Measurement, McGraw-Hill Book Co., New York.

Tosaya, C., 1982, Acoustical properties of clay-bearing rocks, Ph.D thesis, Stanford University.

Winkler, K. and Nur, A., 1982, Seismic attenuation: effects of pore fluids and frictional sliding, Geophysics, 47, 1-15

Winkler, K. and Plona, T. J., 1982, Technique for measuring ultrasonic velocity and attenuation spectra in rocks under pressure, J. Geophys. Res. Vol. 87. No. B13, 10,776-10,780

Winkler, K., 1983, Frequency dependent ultrasonic properties of high-porosity sandstone, J. Geophys. Res. Vol. 88. No. B11, 9,493-9,499

Yin, H. and Nur, A., 1991, Seismic Anisotropic properties of Freeman Jewett Shale in Southeast San Joaquin Basin—A laboratory Experimental Study, Stanford Rock and Borehole Project, Vol. 46.

Appendix B

Fundamentals of acoustic waves in anisotropic media

In this chapter, I review the fundamentals of acoustic anisotropy used throughout Chapter 4 and Chapter 5.

B.1 Generalized strain and stress relation

Hook's law states that strain (S) is linearly proportional to stress (T), or conversely, that stress is linearly proportional to strain. In general, then,

$$T_{i,j} = c_{ijkl} S_{kl}, \tag{B.1}$$

$$i, j, k, l, = x, y, z$$

with summation over the repeated subscripts k and l. The "microscopic spring constants" c_{ijkl} are called *elastic stiffness constants* and they have dimension of stress ($Newton/m^2$). Equation B.1 contains nine equations (all combinations of the subscripts i, j, taking on values of x, y, z), and each equation contains nine strain variables (all combinations of the subscripts l, k, taking on values of x, y, z). Therefore, there are 81 elastic stiffness constants, but not all independent. Because of the elements symmetry in c_{ijkl} matrix,

$$c_{ijkl} = c_{jikl} = c_{ijlk} = c_{jilk} = c_{klij}, \tag{B.2}$$

the constants can be reduced to 21. This is the maximum number of independent stiffness constants for any medium[1].

B.2 Christoffel equation and slowness surfaces

The Christoffel equation was deduced from wave equations. It is convenient to use it when describing waves in anisotropic media.

$$k^2\Gamma_{ij}v_j = \rho\omega^2 v_i \tag{B.3}$$

where $\Gamma_{ij} = l_{ik}c_{kl}l_{lj}$ is called the *Christoffel Matrix.* Its elements are functions only of the plane wave propagation direction and the stiffness constants of the medium.

By rewriting the Christoffel equation, the propagation characteristics of plane waves in an anisotropic solid can be expressed as

$$[k^2\Gamma_{ij} - \rho\omega^2\delta_{ij}][v_{ij}] = 0. \tag{B.4}$$

A dispersion relation is then obtained by setting the characteristic determinant of Equation B.4 to equal zero, as

$$\Omega(\omega, k_x, k_y, k_z) = |k^2\Gamma_{ij}(l_x, l_y, l_z) - \rho\omega^2\delta_{ij}| = 0 \tag{B.5}$$

At a fixed wave frequency ω, this relation defines a surface in k space that gives k as a function of its direction $\hat{\mathbf{l}}$, where, $\hat{\mathbf{l}} = \hat{\mathbf{x}}l_x + \hat{\mathbf{y}}l_y + \hat{\mathbf{z}}l_z$. This is called *wave vector surface.* The wave vector $\hat{\mathbf{k}}$ is always proportional to wave frequency ω. In analysis of Christoffel equation, it is very convenient to consider *slowness surface*, rather than velocity. A slowness surface describe the inverse of the phase velocity as a function

[1]The strains can be expressed as $S_{ij} = s_{ijkl}T_{kl}$, $(i, j, k, l = x, y, z)$
where s_{ijkl} are called compliance constants.

of propagation direction, $k/\omega = 1/V_p$. Note that the slowness surface is independent of frequency ω, unlike the wave vector surface which scales with ω.

Once the characteristic equation B.5 has been solved, the particle velocity polarization may be obtained from the Christoffel equation. In general, numerical computation is required for this procedure, but for special cases the entire calculation can be performed analytically.

B.2.1 Transverse isotropic medium

Symmetry elements in the material further reduce the number of independent stiffness constants. A *transversely isotropic or hexagonally symmetric medium*, like shale, may contains one axis of rotational symmetry, say the Z axis, oriented such that material properties are the same in all directions perpendicular to it. The plane of the circular symmetry is defined by the X and Y axes.

In such a case, it has been proven that there are only five independent nonzero elastic stiffness constants with $c_{66} = 1/2(c_{11} - c_{12})$. In compressed notation, the strain and stress relations and the associated stiffness constants matrix for transversely isotropic media take the form

$$\begin{pmatrix} T_1 \\ T_2 \\ T_3 \\ T_4 \\ T_5 \\ T_6 \end{pmatrix} = \begin{pmatrix} c_{11} & c_{12} & c_{13} & 0 & 0 & 0 \\ c_{12} & c_{11} & c_{13} & 0 & 0 & 0 \\ c_{13} & c_{13} & c_{33} & 0 & 0 & 0 \\ 0 & 0 & 0 & c_{44} & 0 & 0 \\ 0 & 0 & 0 & 0 & c_{44} & 0 \\ 0 & 0 & 0 & 0 & 0 & c_{66} \end{pmatrix} \begin{pmatrix} S_1 \\ S_2 \\ S_3 \\ S_4 \\ S_5 \\ S_6 \end{pmatrix} \tag{B.6}$$

The *Christoffel equation* for transversely isotropic medium appears in the form:

$$k^2 \begin{pmatrix} \alpha & \delta & \epsilon \\ \delta & \beta & \zeta \\ \epsilon & \zeta & \gamma \end{pmatrix} \begin{pmatrix} v_x \\ v_y \\ v_z \end{pmatrix} = \rho\omega^2 \begin{pmatrix} v_x \\ v_y \\ v_z \end{pmatrix} \tag{B.7}$$

where the *Christoffel matrix elements* are

$$\begin{cases} \alpha = c_{11}l_x^2 + c_{66}l_y^2 + c_{44}l_z^2 \\ \beta = c_{66}l_x^2 + c_{11}l_y^2 + c_{44}l_z^2 \\ \gamma = c_{44}l_x^2 + c_{44}l_y^2 + c_{33}l_z^2 \\ \delta = (c_{66} + c_{12})l_x l_y \\ \epsilon = (c_{44} + c_{13})l_z l_x \\ \zeta = (c_{44} + c_{13})l_y l_z \end{cases}$$

and the the directional cosines of the propagation direction may be expressed as

$$\begin{cases} l_x = k_x/k \\ l_y = k_y/k \\ l_z = k_z/k \end{cases}$$

For transversely isotropic materials, the characteristic equation factors when wave propagating in the $X-Y$ plane, that is, normal to the Z-axis. The dispersion relation is independent of the propagation direction in this plane. There is one pure shear mode,

$$\left(\frac{k}{\omega}\right)_2 = \left(\frac{\rho}{c_{66}}\right)^{1/2} \tag{B.8}$$

polarized normal to Z-axis; another pure shear mode,

$$\left(\frac{k}{\omega}\right)_1 = \left(\frac{\rho}{c_{44}}\right)^{1/2} \tag{B.9}$$

polarized parallel to Z-axis; and a pure longitudinal mode,

$$\left(\frac{k}{\omega}\right)_3 = \left(\frac{\rho}{c_{11}}\right)^{1/2} \tag{B.10}$$

polarized any direction perpendicular to the Z-axis.

The characteristic equation also factors when wave propagating in the $X-Z$, or $Y-Z$ plane. Since the *Christoffel equation* can be shown to be symmetric with respect to an arbitrary rotation about the Z-axis, the same dispersion relation will apply for any meridian plane, too. That is, the wave vector surface is always rotationally symmetric in transversely isotropic media.

There is one pure shear mode,

$$\left(\frac{k}{\omega}\right)_2 = \left(\frac{2\rho}{c_{66}\sin^2\theta + c_{44}\cos^2\theta}\right)^{1/2} \tag{B.11}$$

polarized normal to the meridian plane containing k. The other solutions are a quasishear wave,

$$\begin{aligned}\left(\tfrac{k}{\omega}\right)_1 = \; & (2\rho)^{1/2}\{c_{11}\sin^2\theta + c_{33}\cos^2\theta + c_{44} \\ & -\sqrt{[(c_{11}-c_{44})\sin^2\theta + (c_{44}-c_{33})\cos^2\theta]^2 + (c_{13}+c_{44})^2\sin^2 2\theta}\}^{-1/2}\end{aligned} \tag{B.12}$$

and a quasilongitudinal wave,

$$\begin{aligned}\left(\tfrac{k}{\omega}\right)_3 = \; & (2\rho)^{1/2}\{c_{11}\sin^2\theta + c_{33}\cos^2\theta + c_{44} \\ & +\sqrt{[(c_{11}-c_{44})\sin^2\theta + (c_{44}-c_{33})\cos^2\theta]^2 + (c_{13}+c_{44})^2\sin^2 2\theta}\}^{-1/2}\end{aligned} \tag{B.13}$$

with the directional angle θ measured away from the Z axis.

In general, rocks devoid of cracks or fractures along their bedding planes, such as shales, can be considered transversely isotropic with the symmetry axis normal to the bedding, or lamination plane. As with other transversely isotropic media, five independent elastic stiffness constants are sufficient number of the complete description for these rocks.

$$\begin{cases} c_{11} = \rho V_{xx}^2 = \rho V_{yy}^2 \\ c_{33} = \rho V_{zz}^2 \\ c_{44} = \rho V_{xy}^2 = \rho V_{xy}^2 \\ c_{66} = \rho V_{xz}^2 = \rho V_{yz}^2 = \rho V_{zx}^2 \rho V_{zy}^2 \\ c_{13} = \sqrt{4\rho^2 V_{P(45)}^4 - 2\rho V_{P(45)}^2 (c_{11}+c_{33}+2c_{44}) + (c_{11}+c_{44})(c_{33}+c_{44})} - c_{44} \end{cases} \tag{B.14}$$

with $c_{12} = c_{11} - 2c_{66}$.

By measuring five different velocities in different orientations, we can estimate all the elastic stiffness constants in Equation B.14 and characterize a transversely

isotropic medium. Labeling the axes with respect to the transversely isotropic symmetry of the medium, one may often find following notation in geophysics literature

$$\begin{cases} V_{P(\|)} = V_{xx} = V_{yy} \\ V_{P(\perp)} = V_{zz} \\ V_{SH} = V_{xy} = V_{yx} \\ V_{SV} = V_{xz} = V_{yz} = V_{zx} = V_{zy} \end{cases}$$

where $V_{P(\|)}$ refers to P-wave propagating to parallel the earth surface plane, $V_{P(\perp)}$ refers to P-wave propagating perpendicular to the earth surface plane, V_{SH} refers to S-wave propagating and polarized parallel to the earth surface plane, and V_{SV} refers to either S-wave propagating perpendicular and polarized parallel to the earth surface plane, or S-wave propagating parallel and polarized perpendicular to the earth surface plane.

B.2.2 Orthorhombic anisotropic medium

Orthorhombic symmetry has three mutually orthogonal planes of symmetry. In such a case, it has been proved that there are nine independent nonzero constants. In compressed notation, the strain and stress relations and the associated stiffness constants matrix for orthorhombic symmetry takes the form

$$\begin{pmatrix} T_1 \\ T_2 \\ T_3 \\ T_4 \\ T_5 \\ T_6 \end{pmatrix} = \begin{pmatrix} c_{11} & c_{12} & c_{13} & 0 & 0 & 0 \\ c_{21} & c_{22} & c_{23} & 0 & 0 & 0 \\ c_{31} & c_{32} & c_{33} & 0 & 0 & 0 \\ 0 & 0 & 0 & c_{44} & 0 & 0 \\ 0 & 0 & 0 & 0 & c_{55} & 0 \\ 0 & 0 & 0 & 0 & 0 & c_{66} \end{pmatrix} \begin{pmatrix} S_1 \\ S_2 \\ S_3 \\ S_4 \\ S_5 \\ S_6 \end{pmatrix} \tag{B.15}$$

Christoffel equation for orthorhombic medium appears in the form

$$k^2 \begin{pmatrix} \alpha & \delta & \epsilon \\ \delta & \beta & \zeta \\ \epsilon & \zeta & \gamma \end{pmatrix} \begin{pmatrix} v_x \\ v_y \\ v_z \end{pmatrix} = \rho\omega^2 \begin{pmatrix} v_x \\ v_y \\ v_z \end{pmatrix} \tag{B.16}$$

with the *Chiristoffel matrix elements* as

$$\begin{cases} \alpha = c_{11}l_x^2 + c_{66}l_y^2 + c_{55}l_z^2 \\ \beta = c_{66}l_x^2 + c_{22}l_y^2 + c_{44}l_z^2 \\ \gamma = c_{55}l_x^2 + c_{44}l_y^2 + c_{33}l_z^2 \\ \delta = (c_{66} + c_{12})l_x l_y \\ \epsilon = (c_{55} + c_{13})l_z l_x \\ \zeta = (c_{44} + c_{23})l_y l_z \end{cases}$$

For orthorhombic anisotropic materials, the characteristic equation factors when wave propagating in the $X-Y, X-Z$, and $Y-Z$ planes.

In the $X-Y$ plane, the pure shear wave polarized along Z axis is

$$(k/\omega)_1 = \left(\frac{\rho}{c_{44}\cos^2\phi + c_{55}\sin^2\phi}\right)^{1/2}. \tag{B.17}$$

The quasishear wave is

$$\begin{aligned}(k/\omega)_2 = \; & (2\rho)^{1/2}\{c_{11}\cos^2\phi + c_{22}\sin^2\phi + c_{66} \\ & -\sqrt{(c_{66} + c_{11}\cos^2\phi + c_{22}\sin^2\phi)^2 - 4C_I}\}^{-1/2},\end{aligned} \tag{B.18}$$

and the quasilongitudinal wave is

$$\begin{aligned}(k/\omega)_3 = \; & (2\rho)^{1/2}\{c_{11}\cos^2\phi + c_{22}\sin^2\phi + c_{66} \\ & +\sqrt{(c_{66} + c_{11}\cos^2\phi + c_{22}\sin^2\phi)^2 - 4C_I}\}^{-1/2},\end{aligned} \tag{B.19}$$

where $C_I = (c_{11}\cos^2\phi + c_{66}\sin^2\phi)(c_{66}\cos^2\phi + c_{22}\sin^2\phi) - (c_{12} + c_{66})^2\sin^2\phi\cos^2\phi$.

For wave propagating in the $X-Z$ plane, the pure shear wave polarized along Y axis is

$$(k/\omega)_1 = \left(\frac{\rho}{c_{66}\sin^2\phi + c_{44}\cos^2\phi}\right)^{1/2}. \tag{B.20}$$

The quasishear wave is

$$\begin{aligned}(k/\omega)_2 = \; & (2\rho)^{1/2}\{c_{11}\sin^2\phi + c_{33}\cos^2\phi + c_{55} \\ & -\sqrt{(c_{55} + c_{11}\sin 2\phi + c_{33}\cos^2\phi)^2 - 4C_{II}}\}^{-1/2},\end{aligned} \tag{B.21}$$

and the quasilongitudinal wave is

$$(k/\omega)_3 = (2\rho)^{1/2}\{c_{11}\sin^2\phi + c_{33}\cos^2\phi + c_{55} + \sqrt{(c_{55} + c_{11}\sin 2\phi + c_{33}\cos^2\phi)^2 - 4C_{II}}\}^{-1/2} \tag{B.22}$$

where $C_{II} = (c_{11}\sin^2\phi + c_{55}\cos^2\phi)(c_{55}\sin^2\phi + c_{33}\cos^2\phi) - (c_{13} + c_{55})^2\sin^2\phi\cos^2\phi$.

For wave propagating in the $Y - Z$ plane, the pure shear wave polarized along the X axis is

$$(k/\omega)_1 = \left(\frac{\rho}{c_{66}\sin^2\phi + c_{55}\cos^2\phi}\right)^{1/2}. \tag{B.23}$$

The quasishear wave is

$$(k/\omega)_2 = (2\rho)^{1/2}\{c_{22}\sin^2\phi + c_{33}\cos^2\phi + c_{44} - \sqrt{(c_{44} + c_{22}\sin 2\phi + c_{33}\cos^2\phi)^2 - 4C_{III}}\}^{-1/2}, \tag{B.24}$$

and the quasilongitudinal wave,

$$(k/\omega)_3 = (2\rho)^{1/2}\{c_{22}\sin^2\phi + c_{33}\cos^2\phi + c_{44} + \sqrt{(c_{44} + c_{22}\sin 2\phi + c_{33}\cos^2\phi)^2 - 4C_{III}}\}^{-1/2} \tag{B.25}$$

where $C_{III} = (c_{22}\sin^2\phi + c_{44}\cos^2\phi)(c_{44}\sin^2\phi + c_{33}\cos^2\phi) - (c_{23} + c_{44})^2\sin^2\phi\cos^2\phi$.

The directional angle ϕ is measured from the Y axis in the $X - Y$ plane, and the Z axis in the $X - Z$ plane or the $Y - Z$ plane (after Auld, 1973).

If the wave vector direction and polarization direction of particle motion are aligned parallel or normal to the Cartesian coordinates axes, X, Y, or Z, we can deduce the following simple phase velocity equations from the characteristic equation above.

In the $X - Y$ plane, these are

$$\begin{cases} V_{xz} = \sqrt{c_{55}/\rho} \\ V_{yz} = \sqrt{c_{44}/\rho} \\ V_{xy} = \sqrt{c_{66}/\rho} \\ V_{yx} = \sqrt{c_{66}/\rho} \\ V_{xx} = \sqrt{c_{11}/\rho} \\ V_{yy} = \sqrt{c_{22}/\rho} \\ V_{45-xy} = \sqrt{[c_{11} + c_{22} + 2c_{66} + \sqrt{(c_{11} - c_{22})^2 + 4(c_{12} + c_{66})^2}]/4\rho}. \end{cases} \tag{B.26}$$

In the $X - Z$ plane, these are

$$\begin{cases} V_{xy} = \sqrt{c_{66}/\rho} \\ V_{zy} = \sqrt{c_{44}/\rho} \\ V_{xz} = \sqrt{c_{55}/\rho} \\ V_{zx} = \sqrt{c_{55}/\rho} \\ V_{xx} = \sqrt{c_{11}/\rho} \\ V_{zz} = \sqrt{c_{33}/\rho} \\ V_{45-xz} = \sqrt{[c_{11} + c_{33} + 2c_{55} + \sqrt{(c_{11} - c_{33})^2 + 4(c_{13} + c_{55})^2}]/4\rho}. \end{cases} \tag{B.27}$$

And in $Y - Z$ plane, these are

$$\begin{cases} V_{zx} = \sqrt{c_{55}/\rho} \\ V_{yx} = \sqrt{c_{66}/\rho} \\ V_{zy} = \sqrt{c_{44}/\rho} \\ V_{yz} = \sqrt{c_{44}/\rho} \\ V_{yy} = \sqrt{c_{22}/\rho} \\ V_{zz} = \sqrt{c_{33}/\rho} \\ V_{45-yz} = \sqrt{[c_{22} + c_{33} + 2c_{44} + \sqrt{(c_{22} - c_{33})^2 + 4(c_{23} + c_{44})^2}]/4\rho}. \end{cases} \tag{B.28}$$

In the above phase velocity and elastic constant relations, The first subscript of the phase velocities $V_{i,j}$ ($i = x, y, z$ and $j = x, y, z$) stands for the propagation direction of the wave, and the second subscript stands for the wave's particle polarization direction. By the definition of P-wave and S-wave, those waves with different first and second subscripts must propagate as shear waves, while those waves with two same

subscripts must travel as longitudinal waves. Those waves with subscripts of from $45-ij$ are longitudinal waves that propagate on the ij planes with their propagation direction 45° to one of the adjacent principal axes on that plane (Figure 5.2-a).

For this more complicated orthorhombic material, we can still estimate all nine independent elastic stiffness constants. To do this, we need to measure one P-mode and two orthogonal S-mode phase velocities for each of three principal axes, and a P-mode along each of three diagonal directions in three mutually orthogonal planes. we could verify whether the medium possess three orthogonal axes of two-fold symmetry, or whether the sample symmetry is aligned to the measurement symmetry with the above twelve phase velocity measurements. If so, then $V_{xy} = V_{yx}$, $V_{xz} = V_{zx}$, and $V_{xy} = V_{yx}$—these conditions must be satisfied for orthorhombic symmetry. Consequently, all nine elastic stiffness constants can be inferred for describing orthorhombic anisotropic medium.

B.3 Phase velocity and group velocity

With pulse transmission technique in the laboratory. We may only observe group velocities if the medium is anisotropic, even though we would like to measure phase velocities. Along the principal axes, the phase and group velocities are equal even in anisotropic medium, so the stiffness constants could be calculated directly by using equations in section B.2.

For waves propagating along the diagonal paths, the direction of the wavefront normal to the phase velocity direction is not necessarily aligned with the direction of the ray-path, the group velocity direction, because the wavefront, in general, is not spherical in anisotropic medium. This phase front and ray-path misalignment does not allow us to make simple substitutions for $l_i = 0$ or $l_i = 1/\sqrt{2}$ for 45°) in the characteristic equations described in section B.2.

The relations between group velocity and phase velocity in anisotropic media have

been discussed in many studies (Musgrave 1970, Auld 1973, Crampin 1981, Thomsen 1986, Kendall and Thomson 1989). Here we have adapted Auld's notation (Auld, 1973).

For a three-dimensional modulation envelope, the group velocity has the following form

$$\mathbf{v_g} = \hat{x}\frac{\partial\omega}{\partial k_x} + \hat{y}\frac{\partial\omega}{\partial k_y} + \hat{z}\frac{\partial\omega}{\partial k_z}. \tag{B.29}$$

Therefore, the group velocities can be evaluated by

$$\mathbf{v_g} = -\frac{\nabla_k\Omega}{\partial\Omega/\partial\omega}, \tag{B.30}$$

where the gradient of Ω is taken respect to wave vectors k_x, k_y, and k_z.

From Equation B.5, we have the characteristic equation determinant for orthorhombic symmetry as

$$\begin{vmatrix} (\frac{k}{\omega})^2(c_{11}l_x^2 + c_{66}l_y^2 + c_{55}l_z^2) - \rho, (\frac{k}{\omega})^2(c_{66} + c_{12})l_xl_y), (\frac{k}{\omega})^2(c_{55} + c_{13})l_zl_x) \\ (\frac{k}{\omega})^2(c_{66} + c_{12})l_xl_y), (\frac{k}{\omega})^2(c_{66}l_x^2 + c_{22}l_y^2 + c_{44}l_z^2) - \rho, (\frac{k}{\omega})^2(c_{44} + c_{23})l_yl_z) \\ (\frac{k}{\omega})^2(c_{55} + c_{13})l_zl_x), (\frac{k}{\omega})^2(c_{44} + c_{23})l_yl_z), (\frac{k}{\omega})^2(c_{55}l_x^2 + c_{44}l_y^2 + c_{33}l_z^2) - \rho \end{vmatrix} = 0. \tag{B.31}$$

In $Y - Z$ plane, for example, $l_x = 0$, and the dispersion relation can be separated into one linear factor

$$(\frac{k}{\omega})^2(c_{66}l_y^2 + c_{55}l_z^2) - \rho = 0 \tag{B.32}$$

that is pure shear mode, and one quadratic factor

$$[(\frac{k}{\omega})^2(c_{22}l_y^2 + c_{44}l_z^2) - \rho][(\frac{k}{\omega})^2(c_{44}l_y^2 + c_{33}l_z^2) - \rho] - (\frac{k}{\omega})^4(c_{44} + c_{23})^2l_y^2l_z^2 = 0. \tag{B.33}$$

Then Ω can be given as

$$\Omega = (c_{22}k_y^2 + c_{44}k_z^2 - \rho\omega^2)(c_{44}k_y^2 + c_{33}k_z^2 - \rho\omega^2) - (c_{44} + c_{23})^2 k_y^2 k_z^2 = 0 \qquad \text{(B.34)}$$

for quasishear and quasilongitudinal waves, since $l_x = k_x/k$, $l_y = k_y/k$, and $l_x = k_x/k$. The dispersion relation can then be separated by implicit differentiation

$$\begin{cases} \frac{\partial\Omega}{\partial k_x} = 0 \\ \frac{\partial\Omega}{\partial k_y} = 2k_y c_{22}(c_{44}k_y^2 + c_{33}k_z^2 - \rho\omega^2) + 2k_y c_{44}(c_{22}k_y^2 + c_{44}k_z^2 - \rho\omega^2) - 2k_y(c_{44} + c_{23})^2 k_z^2 \\ \frac{\partial\Omega}{\partial k_z} = 2k_z c_{44}(c_{44}k_y^2 + c_{33}k_z^2 - \rho\omega^2) + 2k_z c_{33}(c_{22}k_y^2 + c_{44}k_z^2 - \rho\omega^2) - 2k_z(c_{44} + c_{23})^2 k_y^2 \\ \frac{\partial\Omega}{\partial\omega} = -2\rho\omega(c_{44}k^2 + c_{22}k_y^2 + c_{33}k_z^2 - 2\rho\omega^2) \end{cases} \qquad \text{(B.35)}$$

From the geometric relationships, $\theta = \arccos l_y$, and $\psi = 45° - \theta$ as shown in Figure B.1. Now, we have

$$(V_{ij})_\phi = (v_{ij})_g \cos\psi = (1/\sqrt{2})(l_y + l_z)(v_{ij})_g. \qquad \text{(B.36)}$$

with g implying "group" and ϕ implying "phase". Substituting this relationship between phase and group velocity into above dispersion equation B.34, we get

$$\begin{aligned} v_{45-yz}^4(l_y + l_z)^3(l_y - l_z) + 2v_{45-yz}(l_y + l_z)[l_y^3(v_{yy}^2 + v_{yz}^2) - l_z^2(v_{zz}^2 + v_{yz}^2)] \\ +4(l_z^4 v_{zz}^2 - l_y^4 v_{yy}^2)v_{yz}^2 = 0 \end{aligned} \qquad \text{(B.37)}$$

for quasilongitudinal mode propagating along the diagonal direction in $Y - Z$ plane.

The small v_{ij} represents the group velocities, and that can be estimated through laboratory experiments in various directions. In principle, equations, like B.37 can be solved for l_y and l_z, since we know that $l_y^2 + l_z^2 = 1$. In practice, l_y and l_z can also be determined by iterative substitution. Similar analysis can be done for the $X - Y$ and $X - Z$ planes. The general expressions for stiffness constants as function of group, or ray velocities for orthorhombic symmetry are

$$
\begin{cases}
c_{11} = \rho v_{xx}^2 \\
c_{22} = \rho v_{yy}^2 \\
c_{33} = \rho v_{zz}^2 \\
c_{44} = \rho v_{yz}^2 = \rho v_{zy}^2 \\
c_{55} = \rho v_{xz}^2 = \rho v_{zx}^2 \\
c_{66} = \rho v_{xy}^2 = \rho v_{yx}^2 \\
c_{12} = \frac{\rho}{l_x l_y}\sqrt{[\frac{1}{2}(l_x+l_y)^2 v_{45-xy}^2 - l_x^2 v_{xy}^2 - l_y^2 v_{yy}^2][\frac{1}{2}(l_x+l_y)^2 v_{45-xy}^2 - l_x^2 v_{xx}^2 - l_y^2 v_{xy}^2]} - \rho v_{xy}^2 \\
c_{13} = \frac{\rho}{l_x l_z}\sqrt{[\frac{1}{2}(l_x+l_z)^2 v_{45-xz}^2 - l_z^2 v_{zx}^2 - l_x^2 v_{xx}^2][\frac{1}{2}(l_x+l_z)^2 v_{45-xz}^2 - l_z^2 v_{zz}^2 - l_x^2 v_{zx}^2]} - \rho v_{zx}^2 \\
c_{23} = \frac{\rho}{l_y l_z}\sqrt{[\frac{1}{2}(l_y+l_z)^2 v_{45-yz}^2 - l_y^2 v_{yz}^2 - l_z^2 v_{zz}^2][\frac{1}{2}(l_y+l_z)^2 v_{45-yz}^2 - l_y^2 v_{yy}^2 - l_z^2 v_{yz}^2]} - \rho v_{yz}^2
\end{cases}
\tag{B.38}
$$

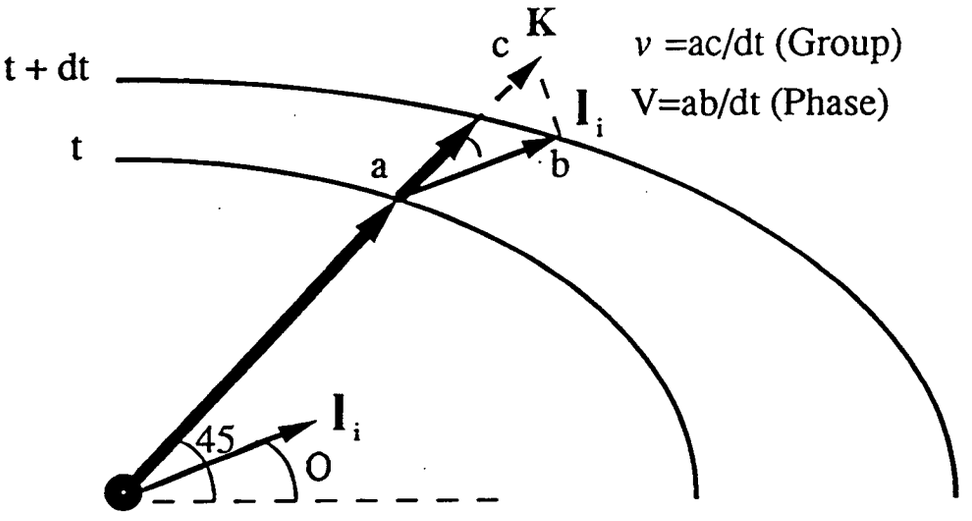

Figure B.1: Geometric relation between group (ray) velocity and phase velocity.

B.4 Summary

Collectively, the relations provided in this appendix allow an experimentalist to deduce the full suit of independent elastic stiffness coefficients (21), not just the transverse isotropy, or orthorhombic anisotropy. The constraint is that shear velocity must vary symmetrically from one axis to another. That is, for example in orthorhombic anisotropic case, $V_{xy} = V_{yx}$,$V_{xz} = V_{zx}$, and $V_{yz} = V_{zy}$. With three-component trans-

ducers and the above constraint, we can readily verify the least anisotropic symmetries of a rock sample under test, or whether the measurement directions are aligned with the rock sample's anisotropic symmetry.

References

Auld, B. A., 1973, Acoustic Fields and Waves in Solids, Vol. 1, New York: John Wiley & Sons, Inc.

Crampin, S., 1984, An introduction to wave propagation in anisotropic media, Geophys. J. R. astr. Soc., 76, 17-28

Muir, F. and Dellinger, J., 1985, A practical anisotropic system, SEP -44, 55-58

Musgrave, M. J. P., 1970, Crystal Acoustics, Holden-Day, Inc.

Musgrave, M. J. P., 1980, On an elastodynamic classification of orthorhombic media, Proc. R. Soc. Lond. A, 374, 401-429

Appendix C

Low impedance cross-well logging downhole source — Invention and technology disclosure

This appendix chapter presents a novel design of borehole seismic source. The design was partially resulted from an in-situ wave velocity and attenuation measurement in unconsolidated marine sediments—San Fransisco Bay marsh— with specially designed low impedance acoustic transducers perform by SRB in 1989. The principal of lowing these transducers acoustic impedance was applied to design the present low impedance borehole seismic source which was awarded U.S. patent, No. 5,069,308. The innovation of the patent is the optimal impedance match between piezoelectric ceramic stack and borehole environment through specially configured mechanical transformer.

C.1 Introduction

Looking back at the accomplishments of the past three decades in the acoustic logging tool field, we can see that development in downhole source design have been spurred on by many motivating forces. The advent of new piezoelectric, structural materials and solid-state electronic devices has led to substantial improvements in downhole transducer performance with respect to frequency range, sensitivity, submerged depth, and output power. Theory has kept abreast of these developments,

particularly in delivering advantages from sonic full waveform recording. These improvements have mostly contributed to the field of acoustic well-logging where the sources and receivers are placed in the same borehole.

As we continue to adapt the source and receiver configuration to cross-well logging (the source in one well and the receiver in another well, and the distance between the two wells may reach a few hundred meters), the output power of a normal piezoelectric source remains very limited, particularly due a large impedance mismatch between the piezoelectric source and the wellbore fluid. Alternative borehole seismic sources, such as air-guns and other nondestructive hydraulic sources, have been developed with sufficient power output, but with less operational convenience than piezoelectric source. The convenience of frequency control in designing piezoelectric source has led people back to the use of piezoelectrical elements for downhole sources, and resulted in "bender bars" or cylindrical "bender bars" as cross-well logging downhole sources. Yet the complex technical process of constructing the "bend bar" with hundreds of piezoelectric elements could result in inconsistencies with the design expected central frequency, output power, and so on.

A simple impedance matching design was devised in U.S. patent, No. 5,069,308, "Low Impedance Down-hole Acoustic Source for Well Logging," by Yin, Harris and Nur (1991). The impedance matching design has combined several new techniques from the fields of acoustic wave generation. First, the vibrating source is a piezoelectric ceramic stack to have a larger displacement output than single piezoelectric ceramic. Second, the displacement produced by the stack is further enlarged by mechanical levers and compliant mechanical transformer for impedance matching. Third, it radiates energy from the excitation of structural flexing modes. The novel aspects of the patent are its conceptual advances in mechanical transformer for improved impedance match and radiation directivity, and its free-flooding cavity structure for balancing pressure and operating the source at great depth.

C.2 Impedance matching principle

Acoustic impedance Z is defined as

$$Z = \frac{P}{u} = \rho V, \tag{C.1}$$

where P is the stress induced by piezoelectric ceramic in response to an applied electrical field; u is the particle velocity, ρ is the density of the PZT-ceramic, V is the acoustic velocity of the PZT-ceramic.

PZT-4, a common piezoelectric ceramic, has an acoustic impedance $Z_p = \rho V_l = 4.6 \times 10^3 m/s \times 7.5 \times 10^3 kg/m^3 = 34.5 \times 10^6 kg/s \cdot m^2$, which is about 20 times that of borehole mud. Since the efficiency of energy transfer across an interface depends on the similarity of two impedances across the interface, coupling would be very poor if the piezoelectric ceramic were in direct contact with the borehole fluid.

By increasing the particle velocity of the response to a given piezoelectric stress, the acoustic impedance may be lowered to required. This idea was first introduced and patented by W.J Toulis, and named as "High Power Flextensional Transducer" in 1963. While the idea has been applied several times since then, seldom has its effectiveness been reviewed as a result of impedance adjustment.

C.2.1 Maximum displacement along an ellipse's axes

Elliptical Integral:

A mathematical analysis on the mechanical transformer may reveal the nature of the flextensional transducers—lowering acoustic impedance. An elliptic function in cartesian coordinates can be expressed as the following

$$\frac{x^2}{a^2} + \frac{y^2}{b^2} = 1. \tag{C.2}$$

Or solved for y,

$$y = \pm\frac{b}{a}\sqrt{a^2 - x^2}. \tag{C.3}$$

The first derivative of Equation C.3 with respect to x is

$$\frac{dy}{dx} = \pm\frac{b}{a}\frac{x}{\sqrt{a^2 - x^2}} \tag{C.4}$$

Assuming a constant circumference of the ellipse, we wish to solve the displacement Δy along the minor axis for a given displacement Δx along the major axis. By means of a line integral, we can express the circumference of an ellipse as

$$S = 4\int_0^a \sqrt{1 + (\frac{dy}{dx})^2}dx \tag{C.5}$$

Insert Equation C.4 into C.5, we get

$$S = 4\int_0^a \sqrt{1 + \frac{b^2x^2}{a^2(a^2 - x^2)}}dx \tag{C.6}$$

By defining parameters $x = at$, and $K = \sqrt{1 - (b/a)^2}$, we have

$$S = 4a\int_0^1 \frac{dt}{\sqrt{(1 - t^2)(1 - K^2t^2)}} - 4aK^2\int_0^1 \frac{t^2dt}{\sqrt{(1 - t^2)(1 - K^2t^2)}} \tag{C.7}$$

It has been proven that no analytical solution of the above elliptical integral C.7 exist. Numerical approximations can be found for the first and second types of elliptical integrals above. The combined solution can be expressed as

$$S = 4aE(\frac{\pi}{2}, k) = 4a\{\frac{\pi}{2}[1 - (\frac{1}{2}K)^2 - (\frac{1\cdot 3}{2\cdot 4})\frac{K^4}{3} - (\frac{1\cdot 3\cdot 5}{2\cdot 4\cdot 6})^2\frac{K^6}{5} \cdots]\} \tag{C.8}$$

Displacement Δy caused by displacement Δx:

Using only the second order term in Equation c.8, we have

$$S \approx 4a[\frac{\pi}{2}(1 - \frac{1}{4}K^2)] = \frac{\pi}{2}[3a + \frac{b^2}{a}] \tag{C.9}$$

This approximation causes about 4% relative error when the ratio of the major axis a over the minor axis b is 5, $a/b = 5$. If we assume a constant circumference, then a change Δx in an ellipse's major axis may yield a change Δy in the ellipse's minor axis, and the relation may be expressed as

$$\frac{\pi}{2}[3(a+\Delta x)+\frac{(b+\Delta y)^2}{a}] = \frac{\pi}{2}[3a+\frac{b^2}{a}] \tag{C.10}$$

which can be rearranged as

$$3a \cdot \Delta x + 2b \cdot \Delta y + \Delta y^2 = 0 \tag{C.11}$$

Neglecting the second order term, we get

$$\Delta y = -\frac{3a}{2b}\Delta x \tag{C.12}$$

Arranging a PZT crystal or a PZT stack which induce a displacement Δx along an ellipse's major axis, we may obtain an enlarged displacement Δy along the ellipse's minor axis, based on Equation C.12. The larger the ratio a/b, the greater the Δy is for a given Δx. Practical limits on this may be imposed by the elastic rigidity of the material used to construct the elliptic shell, the pressure range of the transducer's operating environment.

C.2.2 Increasing particle velocity to lower impedance

Consider the particle velocity u in Equation C.1. Particle acceleration is related to acoustic pressure gradient. From the Newton's Second Law of Motion, the particle velocity u over a quarter cycle of oscillatory motion may be defined as

$$u = \int_0^{\tau/4} \omega^2 \Delta x dt = \pi^2 \cdot \Delta x \cdot f \tag{C.13}$$

where ω is the angular frequency of the oscillating PZT stack, Δx is the displacement produced by the PZT stack, τ is the resonant period of the stack, and f is the resonant

frequency of the stack.

We have demonstrated that an ellipse attains its maximum displacement Δy along its minor axis for a given displacement Δx along its major axis. This mechanism can serve as the basis of designing "mechanical transformer". By placing a longitudinally polarized piezoelectric ceramic stack along the major axis of an elliptically shaped metal beams, we may obtain an enlarged displacement along the beams minor axis (Figure C.1).

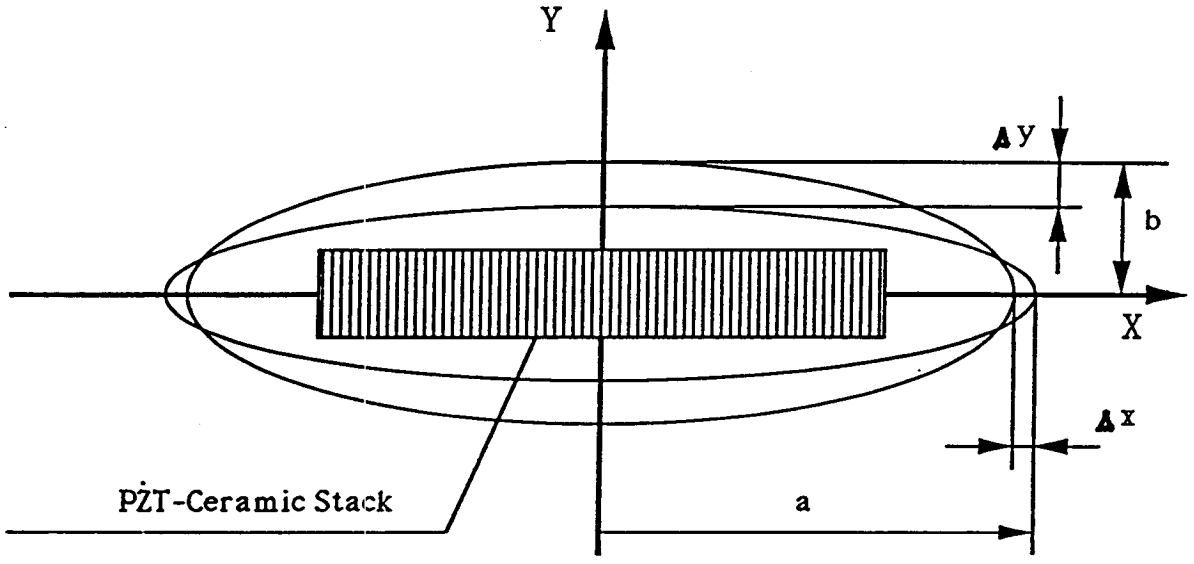

Figure C.1: This schematic diagram shows how an elliptically shaped transducer (flextensional transducer) could lower the impedance. Assuming that circumference of the elliptic remains constant, we have seen that an ellipse has displacement $\Delta y = -1.5(a/b)\Delta x$ along its minor axis for a given displacement Δx along its major axis. Therefore, particle velocity u is increased, and acoustic impedance Z is lowered along the ellipse's minor axis.

Substituting Δx with Δy in Equation C.13, we can see that the maximum particle velocity along the elliptical transducer's minor axis may be enlarged by a factor of $1.5a/b$. Consequently, the acoustic impedance of the transducer as a system may be lowered by the inverse of above ratio, factor $2b/3a$, in Equation C.1. Adjusting the

elliptical transformer's geometry, the a/b ratio, we can match the impedance to a required value. This is the kernel of the so called Flextensional transducers.

C.3 Mechanical transformer design for downhole purpose

In section C.2, we showed how a mechanical transformer can lower the acoustic impedance. In this section, I expanded these ideas to apply the transformer to borehole environment. Figure C.2 is a schematic drawing of the mechanical transformer for borehole use.

To focus acoustic energy into the borehole wall and to radiate energy symmetrically perpendicular to the axis of the borehole, we cut the ellipse along its major axis so that the acoustic energy is focused and radiated from the ellipse concave side. Note that the flextensional transducer radiates energy from ellipse convex side. We place six elliptically curved metal spring beams around the axis in a drum-like shape to provide a symmetric radiation pattern around borehole. To reduce friction among the beams, levers, and PZT stack joints, we can use ball bearings in each of those joint.

C.3.1 Transverse vibration of a uniform beam

For efficient transfer of energy from PZT stack to mechanical transformer, we need to match their resonant frequency. Thus, we need to calculate the resonant characteristics of the beams.

The transverse vibrations of a uniform beam are a special case of the ellipse deformation described in Section C.2.

In Figure C.3, an element of a thin beam was shaded. As the beam flexes in transverse vibration, the element will move up and down along the Y-direction. It may also rotate slightly because the compression in concave side and tension in the

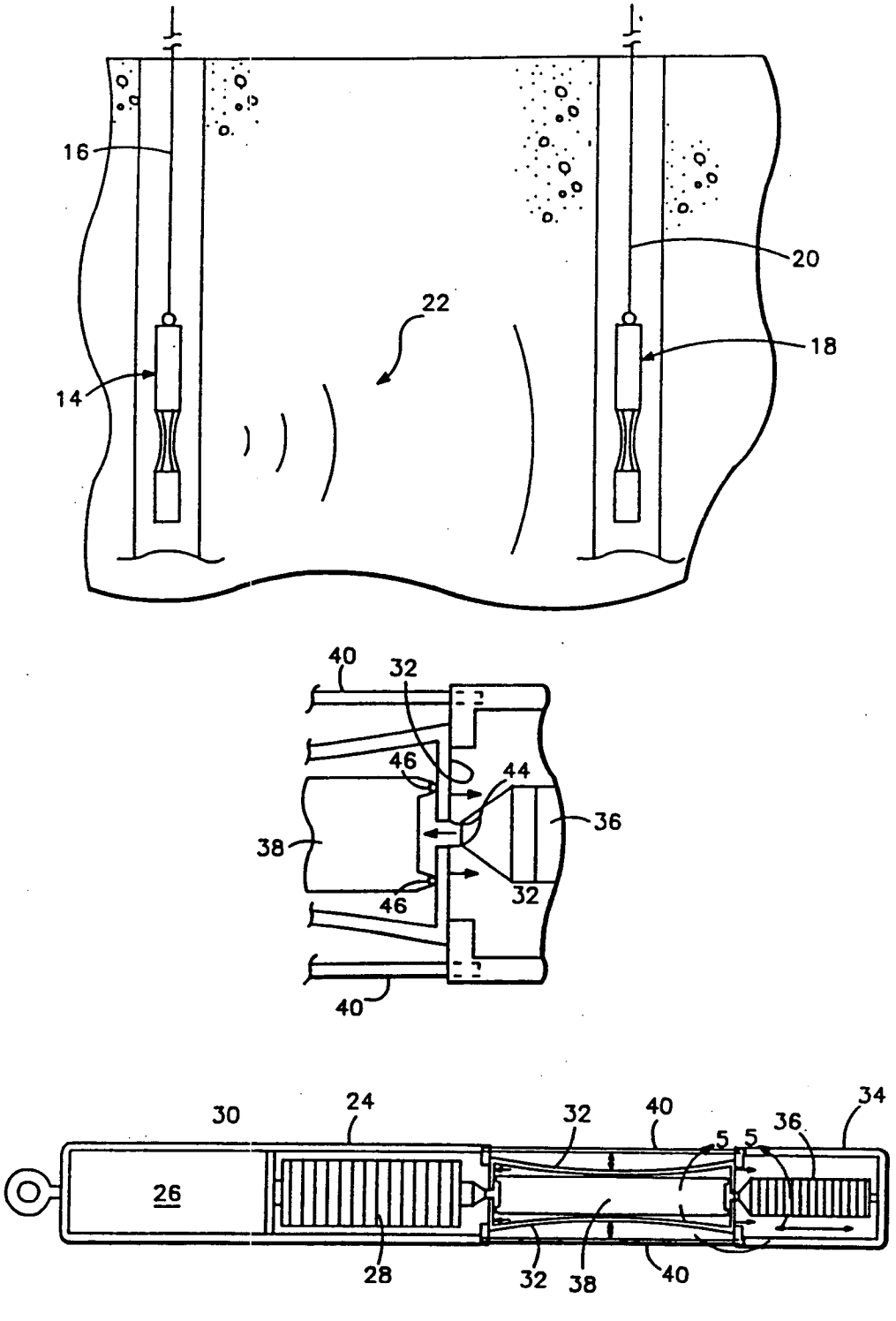

Figure C.2: This is a schematic drawing of the Low Impedance Cross-well Logging Downhole Source. The drawing is not to scale.

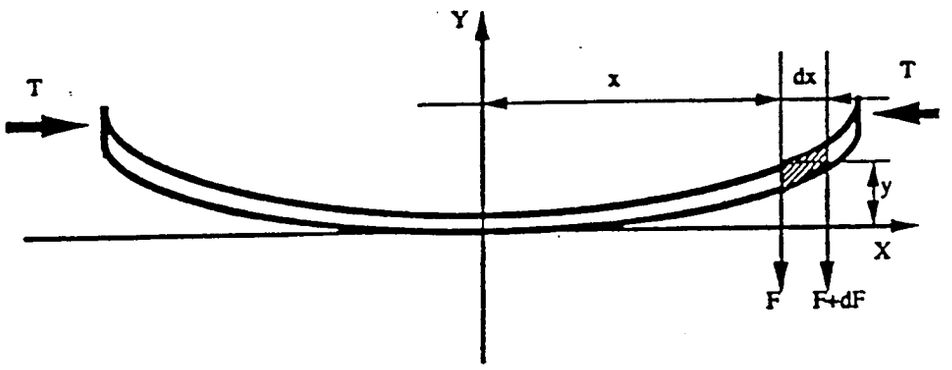

Figure C.3: Schematic drawing of a beam in transverse vibration mode. The driving force T is generated by the piezoelectric ceramic stack.

convex side. Ignoring the inertial properties of an element (dx) in rotation, the element motion at given position x along the beam will only be in the Y-direction as a function of time t, $y = f(x,t)$. The acceleration of the element can be expressed by $\partial^2 y/dt^2$. If the element (dx) has cross-section area a, mass $\rho a dx$, and second area moment I, then the force in the Y direction on the element is

$$\frac{dF}{dx} = \rho a \frac{\partial^2 y}{\partial t^2} \tag{C.14}$$

Hence, for the linear transverse motion, we have

$$-\rho a \frac{\partial^2 y}{\partial t^2} = -\frac{w}{g}\frac{\partial^2 y}{\partial t^2} = EI\frac{\partial^4 y}{\partial x^4} \tag{C.15}$$

where E is the Young's modulus of the material, ρ is material density, w is weight intensity per-unit length of beam, g is gravitational acceleration.

In the case of forced vibration, the equation of motion of an element of the beam can be expressed

$$EI\frac{\partial^4 y}{\partial x_4} + \rho a\frac{\partial^2 y}{dt^2} = T_{dyn}(x,t) - T_{damp}(y,t) \tag{C.16}$$

where $T_{dyn}(x,t)$ is time varying driving force distribution—PZT-stack generated dynamic driving force over unit length applied to the beams in the X-direction, $T_{damp}(y,t)$ is damping force of the borehole fluid on the surface of the vibrating beams which is a function of $\partial y/\partial t$.

The point of this analysis is to find the resonant frequency of the beam, so that it can be matched to the resonant frequency of the PZT-stack. Our beam has a rectangle cross-section, so its area moment of inertia is

$$I = \frac{bh^3}{12} \tag{C.17}$$

where b is the width of the beam's cross-section, and h is the thickness of the beam's cross-section.

Assume the beam has mass m_b, the mass of damping fluid m is applied to the center of the beam, and the length of the beam is l. Then, the natural angular frequency is

$$\omega_n = \sqrt{\frac{48EI}{l^3(m+0.5m_b)}} \tag{C.18}$$

If the beam has a uniform cross-section and a uniform distributed load, then the natural angular frequency is:

$$\omega_n = 22.4\sqrt{\frac{EI}{\mu l^4}} \tag{C.19}$$

where μ is the mass per unit length of the beam cross-section (Baueister, 1978).

With this first order approximation, one can design the natural frequency of the mechanical transformer's beams to match the natural frequency of the PZT-stack. In general, numerical modeling is needed to solve Equation C.16.

C.3.2 Optimum acoustic impedance matching

We have discussed impedance matching principle between the seismic source and its environment. In borehole environment, we need our source's acoustic energy to be coupled efficiently into the surrounding formations that we are investigating, not into the borehole fluid, the mud. By the theory of transmission line, we can either design the source diameter to make a fixed fluid layer thickness between the source and borehole wall, or change the impedance of the fluid layer. In most cases, we may not alter the borehole fluid density to match its acoustic impedance to the seismic source.

If the borehole source is operated in a cased well, the acoustic impedance of the casing Z_L as seen by the source cross over the surrounding borehole mud may be represented by the *Mason Equivalent Circuit* as

$$Z_L = Z_f\left(\frac{Z_s + Z_f \tanh(\phi t)}{Z_f + Z_s \tanh(\phi t)}\right) \tag{C.20}$$

where $\phi = \alpha + i(2\pi f/V_f)$, V_f is the velocity of fluid, f is the frequency of the source, Z_f and Z_s are the impedance of fluid and steel casing, respectively, and t is the thickness of the fluid layer between the source beams and borehole wall (Silk, 1984).

This relation may be useful since the apparent load becomes closer to the acoustic impedance of the source (about 2/3 Z_s). If this is assumed to represent the impedance matching, then Equation C.20 can be used to derive the appropriate value of the fluid thickness t. Since $Z_f \ll Z_s$, we may find that

$$t \simeq \frac{Z_f}{4Z_s}\lambda \tag{C.21}$$

where λ is the acoustic wavelength in the borehole fluid.

From this relation, the optimum fluid gap for coupling acoustic energy into steel casing is about 0.75% of the acoustic wavelength in liquid. Then the gap is just under *one inch* for vibrations with a frequency about 500Hz. The acoustic match degrades

once the liquid gap increases to about 1.0% of the wavelength—just over one inch in our example.

Other choices of suitable impedance matching techniques between two layers has been discussed by Desilets et al., (1978) which recognize the practical utilities of compact ultrasonic pulses.

C.4 Piezoelectric ceramic-stack design for down-hole purpose

Piezoelectric ceramic stack is the mechanical energy source where our borehole seismic source design begins. There are many advantages to use piezoelectric materials as "dynamic driver" of the source. With the piezoelectric ceramics, we can design a series stack having a displacement of up to a few hundred microns. The piezoelectric ceramics directly convert electrical energy into a linear movement, and the stack elements only absorb energy during expansion. It has the advantage of generating a large force to drive the mechanical transformer up to 30,000 Newtons. Thus, the transformer can achieve accelerations of a few thousand times gravity g over a displacement approaching micrometers.

C.4.1 Maximum displacement of PZT-stack

Figure C.4 is a schematic drawing of a PZT stack where the active part consists of many thin ceramic disks between which are thin metallic electrodes to feed in the operating voltage. The thinner the ceramic disk, the higher the electric field across each disk E. The stronger is the E, the greater is the displacement at a given operating voltage. Although the stack can withstand high compressive stress, it has a low tensile strength. For this reason, we design the mechanical transformer to pre-load the PZT stack, allowing it to operate at higher energy level without shattering on rebound from a powerful electric pulse, or from momentum of the transformer springs during resonant operation. in the way of giving the stack a pre-load and only

withstand load in expansion process.

The stack is arranged mechanically in series, and electrically in parallel, as shown in Figure C.4. The expansional displacement of the PZT stack depends on the ceramic substance used, its length l_o, the applied electric field strength, and the force F acting on it either in static or in dynamic operation. The total displacement ΔX can be expressed as

$$\Delta X = E \cdot d_{z3} \cdot n \cdot l_o + \Delta L_f \tag{C.22}$$

where E is the electrical-field strength applied to the ceramics ($E = V/l_o$), d_{z3} is a directional dependent PZT strain constant; n is the total number of ceramics consisting of the stack; l_o is the thickness of each individual ceramic; ΔL_f is the displacement due to pre-load force. The expansional displacement is limited by the maximum field strength with which each single ceramic can be operated without being damaged by dielectric breakdown and the resulting arcing.

In the static case, a piezoelectric stack can be viewed as an elastic body with a given stiffness, just like any other solid. If an external force F_l acts on it, then it will be compressed by the length $L_{fs} = F_l/C_t$, where C_t is the stiffness of the piezoceramics as found in any piezoelectric materials handbook. The bulk longitudinal stiffness of the stack also includes effects from the stiffness of the bonding materials.

In dynamic operation, the external force F_l acting on the stack depends on the expansion of the stack. In our design, the stack is slightly compressed by the transformer's beams. The beams act like a set of springs compressing the piezoelectric stack, whereby the force F_l increases with expansional displacement of the piezoelectric stack. The more rigid the transformer's beam spring constant C_s, the smaller is the displacement which the PZT-stack can offer when operating at a given E-field strength.

Hence, the effective expansion of the stack can be expressed as

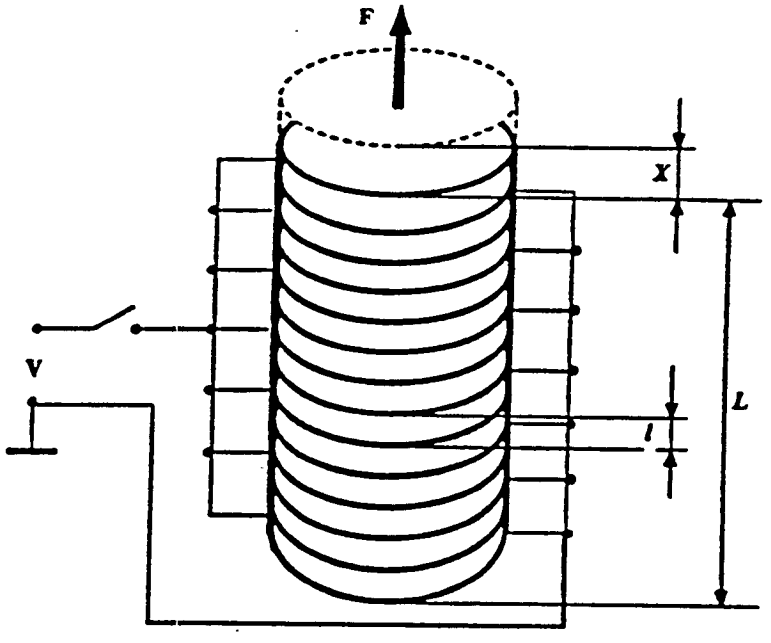

Figure C.4: Schematic diagram of the PZT-stack design and basic configuration of the ceramics. The total expansion of the stack is $\Delta X = d_{z3} \cdot n \cdot V$, where $V = E \cdot l_i$ is the voltage applied to the piezo-ceramics stack, and n is the total number of the ceramic elements. The total length of the stack is $L = \sum_{i=1}^{n} l_i = n \cdot l_o$, assuming each ceramic thickness is l_o.

$$\Delta X_{eff} = V \cdot d_{z3} \cdot n \frac{C_t}{C_t + C_s} \tag{C.23}$$

where C_t is the handbook value of PZT ceramic stiffness, C_s is the spring constant of the transformer beams.

C.4.2 Resonant frequency of PZT-stack

The resonant frequency f_o of a vibrating system depends on its elastic properties C_t and its effective mass m_{eff} as expressed by

$$f_o = \frac{1}{2\pi}\sqrt{\frac{C_t}{m_{eff}}} \tag{C.24}$$

The resonant frequency of a PZT-stack is also subject to this relation, whereby the effective mass is functions of both the stack mountings and any other masses attached to the stack. An external mass attached to the stack lowers the resonant frequency by increasing effective mass. An installed stack can resonate at a frequency very different from its theoretical value which assumes one end of the stack fixed and the other free.

The resonant frequency of a system with additional load can be expressed as

$$f_o' = f_o\sqrt{\frac{m}{m+M}} \tag{C.25}$$

where M is the additional loading mass.

PZT is characterized by rapid response time. If the electric field strength is suddenly increased, the displacement of PZT stack almost occurs instantaneously. This is very useful to stimulate shockwaves.

C.4.3 Dynamic force generated by PZT-stack

The maximum static force of a PZT stack depends on its compressive stiffness and its piezoelectric expansion capacity. If a PZT stack is attached between two rigid walls

so that it can not expand, then it generates a maximum force, or blocking force, of

$$F_{max} = C_t \cdot \Delta X_o \tag{C.26}$$

In the dynamic case, if a sharp voltage pulse is applied to a PZT-stack, the force generated is

$$F_{dyn} = \pm C_t \cdot \Delta X_{eff} = \pm 4\pi^2 \cdot m_{eff} \cdot \Delta X \cdot (f_o')^2 \tag{C.27}$$

Under dynamic loading, ΔX can exceed the static expansion at resonance by a factor of 3. To avoid tensile stress, one must use a mechanical pre-loading. This can be done by the mechanical transformer's spring beams in our design.

C.4.4 Heat accumulation in the PZT-stack

In a piezoelectric ceramics stack of capacity C charged at voltage V, electric energy ($W = 1/2CV^2$) may be stored. Most of the energy cycles back to the power supply, and about 5 to 8 % is converted into heat in the stack.

In static or low frequency operations, the heating of the stack can be neglected. However, the heat-accumulation can become important, if the stack is under dynamic operation at high frequency and high voltage.

The thermal heat Q generated in the stack can be estimated with the following equation

$$Q \approx tan(\delta) \cdot f_o \cdot C \cdot V^2 \tag{C.28}$$

$tan(\delta)$ is the angle loss and equals about 0.05, C is the stack capacitance, and V is the operating voltage applied to the stack.

The company "Physik Instrumente" has manufactured a PZT-stack based on our design. Table C.1 lists the specification of this PZT-stack.

Table C.1: Specifications of the PZT-Stack designed for the source

Expansion:	90 micron (0 to -1,000 V)
	135 micron (0 to -1,000 V)
	180 micron (+500 to -1,500)
Max. Pulling Force:	3500 N
Max. Pushing Force:	30,000 N
Stiffness C_t:	100 N/micron
Capacitance:	Approx. 2.28 μF
Resonant Frequency:	Approx. 1.8 KHz
Polarity:	Negative
Max. Operating Temp.:	200 C^o
Total Length:	Approx. 190 mm
Casing and End piece:	Stainless steel, thread M8.

C.5 Acoustic pressure generated by the source in the borehole environment

The downhole seismic source generates an acoustic pressure wave in the borehole fluid. In the fluid, the displacement caused by the mechanical transformer beams is proportional to the acoustic pressure gradient and described by

$$\frac{dP_a}{dy} = -\rho_f \cdot \omega_c^2 \cdot \Delta y \tag{C.29}$$

where P_a is the generated acoustic pressure in borehole fluid, ρ_f is the borehole fluid density, ω_c is the central frequency of the source, Δy is the maximum displacement of beam at $x = 0$, using the coordinate system of Figure C.1.

Integrating Equation C.29 yields the maximum acoustic pressure P_{max} generated by the source

$$P_{max} = -\int_0^{\Delta y} \rho_f \omega_c^2 \Delta y dy = -\rho_f \cdot \omega_c^2 \cdot (\Delta y)^2 \tag{C.30}$$

Substituting Δy above with the expression of Equation C.12 gives

$$P_{a-max} = -\rho_f \cdot \omega_c^2 \cdot (\frac{3a}{2b}\Delta x)^2 \tag{C.31}$$

By using the mechanical transformer to enlarge displacement, we have not only lowered the impedance but also enlarged the acoustic pressure for a magnitude $(\frac{3a}{2b}\Delta x)^2$.

C.6 Conclusion

The technology described in this appendix has several advantages over direct PZT sources in the borehole environment. It has larger output power and greater efficiency than the bend bar or cylindrical bend bar because the PZT ceramics operate in d_{33} mode. The source can be efficiently driven with either pulse or sweep sequences. It is our wish that this technology would soon be introduced by the logging industry. Application if this technology will enhance the practicality of cross-well seismic tomography as a powerful tool for investigating geologic structures, reservoir petrophysical properties, and for monitoring reservoir development.

References

Albers, V. M., 1965, Underwater Acoustics Handbook - II, University Park, Pa.: The Pennsylvania State Univ. Press, Chaps. 10-12.

Alliag, N. L., 1981, Real Elliptical Curves, North-Holland Publishing Company – Austerdam· New York· Oxford.

Auld, B. A., 1973, Acoustic Fields and Waves in Solids, Vol. 1, New York: John Wiley & Sons, Inc.

Baumeister, T. et al, 1978, Mark's Standard Handbook for Mechanical Engineers, McGraw-Hill Book Company.

Beranck, L. L., 1954, Acoustics, Mcgraw-Hill Book Company, Inc.

Berlincourt, D. A., Cursan, D. R. and Jaffe, H., 1964, Piezoelectric and Piezomagnetic Materials and Their Function in Transducers, in Physical Acoustics, Vol. I, W. P. Mason, ed., New York: Academic Press, Inc., Part A, Chapter 3, pp. 169-270.

Burdic, William S., 1984, Underwater Acoustic system Analysis, Prentice-Hall, Inc., Englewood Cliffs, NJ 07632.

Byrd, P. F. and Friedman, M. D., 1971, Handbook of Elliptical Integrals for Engineers and Scientists, Springes-Verlag New York Heidelberg Berlin.

Hamonic, B., and Decarpigny, J.N., 1988, Power Sonic and Ultrasonic Transducers Design, Springer-Verlag Berlin Heideberg.

Hueter, T. F., 1972, Twenty years in Underwater Acoustics: Generation and Reception, J. Acoust. Soc. Am., Vol. 51, No. 3, P-1025.

Kino, G. S., 1987, Acoustic Waves - Devices, Imaging and Analog Signal Processing, Prentice-Hall Signal Processing Series, Prentice - Hall, Inc.

MacGinley, T.J. and Ang, T.C., 1987,Structural Steelwork-Design to Limit State Theory, Butterworth & Co. Ltd.

Oswin, J. and Dunn, J., 1988, Frequency, Power and Depth Performance of Class IV Flextensional Transducer, Weymouth, Dorset, DT49TZ, United Kingdom.

Selfridge, A. R., 1985, Approximate Material Properties in Isotropic Materials, IEEE Trans. Sonic Ultrason., SU-32, No. 3, 381-394.

Silk, M.G., 1984, Ultrasonic Transducers for Nondestructive Testing, Adam Hilger Ltd, Bristol.

Spotts, M.F., 1985, Design of Machine Elements, Prentice- Hall, Inc., Englewood Cliffs, N.J. 07632

Stainless Steel Handbook, 1985, Allegheny Ludum Steel Cooperation.

Steidel, R.F.,JR., 1979, An Introduction to Mechanical vibrations, John Wiley & sons.

Walshaw, A.C., 1984, Mechanical Vibration with applications, Ellis Horwood Lit.

Wodlett, R. S., 1970, Ultrasonic Transducers: Part 2, Underwater Sound Transducers, Ultrasonics, Vol. 3, pp. 243-253.

Yin, H., Harris, J., and Nur, A., 1991, Low Impedance Down-hole Acoustic Source for Well Logging, U.S. patent, No, 5,069,308.